

IAEA-TECDOC-1292

***Development and characterization
of semiconductor materials
by ion beams***

Final report of a co-ordinated research project



INTERNATIONAL ATOMIC ENERGY AGENCY

IAEA

June 2002

The originating Section of this publication in the IAEA was:

Physics Section
International Atomic Energy Agency
Wagramer Strasse 5
P.O. Box 100
A-1400 Vienna, Austria

DEVELOPMENT AND CHARACTERIZATION OF
SEMICONDUCTOR MATERIALS BY ION BEAMS

IAEA, VIENNA, 2002

IAEA-TECDOC-1292

ISSN 1011-4289

© IAEA, 2002

Printed by the IAEA in Austria

June 2002

FOREWORD

With the aim of promoting research and facilitating more extensive applications of ion beam accelerators for development and characterization of advanced materials, the IAEA established in 1997 a Co-ordinated Research Project (CRP) on Application of MeV Ion Beams for Development and Characterization of Semiconductor Materials.

The CRP is based on applications of MeV ion beams for development and characterization of semiconductor materials with the main focus on the correlation between the structure of investigated materials and their physical properties important for their applications in electronic devices. The materials of concern are those currently used (or contemplated) in semiconductor devices, like CuInSe_2 and $\text{CuIn}_{1-x}\text{Ga}_x\text{Se}_2$ thin films, InGaAs/InP heterostructures, GaAs, GaN, LiNbO_3 , polycrystalline Si, CdTe, CdZnTe, etc. Specific topics include optoelectronic characterization of semiconductor materials and devices by ion microbeams, characterization of thin films, defect transformations in semiconductors, light element analysis in semiconductor materials and microfabrication of semiconductors using ion beams.

The first Research Co-ordination Meeting (RCM) was held in Vienna in June 1998, and the second RCM was held in Zagreb, Croatia, in September 2000. This publication includes results obtained from research undertaken prior to the completion of all contracts and agreements under this CRP in 2001.

As expected, a large amount of research was stimulated by this CRP and resulted in many publications in scientific journals. For example, the role of grain boundaries in the limitation of charge collection efficiency in CVD (chemical vapour deposition) diamond detectors with respect to natural diamond has been assessed and demonstrated. In addition, conditions for blister formation in GaAs were characterized. Possibilities to create oxygen-enriched layers on the surface of a GaAs single crystal were investigated by implantation of In ions. A ten-fold increase in oxygen atom content was observed in the transparent surface layers. Fabrication and properties of hydrogen and/or erbium containing optical layers in lithium niobate produced by annealed proton exchange were studied. The best electro-optic properties were found with the samples having uniformly distributed lithium atoms and very low content of hydrogen.

In addition, this CRP stimulated a number of collaborations between research groups that are expected to last much longer than the CRP itself. This includes associations between persons with very different research backgrounds. Further, a number of participating laboratories have significantly improved their analytical capability for materials characterization. These include developments in Rutherford backscattering spectrometry (RBS), elastic recoil detection analysis (ERDA), nuclear reaction analysis (NRA) and ion beam induced charge/ion beam induced luminescence (IBIC/IBIL) setups.

The IAEA wishes to thank all the scientists who contributed to the progress of this CRP. The IAEA officer responsible for the CRP and for this publication was S. Fazinic of the Division of Physical and Chemical Sciences.

EDITORIAL NOTE

This publication has been prepared from the original material as submitted by the authors. The views expressed do not necessarily reflect those of the IAEA, the governments of the nominating Member States or the nominating organizations.

The use of particular designations of countries or territories does not imply any judgement by the publisher, the IAEA, as to the legal status of such countries or territories, of their authorities and institutions or of the delimitation of their boundaries.

The mention of names of specific companies or products (whether or not indicated as registered) does not imply any intention to infringe proprietary rights, nor should it be construed as an endorsement or recommendation on the part of the IAEA.

The authors are responsible for having obtained the necessary permission for the IAEA to reproduce, translate or use material from sources already protected by copyrights.

CONTENTS

| | |
|--|-----|
| Summary of the co-ordinated research project..... | 1 |
| Characterization of semiconductor and frontier materials by nuclear microprobe technology..... | 15 |
| <i>Jieqing Zhu, Xiaolin Li, Changyi Yang, Rongrong Lu, Jiqing Wang, Panlin Guo</i> | |
| Characterization of semiconductor materials and devices by the IBIC technique..... | 27 |
| <i>M. Jakšić, Ž. Pastuović, T. Tadić</i> | |
| Real time monitoring of electronic materials and devices using microbeams | 41 |
| <i>C. Manfredotti</i> | |
| Study of LiNbO ₃ for optoelectronic applications by ion beam and neutron based analytical techniques..... | 55 |
| <i>J. Špírková, P. Nekvindová, H. Turčičová, J. Vacík, J. Červená, V. Peřina, V. Hnatowicz</i> | |
| Application of Rutherford backscattering and nuclear reaction analysis techniques for investigation of thin films | 67 |
| <i>Á.Z. Kiss, A. Simon, Z. Elekes, F. Ditrói, S. Mészáros, D.L. Beke, G.A. Langer, L. Daróczy</i> | |
| Influence of impurities on silicide contact formation..... | 75 |
| <i>Kh.R. Kazdaev, G.B. Meermanov, R. Kh. Kazdaev</i> | |
| Ion channeling study of defects in multicomponent semiconductor compounds..... | 83 |
| <i>A. Turos, L. Nowicki, A. Stonert</i> | |
| Study of impurity migration processes in semiconductors using the RBS, NRA, and ERD techniques..... | 97 |
| <i>L.P. Chernenko, A.Ju. Didyk, A.P. Kobzev, O.A. Nikonov, V.A. Skuratov M. Kulik, D. Maczka</i> | |
| Comparison of the results on the analysis of semiconductor materials by ERDA and RBS methods | 107 |
| <i>M. Budnar, P. Pelicon, A. Razpet, B. Zorko</i> | |
| Study of the composition of CuInSe ₂ and CuIn _{1-x} Ga _x Se ₂ semiconductor thin films prepared by evaporation followed by annealing using RBS and PIXE and their properties..... | 117 |
| <i>S.M. Firoz Hasan, M. Khaliqzaman, S. K. Biswas, L. Quadir, M. Asad Shariff, M. Mashiur Rahman</i> | |
| Abbreviations | 127 |
| Contributors to Drafting and Review | 129 |

SUMMARY OF THE CO-ORDINATED RESEARCH PROJECT

1. Introduction

This CRP was recommended by the Consultants meeting on Ion Beam Techniques Applied to Semiconductor and Related Advanced Materials, held in April 1997 in Vienna. The consultants proposed to have a CRP in the field of application of MeV ion beams for the development and characterization of semiconductor materials.

The CRP was approved and a first RCM was held in Vienna between 2–5 June 1998, in order to stimulate ideas and to promote collaborations among CRP participants. The goals and practical outcomes of the CRP were defined and several specific topics were identified including: optoelectronic characterization of semiconductor materials and devices by ion microbeams, characterization of thin films, defect transformations in semiconductors, light element analysis. One important recommendation was that sample exchanges among different laboratories be strongly encouraged. The participants presented individual activities on their projects, all subjects of research were identified and linked with approved individual projects. Collaboration among the participants was discussed and established. Some modifications to work plans were adopted.

As proposed during the first RCM, the final RCM was held at the Ruđer Bošković Institute, Zagreb, Croatia, between 25 and 29 September 2000, with the purpose of reviewing/discussing the results achieved during the course of the CRP and to prepare a draft of the final report and associated publication.

The exceptional success and the achievements obtained in this CRP and the strength of collaborations that developed among different laboratories was generally noted.

2. Research collaboration within the CRP

There were many active international collaborations stimulated by this CRP. These collaborations involved exchanging of samples, computer programs, data bases, ideas, etc. The two tables below indicate some of these collaborations. Table I presents collaboration between CRP participants in the topic of optoelectronic characterization of semiconductor materials and devices using microbeams. Table II is primarily involved with research topics related to characterization of thin films, defect transformations in semiconductors and light element analysis, indicating exchange of samples between different CRP groups.

3. Summary of the CRP Research Results

The following sections present the brief summaries of the CRP research results. The results are presented for each research topic, as defined during the first RCM.

TABLE I: COLLABORATION MATRIX WITHIN THE TOPIC OF OPTOELECTRONIC CHARACTERIZATION OF SEMICONDUCTOR MATERIALS AND DEVICES BY ION MICROBEAMS

| Activity/group | GB | RR | RD | DP | IBIL | IBIC | MC |
|----------------|----|----|---------|---------|------|---------|----|
| EPD | A | a | a, b, c | a, b, c | a | a, c, f | g |
| IRB | E | | a, d, f | a, d, f | | a, c, f | |
| SINR | A | | a | a, c | | a, c, f | g |

EPD Experimental Physics Department, University of Torino

IRB Ruder Boskovic Institute, Zagreb

SINR Shanghai Institute of Nuclear Research

| Problem/activity Related symbols: | Material related symbols (exchanged samples): |
|--------------------------------------|--|
| GB Grain boundaries | a CVD diamond |
| RR Radiative recombination | b Natural diamond |
| RD Radiation damage | c GaAs |
| DP Detector performances | d CdTe/CZT |
| IBIL Technology improvement | e Polysilicon |
| IBIC “ “ | f Silicon |
| MC Material chips | g Test material (SiO ₂ on Si) |

TABLE II: COLLABORATION MATRIX WITHIN THE TOPICS OF THE CRP (EXCEPT COLLABORATION IN THE TOPIC OF OPTOELECTRONIC CHARACTERIZATION ... SEE TABLE 1)

| Sample Source | Analyst | | | | |
|---------------|---|--|---|--|--|
| | IJS | UA | AEC | ATOMKI | JINR, Dubna (Kobzev) |
| AEC | CuIn _{1-x} Ga _x Se ₂ RBS | CuIn _{1-x} Ga _x Se ₂ RBS | | CuIn _{1-x} Ga _x Se ₂ RBS | - |
| UA | TaN _x -RBS Ge-H-Si-O/Si-RBS H samples-ERDA | - | TaN _x -RBS Ge-H-Si-O/Si-RBS | - | - |
| JSI | - | - | TiN, Cu,N, etc.-RBS | - | - |
| ICT | LiNbO ₃ -RBS&ERDA Intercomparison LiNbO ₃ -RBS&ERDA | - intercomparison LiNbO ₃ -NRA | - - | - - | - intercomparison LiNbO ₃ -ERDA |
| ATOM KI | - | Si-Ge multilayer- RBS | - | | Si-Ge multilayer -RBS |
| EPD | - | CVD Diamond- RBS | - | CVD Diamond- NRA | - |
| SINS | GaN-RBS&ERDA | H in GaAs-NRA H in GaN-NRA | - | - | - |

3.1. Optoelectronic Characterization of Semiconductor Materials and Devices using Microbeams

3.1.1. THE ROLE OF GRAINS AND GRAIN BOUNDARIES IN THE LIMITATION OF CHARGE COLLECTION EFFICIENCY IN CVD DIAMOND DETECTORS AND OF CONVERSION EFFICIENCY IN POLYCRYSTALLINE SOLAR CELLS

Partners

Experimental Physics Dept., University of Torino — EPD (C. Manfredotti)*
Shanghai Institute of Nuclear Research — SINR (J. Zhu)
Rudjer Boskovic Institute, Zagreb — IRB (M. Jaksic)

Results

High spatial resolution IBIC (Ion Beam Induced Charge) and IBIL (Ion Beam Induced Luminescence) images have been obtained in natural diamond and in CVD (Chemical Vapour Deposition) diamond. Spatial resolution is of the order of 1 μm . Images obtained were covering sample surface areas up to 2 mm \times 2 mm. Two dimensional IBIC maps referring to a specific depth have been obtained by using ions of different energies (protons, alphas, lithium, etc.). IBIL maps have been deconvoluted in order to obtain images related to specific luminescent centres in CVD diamond. Contamination at the grain boundaries of CVD diamond due to the segregation of heavy elements has been carried out by PIXE and RBS (in collaboration with University of Albany, (UA). Contaminations due to Fe, Ti and W have been identified. The role of grain boundaries in the limitation of charge collection efficiency in CVD diamond detectors with respect to natural diamond has been assessed and demonstrated. Charge collection lengths have the same values as dimensions of single grains. Good superposition of IBIC maps and SEM (Scanning Electron Microscopy) images carried out in the same zones have been obtained. IBIC and IBIL images are almost complementary, with the conclusion that collection length of carriers in CVD diamond is limited by radiative recombination at or (more likely) close to the grain boundaries. Grain boundaries were also studied in polycrystalline Si solar cells. Decrease of the IBIC response along the twin boundaries in EFG (Edge-defined Film-fed Grown) silicon was not always related to the position of boundary, indicating passivation of charge traps by impurities. CVD diamond and polycrystalline Si solar cell samples have been exchanged between partners. A visiting scientist (R. Lu) from SINR has spent two years at EPD, Torino.

3.1.2. CHARGE COLLECTION EFFICIENCY DISTRIBUTION IN NUCLEAR RADIATION DETECTORS. EFFECT OF DEAD LAYERS, RADIATION DAMAGE, UNDEPLETED REGIONS, BIAS VOLTAGE AND CONTACTS ON DETECTOR PERFORMANCE

Partners

EPD (C. Manfredotti)*
SINR (J. Zhu)
IRB (M. Jaksic)

Results

Charge collection efficiency has been investigated in CVD diamond, GaAs, CdTe, CZT (Cadmium Zinc Telluride) and Si nuclear radiation detectors. Dead layer contributions to the local decrease of charge collection efficiency have been seen in CdTe and in Si. The spatial distribution of dead layer thickness was measured for several Si(Li) X-ray detector crystals, indicating the origin of incomplete charge collection in these detectors.

Radiation damage effects have been studied in several materials, including natural diamond, both at low doses (“priming effect”) and at large doses. The “primed state” has been deeply investigated in CVD diamond by lateral IBIC as far as spatial effects are concerned: a lengthening of the high collection efficiency regions towards the electrodes and an associated progressive disappearing of low collection efficiency regions has been observed and attributed to a progressive disappearing of space charge zones. Large dose effects have been observed in GaAs Schottky diodes

(uniform decrease of the collection efficiency) and in CVD diamond (exponential decrease of ionoluminescence). Irradiation of well defined areas of CdTe and CZT detectors resulted in a decrease of charge collection efficiency in larger regions than originally irradiated.

The role of undepleted or diffusion regions has been investigated in Si and a specific code has been written in order to obtain the diffusion length of minority carriers from lateral IBIC collection efficiency profiles. Bias voltage effects have been studied in CVD diamond, Si and GaAs and the displacement of the depletion layer as a function of the bias voltage has been directly observed by lateral IBIC. Finally, the role of contacts in the spatial decrease of charge collection length has been observed in GaAs by frontal IBIC and in CdTe and Si by lateral IBIC. Influence of contact materials (In and Au) was studied for CZT.

3.1.3. TECHNOLOGY AND METHODOLOGY IMPROVEMENTS IN IBIC AND IBIL

Partners

IRB (M. Jaksic)*
EPD (C. Manfredotti)
SINR (J. Zhu)

Results

A completely new monochromatic IBIL set up has been built, with an almost complete light collection by an ellipsoidal mirror and a high-resolution wavelength scanning by an external 0.3 m monochromator. The system is fully transportable and it can be easily inserted in suitable scattering chambers and in electron microscopes for cathodoluminescence measurements.

The concept of variation the ion range was introduced in most of IBIC measurements in order to probe various sample depths. In some cases, use of different ions with the same rigidity enabled simple changes in the sampling depth without disturbing the beam optics of accelerator and microprobe. The sample-to-preamplifier distance has been minimized by using special hybrid preamplifiers inserted in the scattering chambers very close to the sample. Tests have been carried out on CVD diamond, GaAs and Si. The data acquisition system has been implemented for on line presentation of mean pulse height intensity for each pixel, enabling minimisation of sample damage by excessive irradiation. A SEIM (Secondary Electron Ion Microscopy) apparatus has been set up in order to compare images with IBIC maps and to identify ion hit position. SEIM images are presently obtained. Micromachining by ion beam lithography in Si has also been attempted with some success.

3.1.4. ION BEAM ANALYSIS FOR COMBINATORIAL MATERIAL CHIP (LIBRARY) SYNTHESIS

Partners

SINR (J. Zhu)*
EPD (C. Manfredotti)

Results

A method has been developed by combining ion implantation and physical masking techniques in order to generate a material library of various ion-implanted samples. Six ion species (C, Ga, N, Pb, Sn and Y) were sequentially implanted to an SiO₂ film grown on a Si wafer through six combinatorial masks. Consequently a material chip (library) with 64 (2⁶) samples was generated. Micro-RBS and micro-PEB (Proton Elastic Backscattering) are applied for characterization of the samples on the material chip to determine the depth-resolved ion distribution in individual samples. It is revealed by the spectrum for co-implanted sample S(Ga, C) that the existence of C induces redistribution of Ga in the SiO₂ film after thermal annealing. The spectrum for co-implanted sample S(Pb, Sn, N) shows that Sn diffusion toward the surface is evident, which causes high luminescent emission from the film when bombarded by an electron beam. This experiment was a successful

combination of ion beam implantation and ion beam analysis for generation of a combinatorial material chip (library). This approach greatly increases the efficiency of the new material synthesis, analysis and optimisation.

3.2. Characterization of thin films

3.2.1. CROSS COMPARISON OF RBS ANALYSIS OF $\text{CuIn}_x\text{Ga}_y\text{Se}_z$ THIN FILMS

Partners

Atomic Energy Centre — AEC (M. Khaliqzaman)
Jozef Stefan Institute- JSI (M. Budnar)
Institute of Nuclear Research, Hungarian Academy of Sciences -ATOMKI (A. Z. Kiss)
University of Albany SUNY — UA (W. Lanford)*

Results

The CuInSe_2 and $\text{CuIn}_{1-x}\text{Ga}_x\text{Se}_2$ samples prepared at AEC were sent to JSI, UA, and ATOMKI. In addition, several thin film standards (TiN , CuN , etc.) were prepared at JSI and UA (TaN_x , SiGe_x) and mailed to AEC.

These samples from AEC in Dhaka were extremely challenging samples. The difficulties were: there were several elements with nearly the same mass and the films were not homogeneous in depth. Different laboratories chose different approaches to overcome these difficulties. One approach was to make a detailed modelling of the spectra from 2 MeV data. A second was to raise the beam energy to (at least partially) separate the different elemental peaks. In addition, PIXE and XRF measurements were made on some samples. Because the analysis of these samples was not straightforward, there were numerous communications between AEC and the laboratories making the RBS measurements, including exchange of raw data and other RBS samples.

The AEC group prepared a report describing this work.

3.2.2. DEVELOPMENT OF THE BEST PROCEDURE FOR DETERMINATION OF THE INTERDIFFUSION OF Si AND Ge IN Si/Ge AMORPHOUS SUPERLATTICE THIN FILMS.

Partners

Institute of Nuclear Research of the Hungarian Academy of Sciences — ATOMKI
(A.Z. Kiss)*
Jozef Stefan Institute — JSI (M. Budnar)
University of Albany SUNY — UA (W. Lanford)
Joint Institute for Nuclear Research — JINR (A. Kobzev)

Results

Amorphous Si-Ge multilayers were prepared by DC magnetron sputtering from alternating elemental targets onto (001) silicon wafers at ATOMKI in Debrecen. The modulation wavelength was designed to range from 10 to 40 nm with nearly equal thickness of Si and Ge sublayers. The total thickness of the Si-Ge films varied from 55 to 220 nm.

The initial plan was to do *in situ* annealing. However, the (unexpectedly) long annealing time (150 hours) — which was needed to achieve measurable intermixing of Si and Ge — made it necessary to perform annealing in a separated vacuum chamber.

The first RBS analyses were performed in Debrecen. The interdiffusion coefficient was determined by measuring the intensity of the first Ge peak in the RBS spectrum as a function of annealing time. As the mobility of the Si is approximately eight times higher than that of the Ge, the

intermixing in Si-Ge multilayers is asymmetrical. Therefore a thickening of the Ge layer is expected to occur. However for the direct observation of this effect very good energy resolution is needed. This makes important to compare the instrumentation available in different laboratories.

Planar alpha particle detectors with better resolution (10 keV) were available in JINR and, hence, samples were also sent there. As expected, the results from JINR show a much better peak/valley ratio than seen at ATOMKI. The full thickness of each Ge layer was about 13 nm and the full thickness of each Si layer was about 23 nm, including the mixed layers with a thickness of about 6.5 nm. Measurements of unannealed samples were also made at UA with high-resolution magnetic spectrometer. These higher resolution spectra provide a more sensitive measurement of the Si-Ge interdiffusion and more measurements with annealed samples are planned in the future.

3.2.3. CROSS COMPARISON OF RBS PROCEDURES FOR “GENERAL” THIN FILM SAMPLES

Partners

Jozef Stefan Institute- JSI (M. Budnar)*
University at Albany — UA (W. Lanford)
Atomic Energy Centre — AEC (M. Khaliqzaman)

Results

The TaN_x samples from UA were sent to JSI and AEC for the RBS measurements and analysis. At JSI the current-normalized RBS measurements with 1.8 MeV He¹⁺ beam were performed, scattering angle was 160°, incidence was at 90°, and charge was 5 μC (with 5 nA current). These measurements showed that the determination of the stoichiometry composition in TaN_x films was strongly dependent on the accuracy of measuring the beam current. By electric insulation of the entire measuring chamber a precise current normalization of the RBS spectra was achieved. The cross-comparison of the results demonstrated the failure of the substrate normalization approach for this type of sample. The data obtained by *the current normalization method* led to excellent agreement between the JSI and the UA results. Due to wide interest in thin nitride layers (tool coatings, surface hardening, microelectronics, etc.) the cross-comparison study resulted in benefits which are of great importance for further IBA studies at JSI.

For further testing of the RBS arrangements two different Ge-H-Si-O/Si samples (H239, H289) were additionally prepared at UA, and sent to JSI and AEC for analysis. For this purpose the He¹⁺ ions had energy of 2.03 (2.1) MeV, RBS scattering angle was 150° (160°), and the charge collected was 10 μC at the JSI measurements.

3.2.4. MOLYBDENUM SILICIDE FORMATION BY ION IMPLANTATION

Partners

Institute of Nuclear Physics — JNP (K. Kazdaev)*

Results

In the study of this problem, it was found that light element impurities (C,N,O) influence silicide formation. For example, the combined implantation of Si and impurities in Mo resulted in the more metal rich silicide (Mo₅Si₃) compared with the MoSi₂ without light element implantation. It was also demonstrated that implantation into the interface between Mo and Si, could destroy the native SiO₂ layer, which, in turn, decreased the silicide formation temperature from 1000 C to 800 C. This implantation across the interface also resulted in an approximately 50% reduction in the conductivity of the silicide formed.

3.2.5. RBS ANALYSIS OF Er IN LiNbO₃

Partners

Institute of Chemical Technology in Prague — ICT (J. Spirkova)*

Results

Samples containing Er³⁺ were fabricated by novel moderate temperature (350 °C) diffusion doping at the Institute of Chemical Technology in Prague. These samples were analysed using RBS at the Institute of Nuclear Physics in Rez. The results of the doping were compared with reference samples fabricated by a standard high temperature approach. Samples with X-cuts (110) were always found to have much more erbium (up to 12 wt.%) compared with the Z-cut (001), where the erbium content did not exceed that one achieved by the standard high temperature procedure (≈ 1 wt.%). The strong anisotropy of the doping was explained on the basis of suitable orientation of the X-cut towards the cleavage planes of the lithium niobate crystals. This hypothesis was confirmed by the moderate temperature in-diffusion of Er³⁺ into various substrate cuts of sapphire which has the same basic crystal structure as LiNbO₃.

3.3. Defect Transformations in Semiconductors

3.3.1. STUDY OF THE SMART-CUT IN GaAs

Partners

Soltan Institute for Nuclear Studies — SINS (A.Turos)*
University at Albany — UA (W.A.Lanford)

Results

Conditions for blisters formation were investigated. Blistering is directly responsible for the formation of microcracks which in turn produce layer splitting. No blistering was observed at temperatures below 100°C even after implantation with a dose as large as 4×10^{17} H/cm². In order to provoke blistering in such samples an annealing at temperatures exceeding 400°C is necessary. Blistering is much more easily obtained upon hot implantation. There are two distinct temperature regions: at temperatures below 90°C no blisters were found, whereas, at temperatures exceeding 120°C appreciably high blister density can be observed. In the second range the temperature at which blistering occurs depends on the implantation dose. The growth of blister dimensions with increasing implantation temperature is reflected in the rapid increase of surface roughness.

GaAs samples implanted with hydrogen were sent to Albany for H-profiling.

A.Turos visited UA in May 1999.

3.3.2. EPITAXIAL LAYER CHARACTERIZATION AND DEFECT ANALYSIS IN COMPOUND SEMICONDUCTORS

Partners

SINS (A.Turos)
UA (W.A.Lanford)

Results:

i) Radiation Damage in InGaAs/InP Heterostructures

A procedure of spectra evaluation has been developed enabling the separate analysis of different sublattices of a layer. Both sublattices of InGaAs epitaxial layers exhibit the same damage buildup behavior upon ion implantation. The amorphisation dose for RT implantation with 100 keV ions of mass about 80 amu is approximately 5×10^{13} at/cm².

ii) Low Temperature Irradiation of GaN

A small recovery stage in N ion implanted GaN was observed at 70 K revealing that the mobility of simple defects, i.e. selfinterstitials or vacancies belonging to the Ga sublattice. The observed stability of defects in Xe-ion bombarded GaN may be due to defect clustering around Xe atoms. In contrast, such an effect was not observed in GaN implanted with miscible elements like Te.

iii) High Temperature Ion Implantation in GaN

After RT implantation, small defect clusters of different size and morphology were formed. The increased defect mobility during ion implantation at 600°C and 700°C resulted in the defect migration to the larger depths and enhanced defect clustering. Important changes were observed after implantation at 800°C. RBS/channeling analysis provided evidence that these defects are predominantly stacking faults.

iv) Characterization of InGaN/GaN Heterostructures

The great advantage of RBS/channeling when applied to analysis of InGaN layers is that it allows direct determination of variety of parameters. These are: In content in strained layers, magnitude of tetragonal distortion and strain, and the crystal lattice quality.

v) Monte Carlo Simulation of Channeling Spectra

The Monte Carlo method for channeling spectra simulations enables not only detailed analysis of the perfection of the crystalline structure of analyzed samples but can also provide information on physical parameters difficult or even impossible to obtain using other experimental methods. This especially concerns the amplitudes of thermal vibration of lattice atoms. Monte Carlo evaluation of channeling spectra taken at different temperatures can be used for determination of such amplitudes and consequently of Debye temperature.

3.4. Light element analysis

3.4.1. DETERMINATION OF THE H CONTENT IN APE LITHIUM NIOBATE

Partners

Institute of Chemical Technology Prague — ICT (J.Spirkova)
Nuclear Physics Institute, Czech Academy of Sciences — NPI CAS (J.Vacik)
University of Albany UA — UA (W.Lanford)
J.Stefan Institute — JSI (M.Budnar) *
Joint Institute for Nuclear Research — JINR (A.Kobzev)

Results

For H profiles determination in annealed proton exchanged (APE) lithium niobate (LiNbO₃) the ERDA arrangement at JSI has been chosen. The profiles obtained showed good agreement with the previously measured Li profiles, as determined by the neutron depth profiling (NDP) method at NPI CAS. Namely, higher concentrations of hydrogen on the surface correspond to lower Li concentration what confirm the PE expectations for the particular cuts.

Besides the task above, some selected LiNbO₃ samples were studied on H profiles in collaboration between ICT, UA, JINR, and JSI. The APE samples prepared at ICT were distributed to the other three institutions and the comparative analysis was performed. At UA the hydrogen analysis of the ICT samples was done by the ¹⁵N nuclear reaction method. The JINR laboratory applied the RBS, NRA and ERDA methods. For ERDA at JNRI the 2.336 MeV He ions were used. The JSI group made the analysis by ERDA method with 1.8 MeV He¹⁺ ions. The results show reasonable agreement within 20–30%.

3.4.2. DETERMINATION OF THE H CONTENT IN GaN

Partners

Soltan Institute for Nuclear Studies — SINS (A.Turos) *

UA — (W.Lanford)

JSI — (M.Budnar)

Results

GaN samples sent to JSI and UA showed that single crystals contain less than ≈ 0.1 at% of H, which is the detection limit of the methods. On the other hand thin foils and sintered powders contained between 0.5 to 5 at% of H depending on the growth conditions. However, no direct correlation was observed.

Extensive H out-diffusion was observed at the beginning of the analysis indicating release of hydrogen atoms from the outermost layers. After this initial period the reaction yield has stabilized.

3.4.3. DETERMINATION OF N IN CVD DIAMOND

Partners

Experimental Physics Department, University of Torino — EPD (C. Manfredotti)

Institute of Nuclear Research of the Hungarian Academy of Sciences — ATOMKI (A. Kiss) *

Results

Before making measurements on these diamond samples, the evaluation of the reported yields of deuteron induced gamma ray emission (DIGE) from thick target materials measured earlier was done in order to provide the basic data needed for the planned measurements.

CVD diamond as a pure carbon material produce high intensity gamma yield with energies less than 7 MeV if bombarded by deuteron beam. From nitrogen the most intensive gamma ray produced well above 7 MeV, at 7.3 MeV. Moreover there are gamma rays also at 8.3 and 9.1 MeV, giving an additional yield to the 7.3 MeV gamma rays. The concept of the measurement was to use a large volume composite HPGe detector (a so called CLOVER detector, having high efficiency for high energy gamma rays), and put a discrimination level for the gamma signals at 7 MeV.

Test measurements using nitrogen containing samples like kapton, or α -benzoinoxin showed good results. However the determination of the 10 ppm or less nitrogen content of the CVD diamond samples provided by EPD was not possible because of the disturbing pile up produced by the intense gamma rays from carbon. A considerable improvement of the detection electronics would be needed to reach the detection limit necessary for the study of CVD diamonds.

3.4.4. OXYGEN IN Si/Ge THIN FILM AMORPHOUS SUPERLATTICES

Partners

ATOMKI (A.Kiss)

UA (W.Lanford)

JINR (A.Kobzev) *

Results

The determination of the depth profiles of oxygen atoms in the Si-Ge multi-layer structure was carried out using the ^{16}O (^4He , ^4He) ^{16}O nuclear reaction that has a very narrow and intensive resonance at the energy of 3.045 MeV. For each sample some spectra were measured in the energy region from 3.03 MeV to 3.11 MeV.

The experimental spectra are in agreement with the calculated ones in all details and with good precision. Moreover, only one model of the multilayer structure have been used for the description of all experimental data obtained at different energies.

A layered structure with the degraded interface has been observed. All layers contained some oxygen impurity (10–13 at%) and there was a SiO_2 layer with the thickness of 17.7 nm situated between the multilayer structure and Si wafer.

3.4.5. DETERMINATION OF O IN APE LITHIUM NIOBATE OPTICAL WAVEGUIDES

Partners

ICT (J.Spirkova) *
NIP CAS (J.Vacik)
JINR (A.Kobzev) *

Results

Six samples (two standards plus four APE samples) fabricated at ICT were sent to JINR for the Proton Backscattering Measurement. The scattering of 1.754 MeV protons allowed measuring the oxygen concentrations at the depth up to 10 μm . It was found that the concentration of oxygen in the APE samples did not change with the depth. The Nb : O ratio remained the same as in the pertinent X- and Z-cut standards, *i. e.* approx. 1 : 3.

3.4.6. CROSS COMPARISON OF ERDA H STANDARDS

Partners

UA (W.Lanford)
JSI (M.Budnar) *

Results

Two H standards (ASM20, ASM35) as prepared at UA were sent to JSI, and analyzed on H profiles by ERDA method. The He^{1+} ions with energy of 1.8 MeV were applied at 77.5° incidence, take-off angle for ERDA was 24° (Al foil 6 μm), take-off angle for RBS was 150° , and collected charge was 20 μCb . The same samples were analyzed with NRA at UA. The intercomparison gives satisfactory results. It is worth to mention that the JSI ERDA arrangement and analytical procedures used have been checked extensively before the above task. In this respect several samples with known H composition, or the ones with known H profiles, had been previously measured.

3.4.7. Li DEPLETION IN APE LITHIUM NIOBATE OPTICAL WAVEGUIDES

Partners

ICT (J.Spirkova) *
NPI CAS (J.Vacik)
Institute of Physics of Czech Academy of Sciences — IP CAS (H.Turcicova)
JSI (M.Budnar)

Results

Maximal depth of the PE layers was 3 μm in both Z- and X- cuts. Annealing of the as-exchanged (PE) samples is the most important step of the APE procedure as it causes a massive transport of lithium from the bulk substrates towards the samples surfaces. Quite generally, the APE X-cuts exhibit more step-like characters of the c_{Li} depth profiles than the Z-cuts indicating a rather different mechanism of formation of the wave-guiding layers. Prevailing mechanism of hydrogen incorporation into the Z-cut structure is substitution of H^+ for Li^+ which is in the X-cut strongly accompanied by an interstitial in-diffusion of the H^+ . The H^+ species form barriers that prevent lithium from moving towards the surfaces during annealing of the samples. The extraordinary refractive index (n_e) and c_{Li} depth profiles have the same shapes but the actual n_e vs. c_{Li} dependence depends on fabrication conditions and structural phases of the wave-guiding layers. The samples with the best electrooptic properties had almost uniform distribution of lithium and very low content of hydrogen. The anisotropy of the H^+ in-diffusion into the lithium niobate substrates is explained on the bases of suitable orientation of the X-cut wafers towards the cleavage planes of the lithium niobate crystal.

Visits exchange

Within the frame of CRP the following visits related to the above subject (4.4.7.) have been realised through the funds of the participating institutions:

- in 1998 : J.Spirkova, H.Turcicova, P.Nekvindova, and M.Slunecko to JSI, Ljubljana
- in 1998 : M.Budnar to ICT, IP CAS, Prague, and to NPI CAS, Rez
- in 2000 : P.Nekvindova to JSI, Ljubljana

4. Conclusions

The goals outlined in the first RCM have been followed closely by CRP members. Indeed, the organization of research results presented in the previous section of this report follows the same list of topics presented in the first RCM report. Namely, all are sub-topics of the following four general problems: *Optoelectronic characterization of semiconductor materials and devices by ion microbeams*, *Characterization of thin films*, *Defect transformations in semiconductors*, and *Light element analysis*.

It is clear from the activities undertaken in the program that MeV ion beam analysis is a key technology in both developed and developing countries. As expected, a large amount of research was stimulated by this CRP and resulted in many publications in scientific journals. In addition, this CRP stimulated a number of collaborations between research groups that are expected to last much longer than the CRP itself. This includes association between persons with very different research backgrounds. Further, a number of participating laboratories have significantly improved their analytical capability for materials characterization. These include developments in RBS, ERDA, NRA and IBIC/IBIL setups. We believe that these improvements in analytical infrastructure will have important positive effects on future educational opportunities and economic developments in participating countries.

PUBLICATIONS OF THE CRP PARTICIPANTS RELATED TO THE RESEARCH TOPICS

VITTONI, E., MANFREDOTTI, C., FIZZOTTI, F., MIRRI, K., GARGIONI, E., POLESELLO, P., LO GIUDICE, A., GALASSINI, S., NAVA, F., VANNI, P., ROSSI, P., IBIC analysis of gallium arsenide Schottky diodes, Nucl. Instr. and Meth. **B158** (1999) 470–475.

MANFREDOTTI, C., FIZZOTTI, F., GARGIONI, E., LU, R., POLESELLO, P., LO GIUDICE, A., VITTONI, E., GALASSINI, S., JAKSIC, M., Evaluation of the diffusion length in silicon diodes by means of lateral IBIC, Nucl. Instr. and Meth. **B158** (1999) 476–480.

- MANFREDOTTI, C., FIZZOTTI, F., POLESELLO, P., VITTONI, E., IBIC investigation on radiation induced effects in CVD and natural diamond, *Nucl. Instr. and Meth.* **A426** (1999) 156–163.
- NAVA, F., VANNI, P., CANALI, C., VITTONI, E., POLESELLO, P., BIGGERI, U., Plasma effect on charge collection efficiency in proton irradiated GaAs detectors, *Nucl. Instr. and Meth.* **A426** (1999) 185–191.
- MANFREDOTTI, C., FIZZOTTI, F., LO GIUDICE, A., POLESELLO, P., VITTONI, E., LU, R., JAKSIC, M., Ion Microbeam Analysis of CVD Diamond, *Diamond and Related Materials* **8** (1999) 1597–1601.
- JAKSIC, M., PASTUOVIC, Z., TADIC, T., New developments of IBIC for the study of charge transport properties of radiation detectors, *Nucl. Instr. and Meth.*, **B158** (1999) 458–463.
- MANFREDOTTI, C., FIZZOTTI, F., LO GIUDICE, A., POLESELLO, P., VITTONI, E., TRUCCATO, M., ROSSI, P., Ion beam induced luminescence maps in CVD diamond as obtained by coincidence measurements, *Diamond and Related Materials* **8** (1999) 1592–1596.
- VITTONI, E., FIZZOTTI, F., LO GIUDICE, A., PAOLINI, C., MANFREDOTTI, C., Theory of Ion beam Induced Charge Collection based on the extended Shockley-Ramo Theorem, *Nucl. Instr. and Meth. Res.* **B 161–163** (2000) 446–451.
- VITTONI, E., FIZZOTTI, F., SANFILIPPO, C., LO GIUDICE, A., PAOLINI, C., MANFREDOTTI, C., JAKSIC, M., Method based on the extended Ramo theorem to interpret charge collection efficiency profiles as determined by lateral IBIC, Presented at 7th ICNMTA, Bordeaux, France, 10 – 15. September 2000.
- JAKSIC, M., PASTUOVIC, Z., BORJANOVIC, V., BOGDANOVIC RADOVIC, I., PIVAC, B., IBIC characterization of defect structures in polycrystalline silicon, Presented at 7th ICNMTA, Bordeaux, France, 10 –15. September 2000.
- PASTUOVIC, Z., JAKSIC, M., Frontal IBIC of CdTe radiation detectors and response to low energy gamma rays, Presented at 7th ICNMTA, Bordeaux, France, 10 –15. September 2000.
- KULIK, M, KOBZEV, A.P., MACZKA, D., Creation of Oxygen-Enriched Layers at the Surface of GaAs Single Crystal, Preprint of JINR, E15-99–265, Dubna, 1999.
- DIDYK, A.Yu., KOBZEV, A.P., ORELOVICH, O.L., SEMINA, V.K., Track Effects in Silicon Irradiated by Swift High Energy Heavy Ions, JINR Communication, E-14-2000-107, Dubna, 2000.
- KOBZEV, A.P., KRAVTCOV, E.A., ROMASHEV, L.N., SEMERIKOV, A.V., USTINOV, V.V., Using of the High-Grade Layered Structures for the Demonstration of the Depth Resolution of the RBS Method, *Vacuum* (in press).
- KAZDAEV, Kh.R., SEIDIGAZIMOV, S.K., KAZDAEV, R.Kh., Influence of the nitrogen and oxygen on silicides formation, Proc. of the 2nd Int. Conf. on Nuclear and Radiation Physics, Almaty (1999) 225.
- SIMON, A., CSIK, A., PÁSZTI, F., KISS, Á.Z., BEKE, D.L., DARÓCZI, L., ERDÉLYI, L., LANGER, G.A., Study of interdiffusion in amorphous Si/Ge multilayers by Rutherford backscattering spectrometry, *Nucl. Instr. and Meth.* **B161–163** (2000) 471–475.
- ELEKES, Z., KISS, Á.Z., BIRON, I., CALLIGARO, T., SALOMON, J., Thick target gamma-ray yields for light elements measured in the deuteron energy interval of 0.7–3.4 MeV, *Nucl. Instr. and Meth.* **B168** (2000) 305–320.
- NEKVINDOVA, P., SPIRKOVA-HRADILOVA, J., SCHROFEL, J., SLUNECKO, M., PERINA, V. and VACIK, J., Localized Moderate Temperature Er³⁺ Doping into Optical Crystals, *SPIE* 3858 (1999) 180–189.
- NEKVINDOVA, P., SPIRKOVA-HRADILOVA, J., SCHROFEL, J. and PERINA, V., Erbium Doping into Lithium Niobate and Sapphire Single Crystal Wafers, *J. Mat. Res.* (2000) (in press).

- SPIRKOVA-HRADILOVA, J., NEKVINDOVA, P., VACIK, J., CERVENA, J., SCHROFEL, J., Possibility of Tailoring n_e vs. c_{Li} Relations in Lithium Niobate Optical Waveguides for Sensors Applications, SPIE 3858 (1999) 190–201.
- BUDNAR, M., ZORKO, B., PELICON, P., SPIRKOVA-HRADILOVA, J., KOLAROVA-NEKVINDOVA, P. and TURCICOVA, H., ERDA Study of H^+ incorporated into Lithium Niobate, Nucl. Instr. and Meth. **B161–163** (2000) 268–272.
- SPIRKOVA-HRADILOVA, J., NEKVINDOVA, P., VACIK, J., CERVENA, J., SCHROFEL, J., Possibility of Tailoring n_e vs. c_{Li} Relations in Lithium Niobate Optical Waveguides, Opt. Mat. (2000) (in press).
- TURCICOVA, H., POLCAROVA, M., BRADLER, J., VACIK, J., CERVENA, J., PERINA, V. and ZEMEK, J., Li Depth Profile Anomaly after Radio-Frequency Hydrogen Plasma Processing of Single Crystal $LiNbO_3$, Surf. Interface Anal., **29** (2000) 260–264.
- TURCICOVA, H., PREUCIL, S., VACIK, J. and CERVENA, J., X-ray, NDP and RBS Surface Analysis of $LiNbO_3$ Single Crystals Modified by Radio-Frequency Hydrogen Plasma, Ferroelectrics **238** (2000) 313–320.
- TURCICOVA, H., PRACHAROVA, J., CERVENA, J. and VACIK, J., Sheet Resistance of $LiNbO_3$ Wafers Processed in Radio-Frequency Plasma of Hydrogen, Czech J. Phys. **50** (2000) 461–465.
- STONERT, A., TUROS, A., NOWICKI, L., BREEGER, B., Analysis of Defects in Multicomponentcrystals by Ion Channeling, Nucl. Instr. and Meth., **B161–163** (2000) 496–500.
- NOWICKI, L., RATAJCZAK, R., STONERT, A., TUROS, A., BARANOWSKI, J., BANASIK, R., PAKULA, K., Characterization of InGaN/GaN Heterostructures by means of RBS/channeling, Nucl. Instr. and Meth., **B161–163** (2000) 539–543.
- GAWLIK, G., TUROS, A., JAGIELSKI, J., BEDELL, S., LANFORD, W.A., Hydrogen-Ion Implantation in GaAs, Vacuum (in press).

CHARACTERIZATION OF SEMICONDUCTOR AND FRONTIER MATERIALS BY NUCLEAR MICROPROBE TECHNOLOGY

Jieqing ZHU, Xiaolin LI, Changyi YANG, Rongrong LU, Jiqing WANG, Panlin GUO
Shanghai Institute of Nuclear Research,
Chinese Academy of Sciences,
Shanghai, China

Abstract

The nuclear microprobe technology is used to characterize the properties of semiconductor and other frontier materials at the stages of their synthesis, modification, integration and application. On the basis of the beam current being used, the analytical nuclear microprobe techniques being used in this project can be divided into two categories: high beam current (PIXE, RBS, PEB) or low beam current (IBIC, STIM) techniques. The material properties measured are the thickness and composition of a composite surface on a SiC ceramic, the sputtering-induced surface segregation and depth profile change in a Ag-Cu binary alloy, the irradiation effects on the CCE of CVD diamond, the CCE profile at a polycrystalline CVD diamond film and a GaAs diode at different voltage biases and finally, the characterization of individual sample on an integrated material chip.

1. Introduction

Many aspects of modern technology depend on the development of semiconductor and other frontier materials that have unique properties. The quality of the materials must be controlled at all the stages in the process of the material development: synthesis, modification, integration and eventual application. MeV ion beam analysis has been widely used to characterize surface properties of materials. Surfaces of many materials are composed of small (μm) grains, crystals and different phase regions. The nuclear microprobe with a reasonable spatial resolution (μm) is suitable to probe these small regions for their composition and structure and to profile their depth distribution.

By means of the nuclear microprobe at SINR and in cooperation with other two CRP groups (University of Torino, Italy and Rudjer Boskovic Institute, Croatia), we have measured the properties of some semiconductor and other frontier materials. They are nitride surface on SiC ceramic, Ag-Cu binary alloy surface, CVD diamond film, GaAs detector, and finally combinatorial material chips. On the basis of the beam current being used, the analytical nuclear microprobe techniques being used in this project can be divided into two categories: high beam current (PIXE, RBS, PEB) or low beam current (IBIC, STIM) techniques.

The mechanical strength of silicon carbide ceramic (SiC) can be much improved by formation of a composite ceramic layer on its surface. The micro-PEB (proton elastic backscattering) technique was used to study the composite ceramic layer (Si_3N_4) made by exposing SiC to N_2 atmosphere at high temperature. The nitride surface results in a remarkable increase of the material strength. The improved properties of the ceramic are dominated by the Si_3N_4 concentration in the composite layer, but not by the layer thickness.

Preferential sputtering-induced surface segregation and localized depth profile change in a Ag-Cu binary alloy was studied by micro-PIXE and micro-RBS. The ion sputtering was performed by Ar^+ beam bombardment. Pronounced changes of the surface concentration and the depth profile have been found at both Cu-enriched solid solution micro-grains and Ag-enriched matrix regions. The bombardment-induced segregation is suggested to be attributed to the composition change in the very near surface region.

Lateral micro-IBIC was used to characterize the electrical behavior of CVD diamond thin film and further to evaluate its quality. By comparing the IBIC results between samples of non-irradiated and irradiated with proton dose of 46 Gy, we found that the average charge collection distance of the diamond film was obviously increased due to the fact that the space charge inside the film was eliminated by irradiation. The change of charge collection efficiency (CCE) at different biases applied on the growth side of the CVD diamond film was investigated by lateral micro-IBIC. The responsibility of the internal electric field for the change was theoretically studied. It was confirmed that the CVD diamond film was similar to a reverse biased p-n junction. Electrons were main contributors to

CCE while holes had high trapping probability in the diamond film. The CCE distribution in a GaAs diode was measured by frontal micro-IBIC technique. The IBIC image produced by helium ion beam had better contrast than that by proton beam because helium ion deposited more energy in the depletion layer of the diode.

We have developed a method combining ion implantation and physical masking technique to generate a material library of various ion-implanted samples. Six ion species have been sequentially implanted to a SiO₂ film through six combinatorial masks and consequently a material chip (library) with 64 (2⁶) samples is generated. RBS and PEB are first applied for characterization of the material chip to determine the depth-resolved ion distribution in the individual sample. It is revealed by the spectrum for co-implanted sample S(Ga, C) that C existence induces the redistribution of Ga in SiO₂ after thermal annealing. It also showed that Sn diffusion approaching the surface for sample S(Pb, Sn, N) is evident, which is a cause of high luminescent emission for this material. The successful combination of ion beam implantation and ion beam analysis greatly increases the efficiency for new material synthesis, analysis and optimization.

The nuclear microprobe at SINR was initially set up for preference of micro-PIXE only. In order to conduct this project, some modification has been adopted and it is described in the first paragraph.

2. Modification of the experimental facilities for this project

The nuclear microprobe at SINR (Shanghai Institute of Nuclear Research) has been able to focus MeV protons or helium ions down to a size of one micron. The microprobe features itself with long focus quadruple lenses, and hence, it obtains good spatial resolution with easy operation. However, it was initially set up for preference of particle-induced X-ray emission (PIXE) experiments only. Before conducting this project, this microprobe has been used for mapping elemental micro-distribution of minerals and biological samples by means of micro-PIXE technique.

The nuclear microprobe has shown its potentialities in applications to semiconductor and some other frontier materials. In order to meet more demands from semiconductor and material science, some new IBA techniques have been developed with the microprobe. As complementary of PIXE, Rutherford backscattering spectrometry (RBS) is useful technique for quantitative measurement of elemental concentration profiles and ionic transport within materials. RBS-channeling can be used to study the micro-structure in crystal materials. Nuclear microprobe technique has been extended to scanning transmission ion microscopy (STIM) to measure the mass thickness of film materials. A system for ion beam induced luminescence (IBIL) and ion beam induced charge (IBIC) measurement has been installed for study of semiconductor materials and microelectronics samples.

Because the beam current of the microprobe is much lower than the ordinary IBA requests, the experiment efficiency is important. A multi-detector system around the microprobe specimen chamber makes it possible to measure a sample with some IBA techniques simultaneously. Different IBA measurement gives out different properties of a specimen. The complex microprobe measurement does much enhance the understanding of the microscopic properties of the specimen from different aspects. In order to cope with the complex microprobe measurements, a multi-detector and multi-parameter data acquisition system is built up successfully in this laboratory.

The new data acquisition system is based on the concept of TQSA (total quantitative scanning analysis) and works by a list mode. It provides the recording of all information associated with a detected data event (e.g. the detected secondary particle energy and the focused beam position). At this mode, no information is lost and the spectra or the distribution maps within any preferential areas or energy windows may be extracted on-line or at any later time. We have implemented the concept of TQSA by designing a digitized beam scanning system and a high-speed data acquisition interface FDAC (fast data acquisition crate). The FDAC provides a modular interface between the Motorola VME data acquisition computer and the scan system and ADC. The data acquisition hardware is described in Fig.1. The VME computer is connected by an ethernet link to an Unix workstation running the X-windows graphical environment. This workstation runs the MPSYS software package. It presents a high level graphical environment for on-line and off-line data treatment for the microprobe experiment. The FDAC has four stations connected to different detector systems. Each of them is triggered by events accepted by a corresponding detector. Up to four different detectors, and hence, four different IBA techniques can work simultaneously in one scanning experiment with the TQSA protocol.

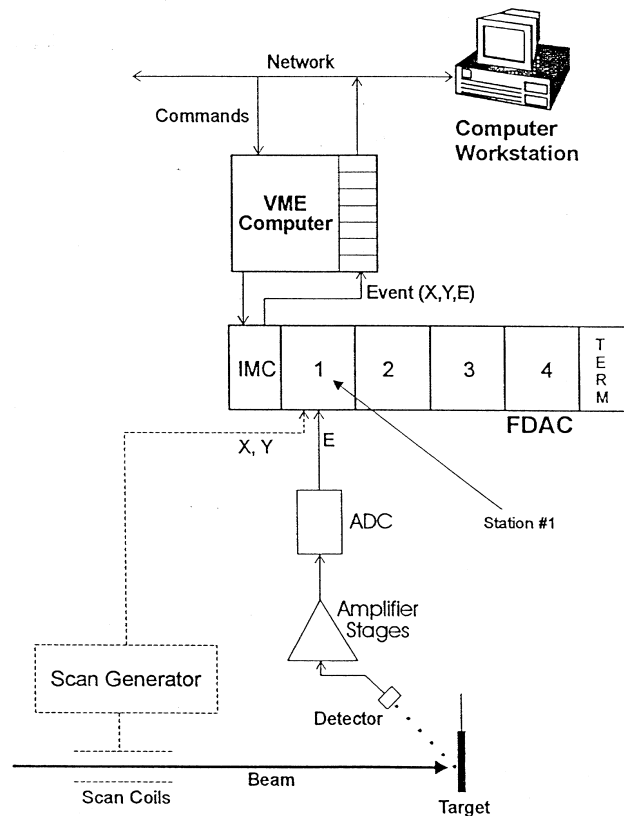


Fig.1. Schematic diagram of the general operation of the new multi-detector and multi-parameter data system hardware with a single detector providing input as a station example.

Some modifications of the microprobe for application to material science have also been made. A new pair of pre-lenses magnetic scanning coils enlarges the scanning area from the ordinary 500 μm by 500 μm to a new area of 2 mm by 2 mm for 3 MeV proton beam. An universal specimen holder is designed for holding several thick and large samples easily. The specimen holder can be moved along three directions and rotated in two axes with large movement ranges. The illumination in the specimen chamber is improved and a side window is attached at the chamber to have better viewing. A pair of X-ray filters is put in front of the Si(Li) detector. It can be moved without the necessity to open the chamber. A small area surface barrier detector with good energy resolution is installed at 135° direction for RBS and channeling experiments. An annular surface barrier detector is installed in front of the sample for light element detection and sample matrix measurement. An off-axis STIM measuring detector is installed at 5° direction, which can be changed from outside the vacuum chamber.

The high current microprobe techniques typically employ beam current in excess of 50 pA focused into a spot of $\geq 2 \mu\text{m}$. The beam current for the low current techniques is typically smaller than that of the high current techniques by a few orders of magnitude. The difficulty for the low current technique is how to produce a low current beam without deteriorating the beam spot resolution. We mount a sample for low current experiment and a piece of glass together on a specimen holder. At first, we focus the ion beam with high beam current while it hits on the glass. The beam spot size and position are measured with a high power optical microscope. The beam position is marked by cross hairs in the view field of the microscope. After that we close down the object slits to 5 μm and adjust the velocity selector of the accelerator to reduce the beam intensity at a level of 500 ions/s. Then, the sample is moved to the marked position by two-dimensional displacement of the specimen holder.

For IBIC measurement we firstly used an ordinary charge sensitive preamplifier which was attached at the outside of the specimen chamber. It transformed the ion-induced charge in the sample into pulse signal. Because of the long distance between the preamplifier and the sample, the electric

noise was not satisfied for high-resolution IBIC measurement. In order to achieve an adequate signal/noise ratio this distance is shortened by moving the first FET of the preamplifier into the specimen chamber. The FET is attached at the specimen holder. The FET capacitance, and hence, the noise are low and unchanged when the sample is moving.

3. Micro-analysis of Si₃N₄/SiC ceramic composite layer by micro-PEB technique

Silicon carbide, one of the high performance ceramic has been widely used in high-temperature structure applications. However, SiC is a relative brittle material. There are pores, cracks and some low density areas in sintered SiC ceramic, which limits its mechanical properties. Taking pre-sintered SiC as substrate, a technology of HIP (hot isostatic pressing) has been developed to form a layer of Si₃N₄/SiC composite ceramic on its surface. The composite layer is generated on the surface of SiC by exposing it in N₂ atmosphere at different temperatures (1850, 1900 or 2000 °C) for a different period of 0.5, 1 or 2 hours [1]. The physical and mechanical properties of the new product are distinctly improved. Are the improved properties dependent on the thickness and the Si₃N₄ concentration in the composite layer? The thickness and the concentration are measured with the non-Rutherford proton elastic backscattering (PEB) technique by means of a focused proton microbeam scanning across the layer.

Because the thickness of nitride layer is only slightly larger than the beam size, the sample surface was polished in a slope of 1° crossing the original target surface and the nitride layer to improve the depth resolution. The thickness of the composite layers and their concentration of Si₃N₄ (as atomic ratio of N/C) in the layers have been determined with this technique and correlated with the HIP processing conditions and the properties of the new materials. And then the processing conditions can be optimized with the results of the microprobe analysis.

The experimental setup and a result are shown in Fig. 2. The scattered protons are detected at 170° by an annular barrier detector. The concentration of Si₃N₄ is about 0.89 on the surface of the nitride layer and sharply decreases to 0.40 at a depth of 1 μm, and then gradually decreases until a sudden drop at a depth about 17 μm from the surface. The distance scale from the surface along the slope is also indicated in Fig. 2 for comparison. The distribution profiles of C and N concentrations along the slope in the composite layer are shown in Fig. 3. There is an interface between the SiC substrate (right) and the nitride surface (left). In considering of the oblique angle, the thickness of the interface is measured as 14 μm. It is showed that the improved properties of the ceramic are dominated by the Si₃N₄ concentration in the composite layer, but not by the layer thickness.

4. Study of localized depth distribution in a binary alloy surface after bombardment by Ar ion

It is known that some binary alloys are composed of micro-regions with different grain phases and different metal enrichment [2]. Preferential sputtering induced surface segregation and depth profile change in an alloy system is an interesting topic [3]. The surface topography is usually studied by Auger electron spectroscopy (AES) and secondary ion mass spectroscopy (SIMS). However, these methods use stripping of atoms from the target surface by ion sputtering. As a result, the atomic compositions are changed during this analysis due to ion bombardment. Rutherford backscattering (RBS) in conjunction with a microbeam technique is a nondestructive method suitable for localized depth distribution analysis.

The Ag-Cu alloy was used in this work. It contains 37% Ag by atoms. The ion sputtering was performed by bombardment of 27 KeV Ar⁺ beam with a flux of $1 \times 10^{17}/\text{cm}^2$. After the Ar ion bombardment the sputtered surface of the sample was observed by electron microscope. We saw that a lot of islanded grains on a strongly textured matrix. The size of the grains was about 10 μm. According to the results of micro-PIXE analysis, the islanded grains were enriched with Cu and the matrix was enriched with Ag. The depth profiles of Cu and Ag in different regions were investigated by micro-RBS. A beam of 2 MeV He⁺ ions was focused to 4 μm in diameter with a current of 1 nA. The depth profiles were determined in both of the Ar⁺ bombarded area and the unbombarded area for comparison. The results revealed the sputtering induced surface segregation and the profile changes.

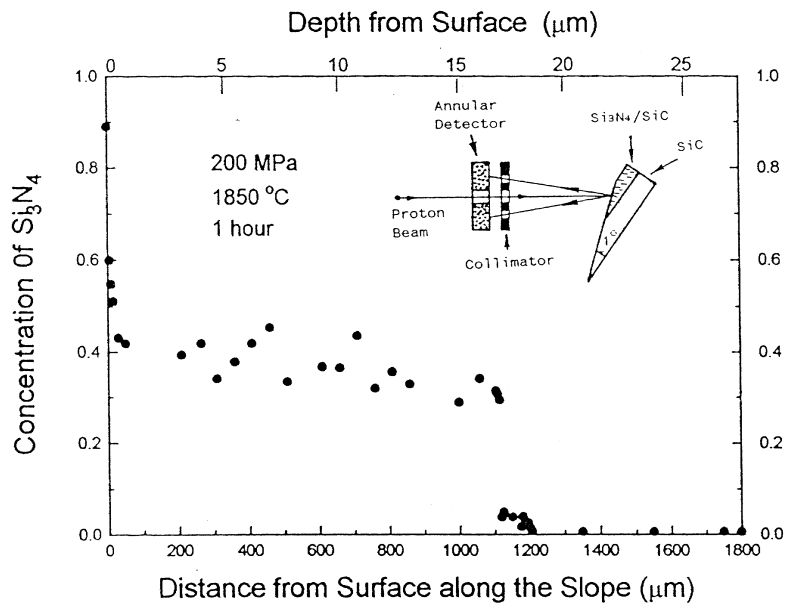


Fig. 2. Depth distribution of Si_3N_4 molecular concentration in a layer of $\text{Si}_3\text{N}_4/\text{SiC}$ composite ceramic on the silicon carbide surface. A diagram of the experimental setup is also displayed in the figure.

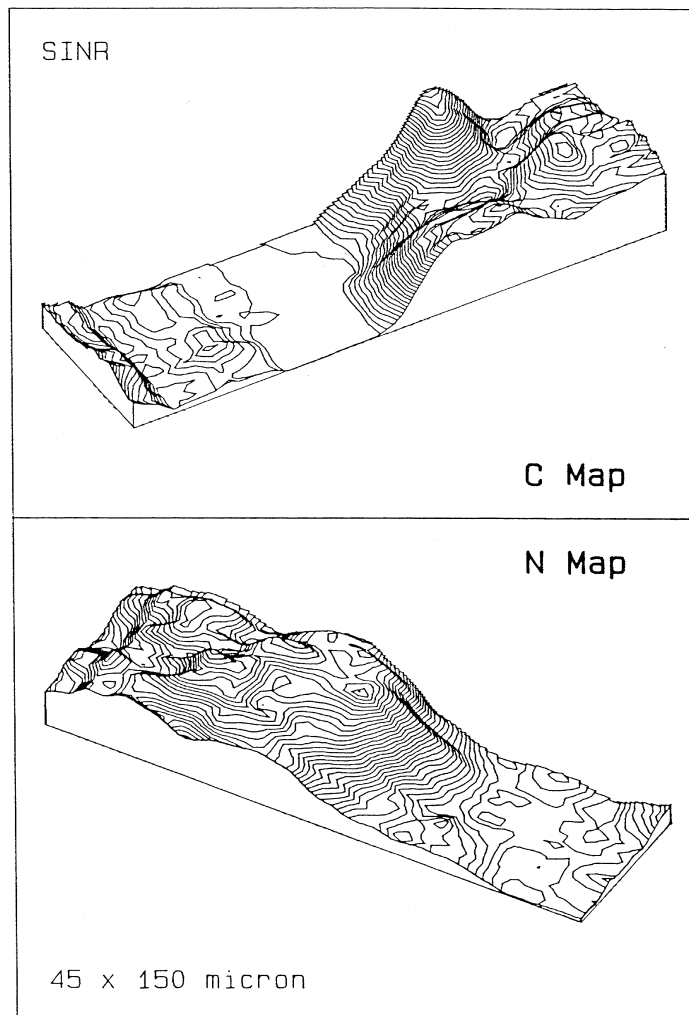


Fig. 3. 3-D contour maps for the distribution profiles of C and N concentration along the slope in a layer of $\text{Si}_3\text{N}_4/\text{SiC}$ composite ceramic.

Fig. 4 shows the Ag concentration depth profile at the Cu enriched micro-grains. The local bulk composition of Ag is about 6.5% before bombardment at these regions. It is in good agreement with the estimated solid solubility of Ag in metal Cu by a phase diagram of Ag-Cu binary alloy. The bombarded curve in Fig. 4 indicates that Ag is relatively enriched in the outermost surface, and sharply decreases to a minimum at a depth of about a few nm from the surface, then increase slowly. This phenomenon, that the Ag solute becomes relatively enriched at the very surface and is depleted in the subsurface at the Cu-enriched solid solution regions, strongly suggests the presence of a sputtering induced Gibbsian segregation (BIGS) effect [4]. The segregation ratio is about 1.3. The Ag concentration depth profile for Ag-enriched matrix region is shown in Fig. 5. A pronounced depletion of Ag is found in the near surface region of the Ag-enriched matrix due to preferential sputtering of Ag under ion bombardment, which is the dominant factor forming the surface topography as described above. No enrichment of Ag is observed in the outermost surface layer.

5. Characterization of chemical vapor deposition (CVD) diamond and GaAs semiconductor detector by ion beam induced charge (IBIC) collection technique

This program was conducted under cooperation with other two CRP groups: University of Torino (Italy) and Rudjer Boskovic Institute (Croatia). The CVD and GaAs samples were prepared at Torino. The nuclear microprobes in Rudjer Boskovic Institute and Shanghai Institute were used for the IBIC experiments.

5.1. Study of irradiation effects on the charge collection efficiency (CCE) of CVD diamond films

Diamond has superlative electrical and structural properties for use in microelectronic devices and radiation hard detectors in high counting rate and high radiation environments including high energy physics experiments. Currently available CVD diamond allows the practical and cost-effective realization of such devices. The quality of CVD diamond is appraised by the collection length d_c , which is the average distance that electron-hole pairs drift apart before being trapped. Usually, the frontal IBIC technique is used to measure the collection length according to a simple linear relation between collection length and the thickness of the diamond film. It is valid only when the collection length is smaller than the thickness of the film. In order to characterize the electrical behavior and further to evaluate the quality of CVD diamond with longer collection length, the lateral micro-IBIC technique was used. A 200 μm thick CVD diamond sample, clamped with two Ti/Au electrodes on both of the growth and the substrate sides, was studied by introducing a 4 MeV proton beam with 4 μm beam size and very low beam current hitting at the lateral cross section of the sample. The electrode on the growth side was added by a fixed bias and the other side referenced to the ground. In the diamond film, the charged carriers were created by the proton beam. The charge pulses, generated by the motion of the charged carriers towards the electrodes due to the presence of the applied electric field, were amplified and recorded by the charge sensitive preamplifier. To evaluate the CCE and the d_c , the pulse heights were normalized to the response of a Si surface barrier detector (nominal 100% CCE) on the basis that the energy for creating a electron-hole pair is 3.6 eV in silicon and 13.2 eV in diamond.

In order to study the irradiation effects on the CCE of CVD diamond, a non-irradiated sample was firstly measured by micro-IBIC. Then, the sample was irradiated by high dose of proton beam (46 Gy) and IBIC was measured on the same area. The measured area was divided into 128 columns along the lateral cross section and the CCE in each column was calculated based on the average IBIC intensity in it. By comparing the IBIC results of non-irradiated samples with those of irradiated ones, it was found that the CCE uniformity of CVD diamond could be much increased by the irradiation. It might be due to the elimination of space charges inside the CVD diamond after irradiation. Fig. 6 shows a diagram of the column numbers at certain CCE intervals versus CCE for the non-irradiated and irradiated sample. It is of interest to note that the curve for the non-irradiated case can be fitted by a continuous line with two Gaussian curves. The curve for the irradiated case can be fitted by one Gaussian curve. The result means that the CCE profile for the non-irradiated sample is a convolution of a low CCE (0.15) part and a high CCE (0.29) part. While for the irradiated sample the high CCE (0.29) dominates the CCE profile. The low CCE part is contributed by the space charge existence in the grain boundary. The process of irradiation can eliminate the cloud of the space charge. This study provides a possibility to effectively improve the electric properties of CVD diamond semiconductors.

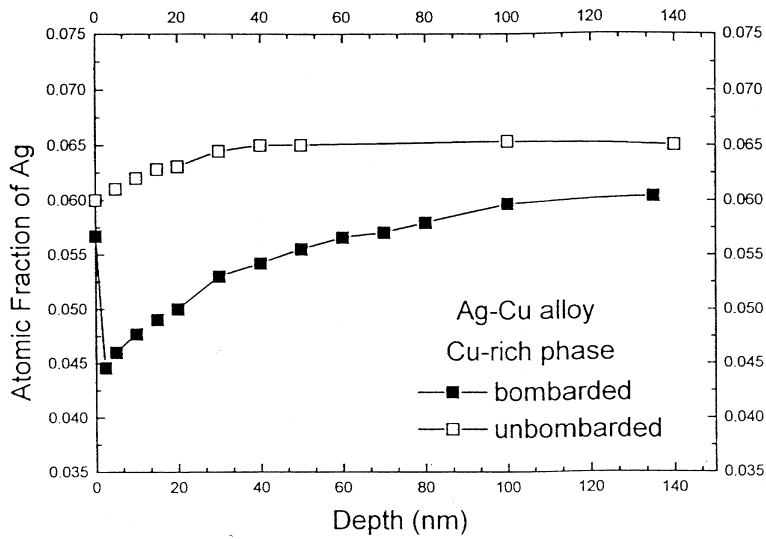


Fig. 4. Depth distribution of Ag at a Cu-enriched micro-grain on the surface of Ag-Cu alloy.

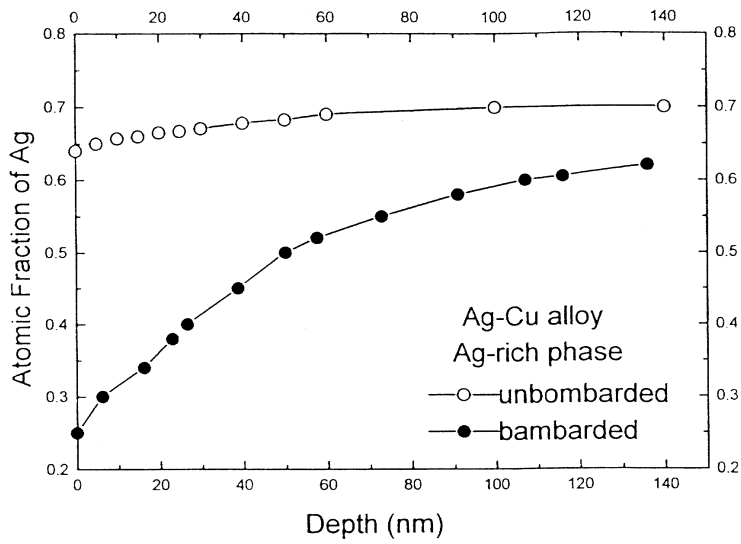


Fig. 5. Depth distribution of Ag at a micro-region of the Ag-enriched matrix on the surface of Ag-Cu alloy.

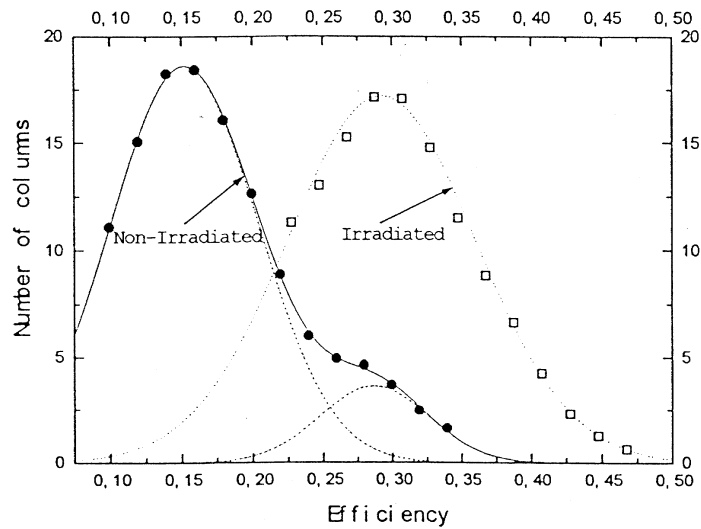


Fig.6. A diagram of the column number at certain interval of charge collection efficiency (CCE) versus CCE for the non-irradiated or irradiated sample.

5.2. Comparison of CCE profiles of polycrystalline CVD diamond film at different voltage biases

CVD diamond is polycrystalline material with columnar structure along the growth direction. This characteristic may affect the electric properties of the material by acting as traps and/or recombination centers, thus degrading its charge collection efficiency (CCE), which is defined as the ratio between the collected and the created charges or numbers of the electron-hole pairs. The information about the electric behaviors of carriers' movements inside the diamond was investigated by the micro-IBIC technique. The dependence of CCE upon the crystalline grain sizes was studied by mapping the IBIC images at different voltage biases. IBIC maps of CCE distributions in the scanning areas were obtained by means of the setting of different windows in IBIC spectrum similar to the process of PIXE elemental maps. The CCE profile along the diamond growth direction can be easily got by averaging the efficiencies in the direction normal to the growth direction. In order to get insight into the electrical and transport properties of charge carries excited by proton beam in diamond, the contributions of electrons and holes to the CCE profile are separately considered.

An extensive investigation on the electrical and transport behaviors of CVD diamond has been made by lateral micro-IBIC. The focused proton beam was scanned over an area of $200 \times 500 \mu\text{m}^2$ of a $200 \mu\text{m}$ thick CVD diamond film. The film was carefully cleaved and clamped with two electrodes on both the growth and the substrate sides. The electrode on the growth side was added by different biases and another side referenced to the ground. Fig. 7(a) shows a typical profile of CCE along the growth direction. Here, the growth side (biased) is on the left and the substrate side (ground) is on the right. It is noted that the CCE profile moves to the growth side with the increase of positive bias voltage from 400 to 600 V. The CCE maximum changes between 25 and 35% in the middle of the film. In the same way, the CCE profiles for different negative biases were obtained and displayed in Fig. 7(b). It is also noted that the highest CCE exists in the layer of growth side with a variation from 42 to 50%. The shape of the CCE profile slightly moves to the substrate side while the negative bias changes from -100 to -400 V. It was concluded that the CVD diamond film is similar to a p-n junction with a reverse bias when a positive voltage applied at the growth side. The electrons are usually the main contributors to CCE while the holes have higher trapping probability in the CVD diamond film. In the case of negative bias, the negative space charge on the growth region may come from the donors of the film and the positive space charge on the substrate region may arise from the acceptors of the film. The neutralization effect is mainly responsible for the elimination of the space charge in the middle of both electrodes.

5.3. Micro-IBIC characterization of GaAs semiconductor detector using proton beam or helium ion beam

GaAs is good semiconductor materials for making micro-electronic devices and radiation detectors. It has potential applications for the manufacture of devices working at high temperature and high power. Because of its high electron mobility, it is wildly used in high frequency and high speed circuits. Schottky barriers are generally needed in order to get low leakage currents. The properties of the devices and the energy resolution of the detectors are much of dependence on the electrical homogeneity of the GaAs materials. The CCE distribution in a GaAs diode was measured by the frontal micro-IBIC technique. The charge was collected by the electrodes at the top and the end of the diode. The resistivity of the GaAs material is $10^7 \Omega\text{cm}$ and the life-time of the carriers is at a level of ns. The thickness of the GaAs chip is $220 \mu\text{m}$. The Schottky barrier is formed between a top layer of Au/Pt/Ti and the GaAs material. The substrate copper layer forms the other electrode of the diode. Data were collected by two-station list model for PIXE and IBIC experiments. Both of the 3 MeV proton beam and 2 MeV helium ion beam was used for comparison.

A reversed bias of 20, 40, 60, 80 or 100 V is applied at the diode. The IBIC intensity is normalized with the PIXE intensity in order to get rid of the influence of the ion beam fluctuation. IBIC is increased while the bias increase. It is because the Schottky barrier is getting wilder and more energy of the incident particles deposits in the depletion layer. Because the helium ion beam has higher stopping power in comparison with the proton beam, it produces more electron-hole pairs in the depletion layer. The IBIC image produced by helium ion beam has better contrast than that by proton beam. According to the thickness of the surface layer and the depletion layer of the chip, a proper species and energy of the incident particles can be selected in order to collect charges at certain depth of the semiconductor chip.

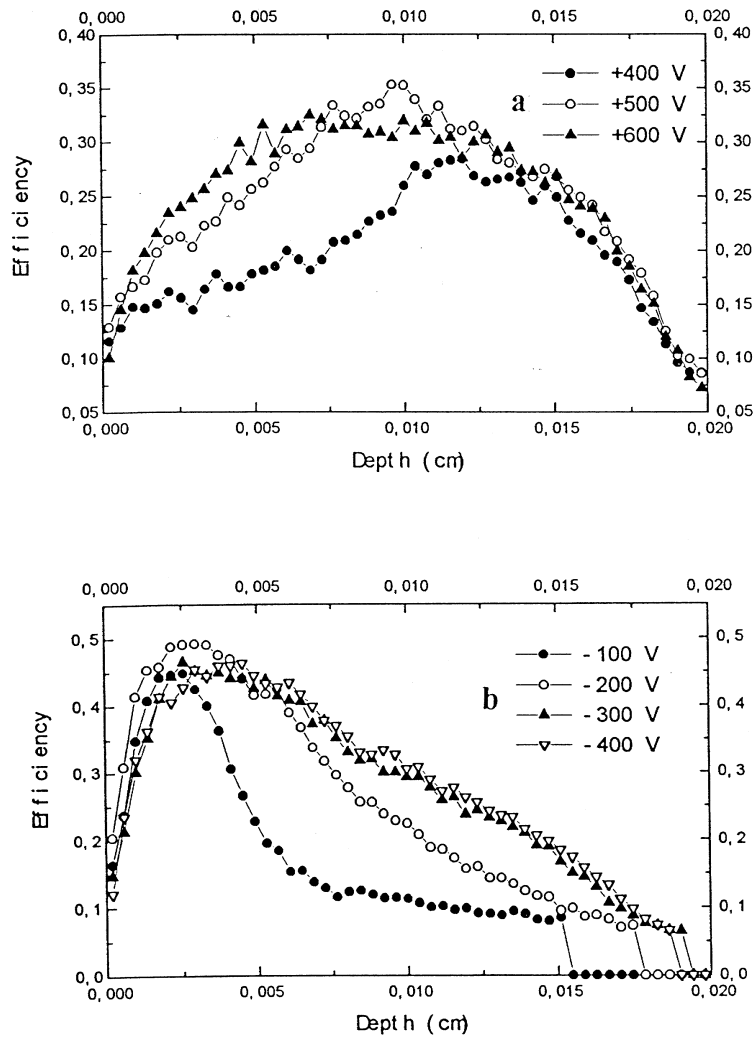


Fig. 7. Charge collection efficiency profile along the CVD diamond growth direction for positive bias (a) and negative bias (b). The growth side (biased) is on the left of the diagram.

5.4. Ion beam synthesis and analysis of combinatorial material chips (libraries)

The combinatorial approach has been widely used for the new drug discovery [5]. Combining the physical masks with thin film synthesis technique [6], integrated material chips (libraries) with a large number of spatially defined different compounds are generated. The combinatorial technique can be widely used in material science to increase the rate of new material discovery and optimization by several orders of magnitude.

During the last few years special interest has been devoted to create new nano-crystals of metals or compounds in SiO_2 , which may exhibit specific optical emission properties and be interesting for photoelectric application. The ion implantation is attractive for this purpose. It generates nano-crystals with well-defined concentration at pre-calculated depths below the host material surface. Our first application of the combinatorial approach in ion implantation is intended to increase greatly the efficiency of sample synthesis and the possibility of novel nano-crystal formation, which may yield higher energy emission.

Although the application of combinatorial approach could revolutionize new material discovery, the in-depth study of the materials libraries is restricted by the difficulty in the phase determination and composition inhomogeneity examination of the small individual samples on the material chips. The electron beam induced cathodoluminescence (CL) technique contribute to the luminescent properties of the materials. The techniques of MeV ion beam Rutherford backscattering spectrometry (RBS) and proton elastic backscattering (PEB) are first applied for characterization of the

combinatorial material chips to determine the depth-resolved ion distribution in the implanted samples.

Boron (P-type) doped 0.5 mm thick single crystal silicon wafers were used for the implantation. SiO₂ thin film of ~ 400 nm was formed by thermal oxidation. Six ion species of C, Ga, N, Pb, Sn and Y were sequentially implanted to the SiO₂ film through combinatorial masks and consequently a library of 64 (2⁶) samples is generated by 6 masking combinations. This approach offers rapid synthesis of samples with potential new compounds formed in the matrix. The generated materials chip was subsequently thermally annealed at 800 ° C for 30 min in Ar gas. Fig. 8 shows the schematic of the combinatorial material chip holder for RBS and PEB analysis. The double arrow lines represent that the holder is controllably moved along X and Y directions to let the selected sample on the chip aligned with the analyzing beam.

RBS analysis was performed by using 2 MeV ⁴He⁺ beam at a scattering angle of 170 °. The spectra obtained by RBS measurements are partially shown in Fig. 9. Fig. 9(a) shows the spectra of the co-implanted samples S(Ga, N) and S(Ga, C). The Ga spectrum of S(Ga, N) is peaked at ~36 nm from the surface. Concerning the N depth range which is estimated to be peaked at ~130 nm from the surface, we can conclude that no GaN crystals formed. Two peaks of Ga spectrum for S(Ga, C) are revealed in Fig. 9(a), which indicates that the C existence induces the redistribution of Ga in SiO₂ after annealing. The profile for C distribution is peaked at ~180 nm from the surface, which matches the location of the lower energy peak of Ga spectrum (172 nm from the surface). It is expected that C induced Ga-related compounds may be formed in the SiO₂ film. Subsequent implantation of Pb or Pb + Sn into the S(Ga, C) samples did not alter the Ga spectrum peak location, as partially shown in Fig. 9(b). By comparing the spectra of S(Ga, Pb, N) and S(Ga, Pb, Sn, N) in Fig. 9(b), it shows that the interaction between Pb and Sn is little.

The previous discussion is also confirmed by the ion concentration depth-profiles calculated with RUMP program, which are shown in Fig. 10, corresponding to Fig. 9. The Ga profile of S(Ga, C) is peaked at 36 and 172 nm from the surface, with corresponding atom fractions of 1.5% and 0.56%, respectively (Fig. 10(a)). The profiling curves of S(Ga, Pb, C) and S(Ga, Pb, Sn, C) also each show two peaks of Ga concentration, located at nearly the same position as that of S(Ga, C). Fig. 10(b) reveals that Sn diffusion approaching the surface for S(Pb, Sn, N) is evident, which is a cause of higher energy luminescent emission when bombarding it with electron beam.

Fig.11 shows PEB spectra of S(C), S(N) and pristine SiO₂ by 3 MeV H⁺ beams at a scattering angle of 170 °. The peak concentration of C for S(C) is 4.12%, calculated using the proton elastic scattering cross section enhancement factors [7]. There is no N revealed in the spectrum of S(N). It is owing to the N diffusion and escaping out off SiO₂ during annealing. The PEB cross sections of light elements C, N and O are enhanced for proton energy > 2.5 MeV. Therefore, the profiling of these elements over a sufficient depth range in a heavy material can be readily accomplished.

We have successfully developed a combinatorial ion synthesis and ion beam analysis technique to study the ion-implanted combinatorial material chips (libraries). It greatly increases the efficiency of sample synthesis, analysis and optimization [8].

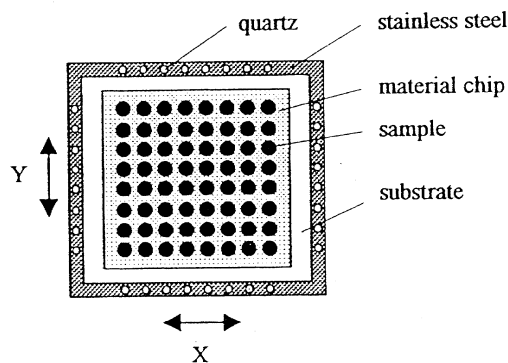


Fig. 8. Schematic of material chip holder for RBS and PEB analysis. The double arrow represent that the holder is able to move along X and Y directions to make the sample aligned with the analyzing beam.

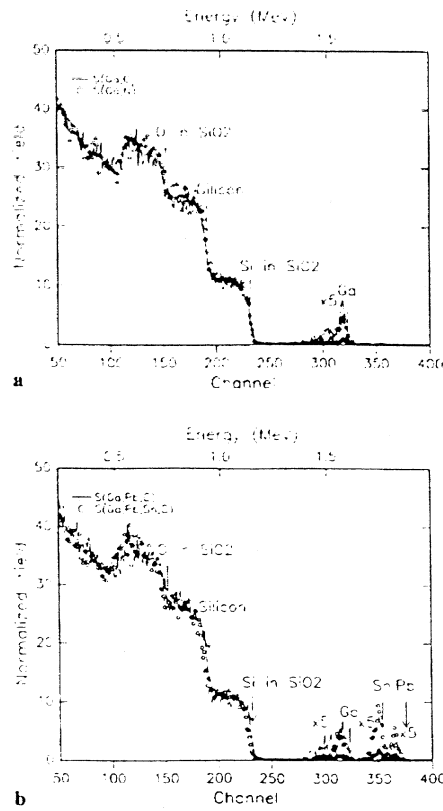


Fig. 9. $2.0 \text{ MeV}^4\text{He}^+$ RBS spectra from material chip after annealing at 8000°C for 30 min in Ar gas. (a) $S(\text{Ga}, \text{C})$ and $S(\text{Ga}, \text{N})$; (b) $S(\text{Ga}, \text{Pb}, \text{C})$ and $S(\text{Ga}, \text{Pb}, \text{Sn}, \text{C})$.

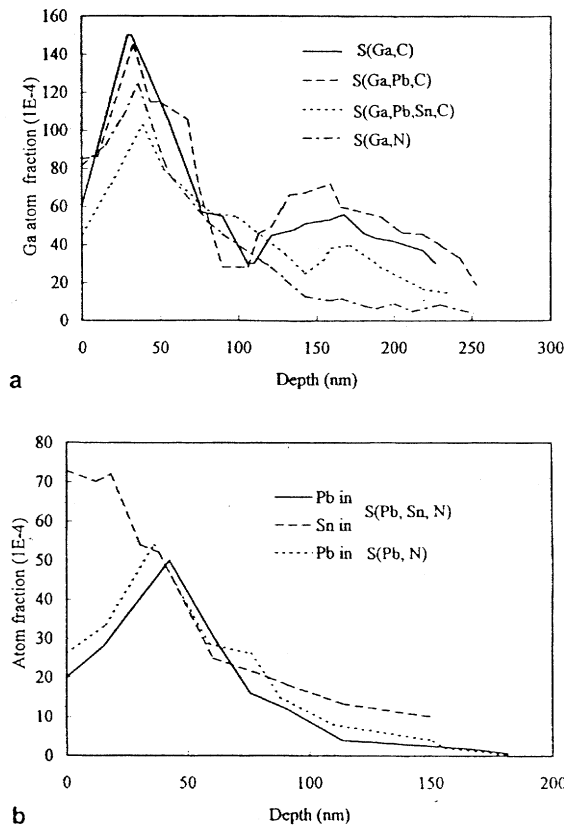


Fig. 10. Ion concentration depth profiles determined from the RBS measurements for the material chip. (a) Ga profiles for $S(\text{Ga}, \text{C})$, $S(\text{Ga}, \text{Pb}, \text{C})$, $S(\text{Ga}, \text{Pb}, \text{Sn}, \text{C})$ and $S(\text{Ga}, \text{N})$. (b) Profiles of Pb and Sn for $S(\text{Pb}, \text{Sn}, \text{N})$ in comparison with Pb profiles for $S(\text{Pb}, \text{N})$.

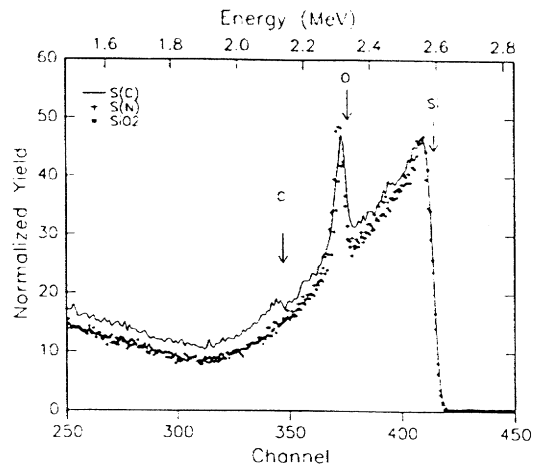


Fig. 11. Proton elastic backscattering spectra using 3.0 MeV H^+ on SiO_2 , $S(C)$ and $S(N)$.

REFERENCES

- [1] J. Shi, D. Jiang, S. Tan, J. Guo, Mater. Res. Bull, 26 (1991) 1277
- [2] Z. Wang, J. Zhang, J. Pan, J. Mater. Sci. Lett. 13 (1994) 427
- [3] G. N. Van Wyk, J. Du Plessis, E. Talauer, Surf. Sci. 254 (1991) 73
- [4] R. Li, C. Li, W. Whang, Appl. Phys. A50 (1990) 169
- [5] B. A. Bunin, M. J. Plunkett, J. A. Ellman, Proc. Natl. Acad. Sci. USA 91 (1994) 4708
- [6] X. D. Xiang, X. D. Sun, G. Briceno, Y. Lou, K. A. Wang, H. Chang, W. G. Wallace-Freedman, S. W. Chen, P. G. Schultz, Science 268 (1995) 1739
- [7] G. Yang, D. Zhu, H. Hu, H. Pan, Nucl. Instr. and Meth. B 61 (1991) 175
- [8] X. Liu, Z. Feng, W. Lu, S. Shen, C. Chen, D. Zhu, J. Hu, M. Li, Appl. Phys. Lett. 1999 75 (17) 25

CHARACTERISATION OF SEMICONDUCTOR MATERIALS AND DEVICES BY THE IBIC TECHNIQUE

M. JAKŠIĆ, Ž. PASTUOVIĆ, T. TADIĆ
Ruđer Bošković Institute,
Zagreb, Croatia

Abstract

The ion beam induced charge (IBIC) analysis is a nuclear microprobe technique that is developed for imaging electronic transport properties of semiconductor devices. In particular, wide gap materials (suitable for development of room temperature semiconductor radiation detectors), are frequently suffering from imperfect charge collection. IBIC technique can be used to image spatial distribution of these imperfections correlating them with different mechanisms of charge loss in a detector. Increasing the capabilities of Zagreb nuclear microprobe IBIC set-up, various problems associated with development of detector materials were studied. CVD and natural diamond, CdTe and CdZnTe, as well as silicon, have been the most frequently analysed materials. Examples of some particular applications are presented.

1. Introduction

Ion beam focused in a nuclear microprobe to a micron spot can serve as a probe for testing different properties of irradiated materials. Semiconductor materials can be characterised by ion microbeams providing spatial distributions of elemental composition, density, crystal structure, or electronic properties. In the case of single ion technique - Ion Beam Induced Charge (IBIC), each single ion creates numerous charge pairs along the stopping path of particular ion in the target. In the presence of electric field, these charge carriers drift towards the electrical contacts, inducing in them a charge pulse. In the electric field free regions, charge carriers diffuse and can therefore also contribute to the induced charge pulse. Characteristics of the charge pulse induced at the electrodes depend on the basic charge transport properties of a device at the particular position that is exposed to the single ion. Scanning of the ion beam across the device results in an image of the collected charge spatial distribution.

2. IBIC technique

By using the conventional nuclear microprobe facility, single ion techniques can be performed without any additional equipment needed. By simple reduction of both object and collimator slits, it is possible to reduce ion beam currents to below 0.1 fA (2000 protons/s). Due to the small divergence of such beam transport, imperfections in focusing and some intrinsic system aberrations have very limited influence on system spatial resolution, making performance of such measurement quite simple. After initial adjustment of beam current using transmission particle detector, spatial resolution check is conventionally performed by STIM (Scanning Transmission Ion Microscopy) image of fine copper or gold grid. STIM detector is also used for calibration of the electronic chain for 100% charge collection efficiency that is supposed to be obtained by silicon particle detector.

Samples for IBIC studies of charge transport properties require either internal electric field or a bias voltage in order to collect the charge pulse at the electrodes. Leakage current through the sample has to be as small as possible, allowing the ion induced charge pulse to be above the noise level. Unlike low band-gap semiconductors such as silicon for which junction barriers are needed, natural and CVD diamond samples as well as CdTe and CsZnTe need just two contacts (usually in planar capacitor geometry) due to their high resistance. This fact exactly matches the properties of solid state ionising radiation detectors, and makes these materials suitable for application of the IBIC technique.

During the recent years, experimental IBIC set-up has been significantly improved allowing study of different problems and samples [1]. In the following sections, the most important characteristics of experimental set-up are described.

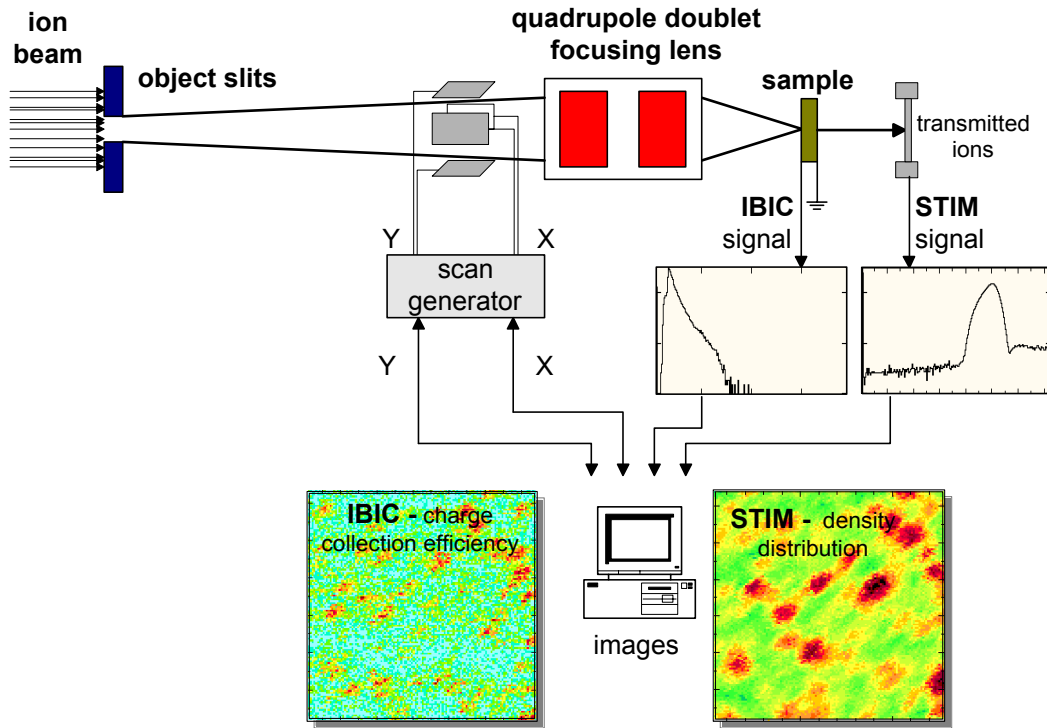


Fig. 1. Schematic presentation of simultaneous IBIC and STIM measurement using nuclear microprobe.

a) lateral and frontal geometry

When an ion penetrates through a material, charge carriers are created along the whole ion range and are proportional to the energy loss. Energy loss (dE/dx) consists of "electronic" and "nuclear" contribution. Charge carriers are created by Coulomb scattering of ions with atom electrons (electron contribution), which is for MeV ions a dominant process. Nuclear contribution however, does not directly contribute to the charge pulse and becomes important only for heavier ions of low energies.

Depending on the orientation of ion trajectory to the electric field in the sample, two variations of the IBIC technique can be performed. These are the "frontal" IBIC where ions enter the sample through the front contact, and the "lateral" version with a surface between the two electrodes being exposed to the ion beam (see Figure 2). Lateral IBIC is used to probe the local variations of charge collection efficiency η which, as a first approximation, can be expressed as:

$$\eta = Q/Q_0 = ((\mu\tau)_e E + (\mu\tau)_h E)/d, \quad (1)$$

where Q is the collected charge, Q_0 is the charge produced by an ion, E is the local value of electric field, $\mu\tau$ is product of mobility and lifetime of charge carriers and d is the sample thickness.

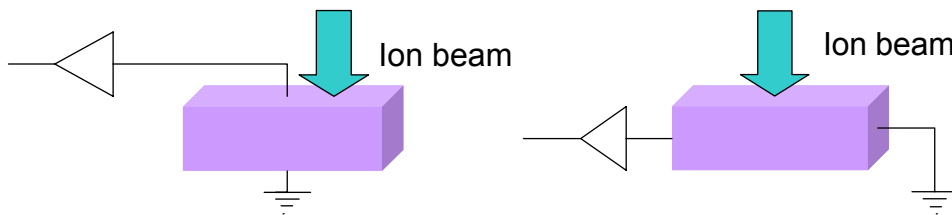


Fig. 2. Schematic presentation of frontal (left) and lateral (right) IBIC experimental set-up.

In this simplified case, assumption that mobility, lifetime and electric field are constant over the whole device was made. However, in most real devices this is not the case. In addition, contribution to the charge pulse can also come from diffusion of charge carriers from the region of device where electric field is zero. A general theoretical approach to predict the charge collection efficiency for simple planar simple geometry of device with both drift and diffusion contribution is presented recently [2,3] on the basis of the Shockley Ramo theorem.

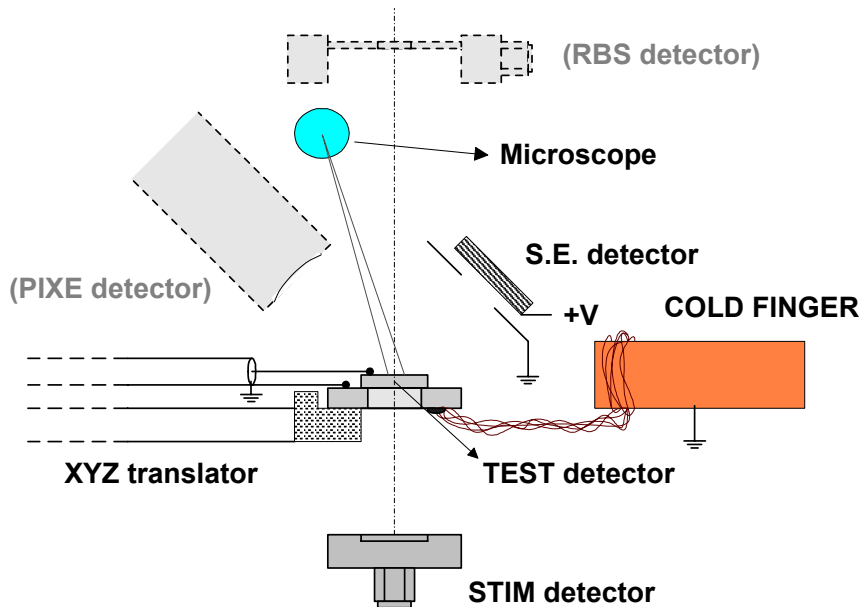


Fig. 3. Schematic presentation of IBIC arrangement in nuclear microprobe scattering chamber.

b) hit detection system

In order to establish correlation between the ion impact on the surface of the IBIC test detector and IBIC pulse, a MSP (Microsphere Plate) detector of secondary electrons was mounted in the chamber for the ion hit detection. In spite of a relatively low hit detection efficiency (about 50% for 5 MeV α particles and less than 10% for 3 MeV protons), useful count rate of a coincident events could still be obtained. In cases of detectors having thickness smaller than the ion range, a STIM detector was used both as a hit detection detector and for measuring the transmitted energy of incoming ions. STIM image of thickness distribution can be valuable for interpretation of the IBIC images.

The importance of hit detection in IBIC, lay in the possibility to image time dependence of charge pulse formation. Since the depleted regions of tested detectors are much thicker and therefore pulse formation is often of the ns order, we have used conventional timing modules in these preliminary measurements. Future use of waveform digitiser oscilloscope triggered by hit detection detector is planned.

c) electronic chain/samples

A standard electronic chain used for the charge particle energy detection is used for IBIC as well. It consists of the charge sensitive preamplifier (Canberra 2004), spectroscopy amplifier (Canberra 2020) and ADC. The electronic chain is first calibrated with ions of known energy, using the silicon charge particle detector having 100% charge collection efficiency and known energy required for the production of a single electron hole pair (3.6 eV). The most convenient is the use of STIM detector for this purpose. Since the value of pair production energy is different for different materials (see table 1.), 100% efficiency regions in diamond (e-h pair creation energy 13.2 eV) will produce pulses by factor 3.66 lower than silicon.

TABLE 1. ENERGY NEEDED TO PRODUCE ONE ELECTRON HOLE PAIR IN DIFFERENT SEMICONDUCTORS.

| material | Energy per e-h pair (eV) |
|-----------|--------------------------|
| Si (77 K) | 3.76 |
| Si(300 K) | 3.62 |
| CdTe | 4.43 |
| CdZnTe | 4.67 |
| diamond | 13.2 |

In addition to radiation detectors, which are normally designed to have small enough leakage current when a bias is applied, IBIC can be also used for studies of wide range of other materials. These have sometimes too high leakage current, which increases the noise dramatically. Decreasing the sample temperature can result in increased resistance and therefore smaller noise. Therefore, a cold finger cooled to a liquid nitrogen temperature is mounted in the microprobe chamber too (see Fig. 3).

d) data acquisition, scan control

Nuclear microprobe data acquisition system based on the newly developed SPECTOR software records each pulse height (proportional to the collected charge) and corresponding x and y position of the ion that induces the charge pulse.

Collected events can be sorted to the XY intensity maps (images) of different pulse height regions, where the grey level indicates the number of events in particular (x,y) pixel. Alternatively, a mean pulse height can be calculated on line for each pixel. In this case grey level represents the mean pulse height. Storage of all accumulated events in the list mode, allows also sorting of pulses that correspond to the particular sample region.

The same data acquisition program controls the beam-scanning pattern as well. Points, lines and different shaped areas of the sample can be selected for analysis. In the case of materials that are most sensitive to radiation damage and use of heavier ions, ion rates down to one count per pixel can be achieved using external scan trigger.

e) ions of same rigidity

Important advantage of IBIC over similar techniques OBIC and EBIC makes a fact that different ions and their energies could be used in order to observe charge pulse that originates from the various sample layers. The list of ion ranges in Si and CVD diamond that were used in our recent IBIC experiments is presented in Table 2.

TABLE 2. LIST OF IONS AND ENERGIES USED FOR IBIC STUDIES OF DIFFERENT MATERIALS AND CORRESPONDING ION RANGES.

| ion | energy (MeV) | Material | range (μm) |
|-----------------|--------------|-------------|-------------------------|
| protons | 3 | Si | 90 |
| protons | 4.5 | Si | 178 |
| Li ⁷ | 2.667 | Si | 5.3 |
| Li ⁷ | 4.5 | Si | 8.5 |
| O ¹⁶ | 7.875 | Si | 4.5 |
| protons | 6 | CVD diamond | 150 |
| protons | 2 | CVD diamond | 24 |
| alpha | 2 | CVD diamond | 3.5 |

A particular convenient way of making the IBIC experiment using two different ion ranges, is to select two different ions having the same magnetic rigidity. In the two such examples (circles in Table 2.), both significant and small change in range was achieved. Only the terminal voltage has to be adjusted, while all other beam transport parameters including the microprobe beam focusing remain unchanged. In some examples, like the one where we used Li(OH) sputtering target in the sputtering negative ion source, three different ions can be injected in accelerator.

3. Charge transport properties in semiconductor radiation detectors

3.1. CdZnTe

Relatively simple example of IBIC usefulness is the performance of lateral IBIC on planar CdZnTe detectors [4]. Several simple (symmetric metal/semiconductor/metal) CZT detectors ($5 \times 5 \times 2 \text{ mm}^3$) with different metal contacts (In-In, In-Au, Au-Au) were measured and charge transport properties were calculated. An important characteristic of both CdTe and CdZnTe is that hole mobility is rather low and generally holes do not contribute to the charge pulse at all. In Figure 4., a line scan between the two electrodes is performed as a function of bias voltage. A positive bias is applied to the left electrode, where the lowest IBIC pulse is observed. At this position the hole contribution to the IBIC pulse is dominant. At the other (right) electrode, electron contribution is dominant and the maximum pulse height is observed.

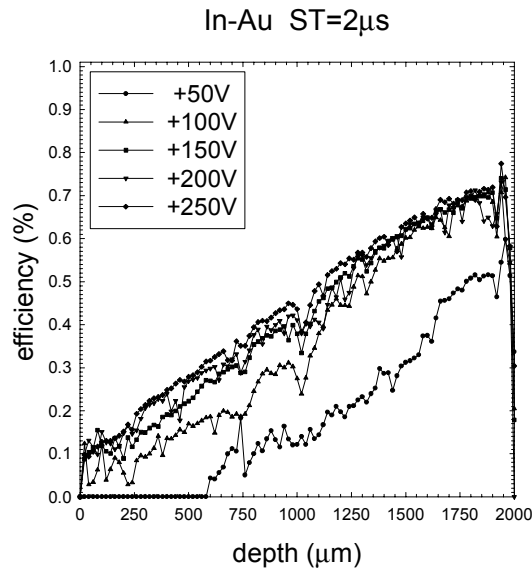


Fig. 4. Lateral IBIC line scan between two electrodes of CdZnTe detector with In-Au contacts. Positive electrode is left, indicating that only electrons contribute to the creation of pulse.

This can be explained by the Hecht equation that gives an induced charge on the contacts:

$$Q(x) = N_0 e \left\{ \frac{\lambda_e}{d} \cdot \left[1 - e^{-\frac{x_e}{\lambda_e}} \right] + \frac{\lambda_h}{d} \left[1 - e^{-\frac{x_h}{\lambda_h}} \right] \right\}, \quad (2)$$

where N_0 is the number of electron-hole pairs created, e is the elementary charge, d is the distance between the contacts of the detector (detector thickness), λ_e (λ_h) is the electron (hole) drift length and x_e (x_h) is the distance electrons (holes) travel respectively. If only charge collection efficiency in the vicinity of grounded electrode (cathode) is taken into account, the distance the holes have to travel is practically zero and the hole contribution to the induced charge is negligible. The collected charge is

due to electrons that have to travel the whole width of the detector, d . Under these conditions Eq.(2) reduces to the single carrier Hecht equation

$$Q_m = N_0 e \left\{ \frac{\lambda_e}{d} \cdot \left[1 - e^{-\frac{d}{\lambda_e}} \right] \right\}. \quad (3)$$

If the pulse height is not saturated with respect to the bias i.e., the drift lengths are less than the detector thickness, the carrier drift lengths can be expressed in terms of the transport properties of the material and the applied bias voltage as:

$$\lambda_{e,h} = \frac{(\mu \cdot \tau)_{e,h} \cdot V}{d} \quad (4)$$

where μ is the carrier mobility, τ is the carrier lifetime and V is the applied bias voltage. Here a uniform electric field is assumed. Substituting Eq.(3) into Eq.(2) the bias dependence of the collected charge generated near cathode is

$$Q(V) = N_0 e \cdot \frac{(\mu \cdot \tau)_e \cdot V}{d^2} \left[1 - e^{-\frac{d^2}{(\mu \cdot \tau)_e \cdot V}} \right]. \quad (4)$$

In our case the pulse height saturation occurs at approximately 150 V for CZT with In-Au and Au-Au contacts. A slab approximately 40 μm thick (a width of 2 pixels) next to the cathode was chosen for the calculation of the mobility-lifetime product for electrons, $(\mu \cdot \tau)_e$. Eq.(4) was fitted to charge collection efficiency data for each pixel from that slab using $(\mu \cdot \tau)_e$ as a fitting parameter. Values of $(\mu \cdot \tau)_e = (3.16 \pm 0.09) \times 10^{-4} \text{ cm}^2/\text{V}$ for CZT detector with In-Au contacts and $(\mu \cdot \tau)_e = (2.37 \pm 0.25) \times 10^{-4} \text{ cm}^2/\text{V}$ for CZT detector with Au-Au contacts were obtained.

These values are lower than published previously, which is partially explained by the imperfect matching of the contact area and the edges of the front detector surface. Since this is very important for this kind of the detector design, we performed an additional "inclined" IBICC measurement showing charge collection efficiency at the two lateral surfaces as well as the one frontal electrode. There can be seen that the charge collection efficiency at the front surface of the detector is not uniform due to the localized damage of contact, which also does not extend up to the edge as expected. Therefore, potential difference between the two edges could be lower than the applied voltage used in calculations. This measurement stressed the importance of contact quality and fabrication procedures. Contact imperfections could be either due to a mechanical damage of the contact or a contact production process.

3.2. *Si(Li) x-ray detectors*

A typical example of IBIC employed as a surface technique is our recent study of incomplete charge collection (ICC) at the surface of Si(Li) x-ray detectors [5]. An important advantage of heavier ion over more commonly used protons can be seen from Figure 5, where energy loss for two types of ions is shown. It is visible that rather small changes in surface ICC or "dead layer" can influence much more the total IBIC signal if heavier ion is used.

For decades, being a subject of numerous studies, this "dead layer" or more correctly - surface ICC layer is to a certain extent responsible for the low energy tailing features of the x-ray peak shape.

Our results of IBIC measurements using the small penetration Li^6 ions showed large differences among detector crystals being tested. From almost negligible ICC observed in one of the tested Si(Li) diodes, to more typical values of about 200 nm equivalent silicon dead layer, the common feature of all tested detectors is inhomogeneous ICC.

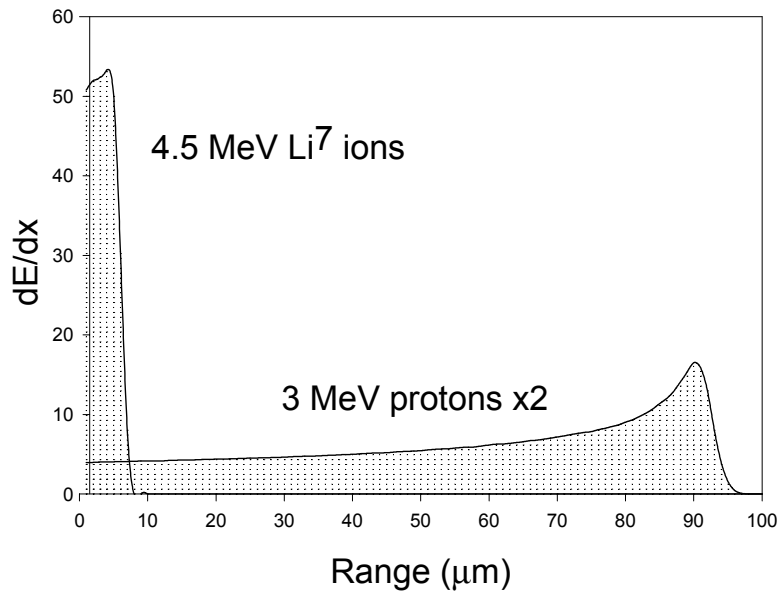


Fig. 5. Energy loss of protons and Li ions in silicon.

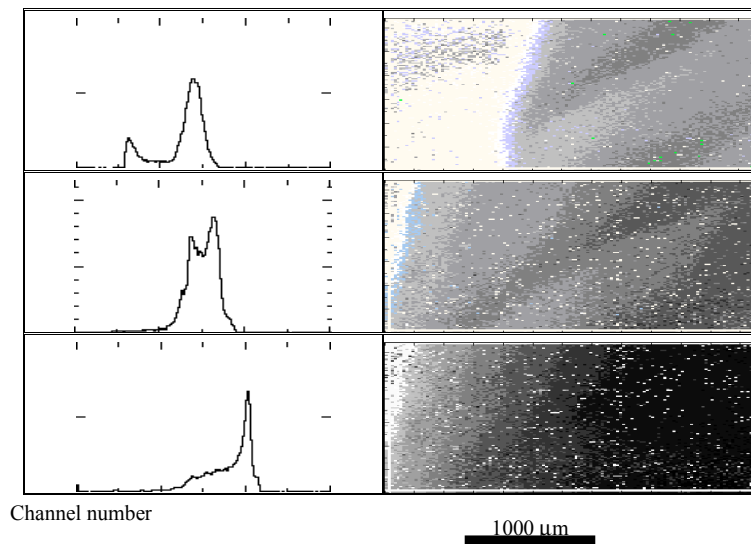


Fig. 6. IBIC measurement of Si(Li) detector diode using 2.67 MeV Li^6 ions. Left column presents the total pulse height spectra. IBIC images (mean presentation), with dark regions having high pulse heights, are obtained with three bias voltages (100 V - up, 300 V - middle, 1000 V - down). Detector central region is at the right of the image. Scan size was $1 \times 3 \text{ mm}^2$. Note the increase of the depletion region area as the bias voltage increases.

3.2.1. CVD and natural diamond

Frontal IBIC is in particular important in the characterisation of the novel detection materials. In the development stage, most of these materials are characterised by an inhomogeneity in charge collection, which results in poor energy resolution. One example of such a material is a polycrystalline diamond, which has quite poor collection efficiency. In most of the cases, this material can not be used for the spectroscopic purpose, but due to its radiation hardness and chemical inert nature, it can be used in many applications in hostile environment. For the initial testing of the overall charge collection homogeneity, frontal IBIC as shown in Fig. 7, has to be applied.

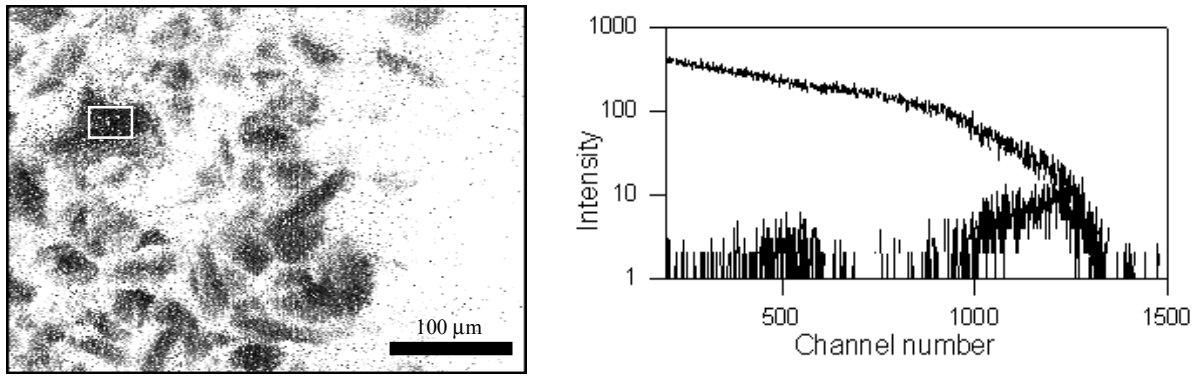


Fig. 7. IBIC measurement of CVD diamond detector. Frontal IBIC image (upper) was obtained using 2 MeV proton beam with a scan size of $420 \times 300 \mu\text{m}^2$. Total pulse height spectrum (T) shows inability of this CVD diamond detector to resolve energy of the ion. Still, the high IBIC signal region denoted with square clearly shows the energy peak (A).

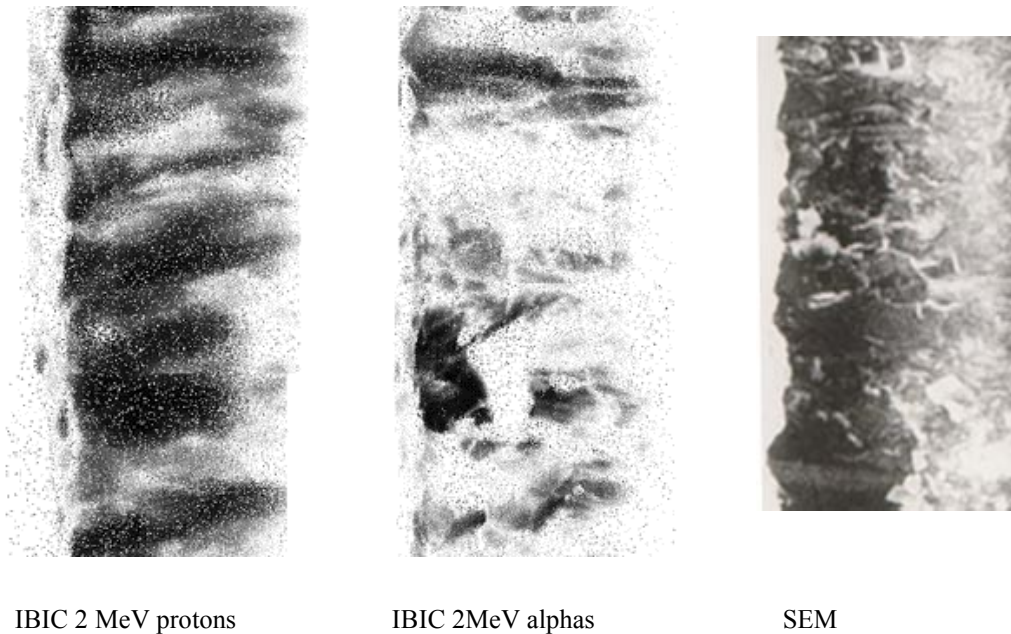


Fig. 8. Lateral IBIC analysis of the cleaved surface of commercial grade CVD diamond detector. A SEM image of the same region is shown on right.

Another possible orientation of the sample respective to the beam direction is illustrated in [6]. In the cleaved section of CVD diamond sample, charge collection efficiency distribution along the line or area between two electrodes is directly measured. In addition, the space charge effects are in lateral IBIC reduced to a minimum. Example of lateral IBIC measurement is given in Fig.8 that presents two IBIC images of the same region using protons (24 μm range) and alpha particles (3.5 μm range). They do not show significant similarity. Quite different range and energy loss can explain this difference. Short ion path for alpha particles give much higher importance to the cleaved surface. It is therefore easier to correlate alpha IBIC image to the SEM picture of sample morphology. Such example is the high efficiency region extending from electrode to electrode, which corresponds to the long crystal visible at the top of the SEM picture. Such analogy once more corroborates our previous observations that have put in evidence the strong influence of the polycrystalline nature of CVD diamond on its electronic properties. Still, it is interesting to note that some of the crystals at the cleaved surface show collection efficiency close to 50% in spite of the small range of alpha particle (3.5 micrometers).

electronic properties. Still, it is interesting to note that some of the crystals at the cleaved surface show collection efficiency close to 50% in spite of the small range of alpha particle (3.5 micrometers).

With a sufficiently fast data acquisition, count rates of up to 10 kHz can be quite well processed using the conventional electronic chain. However, in spite of quick analysis, high beam currents will more probably affect reproducibility of IBIC results due to various effects.

In the case of CVD diamond, excessive number of charge carriers created in small volume, changes the equilibrium distribution of electric field inside of the device. Such formation of space charge clearly affects the IBIC response. This effect is frequently observed in attempts to decrease the scan size and resolve the IBIC response close to the grain boundaries.

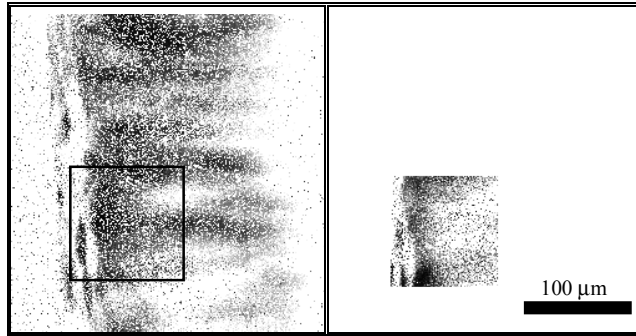


Fig. 9. Lateral IBIC scan of a CVD diamond detector using a 2 MeV proton beam (left). Note the difference in IBIC response of the central part of the square region scanned separately (right) with a same beam current (aprox. 1000 particles/second).

Example of such an attempt is presented in Fig. 9. Here, lateral IBIC was performed twice on a particular region of CVD diamond sample. First image (left) was obtained by scanning the whole area, while for the second image (right) part of the region was scanned while the beam intensity was maintained constant. Much higher charge per unit area injected to the region in the same time enabled the space charge formation. Clear decrease in charge collected from the central region of reduced scan area is observed.

Higher ion dose applied to CVD diamond can also destroy the space charge and average out the IBIC response among regions previously having high and low collection efficiency. On the other hand in the case of natural diamond, excessive ion currents applied for a longer period cause the saturation of trapping centres, which results in increased charge collection. More detailed discussion of CVD and natural diamond charge collection properties effects can be found in references [7,8].

3.2.2. Defect structures in polycrystalline silicon

The low cost polycrystalline substrates used in solar cell production suffer of high concentration of impurities and defects. The influence of the particular defect on the electrical properties of material is important information and can be obtained only by application of different characterisation techniques. Various samples of edge-defined film-fed grown (EFG) and Czochralski (Cz) silicon were analysed by IBIC as well as Deep Level Transient Spectroscopy (DLTS) in order to identify the most important deep levels in band gap. Influence of twin boundaries in EFG samples and high oxygen content of Cz material on IBIC results were studied as well as the IBIC induced defects in test samples [9].

Silicon sheets for this study were grown at Mobil Solar Energy Corp. (now ASE Americas Inc.) in EFG ribbon system. The samples were boron-doped, with resistivity 2-4 Ωcm , and sulphur-doped with about 200 μm thickness. Samples were grown in argon atmosphere with addition of CO_2 gas. Floating zone (FZ) and Czochralski grown (CZ) single crystals were also boron doped.

All samples were cleaned and after that about 30 μm of the surface layer was etched from both surfaces with CP-4 etch. Gold and aluminium was evaporated through shadow masks on clean surface to form Ohmic and Schottky barrier contacts respectively. Both I-V and C-V measurements were taken to insure the integrity of the diode characteristics. Some samples were upon cleaning and planar etching annealed in vacuum better than 10^{-5} Pa. After the annealing samples were planar etched again and than diodes were made.

a) EFG silicon

The main characteristics of multicrystalline edge-defined film-fed grown - EFG silicon, is existence of large density of intergrain defects (dislocations, twin boundaries), very high carbon content (10^{18} atoms/cm²) and relatively low oxygen content (10^{16} atoms/cm²). Increasing the oxygen content in EFG material showed to have positive effects on the efficiency of solar cells. Since oxygen and other impurities in silicon tend to segregate along the structural defects, techniques such as IBICC or EBIC applied on EFG silicon can provide spatial information about the positions of electrically active defects. In addition to IBICC performed with proton and Li⁷ beam, a DLTS measurements were performed on the same samples in order to find the most prominent deep levels that are responsible for charge trapping processes.

In Fig. 10, line scan IBICC profile of the as received EFG sample shows prominent loss of CCE on all twin boundaries of studied sample. CCE profile is similar to expected one for grain boundary as modelled previously by Donolato. Significantly lower IBICC signal was obtained for 3 MeV protons, when compared to 4.5 MeV Li⁷ ions, indicating that diffusion length of minority carriers (electrons) is much lower then in single crystal silicon.

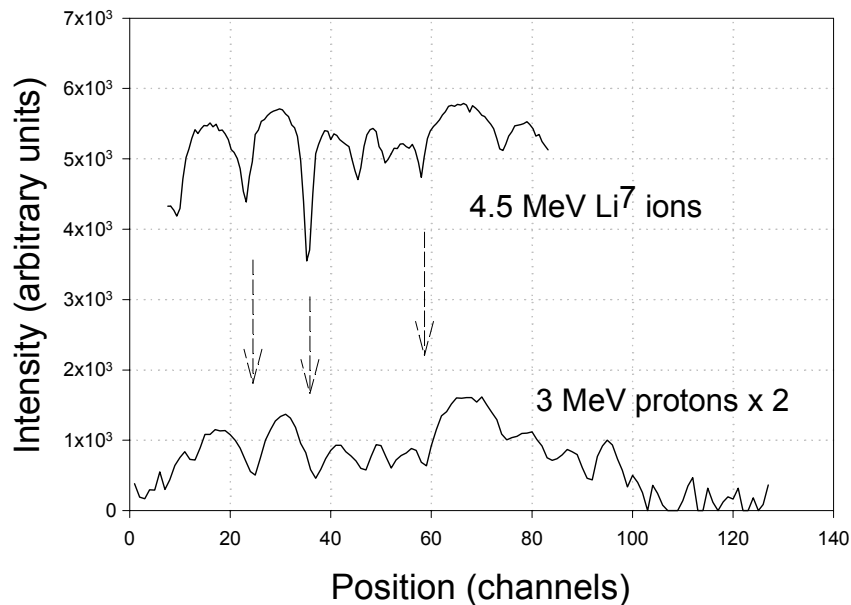


Fig. 10. Line IBICC scan (100 channels = 1mm) over the as received EFG silicon sample. Upper curve corresponds to the 4.5 MeV Li⁷ ions, while lower curved multiplied by 2 corresponds to the 3 MeV protons.

Comparison of Li⁷ IBICC response obtained at sulphur doped sample and same sample annealed at 750 C, lead to the conclusion that some of the twin boundaries are electrically passivated with annealing. Some of the twin boundaries visible optically can not be recognised in IBICC image in spite of rather small range of Li⁷ ions. As it is seen in Fig. 11., in addition to lines of decreased CCE, two bands of low CCE not directly associated by twin boundary are also visible. Since the mechanism of charge loss can not be attributed to any particular impurity without additional elemental distribution analysis, further microprobe NRA and PIXE are planned to clarify this behaviour.

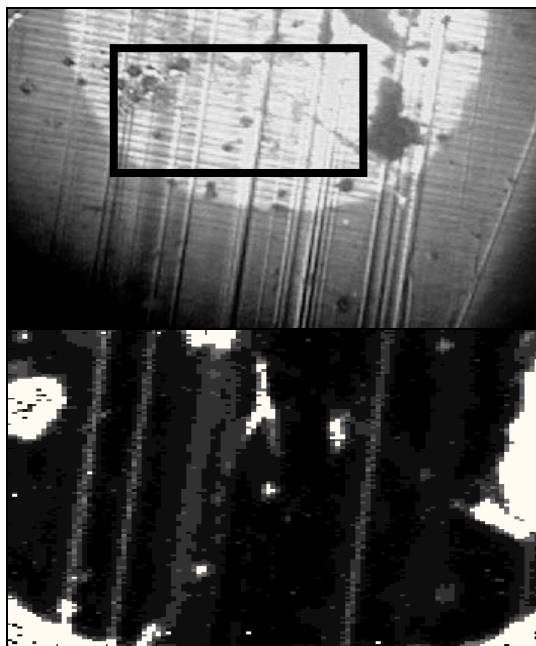


Fig. 11. Optical micrograph (up) and 4.5 MeV Li⁷ IBICC image (down) of the EFG sample annealed at 750^o for three hours. Rectangle indicates region of IBICC scan. White regions in IBICC map correspond to the mechanical damage of aluminium contact.

In the most of EFG samples analysed by DLTS as well, a prominent peak at $E_T=0.36$ eV above the valence band was found. This peak consists most likely of several deep levels and as it was shown previously, most of those are oxygen related.

b) Cz silicon

As large number of twins and dislocations characterise EFG silicon, monocrystalline Czochralski material is characterised by its very high oxygen content (10^{18} atoms/cm²). When compared to float zone (FZ) silicon having by 2%-3% absolute higher solar cell efficiency than Cz silicon, as well as much lower oxygen content, it is generally believed that oxygen could be responsible for this difference. Since formation of defect clusters of segregated oxygen could be one of the reasons in CCE decrease, IBIC was planned to be performed on wide range of sampling depths. Three different ions (3 MeV protons, 4.5 MeV Li⁷ and 7.875 O¹⁶ ions) have range in silicon 90, 8.5 and 4.5 μ m respectively.

When comparing proton with Li⁷ IBICC image obtained at the same sample (Fig. 12.), no correspondence in any of features can be established. Due to the much larger diffusion length, proton IBICC corresponds to much deeper regions in the sample, while Li IBIC presents near surface region. Lines and patches of low CCE dominate in this near surface IBIC measurement. Although sample surfaces were etched 30 μ m deep, lines (scratches) in IBIC image correspond to the induced damage during the sample polishing. There is no observed effect of this surface imperfection on the proton IBIC result.

In order to confirm importance of oxygen in charge loss of Cz solar cells, we tried to find inhomogeneities in oxygen distribution using NRA imaging and O¹⁶(d,p₁)O¹⁷ nuclear reaction. Unfortunately, homogeneous response and rather weak signal to noise ratio could not be correlated with both frontal and lateral IBIC images of Cz samples.

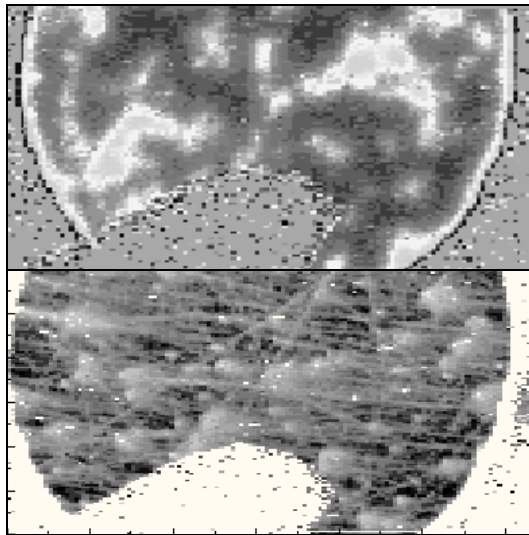


Fig. 12. Typical IBIC images of 3 MeV proton (up) and 4.5 MeV Li^7 (down) scan over the Cz silicon sample. No correspondence between regions of low CCE (bright) can be observed.

3.2.3. Radiation damage

In conventional IBIC experiments using protons, radiation damage is negligible problem. However, ability to have a tuneable intensity radiation source, on-line study of radiation damage in IBIC samples is possible [10]. As an example, in Fig. 13. a degradation of CdTe sample after irradiation with 3 MeV protons is given.

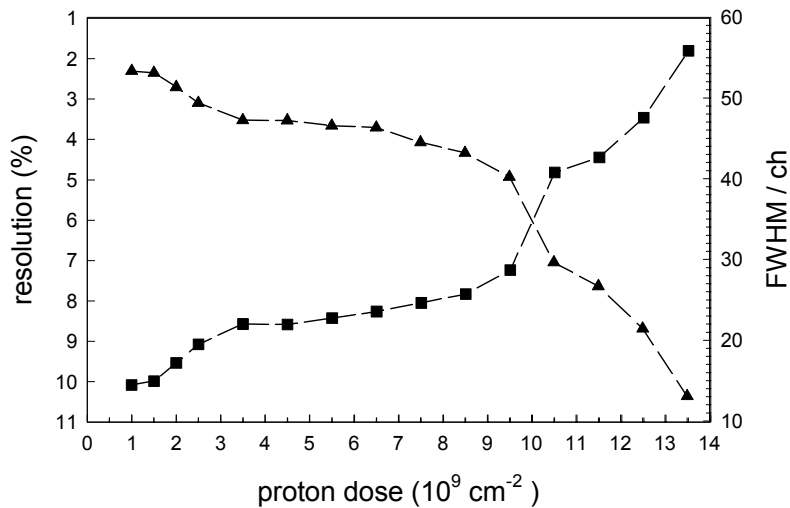


Fig. 13. Energy resolution degradation (triangles) of IBICC peak and the increase of peak's FWHM (squares) as a function of proton irradiation dose.

In attempt to image the damage introduced by protons, an IBIC analysis of broader sample area showed that the IBIC signal reduction is observed in much larger area then one originally irradiated. Possible answer to this observation can be described by changes in electric field, or decreased mobility of charge carriers in vicinity of damaged region.

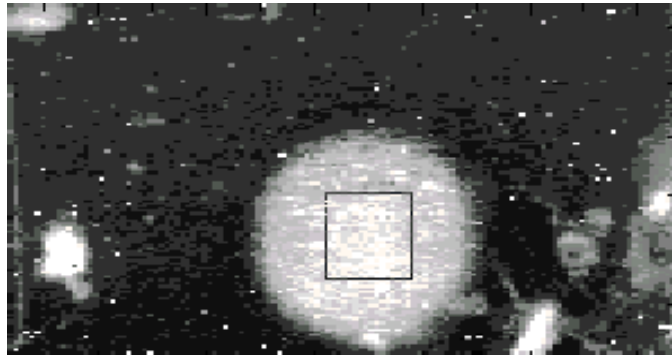


Fig.14. IBICC image of CdTe damaged area (lower charge collection efficiency), approximately $700 \times 350 \mu\text{m}^2$. Proton micro-beam irradiated area ($100 \times 100 \mu\text{m}^2$) is indicated by square.

4. Conclusion

As it is discussed in the previous chapters, IBIC technique showed remarkable capabilities of focused ion beam of MeV energy for testing the charge collection properties in semiconductor materials and in particular semiconductor radiation detectors. Development of various novel materials that are now under tests (e.g. CVD diamond with considerable radiation hardness, or CdZnTe - perspective room temperature gamma detector), increase the need for IBIC applications and IBIC further development. Therefore our future plans will be mostly concentrated in development of theoretical and experimental aspects of IBIC in research of novel radiation detector materials. However, in the cases where elemental composition of these materials is influencing its electrical properties, other nuclear microprobe methods will be applied as well (ERDA, IBIL, PIXE, RBS).

REFERENCES

- [1] JAKŠIĆ, M., PASTUOVIĆ, Ž., TADIĆ, T., New developments in IBIC for the study of charge transport properties of radiation detector materials. , Nucl. Instr. and Meth. 158 (1999) 458-463.
- [2] VITTONI, E., FIZZOTI, F., GARGIONI, E., LU, R., POLESELLO, P., LO GIUDICE, A., MANFREDOTTI, C., GALASSINI, S., JAKŠIĆ, M., Evaluation of the diffusion length in silicon diodes by means of the lateral IBIC technique. , Nucl. Instr. and Meth. 158 (1999) 476-480.
- [3] VITTONI, E., FIZZOTI, F., LO GIUDICE, A., PAOLINI, C., MANFREDOTTI, C., Nucl. Instr. and Meth. 161-163 (2000) 446.
- [4] PASTUOVIĆ, Ž., JAKŠIĆ, M., JAMES, R. B., CHATTOPADHYAY, K., MA, X., BURGER, A., Influence of electrical contacts on the charge collection profiles in CdZnTe studied by focused proton beams, accepted for publication in Nucl. Instr. and Meth. A.
- [5] JAKŠIĆ, M., FAZINIĆ, S., TADIĆ, T., BOGOVAC, M., BOGDANOVIĆ, I., PASTUOVIĆ, Ž., IBIC study of charge collection properties in Si(Li) detectors, Nucl. Instr. and Meth. B136-138 (1998) 1327-1332.
- [6] JAKŠIĆ, M., TADIĆ, T., ORLIĆ, I., OSIPOWICZ, T., VITTONI, E., MANFREDOTTI, C., Imaging of charge collection properties of CVD diamond using high resolution ion beam induced charge technique with protons and alpha particles, Diamond Films and Technology, 8 (1998) 391-398.
- [7] MANFREDOTTI, C., FIZZOTI, F., POLESELLO, P., VITTONI, E., TRUCCATO, M., LO GIUDICE, A., JAKŠIĆ, M., ROSSI, P., IBIC and IBIL microscopy applied to advanced semiconductor materials, Nucl. Instr. and Meth. B136-138 (1998) 1333-1339.
- [8] MANFREDOTTI, C., FIZZOTTI, F., LO GIUDICE, A., POLESELLO, P., VITTONI, E., LU, R., JAKŠIĆ, M., Ion microbeam analysis of CVD diamond. Diamond & Related Materials. 8(8-9):1597-1601, 1999.

- [9] JAKŠIĆ, M., BORJANOVIĆ, V., PASTUOVIĆ, Ž, BOGDANOVIĆ RADOVIĆ, I., PIVAC, B., IBICC characterisation of defect structures in polycrystalline silicon, submitted for publication in Nucl. Instr. and Meth. B.
- [10] PASTUOVIĆ, Ž., JAKŠIĆ, M., Frontal IBICC study of the proton induced radiation damage in CdTe detectors, submitted for publication in Nucl. Instr. and Meth. B.

REAL TIME MONITORING OF ELECTRONIC MATERIALS AND DEVICES USING MICROBEAMS

C. MANFREDOTTI

Experimental Physics Department, University of Torino,
Torino, Italy

Abstract

IBIC and IBIL techniques with proton microbeams of diameter of the order of 1 μm and of energy in the interval 2 MeV–6 MeV have been used in different configurations and geometries in order to characterize frontier semiconducting or insulating materials like GaAs and CVD diamond, or more traditional materials like Si, by looking at space distribution of important transport parameters like drift and diffusion lengths. By applying lateral IBIC in GaAs Schottky diodes it had been possible to follow directly the widening of depletion region as a function of bias voltage, while for Si drift/diffusion structures a particular code has been developed in order to measure directly the diffusion length and lifetime of minority carriers. In CVD diamond both IBIC and IBIL measurements have been performed in frontal and lateral geometries. The main results are represented by the correlation between IBIC maps and morphology of the grains, with the conclusion that collection length is limited by the grain dimensions, by the proof of the validity of the linear model, by the clarification of the spatial behaviour of the “primed” or irradiated state in terms of homogeneization and improvement of charge collection length and, finally, by the observation of a quasi-complementarity in space between IBIC and IBIL maps, with the conclusion that in CVD diamond the recombination is mainly radiative. Moreover, concerning nitrogen content, a method has been proposed in order to forecast the detector quality of CVD diamond from IBIL spectra.

1. Introduction

IBIC (Ion Beam Induced Current or Charge) seems to be the only method by which it is possible to obtain two-dimensional maps of important transport parameters in semiconductor devices, like drift and diffusion length, mobility and lifetime, etc. By the same method and under particular conditions, also electrical field profiles in the active regions of the devices are obtained. IBIC in the past was generally used to investigate structures and devices, which were characterized by thin depletion layers and thick diffusion substrates. In this version, IBIC is very similar to EBIC, apart from longer penetration depth of light ions.

IBIL (Ion Beam Induced Luminescence) is another important technique, which can supply spatial informations on specific radiative recombination centers in optoelectronic materials and devices. IBIL, until now, has been particularly used for rare earth detection in minerals in connection with PIXE (Particle Induced X ray Emission) or in order to follow radiation damage in semiconductor materials.

A quite different approach is presented in this report, in which IBIC is used for imaging totally depleted regions of insulators and semiconductors, relying only in carriers drift in order to measure and to map the drift length or charge collection length. Diffusion is neglected and narrow collected energy peaks are displayed for homogeneous materials, in which either the collection length or the electrical field profile can be measured, emphasizing effects close to contacts or to diffusion regions. In the case of non-homogeneous materials, like polycrystalline Si or CVD diamond, collection efficiency and collection length maps can be obtained, enlightening the electrical or transport inhomogeneity of the material. This is particularly true for what we called “lateral IBIC” (see Fig. 1), in which the charge collection efficiency is directly measured on a cross-section of the sample. A big advantage of this method is to avoid plasma recombination of carriers because the direction of the electrical field is perpendicular to the axis of the ionized charge drop produced by the ion. Because of the presence of a strong Bragg peak in the energy loss distribution as a function of depth, the relevant data can be attributed to a specific depth region, and they are not particularly influenced by the surface, even if it not natural or as-grown (i. e. lapped, polished or cleaved).

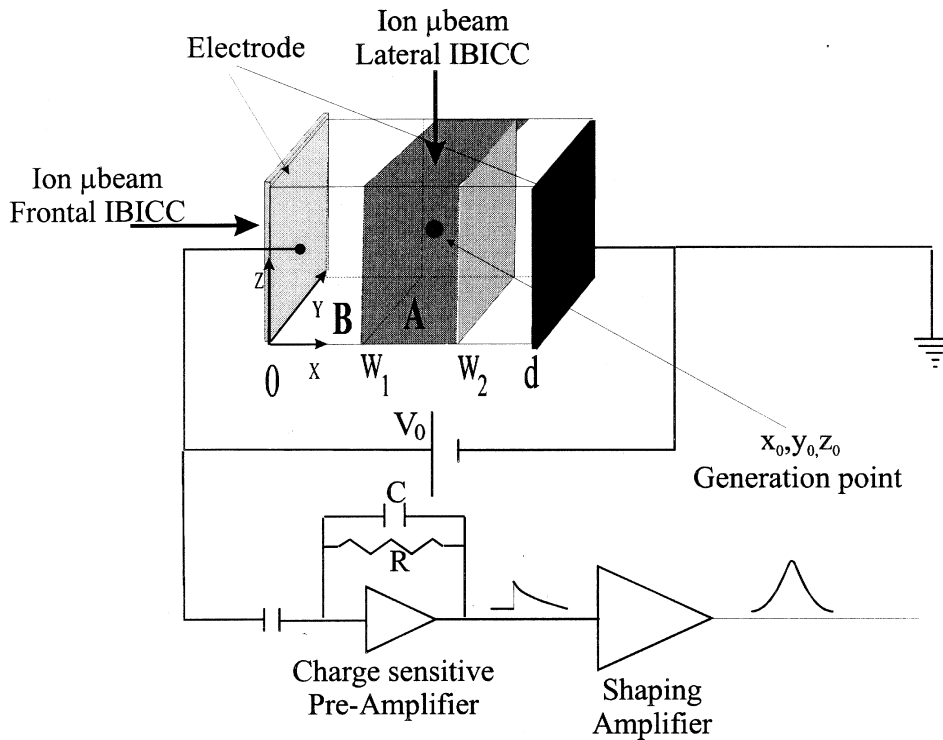


Fig. 1. Schematic of IBIC sample geometry. The B region is in general the highly doped dead layer in front of the structure, the A region is the depletion layer in which electrical field is present, while the last one is the diffusion region.

2. Experimental

IBIC measurements in Si, GaAs and in natural and CVD diamond have been generally carried out in this work by using the 6 MeV proton microbeam of the Ruder Boskovic Institute (Zagreb, Croatia), with ion beam focused to about 2–3 μm in diameter and with extremely low currents, in order to get no more than 100–1000 c/s. IBIL measurements have been performed with the 2.5 MeV microbeam facility at the INFN Legnaro Laboratories, Italy, which displays approximately the same characteristics. In the case of many IBIL measurements, larger intensities have been used, because of the small solid angle seen by the two phototubes, put in coincidence in order to lower the noise as much as possible. The low counting rate both in IBIC and in IBIL, together with the necessity of avoiding long counting times particularly in the case of materials with short collection lengths (CVD diamond, GaAs), has the important and obvious drawback of statistical fluctuations in the obtained maps. For the characterization of materials, however, and in contrast with the requirements for microdevices investigations, a high spatial resolution is not needed, and merging of nearby pixels' contents helps in order to keep statistical fluctuations in a reasonable range.

The charge (IBIC) signal (see Fig. 2) was recorded by a standard charge-sensitive electronic ORTEC chain as a function of the hit position and the collection efficiency was calculated with respect to a standard surface barrier Si detector (efficiency 100%). The panchromatic IBIL spectra were recorded by two Hamamatsu R647-01 phototubes mounted 1 cm apart from the sample and at an angle of 135° and 225° with respect the beam axis. The resolving time of the coincidence system was less than 10 ns. IBIL signals, proportional to the number of emitted photons weighted over the spectral response of the photocathodes (350–600 nm) were also mapped as a function of the proton hit position onto the sample. IBIL was recorded at zero bias, but in the same regions as IBIC. Shaping times from 0.5 μs to 4 ms were used both for IBIC and IBIL.

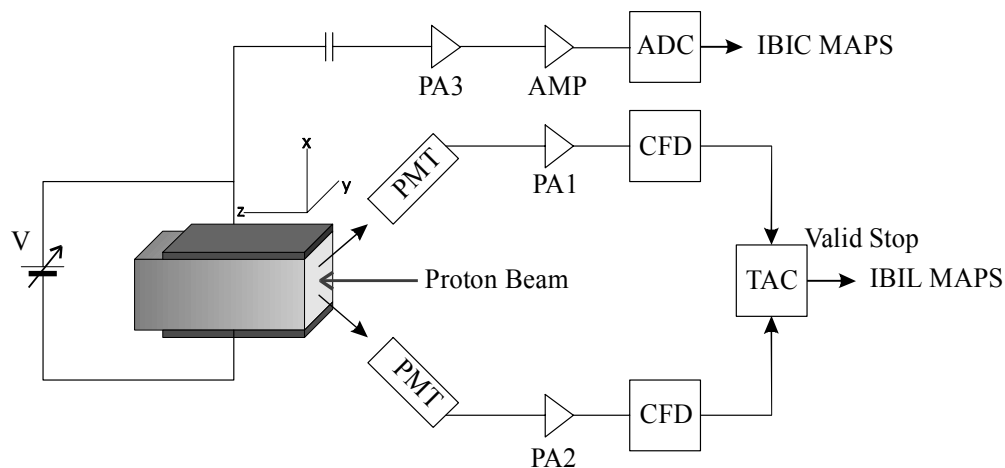


Fig. 2. Lay out of the electronics used in combined IBIC/IBIL measurements in the case of panchromatic IBIL.

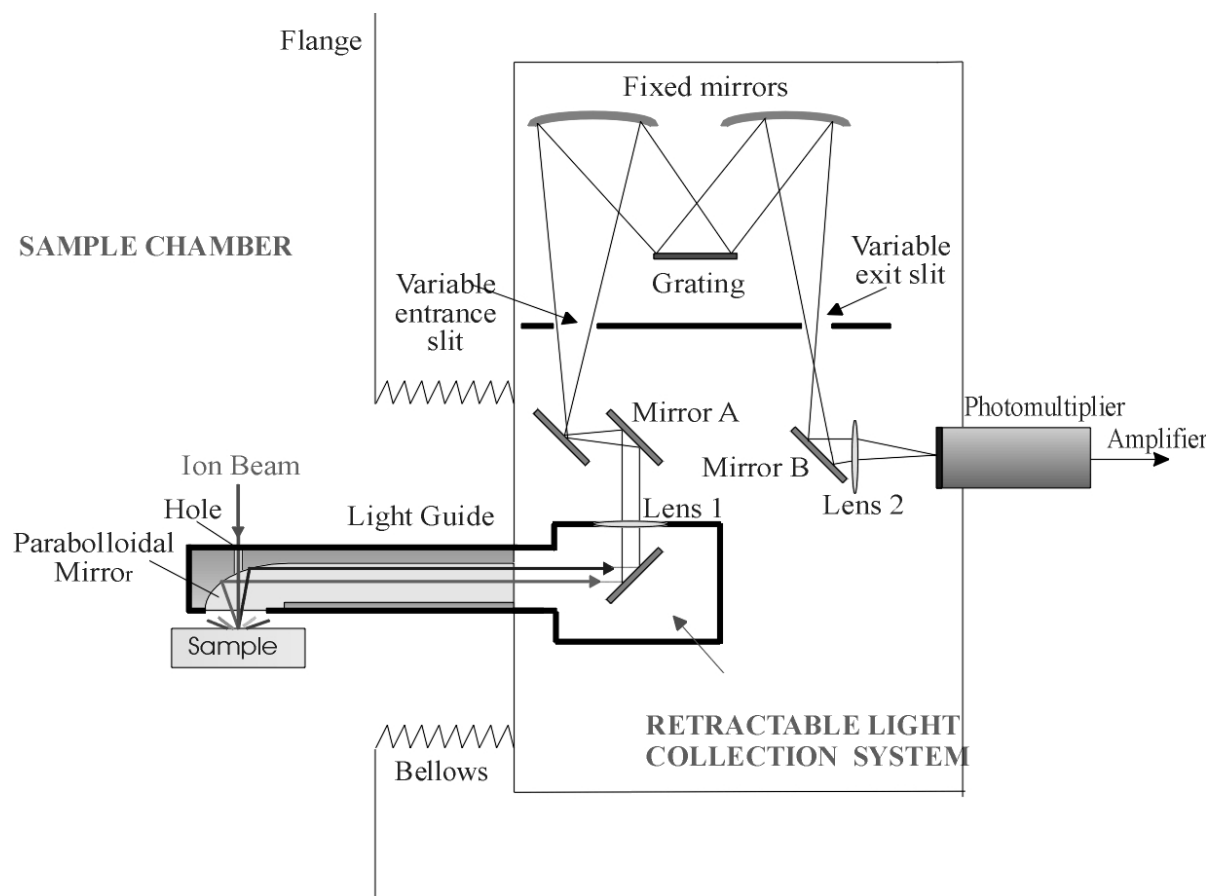


Fig. 3. Schematic of IBIL set up for the monochromatic version of the system.

Recently, a completely new version of the apparatus has been set up, as shown in Fig. 3, which allows for an almost 2π solid angle for light collection, with a light transport outside of the scattering chamber by a vacuum light pipe which does not introduce absorption even at the highest or at the lowest wavelengths and a standard 0.25 m Jobin-Yvon monochromator and a wide spectral range phototube. The proton or ion beam hits the sample after crossing a hole in the metal mirror (1 mm of diameter). The signal from the phototube is recorded using a standard amplification chain. When the microbeam is in a certain position, a gate is open (about 70 μs duration) to allow to collect pulses through the amplification chain until the beam moves to the next position. The (x, y) coordinates of the beam are recorded together with the number of pulses. Scan area in the present case is $0.5 \times 0.5 \text{ mm}^2$ and the scan time, for a map of 512×512 pixels, is of the order of 18 s. Several minutes are

needed in order to get a good map, depending on the radiative efficiency of the sample. Maps at a certain wavelength can be carried out also by using interference filters instead of the monochromator. When an IBIL map is not needed, by defocusing the microbeam it is possible to work with a relatively wide beam of dimensions comparable with the scan area, in order to get simply average IBIL spectra as a function of wavelength by the automatic scan of the monochromator and by collecting and amplifying the output current from the phototube. Beam current intensities are generally of the order of 700–800 pA in order to have a good signal. Together with IBIL, it is possible to get PIXE by collecting X ray pulses due to protons with a Si(Li) detector placed in the same scattering chamber as in EDAX (Energy Dispersive Analysis by X ray) in standard SEM microscopes, with the advantage of a much better sensitivity because of absence of bremsstrahlung background.

3. Results and discussion

3.1. Spatial evolution of electrical field in GaAs Schottky diodes

GaAs is a good candidate material for particle and X ray detection. Due to its relatively low resistivity, Schottky barriers are generally needed in order to get low dark currents. Some complaints were due in the past to the non-excellent energy resolution of some available material in alpha particles spectra. In fact, by using 2 MeV protons hitting the front (Schottky) electrode, two peaks are visible in the multichannel spectrum carried out on a region of a fraction of mm² in surface area (Fig. 4). The reason for this “subtle” broadening of the full energy peak was soon understood: the collection efficiency maps showed that the sample was “electrically” inhomogeneous and it was characterized by two complementary regions of slightly different collection efficiency (see Fig. 5). Similar results were obtained by hitting the bottom electrode. Explanations for this astonishing result were not clear at that time.

Lateral IBIC measurements were also performed on specially cleaved and passivated cross-section of a GaAs device. Fig. 6 shows the enlargement of the depletion region from Schottky electrode towards the back one at increasing bias voltages for a sample 250 μm thick. These profiles, reported as collection efficiency values, are in good agreement with the profiles of the electrical field as obtained by a Kelvin probe, since in the most parts of the curves the collection efficiency is proportional to the drift length and, therefore, also to the electrical field. We were able, by this way, to measure directly and “visibly” the depletion layer width as a function of bias, as shown in Fig. 7. It has to be noted that, while Kelvin probe measures only the surface potential, IBIC supplies, through the collection efficiency, a measure of the electrical field *in the bulk*.

Maps of lateral IBIC indicated that the sample was almost uniform, that it did not show any “two phase” behaviour and that, as a consequence, the inhomogeneity could be attributed to some “electrode” effect.

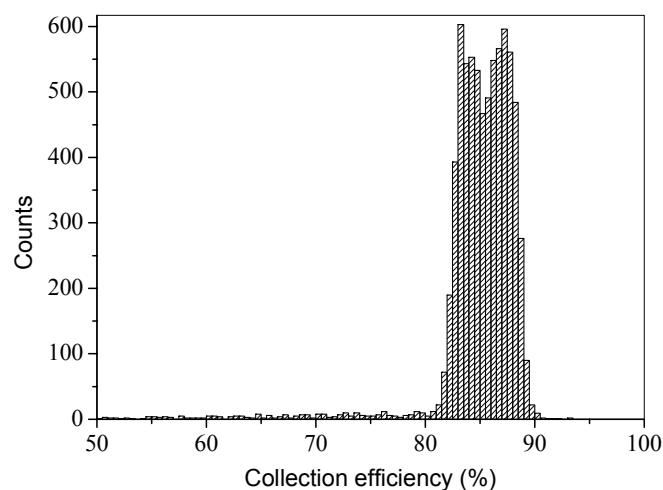


Fig. 4. Alpha (Am-241) multichannel spectrum as obtained by frontal IBIC on a Schottky side of a GaAs diode.

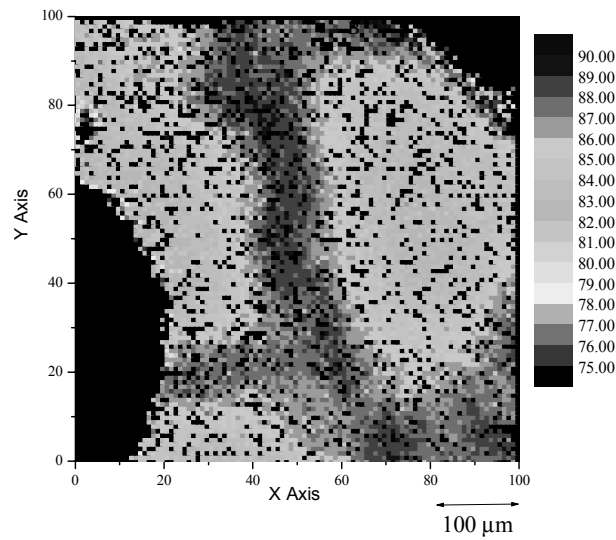


Fig. 5. Frontal IBIC map on a Schottky side of the same GaAs diode quoted in Fig. 4, showing zones of different charge collection efficiency .

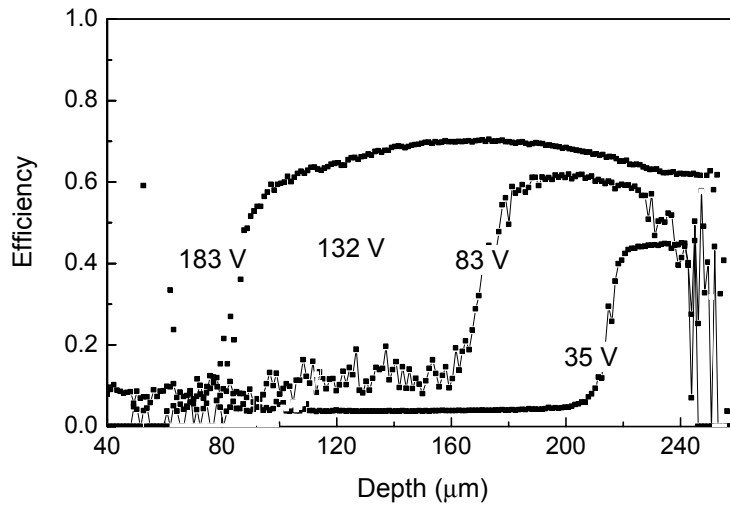


Fig. 6. Profiles of the charge collection efficiency at different bias voltages as obtained by lateral IBIC on a cleaved cross section of a GaAs Schottky diode. The Schottky contact is at the right hand side.

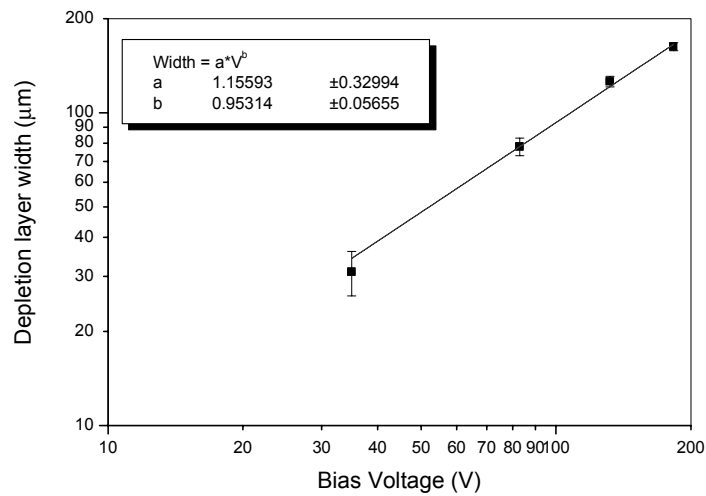


Fig. 7. Behaviour of the thickness of the depletion region as a function of the bias voltage as derived from the profiles shown in Fig. 6.

3.2. Unidimensional Si drift/diffusion structures

For obvious reasons, the structures investigated by the lateral IBIC were the thick ones, very common to power Si devices. An example is given in Fig. 8, where a doping profile of a typical p^+-n-n^+ structure is reported, as measured by spreading resistance. On structures like this one, on which maps and profiles of the collection efficiency from one electrode to the other one have been measured by lateral IBIC using a 5 MeV proton beam with a penetration depth of 215 μm , several attempts have been made in order to set up a complete code for data interpretation. The first one was based on a Monte Carlo approach extended to the diffusion and the drift regions, both included in the region n of Fig. 8 and corresponding to the zones (w_2-d) and (w_1-w_2) of Fig. 1 respectively. The electrical field profile was derived by GEMINI code and in each slab in which the drift-diffusion zone was divided, electrons and holes were allowed to move according to their mobilities (drift) and diffusion coefficient (diffusion) in subsequent time steps, taking their trapping time as a parameter and asking in each slab for the probability to be trapped. Mobilities were calculated with standard equations. The depletion region was defined as limited by the coordinate in which diffusion and drift got the same probability. Assuming reasonable starting values for electrons and holes trapping time, it was possible to deconvolute the collection efficiency profile in the contributions of electrons and holes which gave the best fit to the experimental curve. By this method, which was time consuming because there were no hints concerning the search for the best trapping time values, it was possible to determine trapping times in Au doped and undoped n regions.

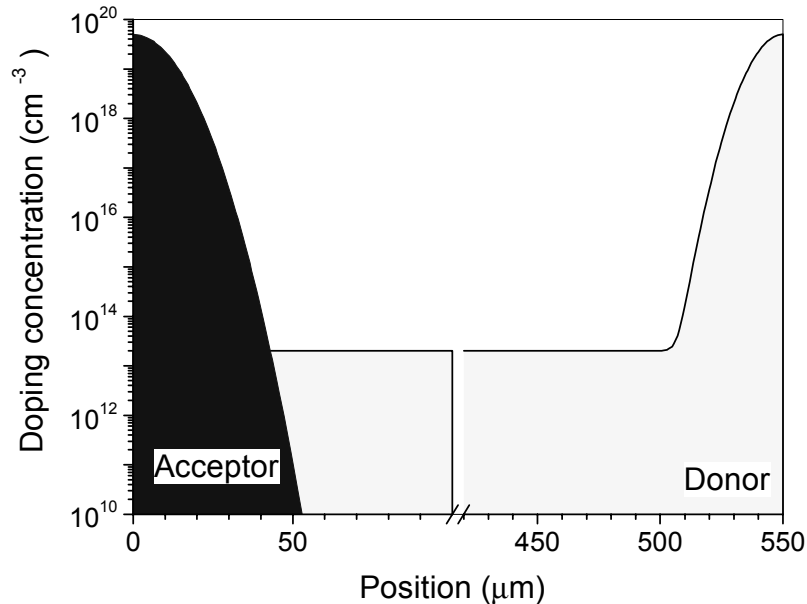


Fig. 8. Doping profile of a p^+-n-n^+ Si structure used in power devices.

The second approach was based on the extended Ramo theorem and it was mainly centered towards the fit of the exponential decay of the collection efficiency in the diffusion region in order to obtain the diffusion length and the lifetime of minority carriers diffusing towards the drift region (holes in this case). The fits in the selected cases were good and the lifetimes derived by this way were in good agreement with data obtained with other methods or with values expected from the material under consideration. Some problems however arised concerning the exact determination of the depletion zone width (defined here as the limit at which the exponential fit stopped to work), particularly in cases in which doping was not uniform, and concerning the relationship between the experimental shaping time and the lifetime, since when the last one was longer a ballistic deficit appeared suddenly. Moreover, the fluctuations of collection efficiency in the steepest decays of collection efficiency needed some consideration. All these topics were taken under examination and a more general theory was obtained which was valid under any relationship between shaping time and lifetime. Since, however, computing procedures were too long (a fit was needed also in this case), a quite different approach was adopted which used Green function method in order to obtain a

“conjugate“ or “adjoint “ of the standard continuity equation for semiconductors in cases when both drift and diffusion were present. The beauty of this approach was that the solution of this equation was exactly the collection efficiency profiles. Mobility profiles were calculated by PISCES code. An example of the results obtained by this approach is shown in Fig. 9 where the contributions of electrons and holes to the collection efficiency are obtained quite easily both in the drift region, where the collection efficiency is almost 100% and in the diffusion region. In the same time, by both methods (Ramo theorem and Green function) a new and rigorous treatment of the behaviour of diffusion/drift regions in frontal IBIC geometry has been also obtained. Of course, lateral IBIC is the unique solution for the exact determination of diffusion length because it is based on a profile and not on the deconvolution of two integrals connected with diffusion and drift separately. Moreover, the assessment of the validity of Ramo theorem, which states that the collection efficiency is dependent only on the external electrical fields, is of paramount importance in order to correctly interpret IBIC data.

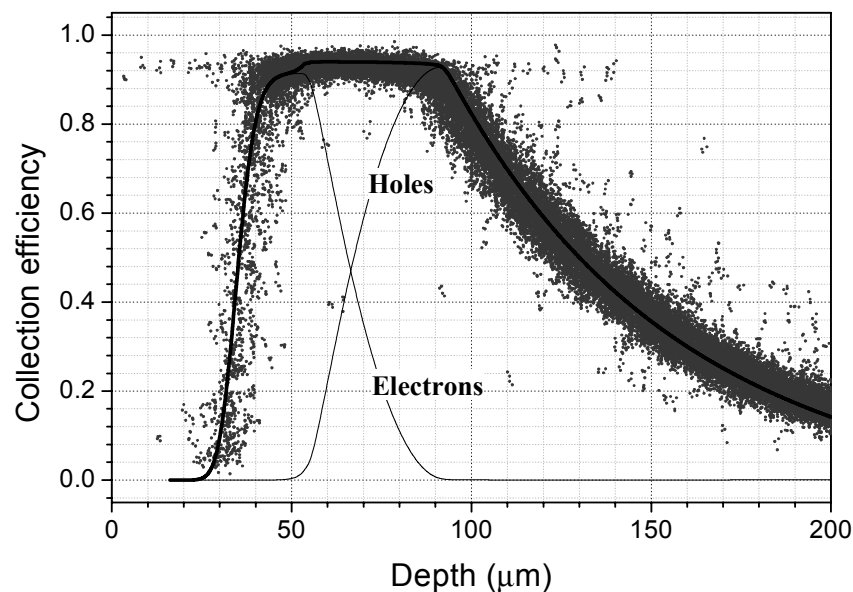


Fig. 9. Experimental charge collection efficiency profile as obtained by lateral IBIC on a structure similar to that reported in Fig. 8 and its deconvolution in terms of contributions of electrons and holes as derived from a calculation method based on the solution of the adjoint of the continuity equation for minority carriers.

3.3. CVD diamond nuclear detectors

CVD diamond is often related to natural diamond as far as the electronic properties are concerned. Even in the case of IIa natural diamonds, the charge collection efficiency is not large, and the best collection lengths are around 100 μm . What has been noticed is a slow increase of collection length with the total proton dose delivered to the sample. This sort of “dose sensitivity“ can be used in order to “write“ into a natural diamond sample with a microbeam. A visual effect is reported in Fig. 10, which shows some profiles of charge collection efficiency along a cross section of a natural diamond sample as obtained by averaging a map over a width of about 25 μm . The total zone length is about 250 μm . The left zone was irradiated by a proton dose of 12 Gy, and the right one by 3 Gy. The profiles increase with the dose, which was delivered in steps of 1 Gy. In fact it was possible to follow the increase in collection efficiency with dose up to a value of 11%, which corresponds to a collection length of about 110 μm for a sample 1 mm thick as in this case. The fluctuations in collection efficiency are of the order of 5–10%. As a matter of fact, by looking at maps obtained both in lateral and in frontal geometry, the uniformity of natural diamond with respect to collection efficiency is noticeable, even at the contacts.

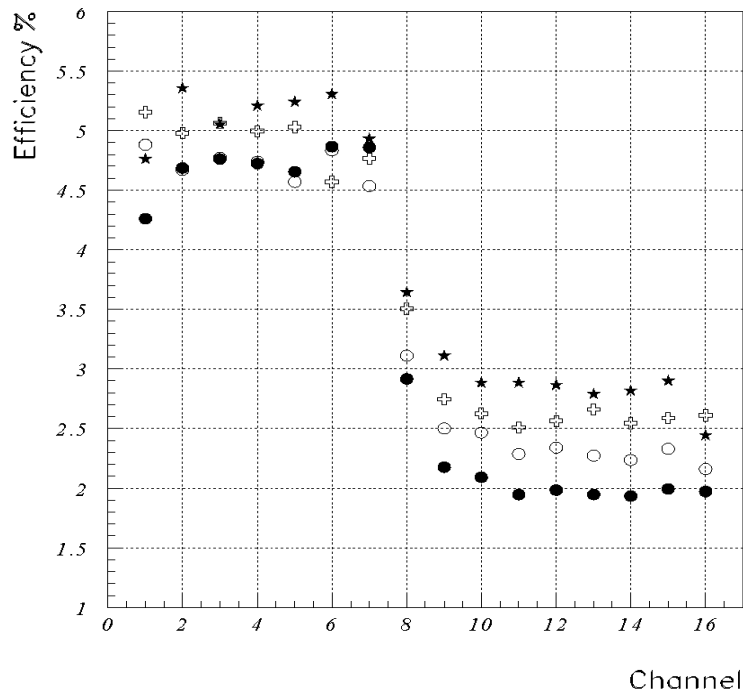


FIG. 10. Lateral IBIC profiles on a natural Iia diamond sample cross section. Proton energy is 5 MeV. Left zone was irradiated up to a dose of 12 Gy and the right one up to 3 Gy. The incremental dose between profiles is 1 Gy.

From 1992 to nowadays, CVD diamond has made remarkable progress that place it as the frontier material that has recorded the best improvements in electrical quality in the recent years. However, as our group has pointed it out several times, CVD diamond, being a polycrystalline material, still displays homogeneity problems, at least for the topmost performances as nuclear detection is assumed to display. The inhomogeneity of collection efficiency was evidenced both in standard “frontal IBIC” experiments and even better in “lateral IBIC”, in which the sample is hit on a cleaved cross-section and the electrodes are placed as close as possible to the borders in order to avoid fringing field effects. The range of a 6 MeV proton in diamond is however so long (150 μm) to be almost comparable with sample thickness (about 400 μm in all the cases) and to make sure that real bulk transport properties are measured. An important advantage of lateral IBIC lies in the fact that the electrical field quickly separates electrons and holes in the plasma created by the proton track ionization and by this way plasma recombination is avoided, making IBIC quantitative. In the standard “frontal” IBIC, on the contrary, holes and electrons drift in the plasma, and direct recombination through a center is much more likely.

Lateral IBIC collection efficiency maps clearly show a columnar or “stripe” structure which is tightly related to the morphological columnar structure as evidenced by SEM.

What can we learn from IBIC maps in CVD diamond, apart from the discovery of these “stripes”? First of all that “stripes” show better collection efficiencies toward the growth side, while the substrate side (CVD diamond films grow on nucleation sites on a silicon surface) collection efficiency is much lower. This is in agreement with the “linear model” which claims for a collection length linearly increasing with sample thickness. Secondly, “counts maps” in which only the number of charge pulses (and not the pulse height) is recorded per each pixel, are more uniform. This explains why “tracking” is really possible with CVD diamond, since in this case only pulses above a certain threshold are important. As a consequence, nuclear spectroscopy is very difficult with CVD diamond, even if a peak in the total pulse height distribution is seen in some cases, particularly for thinner samples. Viceversa, single grains may show a good spectroscopic behaviour, and also relatively large collection efficiencies.

In order to improve the homogeneity of the response of CVD diamond and also to increase the collection efficiency, the detectors are generally “pumped” or “primed” with X ray or electron doses

of the order of 20–100 Gy. We have investigated the spatial effect of priming by looking at samples before and after irradiation, by lateral IBIC and typical results are shown in Fig. 11, which displays plots of the collection efficiency on a region $1 \times 1 \text{ mm}^2$ wide for a not irradiated sample (top) and an irradiated one (bottom). It is evident that after irradiation the regions of higher collection efficiency widen out or, more properly, lengthen towards the two electrodes, which are placed vertically at both ends of the figure (growth side is at the right end side). The difference in efficiency scale indicates that also the top values of efficiency are increasing. Therefore it can be concluded that the spatial increase of collection efficiency is due to the drift of carriers towards the electrodes and to their subsequent trapping in regions extending towards the electrodes. The fact that the sample becomes more uniform in detector response is proved in Fig. 12, which reports multichannel spectra of 4 MeV protons over a $200 \times 200 \text{ }\mu\text{m}^2$ surface area in the not irradiated (continuous line) and irradiated (dashed line) case. The proton dose in this case is 46 Gy.

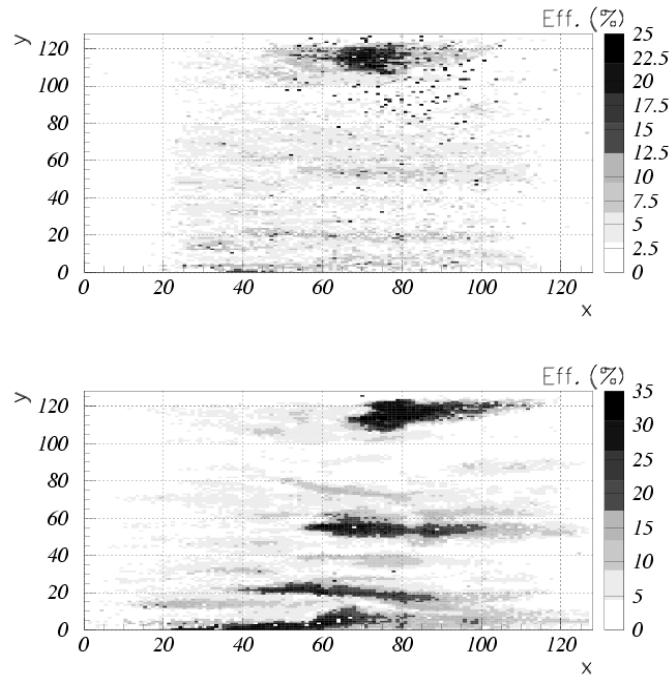


Fig. 11. Lateral IBIC plots over a region $1 \text{ mm} \times 1 \text{ mm}$ surface area of a CVD diamond sample, before (top figure) and after an irradiation up to a dose of 0.3 Gy. Proton energy is 2 MeV and a bias voltage -900 V is applied to the growth side to the right.

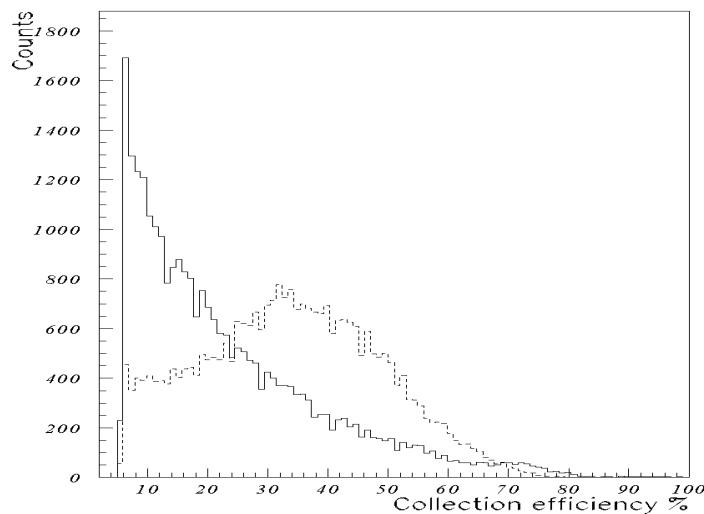


Fig. 12. Lateral IBIC multichannel spectra obtained with 4 MeV protons over a $0.2 \times 0.2 \text{ mm}$ wide area for a CVD diamond sample before irradiation (continuous line) and after irradiation to 46 Gy.

IBIL light emission efficiency may be considered as the "external quantum efficiency" for ion excitation, i.e. the ratio between the total number of photons (at a certain wavelength) emitted during the electronic shaping time and the number of the e-h created pairs. Assuming this definition and neglecting, as a first approximation, both the absorption and the reflection of light in the sample, it is easy to prove that $\eta_{\text{IBIL}}(x,y)$ is proportional to the *ratio* between τ_t (total trapping or recombination time) and τ_r (radiative recombination time) for the optical emission of interest. As a consequence, IBIL maps are certainly more uniform, since it is more likely that the ratio between the above quoted times is more homogeneously distributed than each of them taken separately. According to these considerations, IBIL and IBIC maps, which in principle could be imagined as complementary if radiative recombination dominates, in general are not or not completely: it is sufficient to observe, for instance, that there are regions in which *both* are absent and which are clearly characterized by a strong non-radiative recombination.

In another case light may come also from regions in which, for different reasons (space charge, dead zones, fringing field), the electrical field is zero and collection length too. In any case, we have gathered different cases of complementarity, such as those reported in Figs. 13 and 14, which show respectively a panchromatic IBIL count grey-scale map and an IBIC map carried out on the same region 400 μm high (the thickness of the sample) and 800 μm wide. Growth side is on the top. The bottom region, towards the substrate, is characterized by smaller grain dimensions and by shorter collection lengths, and, by looking at the figure, by higher luminescence and by lower collection efficiencies. As a consequence, it is almost obvious to conclude that in CVD diamond the recombination is almost completely radiative and that, if the grain boundaries effectively determine the maximum collection length, the radiative recombination should come also — even not completely, of course — from disordered regions close to the grain boundaries. As a matter of fact, monochromatic maps carried out in the blue region (the so called A band) are much less uniform and show a low coverage of the map area.

3.4. Nitrogen in CVD diamond

Nitrogen is difficult to detect: in effect, since PIXE is totally inefficient, we tried some NRA reactions such as (d,alpha) and (d, p-gamma) and also with thermal neutrons but, for different and essentially experimental and background reasons, with no success. Nitrogen is however relatively easy to investigate by EPR. In what follows, a qualitative correlation is presented between the nitrogen concentration in CVD diamond, as detected by EPR and therefore only partial, and the results obtained by IBIL measurements in the same samples as a function of the dose delivered by protons.

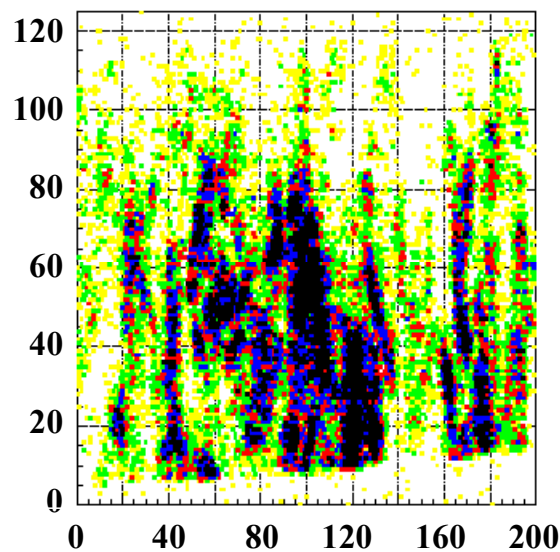


Fig. 13. Panchromatic IBIL counts grey-scale map along a cross section of a CVD diamond sample. Black regions register the highest counting rates. Growth side is at the top, substrate side at the bottom. Sample thickness and length are 400 μm and 800 μm respectively.

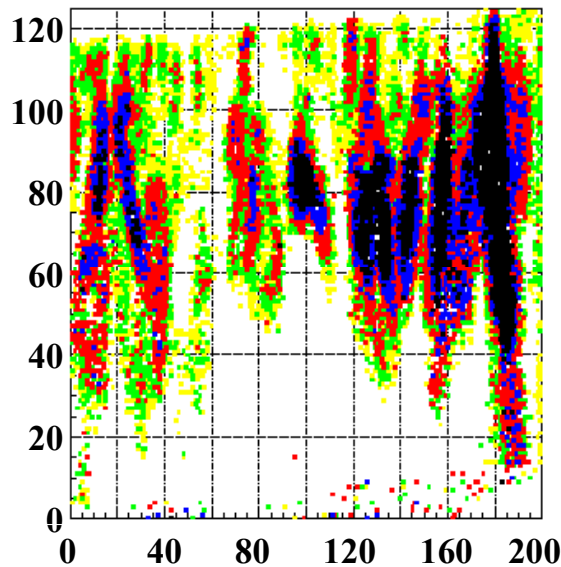


Fig. 14. IBIC collection efficiency map carried out in the same region as in Fig. 13. Black regions correspond to efficiencies larger than 20%. White regions correspond to charge pulses below a fixed threshold.

Fig. 15 shows several IBIL spectra carried out over the diamond sample CM1 in subsequent time intervals. The blue A band at 430 nm progressively disappears with time and proton dose, while the green A band at 510 nm is almost constant as a function of proton dose. IBIL maps, not shown in this work, indicate that A band is not homogeneously distributed in CVD diamond, but also that the different wavelengths included in the A band, from 400 to 460 nm, display exactly the same spatial distribution, with the conclusion that the blue A-band could be attributed to the same radiative center which can have different configurations or to the same cluster of correlated or compensated defects.

Fig. 16 shows IBIL spectra as in the previous figure, carried out in a different CVD diamond sample, R117: spectra are very similar, except for the appearance of a large band (which we can call B) in 580–630 nm interval. The sample R117 is characterized by a larger content of N and by very poor detector performances and very short charge collection lengths.

The decay curve of IBIL intensity of A band, as simply evaluated from the area of the peak, as a function of proton dose, is exponential. This observation could be explained only by an enhancement of the process of centers destruction or removal produced directly by the centers destruction or removal itself.

An evident general observation on the global results is that the B band present only in three of the six CVD diamond samples. The possible explanation is obtained by noticing that the larger N content (or at least the content detected by EPR) is correlated both to the smaller area (or height) of the 432 peak and, moreover, to the exclusive presence of the 600–630 band. It has to be considered that samples with larger N (EPR sensitive) content display shorter charge collection lengths or poorer electronic properties in terms of lifetime and mobility of carriers.

An explanation could be given according the following lines. If one attributes the blue A band to a N–N defect, it is clear that these defects should segregate preferentially in the highly damaged regions close to the grain boundaries, where the creation of defects, like vacancies, is relatively more probable with respect to the crystal regions. It should be mentioned that A band luminescence distribution is concentrated only in some regions which in the IBIL maps correspond to much less than 50% of the total area. These N-related defects are not so important in determining the electronic performances, since it has been demonstrated that charge collection length, in its maximum values, is mainly related to grain dimensions and these defects, present only at the grain boundaries, cannot modify the collection length. Protons, which create vacancies in concentration of at least 10^{19} cm^{-3} according to our estimates, can produce vacancies also (and more likely) in the damaged regions and close to these N-related defects, giving rise to the green A band at 510 nm, which finally once created is not sensitive to damage, since the damage-created N–V–N defect could be continuously created and removed, being transformed in another defect, at a different position in the optical gap.

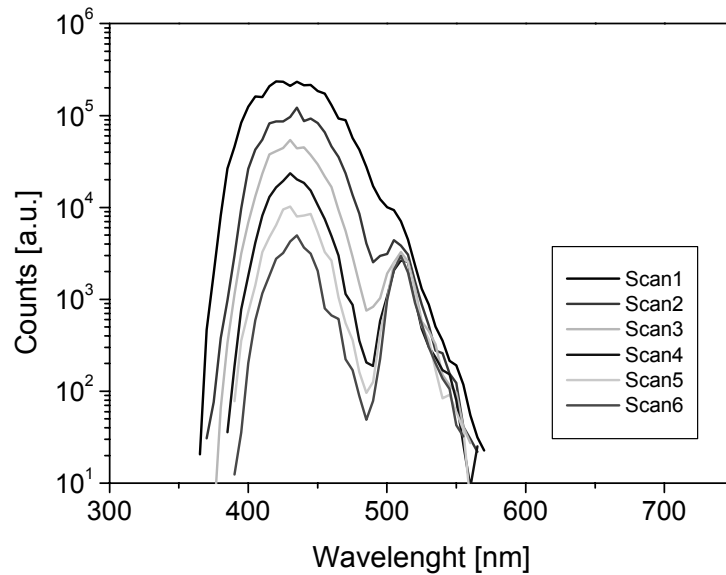


Fig. 15. IBIL spectra obtained by the monochromatic IBIL set up on a CVD sample of detector grade quality. The spectra are strongly decreasing with the dose. The irradiated area has a diameter of 0.5 mm and the protons have an energy of 2 MeV.

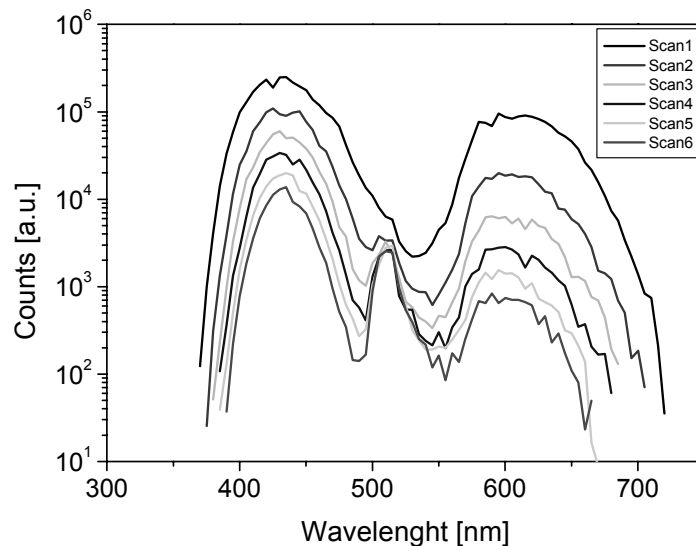


Fig. 16. IBIL spectra obtained in the same conditions of Fig. 16 on a CVD sample of bad quality as a detector.

3.5. Conclusions

It has been demonstrated, in several cases, that IBIC and IBIL with proton microbeams can be profitably used in order to “visualize“ and to follow in real time the behaviour of the electronic transport properties of frontier materials. These observations are very useful not only for verifying the possible applications of these materials in fields like nuclear detection, but also in order to understand better the origins of the limitations in the detection performances. By using an ad hoc developed code and lateral IBIC data, it is also possible to measure the diffusion length of minority carriers in Si structures directly and with an unprecedented precision.

ACKNOWLEDGEMENTS

The author gratefully acknowledges the work carried out by Torino University team (Dr. Vittone, Fizzotti, Lo Giudice, Polesello, Paolini) and by Ruder Boskovic Institute team (Dr. Jaksic, Tadic, Ivanovic) and the very fruitful discussions particularly with Dr. Vittone, Jaksic and Fizzotti.

REFERENCES

- [1] MANFREDOTTI, C., APOSTOLO, G., LO GIUDICE, A., POLESELLO, P., CINQUE, G., TRUCCATO, M., VITTONI, E., EGENI, G., RUDELLO, V., ROSSI, P., "Ion Beam Induced Luminescence and Charge Collection in diamond", *Diamond and Related Materials* 7 (1998) 742–747
- [2] NAVA, F., VANNI, P., CANALI, C., APOSTOLO, G., MANFREDOTTI, C., POLESELLO, P., VITTONI, E., "Analysis of Uniformity of as Prepared and Irradiated S.I. GaAs Radiation Detectors", *IEEE Transaction on nuclear Science* 45,3 (1998) 609–616
- [3] MANFREDOTTI, C., FIZZOTTI, F., POLESELLO, P., VITTONI, E., TRUCCATO, M., LO GIUDICE, A., JAKSIC, M., ROSSI, P., "IBIC and IBIL microscopy applied to advanced semiconductor materials", Presented at 13th International Conference on Ion Beam Analysis (IBA-13), Lisbon, Portugal, July 27- August 1 1997, *Nucl. Instr. And Meth. Phys. Res. B*136-138 (1998) 1333–1339
- [4] NAVA, F., VANNI, P., BIGGERI, U., VITTONI, E., LANZIERI, C., BERTUCCIO, G., CANALI, C., "Electric field and plasma effects on proton-irradiated GaAs detector performance", *Nuclear Instruments and Methods in Physics Research A* 410 (1998) 68–73
- [5] JAKŠIĆ, M., TADIĆ, T., ORLIĆ, I., OSIPOWICZ, T., VITTONI, E., MANFREDOTTI, C., "Imaging of charge collection properties in CVD diamond using high resolution IBIC with protons and alpha particles", *Diamond Films and Technology*, Vol. 8, n.5, (1998) 391–398
- [6] VITTONI, E., MANFREDOTTI, C., FIZZOTTI, F., MIRRI, K., GARGIONI, E., POLESELLO, P., LO GIUDICE, A., GALASSINI, S., NAVA, F., VANNI, P., ROSSI, P., "IBIC analysis of gallium arsenide Schottky diodes" , Submitted at 6th Int. Conf. on Nuclear Microprobe Technology and Applications, Spier Estate, South Africa, 11–16 October 1998
- [7] MANFREDOTTI, C., FIZZOTTI, F., GARGIONI, E., LU, R., POLESELLO, P., LO GIUDICE, A., VITTONI, E., GALASSINI, S., JAKSIC, M., "Evaluation of the diffusion length in silicon diodes by means of the lateral IBIC technique" , Submitted at 6th Int. Conf. on Nuclear Microprobe Technology and Applications, Spier Estate, South Africa, 11–16 October 1998, and to be published in *NIM B*.
- [8] MANFREDOTTI, C., FIZZOTTI, F., LO GIUDICE, A., POLESELLO, P., VITTONI, E., "Lateral IBIC by Single Proton Counting on Diffusion/Depletion Regions : Theory and Experiment" , To be published in the *Proc. of the "15th international Conference on the Application of Accelerators in Research and Industry*, November 4–7, 1998, Denton, Texas.
- [9] MANFREDOTTI, C., FIZZOTTI, F., POLESELLO, P., VITTONI, E., "IBIC investigation on radiation induced effects in CVD and natural diamond" , Presented at 2nd Int. Conf. on Radiation Effects on Semiconductor Materials, Detectors and Devices, Firenze (Italy), 4–6 March 1998, *Nucl. Instr. And Meth. Phys. Res. A*, 426, (1999), 156–163
- [10] NAVA, F., VANNI, P., CANALI, C., VITTONI, E., POLESELLO, P., BIGGERI, U., LEROY, C., "Evidence for plasma effect on charge collection efficiency in proton irradiated GaAs detectors", Presented at 2nd Int. Conf. on Radiation Effects on Semiconductor Materials, Detectors and Devices, Firenze (Italy), 4–6 march 1998, *Nucl. Instr. And Meth. Phys. Res. A*, 426, (1999), 185–191
- [11] VITTONI, E., FIZZOTTI, F., LO GIUDICE, A., PAOLINI, C., MANFREDOTTI, C., "Theory of Ion beam Induced Charge Collection based on the extended Shockley-Ramo Theorem", Presented at 14th International Conference on Ion Beam Analysis (IBA-14) and ECAART-6, Dresden, Germany, July 26–30 1999, *Nucl. Instr. And Meth. Phys. Res. B* 161-163 (2000) 446

- [12] MANFREDOTTI, C., FIZZOTTI, F., LO GIUDICE, A., POLESELLO, P., VITTONI, E., LU, R., JAKSIC, M., "Ion Microbeam Analysis of CVD Diamond" , Presented at "6th International Conference on New Diamond Science and Technology", Pretoria, South Africa, 31-8/4-9 1998., *Diamond and Related Materials* 8 (1999) 1597–1601
- [13] MANFREDOTTI, C., FIZZOTTI, F., LO GIUDICE, A., POLESELLO, P., VITTONI, E., TRUCCATO, M., ROSSI, P., "Ion beam induced luminescence maps in CVD diamond as obtained by coincidence measurements", Presented at "6th International Conference on New Diamond Science and Technology", Pretoria, South Africa, 31-8/4-9 1998., *Diamond and Related Materials*, 8 (1999), 1592–1596

STUDY OF LiNbO_3 FOR OPTOELECTRONIC APPLICATIONS BY ION BEAM AND NEUTRON BASED ANALYTICAL TECHNIQUES

J. ŠPIRKOVÁ, P. NEKVINDOVÁ
Institute of Chemical Technology,
Prague, Czech Republic

H. TURČIČOVÁ
Institute of Physics, Czech Academy of Sciences,
Prague, Czech Republic

J. VACÍK, J. ČERVENÁ, V. PEŘINA, V. HNATOWICZ
Institute of Nuclear Physics, Czech Academy of Sciences,
Řež, Czech Republic

Abstract

The project deals with study of fabrication and properties of hydrogen and/or erbium containing optical layers in lithium niobate (LN). The aim of the project was to get control over the fabrication process so that the properties of the waveguides could be tailored according to the desired applications. The layers were fabricated by annealed proton exchange (APE) and by RF plasma processing. Composition of the fabricated layers, as determined by the NDP, ERDA, RBS and by several other methods, was compared with optical properties of the samples using mostly the mode spectroscopy and photoluminescence spectra. We have found that there was no linear relationship that would unambiguously attribute a value of the refractive index (n_e) increment to the concentration of the un-depleted lithium (c_{Li}) in the APE waveguiding layers. This relationship is an important factor to characterize the particular waveguides and can be strongly affected by fabrication process. The most important fabrication step is the post-proton-exchange annealing, which may shift the n_e vs. c_{Li} relationship into the area of structural α -phase, that is the phase with the low optical loss. The best electro-optic properties were found with the samples with uniformly distributed lithium atoms and very low content of hydrogen. The strong anisotropy of the H^+ as well as the Er^{3+} moderate temperature doping into the LN Z- and X-cuts is explained on the basis of a suitable orientation of the X-cuts towards the cleavage planes of the crystals which enables better incorporation of diffusing particles into the structure. Plasma processing does not allow the production of a lightguiding structure due to many point defects introduced. However, the electrical surface conductivity changes from that of an insulator (short plasma exposure) to that of semiconductor (longer exposures), and finally to almost that of a metal (long exposures).

1. Introduction

1.1. Scientific background

Lithium niobate (LiNbO_3) (LN) is considered to be an outstanding nonlinear optical material, currently used as a substrate for applications in optoelectronics and integrated optics. Since 1982 the fabrication of optical waveguides in LN by proton exchange (PE) in benzoic acid melts at 200–250°C, the PE (replacement of Li with H) process has become an established method for fabrication of low-loss waveguides. Such waveguides in LN substrate (virgin or doped with laser active (LA) ions) can be used in various applications for distribution and harnessing of optical radiation, sensors and, recently, also for optical amplifiers and waveguide lasers. For such a large variety of applications optical parameters, as extraordinary refractive index increment Δn_e , n_e — depth profile, optical loss *etc.* should be tailored. Though many papers dealing with the proton exchange process have been published, there still remain several fundamental issues that have not been fully addressed in the literature. One of them is a relationship between extraordinary refractive index change and composition of the waveguiding layers, esp. concentration of lithium atoms. Another important issue concerns fabrication of active waveguides, *i.e.* doping LN substrates with LA ions and/or fabrication of the PE waveguides in the doped substrates.

1.2. Diffusion Processes at the Fabrication of the Planar Optical Waveguides

Proton exchange technique for fabrication of optical waveguides in LN single crystal wafers is based on a reaction between the surface of the wafers with an appropriate proton source:



The as-exchanged (PE — proton exchanged) waveguides have a large increase of extraordinary refractive index value ($\Delta n_e \leq + 0.12$). However, they are not stable and their electro-optic properties, represented with coefficient r_{33} , are degraded almost to zero. To restore its value and to stabilize the waveguides properties, the second fabrication step, annealing (A), is necessary. The resulting annealed proton exchanged (APE) waveguides are very stable and can be used in a large variety of dynamical optoelectrical devices.

Rare earth doped optical materials have attracted much attention in fabrication of planar waveguide amplifiers and waveguide lasers for a large number of applications in optical communication systems and signal processing systems. The most extensively studied material is single crystalline LN as it is widely used compound for fabrication of very sophisticated integrated optics structures. The most popular laser active dopant is erbium (Er^{3+}), which ${}^4\text{I}_{13/2} \rightarrow {}^4\text{I}_{15/2}$ transition emits in the third low loss telecommunication window around 1.5 μm .

Several techniques for incorporation of Er^{3+} ions into LN have been investigated during the last few years. The most common technique is a bulk doping of the substrates which is done during the crystals growth, however, for many reasons, a localized doping with the laser active particles, which occurs in the well defined area in the substrates surfaces, is much more suitable alternative. A possibility of localized doping of Er^{3+} ions into LN has been studied using pulsed laser deposition, in-diffusion of erbium from metal erbium layer evaporated onto the substrate surface and ion implantation.

1.3. Plasma Processing of LiNbO_3

Plasma processing offers another possibility for the production of surface modification on LN. Processing in low temperature radio-frequency plasma presents such modification in the environment of neutral (molecules, atoms, either in background state or excited) and charged (ions, electrons) particles. The ratio of the charged and neutral particles is about 10^{-6} . Using hydrogen glow discharge, a large amount of H atoms is produced, up to several tens of percent, according to the plasma intensity (i.e. electron mean temperature). From our previous experiments it was known that *lithium escapes from the niobate surface during the hydrogen plasma processing*. On the contrary, *an incorporation of H atoms into the sample surface could be expected*. Thus a new approach of proton-exchange process seemed to be worth studying. According to literature, such study has never been performed.

2. Experiments

2.1. Substrates

Two principal cuts of the LN wafers are commonly used in the optoelectronics applications: the Z-cuts (0001), perpendicular to the C_3 axes, which is also the optical axes of the LN and the X-cuts (11–20), parallel with the C_3 . The samples used in our experiments were congruent (CRYTUR, Czech Republic) one side polished wafers with typical dimensions of $25 \times 5 \times 0.7$ mm.

2.2. Fabrication of the Samples

2.2.1. Proton Exchange (PE) and Post-exchange Annealing (A)

Thoroughly pre-cleaned samples were mounted in a platinum holders and placed into individual silica or platinum beakers that contained reaction melt consisting of pure or lithium salt containing adipic acid. Adipic acid ($\text{HOOC}-(\text{CH}_2)_4-\text{COOH}$) is similar to benzoic acid (which is mostly used for

proton exchange) what concerns its acidity, but it is a non-toxic, safe-to use and environmentally much more friendly proton source than the benzoic acid.

The heating source was an ordinary laboratory oven. The proton exchanged waveguides were fabricated at a temperature of 213°C for times ranging from 30 minutes to 6 hours. Setting of the reaction melt temperature at 213°C comes from our experiments concerning the composition of the reaction melt. According to our thermodynamic considerations, at the temperature of about 210°C there is the highest concentration of H₃O⁺ ions in the reaction melt, which makes the proton exchange process at this temperature to progress most efficiently. Using either lower or higher reaction melt temperatures than approx. 210 °C resulted in fabrication of the PE waveguides which had smaller Δn_e and supported less numbers of modes. The as-exchanged samples were immediately washed with distilled water and acetone in order to remove the remnants of the reaction melt and then they were annealed at temperatures ranging from 250 to 500°C for various times (30 minutes to 100 hours) in another laboratory oven under ambient atmosphere. The annealing was usually done immediately after the proton exchange.

2.2.2. Erbium Doping into LN and Sapphire

Thoroughly pre-cleaned wafers of LN and sapphire were immersed into molten reaction mixture in silica or platinum crucible, which was placed into a laboratory oven Thermolyne FB1300. The reaction mixture consisted of potassium nitrate and erbium nitrate with weight ratio 10: 1 (melt I) or cesium nitrate, barium nitrate and erbium nitrate with weight ratios 76:14:10 (melt II). The melt temperature was set to 350°C or 400°C and the wafers underwent the diffusion reactions for times ranging from 5 to 120 hrs. The post-diffusion annealing processes were done under ambient or oxygen atmosphere in a standard laboratory oven.

The reference samples of Er-locally doped LN were fabricated by diffusion of erbium from 8–11 nm thick metal erbium layers evaporated onto the surface of LN wafers. The diffusion was done in oxygen/water atmosphere at 1060 °C for 60 hrs.

2.2.3. Plasma Processing

The reaction chamber in our facility is based on capacitively coupled radio-frequency glow discharge (tube inner diameter of 23 mm, electrodes 10 cm apart). Thus there is no contamination of samples from inner metal electrodes. The dielectric samples obtain in plasma so called floating potential, which is about –30 V regarding the plasma potential. The modification of sample surfaces thus does not proceed via ion implantation, as in commercial planar reaction chambers, but via interaction of the very surface (up to 10 nm depth) of the sample with low energy ions (~30 eV) and, mainly, with atomic particles. The influence of the external electric field inside the sample can be neglected as its value is about 10 V/cmTorr, which is negligible compared to the local electric fields and bonds in the crystal. The plasma processing briefl is combined with the thermal treatment by a tube resistance furnace. The additional heating controls the diffusion activities in the material.

The pressure of hydrogen ranged from 0.5 ÷ 3 mbar at a flow rate of 8 sccm; r.f. input power (13.56 MHz) was 100 ÷ 300 W; the sample temperature ranged from the room temperature up to 700°C. The exposures to plasma lasted from several tens of minutes up to several hours. The single-domain congruent LN, undoped and doped with Mg and Cu, was used. The wafers were usually 7 × 25 mm² and 1 mm thick.

2.3. Measurement

The waveguides were optically characterized at $\lambda = 633$ nm using the prism coupling technique. The extraordinary refractive index (n_e) depth profiles of the fabricated waveguides were reconstructed from the effective index spectra by means of inverse WKB procedure using piecewise linear approximation to the actual index profiles.

Lithium concentration depth profiles (c_{Li}) in the as-exchanged as well as post-exchanged annealed waveguides were measured by the Neutron Depth Profiling (NDP). The method is based on a reaction of thermal neutrons with ⁶Li: ⁶Li (n,α) ³H. The fabricated samples were irradiated with a

thermal neutron beam from a 6 m long neutron guide (neutron intensity was 10^7 neutrons.cm⁻².s⁻²) and the charged reaction products were recorded by means of Si(Au) surface barrier detector. The accuracy of the NDP method is 5% of the c_{Li} value, the depth resolution is 10 nm. Thus the absolute values of concentrations of lithium, as presented in c_{Li} depth profiles in the diagrams, represent in fact the concentrations of the “NDP active” ⁶Li. Natural abundance of the ⁶Li isotope is 7.5%, however, in the actual samples the ⁶Li/⁷Li ratio may significantly vary (e.g. due to artificial depletion of the ⁶Li isotope from the original natural materials). Thus, to avoid uncertainty induced by this variation, for some considerations we rely on relative changes of c_{Li} instead of their absolute values.

For determination of concentration profiles of the incorporated hydrogen (c_H) the ERDA method was applied. The ⁴He⁺ beam from the Tandem accelerator with 1.8 MeV energy has been selected and the beam currents used were below 10 nA. The reflection geometry was taken with the incident angle of 75° relative to the surface normal, and the take-off angle was 24° with respect to the incident beam. The beam doses of up to 100 μC were normalized by the parallel detection with the RBS detector, the one being used for the determination of the sample matrix composition as well. The 6 μm thick Al foil placed in front of the ERDA detector was chosen to discriminate against detection of the scattered He nuclei, whilst allowing detection of protons recoiled from the sample. With the ERDA set-up the detection limit of 0.1 at.%, detectable depth of up to 0.5 μm, and the depth resolution 30 nm were achieved. The ERDA measurement was performed by the group of Prof. Milos Budnar in the Department of Low and Medium Energy Physics at the J. Stefan Institute in Ljubljana, Slovenia. Few reference samples were for comparison measured simultaneously also in the Frank Laboratory of Nuclear Physics, Joint Institute for Nuclear Research in Dubna, Russia (Prof. Alexander Kobzev), and in the Ion Beam Laboratories at University of Albany, USA (Dr. W.A.Lanford).

Concentration of oxygen in the samples was measured by NRA in Frank Laboratory of Nuclear Physics, Joint Institute for Nuclear Research in Dubna, Russia, by the group of Prof. Alexander Kobzev.

Content of erbium in the samples was determined by the Scanning Electron Microscopy (SEM) and by the Rutherford Backscattering Spectroscopy (RBS). Depth profiles of the incorporated erbium were measured by RBS. The RBS spectra were evaluated by means of GISA 3.99 code 25. The RBS method is favorable for this special case; it offers sufficient sensitivity for heavy admixtures and the depth resolution of 5–10 nm. Nevertheless, some limitations of the RBS method are apparent. First, as the signal from in-diffused Er atoms is distinguishable only in the energy region above the niobium surface edge, the Er detectable depth is restricted to some 200 nm for 2.2 MeV alpha particles. In the present case, the erbium content was determined with respect to the Nb bulk signal. Concentration profiles of lithium in the treated surface layers of LN, as well as in the annealed proton exchanged waveguides fabricated in the Er-doped LN substrates, were checked by the Neutron Depth Profiling (NDP) method.

The composition of the plasma modified surface layers has been measured by nuclear methods RBS, NDP and ERDA. The structure was examined by XRD (X ray Diffraction). The optical properties of the layers were estimated from UV-VIS-IR spectra and electrical properties from sheet resistance measurements.

3. Results and Discussion

3.1. Relations Between Composition and Optical Properties of the PE and APE Waveguides

3.1.1. Lithium [1,2,4–9,13,17,20]

The proton exchange (PE) reaction between the substrate wafers and the reaction melt of adipic acid results in formation of the optical layers with substantial increase of the extraordinary refractive index n_e . The depth of the exchanged layers depends on the used fabrication condition, namely composition of the reaction melt (pure adipic acid or buffered adipic acid, which contained up to 2 mole% of lithium adipate) and the times of the exchange reactions. The depths of the PE layers in our experiments never exceeded 3 μm and the shapes of the both functional depth profiles, c_{Li} as well as n_e , had always step-like characters. The PE guides supported, according to their fabrication

conditions, one, two or three modes. During the post-exchange annealing the lithium ions migrated towards the samples surfaces causing thus the dramatic change of the c_{Li} and n_e depth profiles from the step-like (PE) to graded (APE). Typical example of the lithium distribution in the PE and APE layers is given in Fig.1.

High mobility of lithium ions, due to their very small size and partly ionic character, makes their migration through the LN structure very easy when some energy is added. While in the first fabrication step, PE, transport of lithium occurs mainly *via* the H^+ for Li^+ exchange reaction, the energy added in the form of annealing makes the lithium ions move again, but now is their migration ruled predominantly by their high mobility through the vacancies in the structure. There are two diffusion processes which, according to the actual fabrication conditions, may occur at practically the same time: a) substitution of Li^+ for H^+ during the PE and b) progression of Li^+ towards the samples surfaces caused by the annealing. This progression may be to a certain extent considered as the next step of the substitution of the lithium for the already incorporated hydrogen.

Our experiments have proved that the regime of the post-exchange annealing is the most important parameter of the APE fabrication process as it is the decisive factor for the optical properties of the resulting guides.

Very significant aspect of the fabrication of the APE waveguides is the relationship n_e vs. c_{Li} . An example illustrating that relationship and its change by annealing the as-exchanged sample is given in FIG. 2. From this typical example it is evident that, despite the generally accepted opinion, any increment of the n_e can be attributed to a variety of pertinent c_{Li} and *vice versa*. However, the experimental data of all fabricated waveguides were found to fit a functional dependence [5,14].

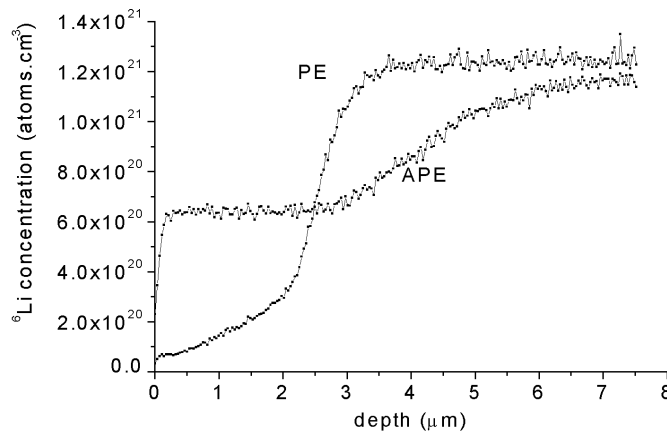


Fig. 1. NDP profiles of 6Li for PE and APE waveguides.

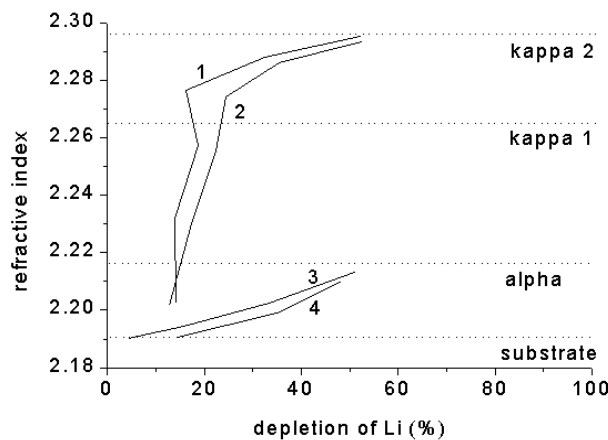


Fig. 2. Relationship between n_e and c_{Li} for APE waveguides after annealing at 300 °C (1–0.5, 2–1.5, 3–9.25 and 4–24 hrs, resp.).

The waveguides suitable for practical applications are expected to be few-ones and should consist only of the *alpha* structural phase. The waveguides consisting exclusively of the alpha phase are characterized with a small increment of the n_e (see FIG. 2) and are expected to have low optical losses and high values of electro-optical coefficient r_{33} . According to our results (see the example in Fig. 2), even within the *alpha* phase, there is quite a large selection of possibilities characterized with various shapes of n_e vs. c_{Li} relationship, so that properties of the fabricated waveguides can be easily tailored for desired purposes.

3.1.2. Hydrogen [8,13,17,20]

Relative amount of hydrogen incorporated into the LN structure by the proton exchange was estimated from the $\nu(\text{OH})$ bands in IR absorption spectra. The results indicated that there is no simple relationship between the hydrogen concentration and optical properties of the fabricated samples esp. what concerns the different crystallographic orientations of the substrate wafers. In order to get direct evidence on how are H^+ species incorporated into the structure we have studied concentration profiles of hydrogen in very thin optical layers fabricated by very short proton exchange. Fabrication of samples and the ERDA measurement were done mostly in a close cooperation with the group of another CRP participant, Prof. Milos Budnar, at the Department of Low and Medium Energy Physics of the Josef Stefan Institute in Ljubljana. The results confirmed our expectation of much better permeability of the X-cuts for penetration of hydrogen than the Z-cuts (see below).

3.1.3. Oxygen

NRA measurement in Dubna has proved that there was no depletion of oxygen in the PE as well as APE samples.

3.2. Importance of the Crystallographic Orientation of the Substrate Cuts for the Diffusion Technologies of the Waveguides Fabrications [1,3,6,8,10,13,15–19]

Quite generally, the APE X-cuts exhibit more step-like characters of the c_{Li} depth profiles than the Z-cuts (Fig. 3) indicating thus a rather different formation mechanism of the waveguiding layers. Prevailing mechanism of H^+ incorporation into the Z-cut structure is substitution of H^+ for Li^+ , which is accompanied by some interstitial H^+ diffusion. X-cuts revealed the same extend of the $\text{H}^+ \leftrightarrow \text{Li}^+$ substitution as was observed in the Z-cuts waveguides fabricated under the same fabrication condition. However, intensities of $\nu(\text{O-H})$ vibration bands in the IR reflectance spectra of the fabricated waveguides, as well as the direct measurement of the concentration depth profiles of hydrogen in the very shallow optical PE and APE layers, always give evidence for much more hydrogen incorporated in the X-cuts. It means, that H^+ for Li^+ substitution in the X-cut is strongly accompanied by an interstitial in-diffusion of hydrogen. H^+ species then form a barrier that prevents lithium to move during annealing towards the surfaces of the wafers, causing thus typical step-like shapes of X-cuts characteristics.

Moderate temperature Er^{3+} doping into the LN wafers from the mixture of erbium containing nitrates was far more successful in the X-cuts, where the amount of the in-diffused Er^{3+} (up to 10 mole%) was approximately 10 times higher comparing with that incorporated in the Z-cuts.

Strong anisotropy of the presented moderate-temperature diffusion process calls for an explanation. The LN structure (C_{3v}^6) can be considered as consisting of octahedrons of oxygen atoms. One third of them is occupied by atoms (or ions) of lithium, in the centers of the second third there are located the atoms of niobium, and the last third of the oxygen octahedrons is vacant. The structure of the LN can be then easily seen as, in fact, a layered one, with the following sequence of atomic planes: –oxygen–lithium–oxygen–niobium–oxygen–. This sequence is from the both sides enclosed in two planes of vacancies, so called cleavage planes (01–12).

Z-cut wafers are oriented perpendicularly to the z-axes (C_3 rotational axes), opening thus straight channels in the structure between the atoms. The X-cuts, on the other hand, are oriented perpendicularly to the x-axes of the crystal. They show a layered-type situation, making thus the vacant “empty” layers easily accessible for penetration of the “foreign” particles into the structure. That may explain much better readiness for the X-cuts to absorb in substantially higher rate the doping ions.

This knowledge was capitalized for the moderate-temperature diffusion of Er^{3+} into sapphire, which is well known to be extremely resistant against diffusion of foreign particles, but structure of that, D_{3d}^6 , is very similar to the structure of LN (C_{3v}^6). Octahedral sites, which are in LN occupied by atoms of lithium and niobium, are in sapphire (Al_2O_3) occupied only by Al atoms.

We have undergone two types of sapphire wafers (cuts) — (11–20) and (01–12) — to a doping procedure, which was done by the same way as the above mentioned melt-doping into LN. After the doping procedure no erbium was detected in the (01–12) cuts, but in the (11–20) cuts, which here represent the X-cuts, we found 700 nm deep erbium containing layers with about 5 wt.% (i.e. 0.6 mol.%) of Er in the surfaces of the samples (Fig. 4). This doping can not be in any case interpreted as an ion exchange reaction, as aluminium is not a mobile ion, being settled in the sapphire structure as a part of its network. Evidently, the erbium doping in this case is done via interstitial diffusion into the surface of the wafers.

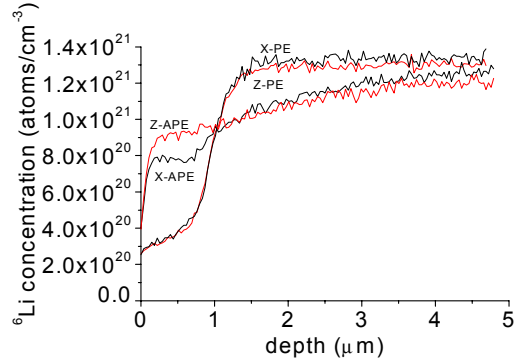


Fig. 3. Difference between ^6Li NDP depth profiles of the PE and APE waveguides in the X- and Z-cuts.

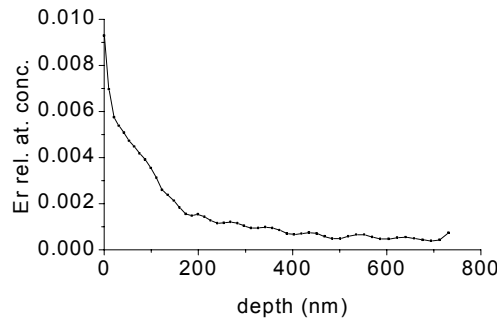


Fig. 4. RBS depth profile of erbium incorporated into the X-cut sapphire by moderate temperature doping.

3.3. Electrooptic Properties of the APE Waveguides

The values of the electrooptic coefficient r_{33} of the α -APE waveguides fabricated by the soft proton exchange were measured by the interference method for every particular mode of the guides. The obtained values increased with the depth (the higher numbers of the modes) of the waveguides. The highest values of the r_{33} (34×10^{-12} m/V) were found in the samples with almost homogeneous distribution of the un-depleted lithium and very low content of hydrogen. The results indicated a possibility to get control over the APE process so that the producers may rely on good reproducibility of fabrication of high quality guides.

3.4. Plasma Processing [11,12,21]

The idea given in the Introduction (proton-exchange induced by plasma treatment) has been tested in a number of experiments. From our previous study it was known that the main reactants are hydrogen atoms. They are effective on the surface in a few processes: either recombine on the sample

surface, heat it and escape back to plasma, or diffuse into the surface and react with oxygen producing OH⁻ radicals, or as water vapor escapes from the surface. Unfortunately, hydrogen bonds are difficult to detect inside the material (except e.g. the infrared absorption by OH groups) and thus only H depth profiles provide information about the surface modification by H atoms. Highly probably they produce LiOH (LiH ?) compounds and thus enable the Li atoms to leave the surface. The chemical reduction caused by hydrogen atoms manifests itself by opacity (slight plasma processing) up to heavy blackening (strong plasma processing) of the sample. The opacity, i.e. light absorption, is detrimental to an eventual use of the plasma processed samples for light guiding. Therefore a bleaching in oxygen atmosphere was necessary at a temperature of 700 °C for 15 minutes.

The first part of the plasma proton-exchange process, i.e. the lithium depletion in the surface layer is demonstrated in Fig. 5. The longer was the plasma exposure, the more profound was the Li depletion (N° 189 for 20 min, N° 192 for 40 min, and N° 191 for 60 min). The depth of the depletion is comparable to that attained by the classical chemical proton-exchange (boiling in an acid). An example of H depth profile as measured by ERD method is given in Fig. 6 to demonstrate the hydrogen penetration into the samples surface. A subsequent annealing at 350 °C should produce an appropriate Li depth profile for the lightguiding layer production. However, after the plasma processing the samples are black and for the lightguiding operation lost. To restore the optical transparency again they have to be annealed for about 10 minutes in an oxygen containing atmosphere at a temperature close to 700 °C. This high temperature treatment, unfortunately, sweeps away the former Li depth profile. Only a very shallow surface layer with a lack of lithium remains and theoretically can form a waveguide. The UV-VIS spectra of thus treated LN were taken and from the interference maxima a depth of 0.4 μm was calculated which had a different refractive index than the bulk. The X ray diffraction measurements have been done on such plasma treated samples and it became evident that a more intense plasma treatment induces irreversible point defects in LN lattice. These defects will undoubtedly lower the lightguiding properties of these layers.

The measurements of electrical conductivity of the hydrogen plasma produced LN layers revealed that the insulation properties of the genuine niobate can be modified according to the exposure time and plasma intensity from that of an insulator to that of a conductor. Fig. 7 presents temperature dependence of the sheet resistance of the same LN samples as in Fig.5. The upper curve belongs to the sample treated in plasma for only 20 min, the middle to that treated for 40 min and the lowest for 60 min. The upper curve corresponds to a conductivity of a semiconductor. The lowest curve approaches to that of a conductor. This finding opens a discussion what kind of charge carriers may appear in the LN after hydrogen plasma treatment. These might be either the same as already exist in the genuine material and plasma only enhances their production, *i.e.* Nb_{Li}⁴⁺, V_{Li}⁺, O_V²⁻, O_i²⁻, OH⁻, (Nb_{Li}⁴⁺, V_{Nb}⁵⁺), (2e)_O, and Nb⁴⁺ ↔ Nb⁵⁺, or some new can be introduced by plasma, e.g. H⁺ ions. An Exp-Decay Fit of the conductivity $\sigma = 1/R$ calculated from the resistances R presented in Fig. 4 revealed the activation energy of 0.02 eV. This is very low value and suggests that some polarons, which are known to have low activation energies, might appear in the material after the processing. Determination of the charge carriers remains so far an open problem as well as a detailed knowledge of all structure changes produced by plasma. Some further diagnostics of the layers are necessary.

4. Conclusions

The NDP measurement revealed a high mobility of the small covalent Li⁺ through the LN structure. The depths of the exchanged (PE) layers in our experiments have never exceeded 3 μm in both Z- and X-cuts. The subsequent annealing of the as-exchanged samples resulted in migration the lithium ions towards the surface of the wafers. While the total amount of the out-diffused lithium is given by the first fabrication step—the proton exchange — the resulting properties of the waveguides depend strongly on the second fabrication step — the regime of the annealing. The waveguides with the best electrooptic properties are those having almost homogeneous distribution of lithium and very low content of hydrogen.

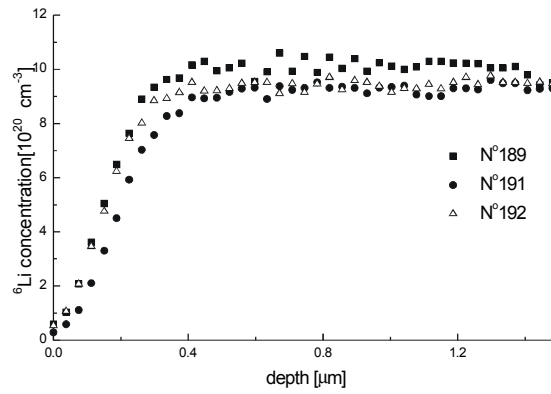


Fig. 5. ${}^6\text{Li}$ depth profile of LN processed in hydrogen RF plasma.

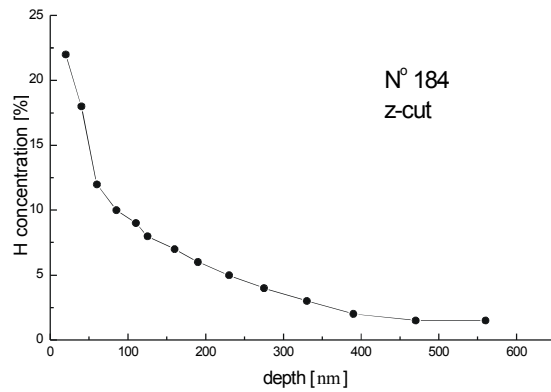


Fig. 6. Hydrogen depth profile of LN processed in hydrogen RF plasma.

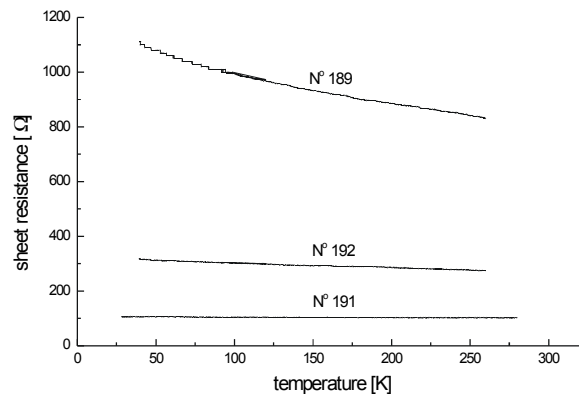


Fig. 7. Temperature dependence of the sheet resistance of LN processed in hydrogen.

The opened access to the layers of the vacant octahedra in the LN X-cuts allowed better penetration of foreign particles into the surfaces of the wafers. This is beneficial esp. in the case of moderate temperature localized doping of LN by erbium. The explanation of this phenomenon was confirmed by the incorporation of Er^{3+} into the “X-cuts” wafers of sapphire demonstrating thus for the first time localized Er^{3+} doping into this material.

As far as the plasma processing of LN, our conclusion is that this method is not suitable for the production of the lightguiding layers the optical properties of which could be comparable to those of classical proton-exchange technology. Nevertheless, new interesting features of the layers produced by plasma processing appeared. The electrical conductivity of the plasma modified surface layers was changing from that of an insulator (short exposure to plasma) to that of a semiconductor (longer

exposure), and finally to almost that of a metal (long exposure at high temperatures). In this study the nuclear methods NDP, RBS and ERDA were of primary importance.

The authors of this Report highly acknowledge a close and fruitful collaboration with other CRP participants, namely M. Budnar (SLO 10037), A. Kobzev (RUS 10036), and W. Lanford (USA 10211).

REFERENCES

- [1] NEKVINDOVÁ, P., ŠPIRKOVÁ-HRADILOVÁ, J., SCHRÖFEL, J., VACÍK, J., and PEŘINA, V., „Optical waveguides in erbium doped LN: moderate temperature approaches“, 8th Vienna Opt(r)ode Workshop, Prague, October 7–8, 1998. Proc. pp. 79–80.
- [2] ŠPIRKOVÁ-HRADILOVÁ, J., NEKVINDOVÁ, P., VACÍK, J. and SCHRÖFEL, J. *Tailoring of lithium vs. extraordinary refractive index relationship in proton exchanged LiNbO₃ slab waveguides*, 8th Vienna Opt(r)ode Workshop, Prague, October 7–8, 1998. Proc. pp. 79–80.
- [3] NEKVINDOVÁ, P., ŠPIRKOVÁ-HRADILOVÁ, J., VACÍK, J., PEŘINA, V. and SCHRÖFEL, J., *Optical properties and composition of erbium doped LN optical waveguide fabricated by moderate temperature procedures*“, MADICA 98 (*Les matériaux et leurs applications aux dispositifs capteurs physiques, chimiques et biologiques*) Monastir, (Tunisie), 9–11 Novembre 1998.
- [4] ŠPIRKOVÁ-HRADILOVÁ, J., NEKVINDOVÁ, P., VACÍK, J. and SCHRÖFEL, J., „New characterization method of proton exchanged slab waveguides in LN“, MADICA 98 (*Les matériaux et leurs applications aux dispositifs capteurs physiques, chimiques et biologiques*) Monastir, (Tunisie), 9–11 Novembre 1998.
- [5] ŠPIRKOVÁ-HRADILOVÁ, J., NEKVINDOVÁ, P., VACÍK, J., ČERVENÁ, J. and SCHRÖFEL, J., „Possibility of tailoring n_e vs. c_{Li} relations in LN optical waveguides for sensors applications“, SPIE, **3858** (1999) 190–201.
- [6] NEKVINDOVÁ, P., ŠPIRKOVÁ, J., SCHRÖFEL, J., SLUNEČKO, M., PEŘINA, V. and VACÍK, J. „Localized Moderate Temperature Er³⁺ Doping into Optical Crystals“, SPIE, **3858** (1999) 180–189.
- [7] NEKVINDOVÁ, P., ŠPIRKOVÁ-HRADILOVÁ, J., VACÍK, J., ČERVENÁ, J. and J. SCHRÖFEL, J., „Lithium concentration profiles in APE:LiNbO₃ optical waveguides“ PHOTONICS '99, Prague, June 26–28, 1999., Accepted for SPIE.
- [8] BUDNAR, M., ZORKO, B., PELICAN, P., ŠPIRKOVÁ-HRADILOVÁ, J., KOLAŘOVÁ NEKVINDOVÁ, P. and H. TURČIČOVÁ, H., „ERDA study of H⁺ incorporated into LN“, IBA 14/ECCART-6, Dresden, July 1999.
- [9] ŠPIRKOVÁ-HRADILOVÁ, J., NEKVINDOVÁ, P., VACÍK, J. and SCHRÖFEL, J., „Neutron Depth Profiling characterisation of proton exchanged LN optical waveguides“, Materials Chemistry MC⁺, (Materials Chemistry forum of the Royal Society of Chemistry), Dublin, July 13–16, 1999. Proceedings of the conference No. 12.
- [10] NEKVINDOVÁ, P., ŠPIRKOVÁ, J., VACÍK, J., ČERVENÁ, J., PEŘINA, V. and SCHRÖFEL, J., „Effect of crystallographic orientation of a substrate to a possibility to fabricate optical waveguides in dielectric materials using low-temperature procedures“. 51. Symp. of Chem. Soc, Nitra (Slovakia), September 6–9, 1999.
- [11] TURČIČOVÁ, H., S. PŘEUČIL, S., VACÍK, J. AND ČERVENÁ, J., „Li Depth Profile Anomaly after Radio-Frequency hydrogen Plasma Processing of Single Crystal LiNbO₃“, 9th European Meeting on Ferroelectricity, July 12–16, 1999, Prague; Ferroelectrics 238 (2000) 313–320.
- [12] TURČIČOVÁ, H., POLCAROVÁ, M., BRADLER, J., VACÍK, J., ČERVENÁ, J., PEŘINA, V. and ZEMEK, J., „X-Ray, NDP and RBS Surface Analysis of LiNbO₃ Single Crystals Modified by Radio Frequency Hydrogen Plasma“, 8th European Conference on Applications of Surface and Interface Analysis, October 4–8, 1999, Seville; Surf. Interface Anal. **29** (2000) 260–264.
- [13] BUDNAR, M., ZORKO, B., PELICAN, P., ŠPIRKOVÁ-HRADILOVÁ, J., KOLAŘOVÁ NEKVINDOVÁ, P. and TURČIČOVÁ, H., „ERDA study of H⁺ incorporated into LN“, Nuclear Instr. Meth. Phys. Res. NIM B **161–163** (2000) 268–272.

- [14] ŠPIRKOVÁ-HRADILOVÁ, J., NEKVINDOVÁ, P., VACÍK, J., ČERVENÁ, J. and SCHRÖFEL, J., "Possibility of tailoring n_e vs. c_{Li} relations in LN optical waveguides", Opt. Mater. **5218** (2000) in press.
- [15] NEKVINDOVÁ, P., ŠPIRKOVÁ-HRADILOVÁ, J., SCHRÖFEL, J. and PEŘINA V., "Erbium doping into LN and sapphire single crystal wafers". J. Mat. Res. (2000), in press.
- [16] NEKVINDOVÁ, P., ŠPIRKOVÁ, J., VACÍK, J., ČERVENÁ, J., PEŘINA, V. and J. SCHRÖFEL, J., "Importance of crystal structure of the substrate for diffusion technologies of waveguides fabrication", E-MRS — IUMRS- ICEM 2000, Symp. P (Crystal Chemistry of functional materials), Strasbourg, May 30–June 2.2000. Int. J. Inorg. Mat., accepted.
- [17] NEKVINDOVÁ, P., ŠPIRKOVÁ-HRADILOVÁ, J., VACÍK, J., ČERVENÁ, J., BUDNAR, M., ZORKO B., PRIMOZ, P. and SCHRÖFEL, J., "Properties of H:LiNbO₃ optical layers", XIVth International Symposium on the reactivity of Solids, (Budapest 27–31 August 2000).
- [18] NEKVINDOVÁ, P., ŠPIRKOVÁ, J., VACÍK, J., ČERVENÁ, J. and PEŘINA, V., "Effect of crystallographic orientation of substrate wafers for medium temperature diffusion processes into optical crystals", XIVth International Symposium on the reactivity of Solids, (Budapest 27–31 August 2000).
- [19] ŠPIRKOVÁ, J., NEKVINDOVÁ, P., VACÍK, J., ČERVENÁ, J., PEŘINA, V. and SCHRÖFEL, J., "Importance of various crystallographic orientations of the substrate cuts on incorporation of foreign particles into the structure of the C₃ optical crystals", Solid State Chemistry 2000 (Prague, 3–8 September, 2000).
- [20] NEKVINDOVÁ, P., ŠPIRKOVÁ, J., VACÍK, J., ČERVENÁ, J., BUDNAR, M., ZORKO B., PRIMOZ, P. and SCHRÖFEL, J., "Properties of hydrogen containing optical layers in LN", Solid State Chemistry 2000 (Prague, 3–8 September 2000).
- [21] TURČIČOVÁ H., PRACHAŘOVÁ J., ČERVENÁ J. and VACÍK J., "Sheet resistance of LiNbO₃ wafers processed in radio-frequency plasma of hydrogen", Czech. J. Phys. **50** (2000), Suppl. 53, 461–465.

APPLICATION OF RUTHERFORD BACKSCATTERING AND NUCLEAR REACTION ANALYSIS TECHNIQUES FOR INVESTIGATION OF THIN FILMS

Á.Z. KISS, A. SIMON, Z. ELEKES, F. DITRÓI, S. MÉSZÁROS
Institute of Nuclear Research of the Hungarian Academy of Sciences.
Debrecen, Hungary

D.L. BEKE, G.A. LANGER, L. DARÓCZY
Kossuth L. University,
Debrecen, Hungary

Abstract

A study of the intermixing of the elements in amorphous Si-Ge multilayers have been carried out using Rutherford backscattering Spectrometry (RBS) technique. Interdiffusion coefficient was determined by measuring the intensity of the first Ge peak (having best depth resolution) in the RBS spectrum as a function of annealing time. The oxygen content of the multilayer was measured by the resonance elastic scattering method in co-operation with Dubna. A cross comparison of multilayered films were performed between the laboratories in Debrecen, Dubna, Albany and Dhaka. An essay to determine the nitrogen content of CVD diamond by the deuteron induced gamma ray emission method has been done.

1. Introduction

Ion beam analytical methods using MeV energy beams are very useful for determination of elemental concentrations, depth distribution, surface topography especially of thin films, because of their near surface character. They are sensitive for many elements, capable of performing multielemental analysis even in small amount of material, and — in most cases — they are nondestructive.

In this paper the results of the co-ordinated research program are presented as follows:

- a) the study of amorphous Si-Ge multilayer samples (trying to resolve the successive Ge and Si layers as well as possible, to determine the oxygen content of the samples),
- b) a cross comparison of RBS analyses of $\text{CuIn}_{(1-x)}\text{Ga}_x\text{Se}_2$ films,
- c) an essay on determination of N content of Chemical Vapour Deposited (CVD) diamond samples with the use of the deuteron induced gamma ray emission (DIGE) technique.

2. Method

The facility used for the characterisation of thin films is the 5 MV Van de Graaff accelerator of ATOMKI equipped with a scanning nuclear microprobe commercially available from the Oxford Microbeams Ltd [1]. The octagonal sample chamber is equipped with an XYZ target manipulator stage. A long working distance binocular zoom microscope viewed by a colour CCD camera is used for monitoring the beam on the front face of the sample and for observing the specimen under bombardment. The sample chamber is furnished with detectors capable to detect X rays, backscattered particles, gamma rays and secondary electrons simultaneously [2]. This chamber is regularly used for RBS analysis both with macro- and micro-beam.

Backscattered particles are detected by a partially depleted CANBERRA PIPS detector of 50 mm^2 active area, 14 keV nominal resolution set at 160° to the direction of the beam. Both the hardware and software of the data acquisition and scan control system have been provided by Oxford Microbeams Ltd. and built on an IBM compatible PC (Pentium processor) with MS Windows system software environment (Windows 95 at present). The RBX computer programme package [3] is used for the evaluation of the measured RBS spectra.

For the analysis of the DIGE measurements a Clover-Ge-BGO detector system has been used, which consists of a so called ‘clover’ type composite HPGe detector surrounded by a bismuth-germanate (BGO) anti-Compton shield [4]. The evaluation of gamma spectra were performed by computer codes FLORENCE (not published) and FORGAMMA [5].

3. Investigation of amorphous Si-Ge multilayers

Multilayers are of considerable industrial interest because of their specific properties and many promising areas of applications in electronics or optics like X ray and UV mirrors, giant magnetic resistance and magnetic recording, etc [6]. However, the multilayers as artificial, compositionally modulated materials are not equilibrium structures. In particular, they have high interfacial density gradients and sufficient atomic mobility even at moderated temperatures, hence changes in the composition profile are expected to occur. Thus, investigation of the thermal stability and understanding of the factors controlling structural changes of these multilayers is very important for the interpretation of their operation and prediction of their lifetime.

Concerning amorphous Si-Ge multilayers the mechanism of their diffusional homogenisation is still an open question. First of all the diffusional asymmetry (manifested in the strong concentration dependence of the interdiffusion coefficients) and the strong porosity formation during the diffusional mixing are the most important factors indicating the need of a better understanding of the above process. The strong concentration dependence can result in non-linearities in the diffusion process.

The interdiffusion and thermal stability of amorphous Si-Ge multilayers were studied previously in experiments where low-angle X ray diffraction was used [7,8]. The low angle X ray diffractometry is a powerful, widely used technique for determining the interdiffusion and thermal stability in compositionally modulated Si-Ge films. However the X ray approach limits the repeat length of multilayered films to a few nm in order to have acceptable reflection angles with the available X ray wavelength. An alternative non-destructive technique is the RBS. Using glancing incidence geometry the depth resolution of it is such that the composition modulation is detectable in Si-Ge multilayers with respect to a distance of the order of 3–5 nm.

The combination of our previous techniques (i.e. X ray diffractometry, etc.) with the Rutherford backscattering technique and other IBA methods, could help us to measure the concentration profile directly, as well as to determine possible impurities in the samples.

4. Sample preparation and measurement

The amorphous Si-Ge multilayers were prepared by DC magnetron sputtering from alternating elemental targets onto (001) silicon wafers [9]. The dimension of the substrates were $10 \times 10 \times 0.3 \text{ mm}^3$. The base and argon pressure during the deposition were $5 \cdot 10^{-7}$ mbar and $5 \cdot 10^{-3}$ mbar, respectively. The sputtering rates of Si and Ge were adjusted between 0.1 – 0.25 nm s^{-1} . The modulation wavelength was designed to range from 10 to 40 nm with nearly equal thicknesses of sublayers which were monitored in situ using vibrating quartz crystal method. The total thicknesses of the Si-Ge films varied from 55 to 220 nm. To get sharp interfaces, the sputtering process was interrupted after the deposition of each Si and Ge sublayer and a delay of 1 s was inserted between the closing and opening of the shutters.

For annealing a construction of a furnace in the scattering chamber of the nuclear microprobe has been made. The aim was to perform in situ annealing during the RBS analyses which was thought to be more precise and safe. However, the long annealing time (150 hours) — which was needed to achieve measurable intermixing of Si and Ge — made it necessary to perform annealing in a separated vacuum chamber. Thus the specimens were placed in high purity (99.999%) Ar atmosphere. In order to prevent the crystallisation, the annealing temperature was chosen definitely lower than the phase-transformation temperature of the amorphous Ge. As above $\sim 430^\circ\text{C}$ for amorphous Ge and $\sim 630^\circ\text{C}$ for amorphous Si rapid crystallisation sets in, we chose 410°C for the annealing treatments. The temperature was measured by a Ni-Cr-Ni thermocouple attached to the sample holder and controlled within a few $^\circ\text{C}$. Corrections for annealing durations were made by taking into account the heating up and cooling-down times.

The RBS analyses were performed at $E_\alpha = 1000$ keV. For increasing the depth resolution glancing incidence was applied. The sample was tilted to 60° using a home-made sample manipulator. For the measurements the detector was collimated down to $\Omega = 5$ msr. The measurement parameters were optimized by calculating the depth resolution for Ge and Si at different depths, depending on ion energy, incidence angle, detector resolution and its solid angle. Fig. 1. Shows a typical RBS spectrum for the above mentioned samples and conditions.

5. Results

5.1. Interdiffusion

The interdiffusion coefficient was obtained by evaluating the decrease of the oscillation amplitudes of the measured RBS spectra. As the depth resolution decreases with increasing depth — from where the ions scatter back — we have chosen the first Ge peak to monitor the changes caused by the annealing treatment. The maximum of the first Ge peak was determined by a fitting procedure and its annealing time dependence is illustrated in Fig. 2.

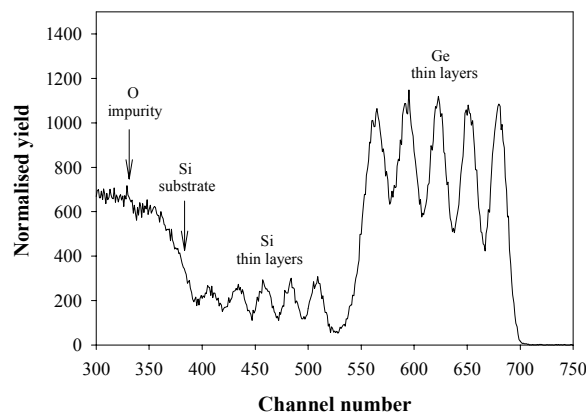


Fig. 1. Typical RBS spectrum of a Si-Ge multilayer.

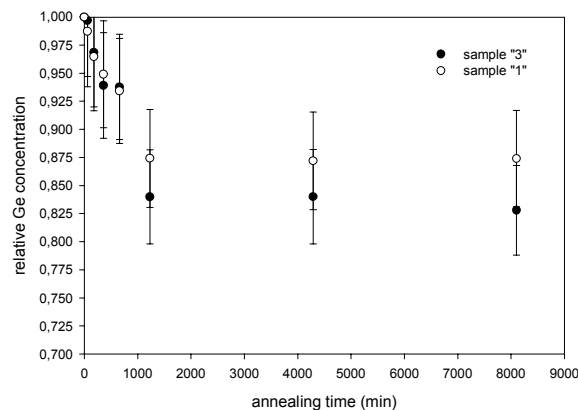


Fig. 2. Ge amplitude modulation in the first layer as a function of annealing time.

In order to obtain the interdiffusion coefficient (\tilde{D}) for the process we used the same procedure as in ref. [10], where the calculations were made on the base of Fick's second equation. For the details of these calculations see ref. [11]. As a result the value $\tilde{D} = (4.35 \pm 0.22) \cdot 10^{-22} \text{ m}^2 \text{ s}^{-1}$ was obtained for the beginning of the interdiffusion process, which characterises the Si diffusion in pure Ge. After a long annealing treatment (150 hours at 410°C) \tilde{D} was $(4.55 \pm 0.25) \cdot 10^{-23} \text{ m}^2 \text{ s}^{-1}$, which is characteristic for a $\text{Si}_{0.2}\text{Ge}_{0.8}$ alloy. Our results confirm the theoretically predicted strong concentration dependence of the interdiffusion coefficient.

5.2. Comparison of different methods

As the mobility of the Si is approximately eight times higher than that of the Ge, the intermixing in Si-Ge multilayers is asymmetrical. Therefore a thickening of the Ge layer is expected to occur, which could cause a visible change in the shape of Ge peaks in the RBS spectra. However for the direct observation of this effect very good energy resolution and optimal measuring conditions are needed. This makes important to compare the instrumentation available in different laboratories. With our instrumentation a depth resolution of 5 nm could be achieved for the first Ge layer at 10–20 nm depth. The experimental observation of the above effect was ambiguous at these experimental conditions.

A better progress can be achieved by using higher resolution RBS analysis or other methods. In this respect the co-operation with the laboratories in Dubna and Albany seemed to be fruitful. In Dubna a particle detector with better resolution (up to 10 keV) and better geometrical conditions are available, hence, samples were also sent there. As expected the results from Dubna show a much better peak/valley ratio (Fig. 3.) than seen in our laboratory.

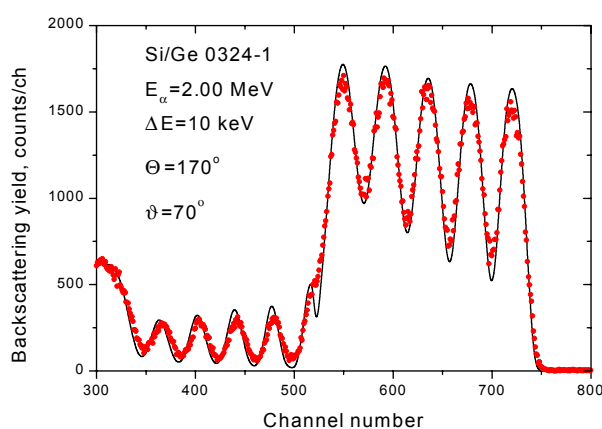


Fig. 3. Measured and simulated RBS spectrum of a Si-Ge multilayer (measured in Dubna [12]).

Measurements of the samples before annealing were also done in Albany where a high-resolution magnetic spectrometer was used. Like such systems it has an energy resolution more than an order of magnitude better than that of Si detectors. These higher resolution measurements provide a more sensitive measurement of the Si-Ge interdiffusion therefore further measurements of the annealed samples are planned in the future.

For the determination of the oxygen content of some Si-Ge multilayers and its depth distribution using the $^{16}\text{O}(\alpha,\alpha)^{16}\text{O}$ resonance scattering method, see the report of A. Kobzev in this TECDOC.

6. Cross comparison of CuInGaSe films

Eight $\text{CuIn}_{(1-x)}\text{Ga}_x\text{Se}_2$ samples were received for the cross comparison measurement. RBS spectra were measured at $E_{\alpha} = 2$ MeV. The compound masses were not resolved well (Cu and Ga), at this energy, thus a careful simulation was required for a reliable determination of the elemental composition. For more details see the corresponding papers in this final report.

7. Nitrogen determination

Before applying one of the nuclear reaction analysis methods (NRA) — the so called deuteron induced γ ray emission (DIGE) — for nitrogen determination in CVD diamond, we have made a completion of our earlier work [13], in order to provide basic data, which are still missing in the

literature. In some cases old results have also been revised. Namely the more detailed investigation of the results in ref. [13] showed [14] that the programme package FLORENCE used for the evaluation of the measured gamma ray spectra cannot handle correctly those peaks which are not totally resolved, and this is the case also with single peaks showing Doppler broadening. Therefore a reanalysis of the experimental data was made at ATOMKI with the use of the programme package FORGAMMA [5] capable to analyze complex, unresolved γ ray peaks and also line shapes with Doppler broadening. (The results obtained for a large interval of elements — i.e. from Li to Ca — are published elsewhere [15]).

In Fig. 4., a γ ray spectrum of nitrogen bombarded by deuteron beam of 1.8 MeV and thick target absolute yield curves of the stronger γ rays in the deuteron energy range of 0.7–3.4 MeV are plotted together. A table listing the energies of γ rays originating from the sample and the nuclear reactions via the γ rays produced are added to the figure. The energy values of peaks for which yield curve is shown and proposed to be selected for elemental analysis are typed in bold, the other peaks originating from the element in question are normal typed. As it is seen, the spectrum collected on nitrogen target (TaN) is rich in peaks due to the numerous γ ray transitions in the residual ^{14}N nucleus, nevertheless it is complicated because of the presence of the strong escape peaks of the high energy γ rays.

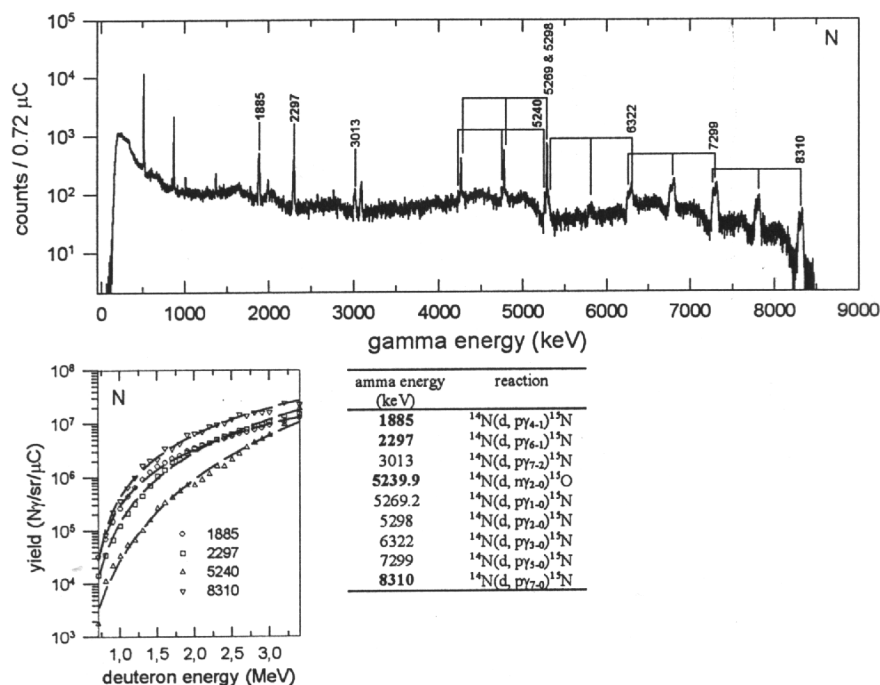


Fig. 4. γ ray spectrum of nitrogen bombarded by deuteron beam of 1.8 MeV and thick target absolute yield curves of the stronger γ rays in the deuteron energy range of 0.7–3.4 MeV. A table listing the energies of γ rays originating from the sample and the nuclear reactions via the γ rays produced [15].

It was found that the measured yields could be fitted by a rather simple three-parameter equation:

$$Y = Y_0 \cdot (E_d - E_{d0})^a$$

where Y is the absolute γ ray yield, E_d is the deuteron energy; Y_0 , E_{d0} and a are the fitting parameters. These parameters and the fitting coefficient (R^2) for each nitrogen transition are listed in Table 1. The R^2 coefficient shows that a rather good fit could be achieved. The use of the above equation gives a useful tool in elemental analysis for concentration calculations.

TABLE 1: FITTING PARAMETERS Y_0 , E_{d0} , a AND FITTING COEFFICIENT (R^2) FOR EACH NITROGEN TRANSITION.=

| E_γ [keV] | A | E_{d0} | Y_0 | R^2 |
|------------------|--------|----------|---------|--------|
| 1885 | 2.0240 | 0.5647 | 1590121 | 0.9968 |
| 2297 | 2.7811 | 0.4861 | 916118 | 0.0065 |
| 5239.9 | 4.1438 | 0.2496 | 89940 | 0.9882 |
| 8310 | 2.1905 | 0.5771 | 2820529 | 0.9959 |

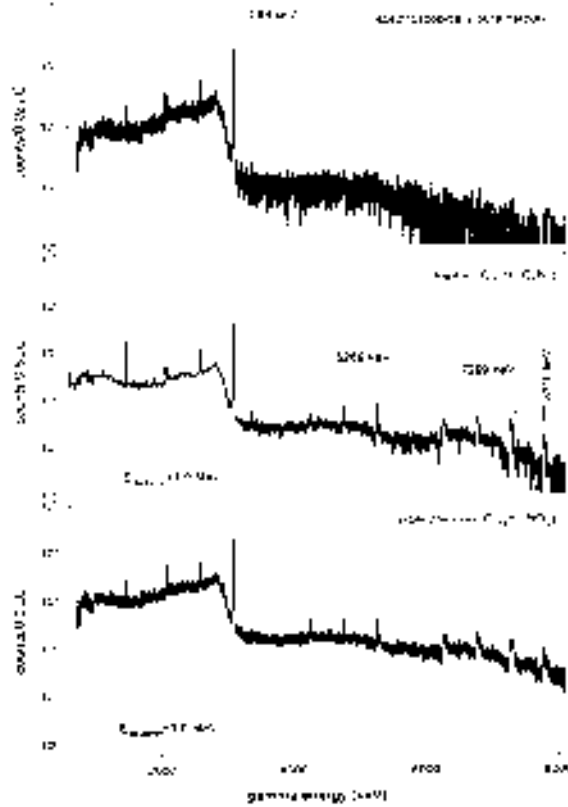


Fig. 5. γ ray spectra of pure carbon, kapton ($C_{22}H_{10}O_5N_2$) and α -benzoinoxin ($C_{14}H_{13}NO_2$).

CVD diamond as a pure carbon material produces high intensity gamma yield with energies less than 7 MeV if bombarded by deuteron beam. From nitrogen the most intensive gamma ray emerges at 7.3 MeV, moreover there are gamma rays also at 8.3 and 9.1 MeV, giving an additional yield to the 7.3 MeV gamma ray. Thus the concept of the measurement was to use a large volume Ge detector (a so called CLOVER detector, having high efficiency for high energy gamma rays), and put a lower discrimination level for the gamma signals at 7 MeV. Test measurements were performed at $E_d = 1$ MeV, where a better nitrogen/carbon yield could be achieved than at 1.8 MeV. The target current varied between 0.5 and 1.0 nA. Fig. 5. shows the measurement results.

Here the spectra of spectroscopically pure carbon, kapton ($C_{22}H_{10}O_5N_2$), α -benzoinoxin ($C_{14}H_{13}NO_2$) — to determine detection limit are seen. The upper figure shows however, that the very high gamma yield from the carbon produced an unexpectedly high pile up in almost all the region where the appearance of the nitrogen peaks was expected.

From these measurements we had to conclude, that the determination of the 10 ppm or less nitrogen content of the CVD diamond samples provided by EPD, Torino is not possible. A considerable improvement of the detection electronics would be needed to reach the detection limit necessary for the study CVD diamonds.

8. Conclusion

The results of the above applications of ion beam analysis methods with the use of MeV ions could lead us to technical improvements of the analytical facilities and developments of the methods for the investigation of multilayered thin films and for the determination of light elements in these kind of materials.

REFERENCES

- [1] RAJTA, I., BORBÉLY-KISS, I., MÓRIK, GY., BARTHA, L., KOLTAY, E., KISS, Á.Z., Nucl. Instr. and Meth., B 109 (1996) 148–153.
- [2] SIMON, A, PÁSZTI, F., UZONYI, I., MANUABA, A., KISS, Á.Z. Vacuum 50 (1998) 503–506.
- [3] KÓTAI, E., Nucl. Instr. and Meth., B 85 (1994) 588.
- [4] ELEKES, Z., KISS, Á.Z., GYÜRKY, GY., SOMORJAI, E., UZONYI, I. Nucl. Instr. and Meth. B158 (1999) 209–213.
- [5] SZÉKELY, G., Comp. Phys. Comm. 34 (1985) 423.
- [6] FERT, A., Mater. Sci. Forum, 59/60 (1990) 439.
- [7] SPAEPEN, F., J. of Magnetism and Magnetic Materials, 156 (1996) 407.
- [8] PROKES, S.M., SPAEPEN, F., Appl. Phys. Lett. 47(3) (1985) 234–236.
- [9] BEKE, D.L., LANGER, G.A., KIS-VARGA, M., DUDÁS, A., NEMES, P., DARÓCZY, L., KERÉKES, GY., ERDÉLYI, Z., Vacuum, 50 (1998) 373–383.
- [10] TADAYYON, S.M., YOSHINARI O., TANAKA, K., JPN. J.Appl. Phys. 31 (1992) 2226.
- [11] SIMON, A., CSIK, A., PÁSZTI, F., KISS, Á.Z., BEKE, D.L., DARÓCZY, L., ERDÉLYI, Z., LANGER, G.A., Nucl. Instr. and Meth. 161 (2000) 471.
- [12] KOBZEV, A., Condensed Matter Division, Frank Laboratory of Neutron Physics, Joint Institute of Nuclear Research, Dubna, Russian Federation, private communication.
- [13] KISS, Á.Z., BIRON, I., CALLIGARO, T., SALOMON, J., Nucl. Instr. and Meth. B 85 (1994) 118.
- [14] ELEKES, Z., J. of Undergraduate Research in Physics, 16 (1997) 7.
- [15] ELEKES, Z., KISS, Á.Z., BIRON, I., CALLIGARO, T., SALOMON, J., Nucl. Instr. and Meth. B168 (2000) 305.

INFLUENCE OF IMPURITIES ON SILICIDE CONTACT FORMATION

KH.R. KAZDAEV, G.B. MEERMANOV, R.KH. KAZDAEV
Institute of Nuclear Physics of National Nuclear Center,
Almaty, Kazakhstan

Abstract

Research objectives of this work are to investigate the influence of light impurities implantation on peculiarities of the silicides formation in molybdenum monocrystal implanted by silicon, and in molybdenum films sputtered on silicon substrate at subsequent annealing. Implantation of the molybdenum samples was performed with silicon ions (90 keV, $5 \times 10^{17} \text{ cm}^{-2}$). Phase identification was performed by X ray analysis with photographic method of registration. Analysis of the results has shown the formation of the molybdenum silicide Mo_3Si at 900°C . To find out the influence of impurities present in the atmosphere (C,N,O) on investigated processes we have applied combined implantation. At first, molybdenum was implanted with ions of the basic component (silicon) and then — with impurities ions. Acceleration energies (40keV for C, 45 keV for N and 50 keV for O) were chosen to obtain the same distribution profiles for basic and impurities ions. Ion doses were $5 \times 10^{17} \text{ cm}^{-2}$ for Si-ions and $5 \times 10^{16} \text{ cm}^{-2}$ — for impurities. The most important results are reported here. The first, for all three kinds of impurities the decreased formation temperatures of the phase Mo_3Si were observed; in the case of C and N it was $\sim 100^\circ$ and in the case of nitrogen — $\sim 200^\circ$. Further, simultaneously with the Mo_3Si phase, the appearance of the rich-metal phase Mo_5Si_3 was registered (not observed in the samples without additional implantation). In case of Mo/Si-structure, the implantation of the impurities (N,O) was performed to create the peak concentration ($\sim 4 \text{ at} / \%$) located in the middle of the molybdenum film ($\sim 150 \text{ nm}$) deposited on silicon substrate. Investigation carried out on unimplanted samples showed the formation of the silicide molybdenum MoSi_2 , observed after annealing at temperatures $900 \div 1000^\circ\text{C}$, higher then values $500\text{--}600^\circ\text{C}$ reported in other works. It is discovered that electrical conductivity of Mo_5Si_3 -films synthesized after impurities implantation is lower ($40\text{--}50 \ \Omega\text{cm}$) than for MoSi_2 -films arising without implantation ($90\text{--}100 \ \Omega\text{cm}$). To destroy the native SiO_2 -layer on Si-surface by decreasing the formation temperature of the silicides, the ion implantation of the Mo/Si-interface region was carried out. Implantation was realized with dose of $5 \times 10^{16} \text{ cm}^{-2}$ and energies of 180 keV (N), 200 keV (O), 160 keV (C). It is found that as a result of ion mixing process after implantation the traces of the hexagonal MoSi_2 -phase arises. The second peculiarity is the reduction of the temperature where formation of the rich-metal phase Mo_5Si_3 begins for approximately 200° (compared with the case of ion implantation in the centre of deposited metal film). It is found that electrical conductivity of the obtained Mo_5Si_3 -films synthesized after N-, C- or O — implantation is lower ($30\text{--}60 \ \Omega \text{ cm}$) that for MoSi_2 -films arising without ion implantation.

1. Introduction

Because of the low resistivity and high temperature stability, refractory metals and their silicides are vigorously investigated for their applicability as interconnected and contact materials in semiconductor electronics. In conventional technology, metal silicides are obtained by codeposition techniques. At the present time, application of ion beam techniques to the formation of metal silicides has attracted much interest. Research in this field centers around two areas, namely, ion mixing and ion beam synthesis. In ion beam mixing, inert gas ions are implanted into metal/silicon — structure in order to mix interface through cascade and recoil mixing when the implantation is carried out at low temperature, and radiation enhanced diffusion when the substrate is intentionally heated during implantation [1]. In ion beam synthesis, the metal content needed in metal silicide is supplied by directly implanting the silicon substrate with metal ions to a dose determined by composition of the particular silicide studied [2]. In both cases it was noticed that presence of impurities has strong influence on the formation of the silicide itself. Among these impurities oxygen, nitrogen and carbon, ever present in the real manufacturing environment, greatly alter the growth of metal silicides [3]. For example, after implantation of oxygen in nickel layer of the nickel/silicon — structure and subsequent annealing, the formation of silicon oxides barrier is observed, but at its implantation in semiconductor layers the silicide grows without barrier [4]. Implantation of nitrogen in titanium layers on silicon substrate leads to forming the phase Ti_5Si_3 , compared with TiSi_2 that is observed without nitrogen implantation [5]. However, such works are far insufficient for understanding the mechanism of the impurities influence on the growth of metal silicides. On the other hand, understanding of the role of

impurities is impotent to avoid unwanted effects and it also may lead to the possibility of using impurities to control silicide growth.

Research objectives of this work consists in investigation of influence of light impurities implantation on peculiarities of the silicides formation first of all in molybdenum monocrystal implanted by silicon, and on the other hand in molybdenum films sputtered on silicon substrate at subsequent annealing.

2. Experimental

For investigation on molybdenum, (110)-oriented monocrystalline samples with a purity 99,96% were used. Studies of the silicides formation in molybdenum/silicon-structures were performed on (100)-oriented Czochralsky-grown silicon samples (p-type, thickness of 0,430 mm and conductivity of 4,5 Ωcm) grown on the molybdenum films. The sample thickness of about 150 nm was obtained through sputtering by using a magnetron source at 200^oC, -230V substrate bias and pressure of about 10⁻⁶ Torr. Thicknesses of the deposited layers were measured by X ray fluorescence method.

Ion implantation of the samples was carried out with heavy ion accelerator "Vezuvii-2-450". After ion implantation the samples were annealed in the temperature range of 400-1200^oC with step of 100^o during 1-3 hours. Phase identification was performed by X ray analysis with photographic method of registration [6]. Exposition times lasted for 12-15 hours. Conductivity of the surface layers was measured with four-point probe method.

3. Implantation in molybdenum

Implantation of the molybdenum samples was performed with silicon ions at acceleration energy $E = 90 \text{ keV}$ with doze $\Phi = 5 \times 10^{17} \text{ cm}^{-2}$. At these parameters, the average concentration of the implanted impurities gets up approximately to 50%. Fig.1. presents rayograms of the molybdenum surface implanted with silicon ions after subsequent annealings. Table 1 shows the example of phase identification of the resulted film after annealing at 900^oC. Analyses of the results have shown that after implantation the reflected diffraction lines arise on rayograms, while the halo arise from polycrystalline and amorphous phases of molybdenum consequently. Simultaneously the widening of the reflex from monocrystalline molybdenum is observed, characterizing an appearance of the deformation layers between implanted region and matrix. Subsequent annealing leads to disappearance of the halo around the reflex and lines that bear witnesses about decreasing the residual deformation in the strain regions and recrystallization of the implanted layers.

When annealing temperature reaches 900^oC, full set of lines arises on rayograms, originating from molybdenum silicide Mo_3Si having cubic lattice. Further rise of the temperature leads to appearance of the reflex from molybdenum carbide Mo_2C , which appears, as shown in additional experiments, due to interactions of the molybdenum surface with carbon from the furnace atmosphere.

The reference [7] shows that annealing of the molybdenum films implanted with silicon ions at 800^oC leads to formation of MoSi_2 -phase.

We have applied combined implantation to find out the influence of impurities present in the atmosphere on investigated processes. At first, molybdenum was implanted with ions of the basic component (silicon) and then with ions of the impurities (nitrogen, carbon or oxygen). Acceleration energies (45 keV for N and 50 keV for O) were chosen to achieve the same distribution profiles for basic and impurities ions. Ion doses were $5 \times 10^{17} \text{ cm}^{-2}$ for Si-ions and $5 \times 10^{16} \text{ cm}^{-2}$ — for N- or O-ions.

The most important results are reported here. At first, for all three kinds of the impurities the decreasing formation temperatures of the phase Mo_3Si were observed; in the case of carbon and nitrogen it was $\sim 100^\circ$ and in the case of nitrogen $\sim 200^\circ$. Further, simultaneously with phase Mo_3Si , the appearance of the rich-metal phase Mo_5Si_3 was registered, This was not observed in the samples without additional implantation.

The effect of the impurity influence on phase formation was observed earlier [8]. In vanadium monocrystals the structure conversion from bcc into hcp takes place when samples have even a trace of nitrogen. In titanium an analogous conversion is observed in "clear" samples. Satisfactory model explaining this phenomena has not been yet presented.

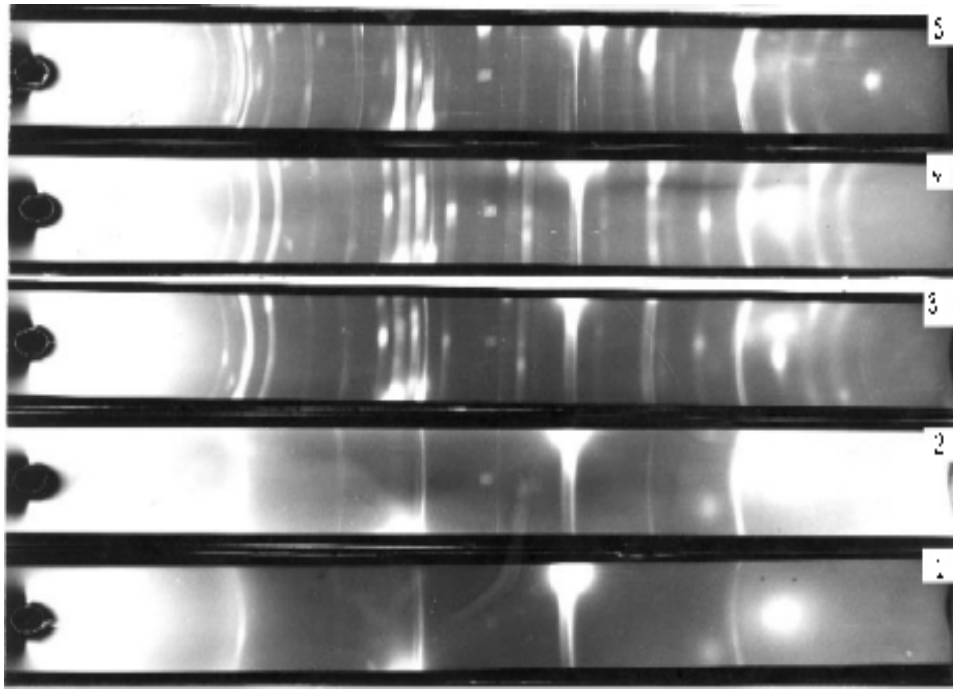


Fig. 1. Surface rayograms of the molybdenum implanted by silicon ions after implantation (1) and annealing at 800^o (2), 900^o (3), 1000^o (4), 1100^o (5).

TABLE 1: IDENTIFICATION OF PHASE IN MOLYBDENUM AFTER IMPLANTATION BY SILICON IONS AND ISOCHRONAL ANNEALING (900^oC)

| Experiment | | Mo ₃ Si | |
|------------|-------|--------------------|--|
| d, Å | d, Å | hkl | |
| 3,45 | 3,46 | 110 | |
| 2,47 | 2,45 | 200 | |
| 2,19 | 2,19 | 210 | |
| 2,00 | 2,00 | 211 | |
| 1,73 | 1,73 | 220 | |
| 1,55 | 1,55 | 310 | |
| 1,41 | 1,41 | 22 | |
| 1,36 | 1,36 | 320 | |
| 1,31 | 1,31 | 321 | |
| 1,22 | 1,22 | 400 | |
| 1,07 | 1,07 | 421 | |
| 0,958 | 0,959 | 510 , 431 | |
| 0,908 | 0,908 | 520 , 432 | |
| 0,893 | 0,893 | 521 | |
| 0,864 | 0,864 | 440 | |
| 0,838 | 0,838 | 530 , 433 | |
| 0,806 | 0,804 | 610 | |
| 0,793 | 0,793 | 611 . 532 | |

4. Implantation of Mo/Si structure

Results presented in the preceding section have shown that presence of the light impurities (nitrogen, oxygen or carbon) may render essential influence on phase transformations, when interaction of molybdenum and silicon atoms takes place. We decided to check a possibility of using these phenomena for silicides contact formation. In conventional technology, the silicide contacts are prepared by sputtering of thin metal films on the silicon surface, with resulted structures exposed to annealing at definite temperature. In case of molybdenum, only MoSi_2 -phase is formed. Attempts to obtain the phases with other composition were not successful. In this work we have tried to change the situation by implantating impurities in thin molybdenum films, sputtered on the silicon substrate before annealing.

The ion energies (80 keV for N and 90 keV for O) were chosen in order to locate the peak concentration (~ 4 at.% for doses $5 \times 10^{16} \text{ cm}^{-2}$) in the middle of the molybdenum film

Investigation carried out on unimplanted samples showed (Fig. 2) that after deposition the Mo films contain the high-temperature phase $\gamma\text{-Mo}_2\text{N}$. This phase is unstable and disintegrates within the temperature range of $600\text{--}700^\circ\text{C}$. The appearance of this phase is not unexpected because the deposition processes may be represented as low-energy implantation, and $\gamma\text{-Mo}_2\text{N}$ - and $\delta\text{-MoN}$ -phases can be formed by means of recoil implantation of accelerator residue gases [9].

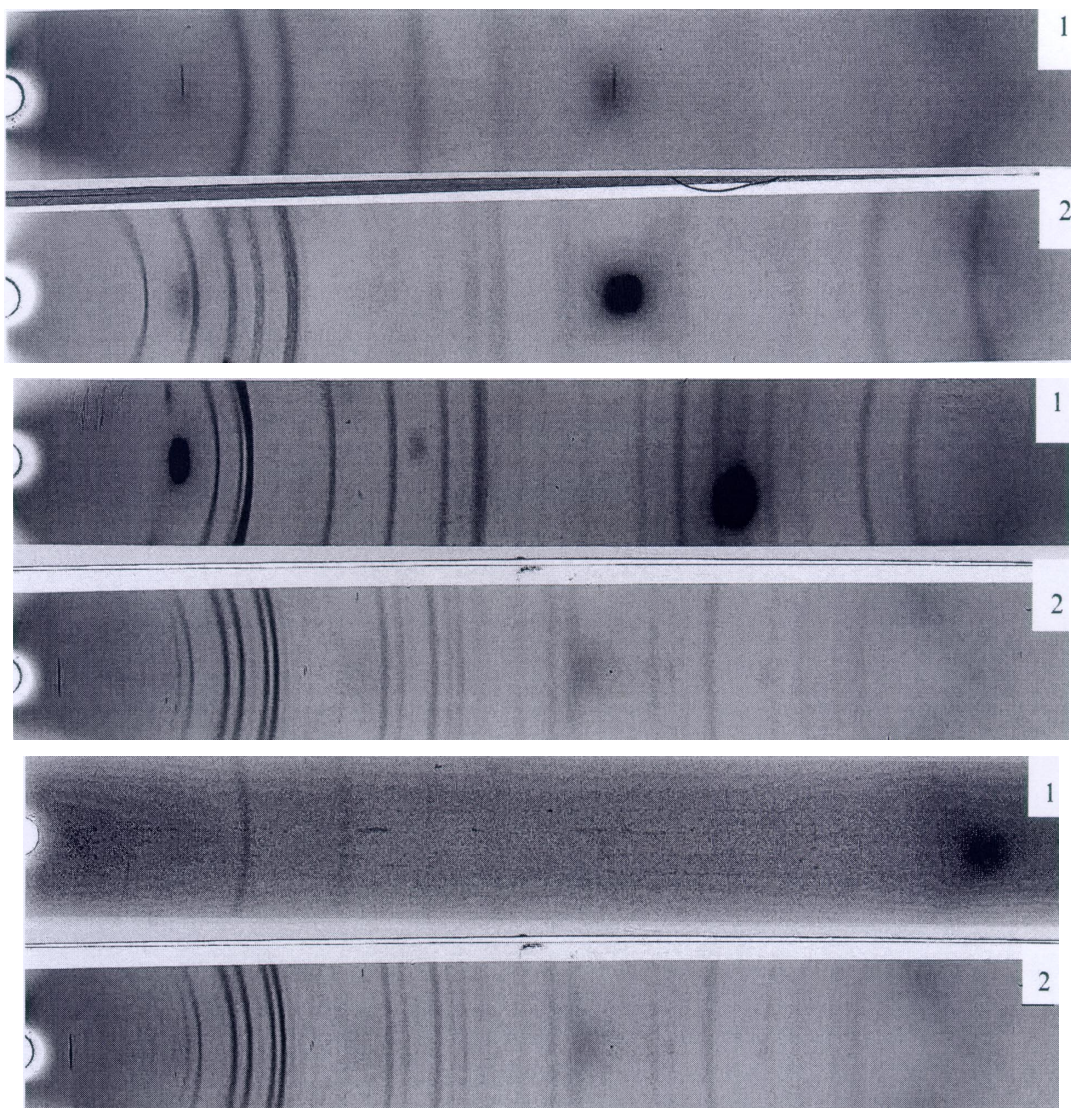


Fig. 2. X rayograms Mo/Si — structures: a) after sputtering of Mo on Si —substrate (1) and annealing at 1200°C ; b) after N — implantation Mo/Si — structure and annealing at 650 (1) and 1200°C (2); c) after O — implantation (1) and annealing at 750 (2) and 1200°C (3).

The formation of the silicide molybdenum MoSi_2 was observed after annealing at temperatures of $900 \div 1000^\circ\text{C}$. These temperatures are higher than values ($500\text{--}600^\circ\text{C}$) reported in other works [10]. In case of N-implantation, after disintegration of $\gamma\text{-Mo}_2\text{N}$ phase at $700\text{--}800^\circ\text{C}$, the Mo_2O_3 -phase arises in Mo films. Apparently, a thermodesorption process of the implanted nitrogen causes the formation of this phase from the samples in this temperature range [11]. Analogous effect of the catastrophe oxidation of Ti by annealing in oxygen atmosphere was observed for the N-implanted Ti-samples [12].

In the range of $900\text{--}1000^\circ\text{C}$, the formation of Mo_5Si_3 phase takes place instead of MoSi_2 phase, as was observed in unimplantation samples. Implantation of oxygen ions causes formation of ordered solid solution of oxygen in molybdenum, leading to the formation of a bcc-superstructure with lattice parameter exceeding the molybdenum one approximately for 10%. At 800°C this solution is disintegrated and the Mo_3O phase appears. At the further annealing until $900\text{--}1000^\circ\text{C}$, as well as in case of N-implantation, formation of the Mo_5Si_3 phase is observed. In cases of (N+O)- and (O+N) implantation essential distinctions in the silicide formation process from cases of N- and O-implantation were not observed.

It is observed that electrical conductivity of Mo_5Si_3 -films synthesized after N- or O-implantation is lower ($40\text{--}50$) Ωcm than for MoSi_2 -films arising without implantation ($90\text{--}100$) Ωcm .

Thus, conducted investigations have shown that implantation of the light impurities in Mo-film of the Mo/Si — structure allow to change the phase transformation mechanism, and to receive more rich-metal phase with lower resistivity at annealing, than in the case of unimplanted samples. However, interaction between silicon substrate and deposited Mo-film starts at sufficiently high temperature that is detrimental for silicon technology. At the same time, investigations of Mo/Si-contacts formation with thermal method have shown that presence of native silicon oxide at Mo/Si-interface rises a beginning of the silicide formation temperature [13]. On the other hand, by using the ion mixing technique makes it possible to reduce the reaction temperature between silicon substrate and deposited metal films [14]. That's why we have tried to use ion implantation for getting of the rich-metal silicide phase, and the second, to reduce the formation temperature of the silicides. To reach this goal, we have carried out the implantation of the Mo/Si-interface region with light ions. Implantation of the samples was realized with the dose of $5 \times 10^{16} \text{ cm}^{-2}$ and energies of 180 keV (N), 200 keV (O), 160 keV (C). The ion energies were chosen in order to locate the peak concentration (~ 3 at. %) in the Mo/Si-interface region ($R_p \sim 150 \text{ nm}$; $\Delta R_p \sim 60 \text{ nm}$). Among the obtained results (Fig. 3.), it is possible to mark two peculiarities: (i) the appearance of the traces of the hexagonal MoSi_2 -phase on the rayograms after implantation, arising as the result of ion mixing process; (ii) reduction of the rich-metal formation temperature approximately for 200°C compared to the case of ion implantation in the middle of deposited metal film. This is caused by destroying the native diffusion SiO_2 -barrier between silicon substrate and deposited Mo-films.

It is observed that electrical conductivity of the obtained Mo_5Si_3 -films synthesized after N-, C-O, O implantation is lower ($30\text{--}60 \Omega \text{ cm}$) than for MoSi_2 -films, arising without ion implantation ($90\text{--}120 \Omega \text{ cm}$).

5. Discussion

As a result of the performed research we have got three varieties of the silicide phases: Mo_3Si , MoSi_2 and Mo_5Si_3 . Among them, Mo_3Si -phase is formed in molybdenum implanted with silicon ions; MoSi_2 -phase is synthesized in thin molybdenum films and molybdenum/silicon-structures; Mo_5Si_3 -phase is stabilized when molybdenum is implanted with light impurities (nitrogen, oxygen or carbon).

In our opinion the reason for divergence in phase formation that takes place in thin films and massive samples of Si-implanted molybdenum is in their dimensions. In thin films with their thickness not exceeding 100 nm, the annealing leads to diffusion of the implanted impurity. In this case, the diffusion process is limited by thickness of the sample and average concentration. In massive samples diffusion processes deep into sample are not limited. Therefore, impurity concentration in the implanted layers will fall unbrokenly with annealing until the temperature does not reach the formation temperature for a definite phase. In this case one may expect a formation of the phases with lower concentration of the implanted impurity. That is why in Si-implanted massive samples Mo_3Si -phase is formed, and in thin films MoSi_2 -phase is synthesized.

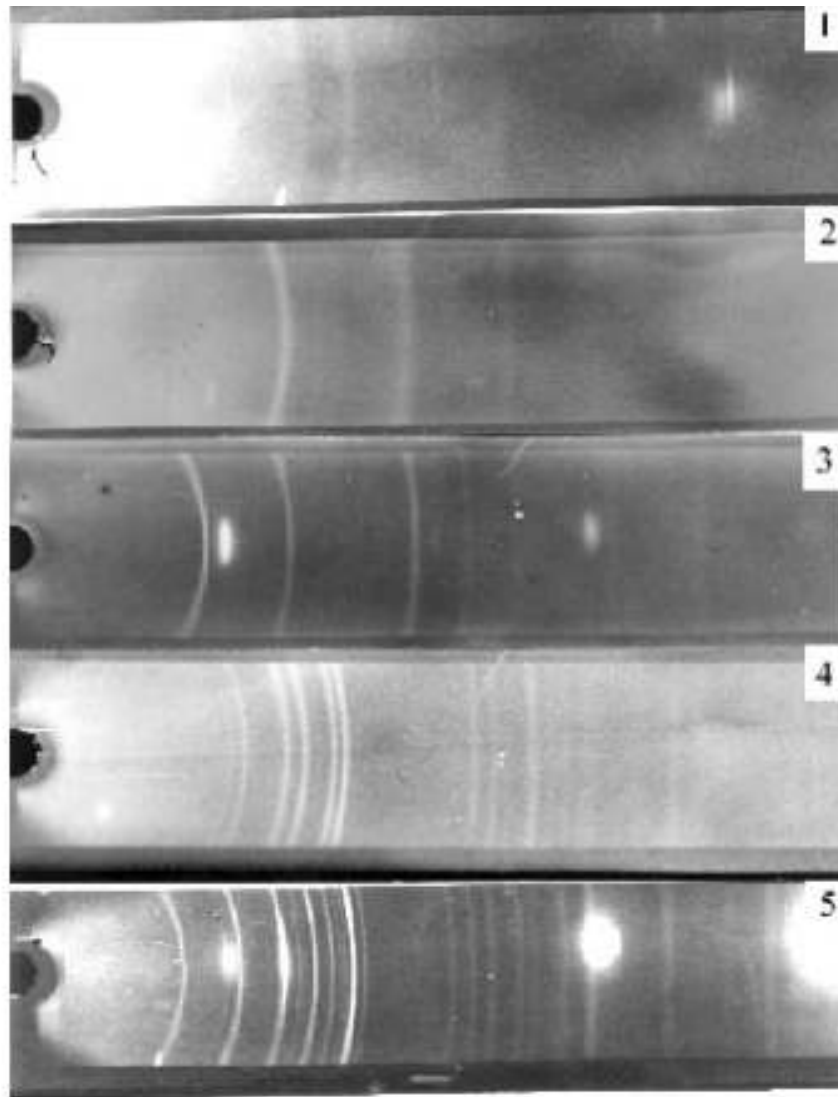


Fig. 3. X rayograms of the Mo/Si — structure after sputtering M-film (1), O — implantation (2), and annealing at 600 (3) and 800⁰C (4). It is shown the X — rayogram of the unimplanted Mo/Si — structure after annealing at 1000⁰C (5).

The physical mechanism responsible for the formation of the phases in metal/silicon structures have not been yet identified. The simplest way to explain the phase formation is to assume that all the phases which have the fastest growth rate always dominate. But this interpretation can easily be eliminated. For example, in ref. [15] it has been shown that in case of Pt/Si-structure, PtSi and Pt₂Si should be present at the same time since their growth rate is almost the same. Moreover, the appearance of the second phase after a well defined time, and decomposition experiments, are evidence against the concept of the formation of all the phases at the same time.

Several attempts have been reported in the literature to find correlation between the appearance of the phases and the thermodynamic properties of compound; generally, the stability have been used and the values have been inferred from phase diagram. According to this criterion, the same sequences should always be observed. There are several experimental observations, which indicate that stability arguments cannot explain the phase formation. An analysis of the data reported in the ref. [16] reveals that two different compounds, PtSi and Pt₁₂Si₅, are formed at almost the same temperature and in the same system. Moreover, according to the phase diagram, Pt₁₂Si₅ should never form in place of PtSi, since the former is less stable than the latter. Another experiment yielding results against the stability concept is described in the ref. [15]. The metal-silicon compound grows in one case and shrinks in the other, although the two adjacent phases are the same in both cases. Again, according to stability arguments, CoSi should never disappear since it is much more stable than Co₂Si.

To explain the sequence in compound formation, Ottaviani [17] have proposed an automistic model which assumes that the selective growth of a phase is mainly initiated by an interface composition that is governed in turn by the flux of the various elements to the interface. The model can account for the experimental results. For example (see ref. [17]), the growth of PtSi-forms are known: Pt_4Si , Pt_2Si , Pt_5Si_2 , $Pt_{12}Si_5$, Pt_7Si_3 , Pt_2Si , Pt_6Si_5 , $PtSi_2$ occur because the interface change composition and the change is due to the disappearance of free metal. In the presence of platinum, Pt_2Si continues to grow since platinum is supplied to the Si-Pt interface. Once the platinum has been consumed, the flux of platinum is suppressed and new phase can grow. How the flux of platinum is suppressed, or decreased, is not important. The same model can also be applied when the silicon is consumed and, in the presence of an excess of platinum, metal-rich phases can grow. In bulk examples the thickening of the growing phase reduces the flux of materials. After a critical length the composition at the interface changes and a new phase can grow with a new phase present, the diffusion coefficient can change and can produce a shrinkage of some phases and increase for other.

During the growth of the silicide either the silicon or the metal can move. Generally, there is a predominance of one species, either the metal or the silicon, and the relative contribution is a function of the temperature. At high temperatures for refractory metals the silicon is main moving specie [17]. The only exemption is in the case of rare earth metals where the silicon is main moving specie at low temperatures. That's why for molybdenum-silicon system, observed processes may be presented as shown in Fig.4. Additional diffusion barrier in this case represents the native Si_2O_2 -layer on the silicon surface which rises the beginning of the silicide formation.

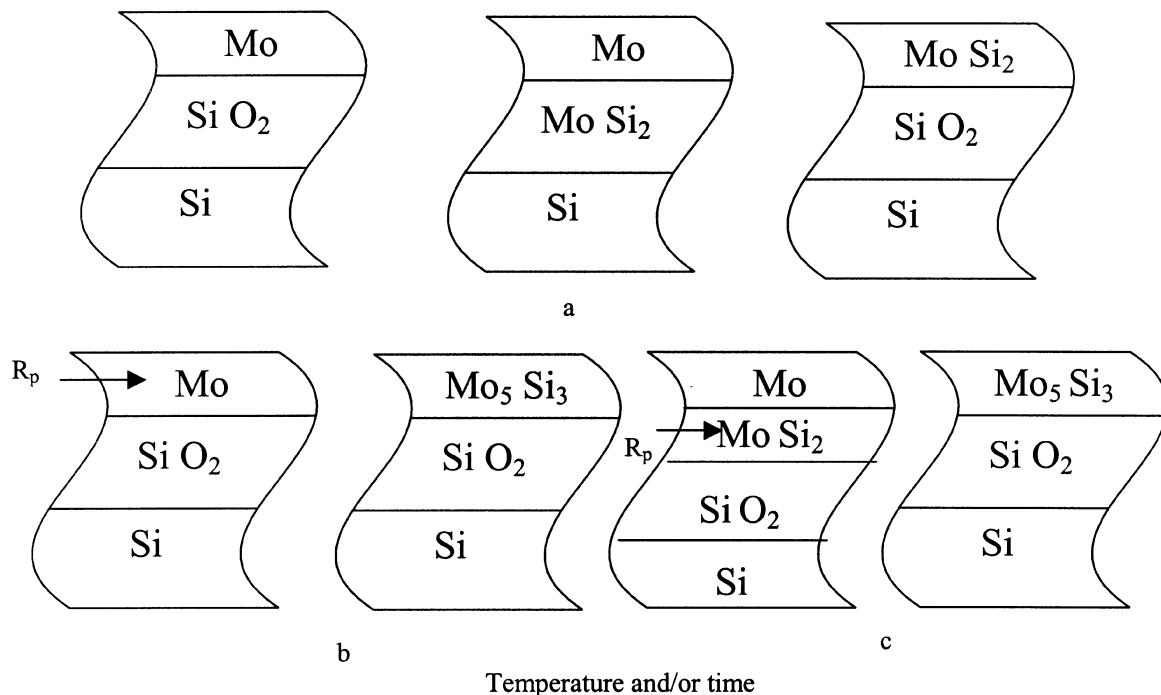


Fig. 4. Scheme of the silicide formation in unimplanted (a) and implanted with impurities in the middle of Mo-films (b) and Mo/Si — interface (c).

The experiments with impurities can be explained by the same model. In fact, when the metal is the main moving species its diffusion is decreased and silicon-rich phase can grow. If silicon is main moving specie, the new phase will be metal-rich. On the other hand, an annealing on thin molybdenum films, where one can obtain a designed uniform distribution profile of the implanted silicon, does not lead to formation of metal-rich phase Mo_5Si_3 . It remains to suppose that such impurities as nitrogen, oxygen or carbon take part in forming the Mo_5Si_3 -phase stabilizing its structure. It is possible that this phase does not exist without a presence of the impurities. Therefore the formation of the Mo_5Si_3 -phase can be expected in a wide enough concentration region. That's why this phase is formed both in Si-implanted molybdenum and in Mo/Si-structures at annealing. At this time one can't ignore the suppressing of the mutual diffusion of metal and silicon due to the presence the impurities.

REFERENCES

- [1] HAMDI A., NICOLET M.A., Thin Solid Films. B32 (1984) 357.
- [2] SANCHEZ F.N., NAMAR F. ET.AL., Mater.Res.Soc.Symp.Proc. 51(1986)439.
- [3] BLATNER R.J., EVANS C.A., LAU S.S., MAYER J.W., ULRICH B.M., J.Electrochem. Soc. 122 (1975)1372.
- [4] SCOTT D.M., NICOLET M.A., Nucl. Instr. And Meth. 182/183 (1981)655.
- [5] GUDLIELMACCI G.M., GILET M., Surface Sci. 94 (1980)424.
- [6] ABASHINA A.V., AKCHULAKOV M.T., KADYRGANOV K.K., KAZDAEV KH.R., MELIHOV V.D., Poverhnostj. 4 (1987) 62.
- [7] AFANASJEV G.V., GIASSAMIDZE A.M., KALININ A.M., Poverhnostj. F.H.M. 12 (1986).
- [8] GOLIDSHMIT H., Mir. 1.424s., 2.464s. (1971).
- [9] Akchulakov M.T., Kadyrganov K.K., Kazdaev Kh.R. Izvestia AN KazSSR. Ser.Fizmat. N6 (1986)20.
- [10] HO K.T., NICOLET M.-A., SCOTT D.M., Thin Solid Films. N.127 (1985)171.
- [11] KAZDAEV KH.R., AKCHULAKOV M.T., SEJDIGAZIMOV S.K. , BAJADILOV E.M., 8-th Intern.Conf. "Surface modification of Metals by Ion Beams". Kanazaws. Japan. (1993) 0-04.
- [12] KAZDAEV KH.R., SEIDIGAZIMOV S.K., UTAROV S.G., Intern. Conf. Nuclear and radiation Physics. Almaty. (1997) 191.
- [13] YANAGISAVA S., FUKUYAMA T. J., Electrochem.Soc. 127 (1980) 1150.
- [14] WANG K.L., CHIANG S.W., BACON F., REIHL R.F., Thin Solid Films. 74 (1980) 239.
- [15] CANALI C., CATELLANI C., PRUDENZATI M., WADIN W.I., EVANS C.A., Jr.Appl.Phys.Lett. 31 (1977) 43.
- [16] MAJNI, COSTATO M., PANINI F., GELOTTI G. J., Phys.Chem.Solids. 46(1985)631
- [17] OTTAVIANI G., Thin Solid Films. 140 (1986) 3.

ION CHANNELING STUDY OF DEFECTS IN MULTICOMPONENT SEMICONDUCTOR COMPOUNDS

A. TUROS, L. NOWICKI, A. STONERT
The Andrzej Soltan Institute for Nuclear Studies,
Warsaw, Poland

Abstract

Compound semiconductor crystals are of great technological importance as basic materials for production of modern opto- and microelectronic devices. Ion implantation is one of the principal techniques for heterostructures processing. This paper reports the results of the study of defect formation and transformation in binary and ternary semiconductor compounds subjected to ion implantation with ions of different mass and energy. The principal analytical technique was He-ion channeling. The following materials were studied: GaN and InGaN epitaxial layers. First the semi empirical method of channeling spectra analysis for ion implanted multicomponent single crystal was developed. This method was later complemented by the more sophisticated method based on the Monte Carlo simulation of channeling spectra. Next, the damage buildup in different crystals and epitaxial layers as a function of the implantation dose was studied for N, Mg, Te, and Kr ions. The influence of the substrate temperature on the defect transformations was studied for GaN epitaxial layers implanted with Mg ions. Special attention was devoted to the study of growth conditions of InGaN/GaN/sapphire heterostructures, which are important component of the future blue laser diodes. In-atom segregation and tetragonal distortion of the epitaxial layer were observed and characterized. Next problem studied was the incorporation of hydrogen atoms in GaAs and GaN. Elastic recoil detection (ERDA) and nuclear reaction analysis (NRA) were applied for the purpose.

1. Radiation Damage in InGaAs/InP Heterostructures

1.1. Background

InGaAs/InP epitaxial layers are of a great a great importance for optoelectronic applications, especially for development of high efficiency laser diodes. The energy gap of multicomponent semiconductors depends on the lattice constant, which according to the Vegard's law changes linearly with the content of a given component. The RBS technique is well suited for analysis surface layer composition. Furthermore, ion channeling is a well-established technique for determination of crystalline perfection. Thus, the reported experiments were carried out by means of the RBS/channeling technique. The 2 MeV ^4He beam from the Van de Graaff accelerator LECH at the Andrzej Soltan Institute for Nuclear Studies was used.

1.2. Results

Fig. 1 shows the RBS random spectrum for the 1 μm thick InGaAs/InP heterostructure. Such spectra can be evaluated using the RUMP code [1], which enables the calculation of the component spectra (also shown in Fig. 1). The relative height of each component spectrum is a measure of the content of corresponding element.

Fig. 2 shows the $\langle 100 \rangle$ aligned spectra for InGaAs epilayer before and after ion implantation with different doses of 100 keV Kr ions. The crystalline perfection of the investigated epilayer was determined by the comparison of the aligned spectrum with the random one. The typically obtained χ_{min} value of 4–5% indicated good quality of the virgin crystal.

Evaluation of channeling data measured for multicomponent samples requires special procedures. In the course of this project a graphic method of separation of channeling spectra from two different sublattices has been developed. In such a way one obtains two separate channeling spectra, which can be analyzed by means of the two-beam approximation [2].

Fig.3. shows the evolution of the defect depth distributions for different Kr-ion doses calculated using the described above method for GaAs sublattice. The defect distributions calculated with the TRIM code [3] are also shown for comparison.

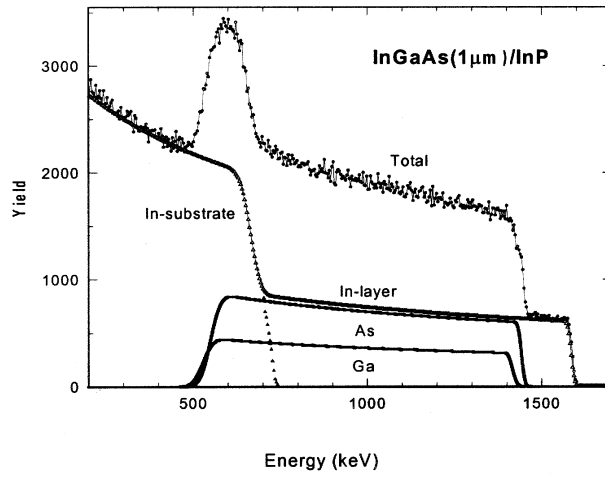


Fig. 1. RBS random spectrum for InGaAs(1µm)/InP heterostructure.

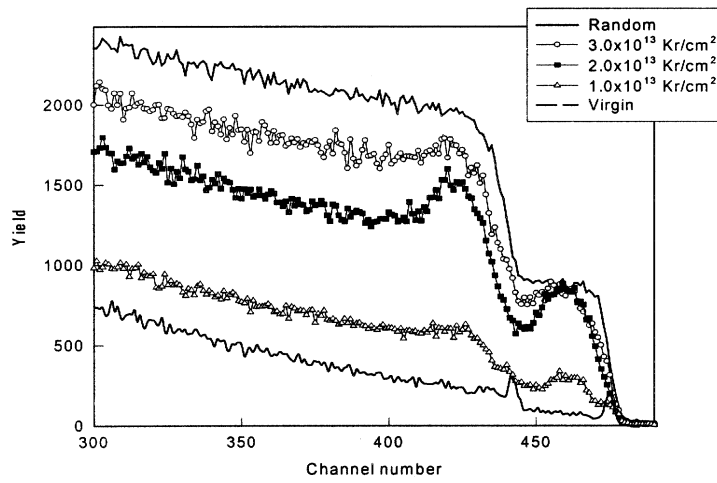


Fig. 2. Random and aligned spectra for InGaAs epilayer before and after ion implantation with different doses of 100 keV Kr ions.

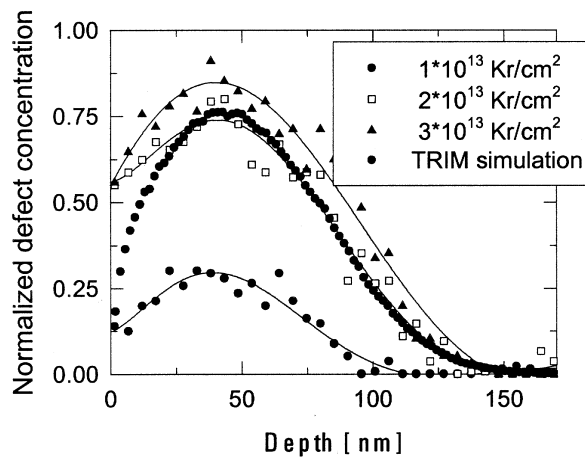


Fig. 3. Defect depth distributions in the GaAs sublattice produced by implantation with different Kr-ion doses.

The depth range of damage remains essentially the same for all indicated doses, however, the defect content increases at the beginning rapidly and shows the saturation effects at the dose of 3×10^{13} Kr/cm². It should be pointed out that the damage evolution in both sublattices is the same within the experimental error.

As illustrated in Fig. 4 for doses exceeding at 5×10^{13} As/cm² implanted regions became amorphous. With increasing ion dose the amorphous region extends to the greater depths, which is due to the accumulation of damage in the tail region of depth distributions of implanted ions.

InGaAs epilayers were also implanted with different doses of 100 keV N ions. In contrast to the heavy ion bombardment N-ion implantation did not produce important damage up to the dose of 5×10^{15} N/cm², i.e. ten times higher than the amorphisation dose for As-ion implantation. The maximum defect content was below 10 at.%. Since the higher doses are technologically irrelevant this experiment was stopped at this stage.

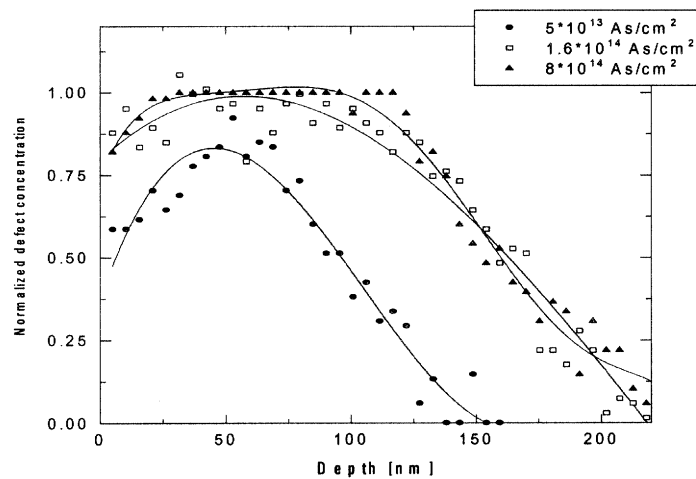


Fig. 4. Defect depth distributions in the GaAs sublattice produced by implantation with different As-ion doses.

1.3. Conclusions

The outcome of this part of the study can be summarized as follows:

- RBS/channeling is a suitable technique for the analysis of multicomponent epitaxial layers,
- InGaAs epitaxial layers of good crystalline quality can be produced by the metalorganic vapor deposition (MOCVD) technique,
- The procedure of spectra evaluation has been developed enabling the separate analysis of different sublattices of a layer,
- Both sublattices of InGaAs epitaxial layers exhibit the same damage buildup behavior upon ion implantation,
- The amorphisation dose at RT for 100 keV ions of mass about 80 amu amounts to 5×10^{13} at/cm²,
- N-ion implantation produces only few defects in InGaAs, which is apparently due to the fact that according to the TRIM code calculations 100 keV N ions do not create collisions cascades.

2. Low Temperature Irradiation of GaN

2.1. Defect Mobility at Low Temperatures

Properties of defects in III-N semiconductor compounds have been extensively studied by various techniques over the last few years [4–8]. Point defects and their complexes determine the electrical properties of semiconductors, diffusion of impurities and the recovery of crystalline lattice after ion bombardment and subsequent annealing. Interstitial defects can be directly observed by the

RBS/channeling technique. As channeling is almost exclusively sensitive to displaced atoms, it has been expected that the application of this technique will provide valuable and complementary information on the defect structures in III-N compounds.

Ion implantation at 51 K with 150 keV N ions to fluences ranging from 0.5×10^{14} at/cm² to 6×10^{14} at/cm² and RBS/channeling measurements using 1.4 MeV He ions were carried out. The beams from an ion implanter and a Tandem accelerator can be delivered to the same experimental chamber, which makes it possible to perform both ion implantation and RBS/channeling analysis without changing the temperature and the vacuum.

The experiment was performed in three stages: (i) the sample was mounted in a cryogenic goniometer and cooled down to 51 K where it was aligned and subsequently implanted with N ions, (ii) $\langle 0001 \rangle$ aligned channeling spectra were measured without changing the temperature at different time intervals, (iii) the sample was slowly warmed up to room temperature. During the warming-up, the aligned spectra were measured; the measurements time was about 10 min, and the corresponding temperature change was smaller than 4 K.

As can be seen in Fig. 5 the value of $\chi_{\min} = 2\%$ for the virgin crystal indicated its good crystalline perfection. The energy spectrum for the implanted sample exhibits continuous increase of the backscattering yield with implanted dose. Next the sample was warmed up to the room temperature. Only a small decrease of the channeling yield in the channel interval 140–200 can be noticed at 70 K. This is apparently due to the mobility of simple defects in the Ga sublattice. There are essentially no changes in the shape of the spectra up the temperature of 300 K.

2.2. Heavy Ion Bombardment

GaN single crystals were implanted with 150 keV Xe ions at 15 K to the fluence of 4.5×10^{14} Xe/cm². Fig. 6 shows the results of Xe-ion implantation. No changes in the damage peak (channels 360–400) were observed, whereas the low energy part of the spectrum continuously increased with increasing temperature. The constant area of the damage peak indicates that there are no defect transformations in the implanted region. The increase of dechanneling is attributed to the accumulation of defects produced by the analyzing beam.

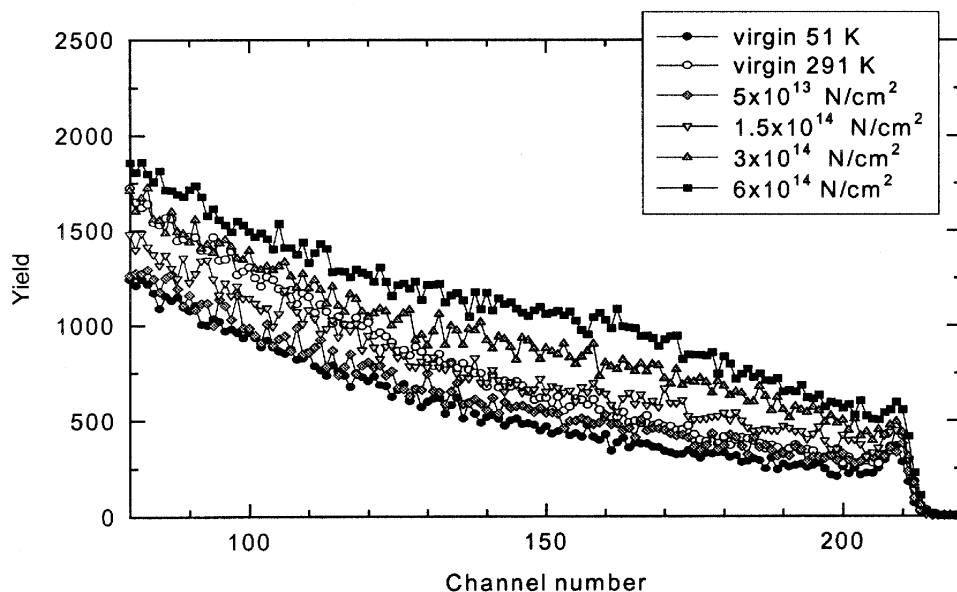


Fig. 5. $\langle 0001 \rangle$ aligned spectra for GaN single crystal before and after ion implantation with different doses of 150 keV N ions at 51 K.

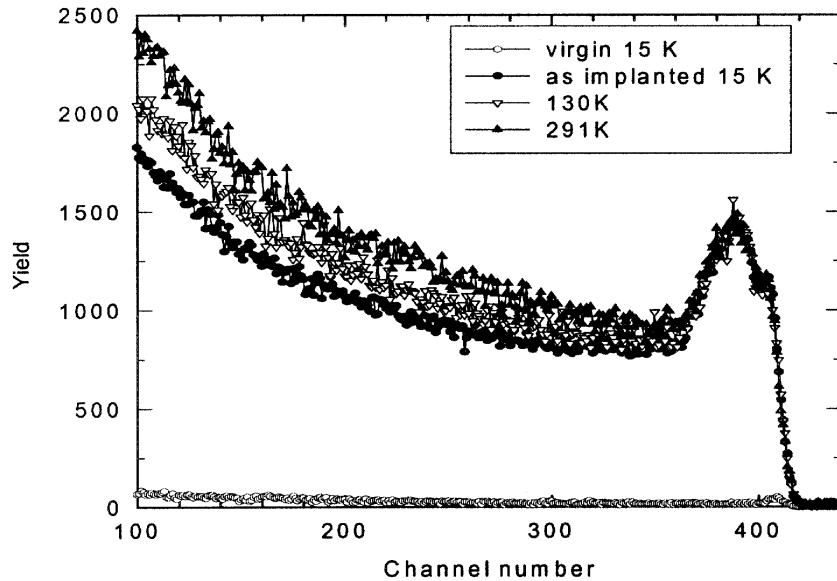


Fig. 6. The evolution of the spectra upon warming up to RT for GaN single crystal implanted with $4.5 \times 10^{14} \text{ Xe/cm}^2$ at 15 K.

Similar experiment was performed for GaN sample implanted with Te ions. The evolution of the spectra upon warming up to RT reveals only a small decrease of the damage peak at 70 K. The minimum was attained at 130 K and is apparently due to the simple defect mobility. Their further clustering leads to the subsequent increase of the damage peak.

2.3. Conclusions

Small recovery stage in N ion implanted GaN observed at 70 K reveals the mobility of simple defect i.e., selfinterstitials or vacancies belonging to the Ga sublattice. The fact that the major part of defects is stable up to RT can be attributed to important defect clustering occurring even at very low temperatures. It is well known that implanted noble gas atoms are very effective in trapping defects, especially vacancies. The stability of defects in Xe-ion bombarded GaN can also be due to defect clustering around Xe atoms. In contrast, such an effect has not been observed in GaN implanted with miscible elements like Te.

3. Ion Implantation in GaN at High Temperatures

3.1. Mg-ion Implantation

GaN epitaxial layers on sapphire were implanted with Mg-ions at three different energies and doses (30 keV- $2.8 \times 10^{14} \text{ Mg/cm}^2$, 80 keV- $7.0 \times 10^{14} \text{ Mg/cm}^2$, and 200 keV- $8 \times 10^{14} \text{ Mg/cm}^2$) in order to obtain uniform depth distributions of dopants and defects extending from the surface up to the depth of approx. 300 nm. Ion implantation was performed at RT, 600°C, 700°C, and 800°C. The aim of this study was to introduce the p-dopants into the GaN crystals in a manner that might ensure their high electrical activity. Since ion bombardment induced defects in GaN are very resistant to annealing it was thought that ion implantation at high temperatures can facilitate both crystal lattice recovery and lattice site incorporation of dopant atoms. The structure of as-grown and implanted epilayers was examined using the RBS/channeling. Fig. 7 shows the aligned spectra for GaN epilayers implanted at different temperatures.

The ion implantation at RT produces a clearly visible damage peak between channels 600 and 700. One notes strong decrease of damage peak and the dechanneling behind it after implantation at 800°C. In order to elucidate the residual defect structure the energy dependent dechanneling analysis was performed. Such measurements are based on the dechanneling cross section dependence on analyzing beam [2]. The variation of the channeling minimum yield χ_{\min} measured directly behind the damage peak as a function of the incident ^4He -ion energy is shown in Fig. 8.

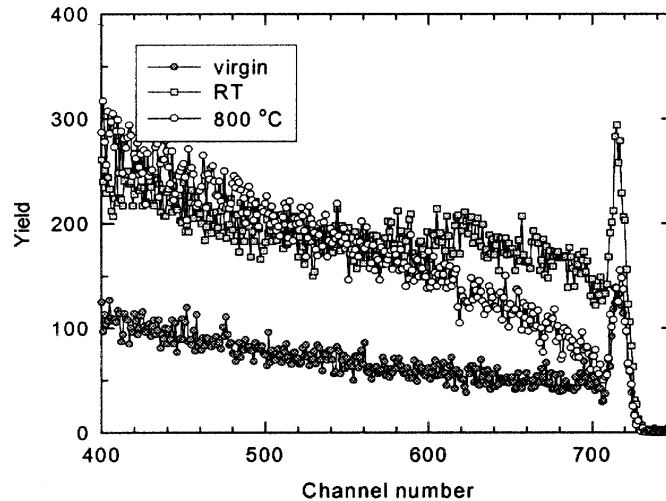


Fig. 7. Aligned spectra for virgin and ion implanted GaN epilayers subjected to Mg-ion implantation at different temperatures.

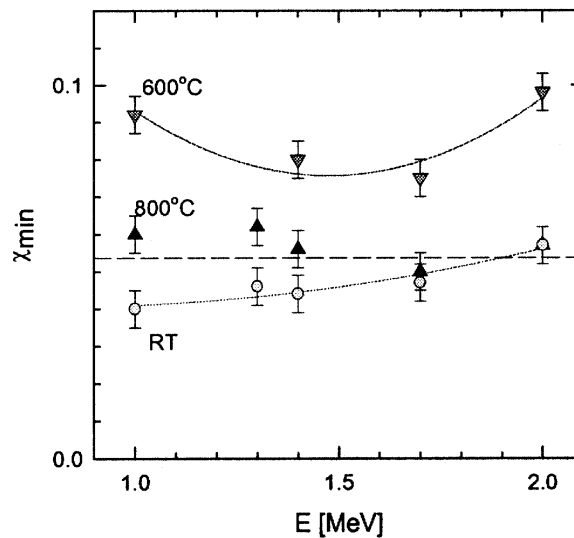


Fig. 8. Results of the energy dependent analysis of GaN epilayers implanted at different temperatures.

3.2. Conclusions

After RT implantation the small defect clusters of different size and morphology were formed. In the implanted region a non-uniform increase of the lattice parameter was observed due a rather large compressive strain produced by defects. The increased defect mobility during ion implantation at 600°C and 700°C resulted in the defect migration to the larger depths and enhanced defect clustering. Important changes were observed after implantation at 800°C. X ray diffraction revealed that defects produced at this temperature are to the high extent coherent with the host lattice. RBS/channeling analysis provided evidence that these defects are predominantly stacking faults.

4. Characterization of InGaN/GaN Heterostructures

4.1. Background

In last years, the InGaN/GaN heterostructures have attracted a great interest because of their application for the production of light emitting devices [9]. The extensive utilization of $\text{In}_x\text{Ga}_{1-x}\text{N}$ alloy as the active layer is principally due to the tunability of its energy gap. By changing its composition light spectrum from the red ($x=1$) to near ultraviolet ($x=0$) can be covered. In spite of the large efforts, the growth and properties of InGaN have not been completely optimized or understood yet. The difficulty of growing InGaN epitaxial layers on GaN substrates is principally caused by the large difference of lattice constant between these two materials of 11% [10]. It results in the large strain even in the layers of low In-concentrations. At higher In-concentrations two types of structural transformations are observed: phase separation and atomic ordering [11]. The observed phase separation is driven by the strain. To reduce the strain energy of the system In atoms are expelled from the InGaN lattice to form an alloy of different composition.

4.2. Results

InGaN alloy layers were grown by the MOCVD technique at a temperature of 800°C. Before the deposition of InGaN layers, a few μm thick GaN layers were grown on c-plane sapphire at a temperature of 1050°C. The thickness of InGaN layers varied from 30 nm to 110 nm and their composition ranged from $x = 0$ to $x = 0.12$.

Samples were characterized using RBS/channeling as the analytical method for the determination of principal properties of epitaxial layers, like: In-content, thickness, crystalline perfection, lattice distortion, and stress. 2 MeV ^4He -beam was applied. The detection angle was 165° and the energy resolution was 15 keV.

Fig. 9 shows the high-energy portions of random and aligned spectra for the InGaN/GaN heterostructure. The arrows indicate the scattering energy of Ga and In atoms at the surface. For InGaN layers of thickness not exceeding 120 nm the In peak is well separated from the Ga continuous spectrum. Since the height of the In peak is a measure of its content the flat top of the peak confirms the In uniform concentration in the layer. The aligned spectrum taken for a heterostructure of $x = 0.03$ revealed $\chi_{\min} = 2\%$ for Ga and $\chi_{\min} = 6\%$ for In indicating its reasonable crystalline quality as compared to $\chi_{\min} = 2\%$ for Ga in the GaN substrate. The χ_{\min} values for both elements increase with the In content as shown in Fig.10. The increase is linear as demonstrated by solid line in Fig.10 fitted to the data by the least square method. It has been observed that such linear dependence holds up to $x = 0.30$ (not shown in Fig.10). One notes the χ_{\min} for Ga is always lower than that for In although the difference between them changes rather accidentally.

In order to study the lattice distortion in the $\text{In}_x\text{Ga}_{1-x}\text{N}$ layer with $x = 0.09$ the angular scans were measured for different axes in the $(1\bar{2}10)$ plane. Fig.11 shows the angular scans measured for the principal $[0001]$ axis and $[10\bar{1}1]$ axis. Three windows were set: (i) — for Ga in the bulk, (ii) — for Ga in the layer, and (iii) for In in the layer. For the $[0001]$ axis all three dips have the same location of their minimum but slightly different critical angles: $\Theta_c = 0.74^\circ$ for Ga in the bulk and $\Theta_c = 0.80^\circ$ for Ga and In in the epilayer. Completely different behaviors exhibit the dips for the $[10\bar{1}1]$ axis. Both layer dips are significantly shallower but the In and Ga dips are shifted towards lower angles with respect to the bulk Ga dip. The negative value of $\Delta\Psi = \Psi_{\text{epi}} - \Psi_{\text{bulk}} = -0.35^\circ$ indicates the tetragonal distortion of the InGaN layer due to the tensile stress in the perpendicular direction.

The c/a ratio amounts to $\sqrt{3}/\tan \Psi_{\text{epi}} = 1.670$. Powell et al. [12] showed that for GaN epitaxial layer on sapphire $a_b = 0.3185$ nm. Assuming that the InGaN layer has not relaxed, i.e. $a_{\text{epi}} = a_b$, c amounts to 0.5244 nm. In order to calculate perpendicular $\epsilon^\perp = (c_{\text{epi}} - c_b)/c_b$ and parallel $\epsilon^\parallel = (a_{\text{epi}} - a_b)/a_b$ strains in the layer lattice constants of relaxed $\text{In}_x\text{Ga}_{1-x}\text{N}$ are necessary. The data for InN were taken from Paszkowicz [13] and $c_b = 0.52039$ nm and $a_b = 0.31994$ nm for $x = 0.09$ were calculated using Vegard's law. The deduced values are: perpendicular strain $\epsilon^\perp = 0.77\%$, and parallel strain $\epsilon^\parallel = -0.45\%$. These parameters indicate that the layer is under tensile stress in the perpendicular direction and under the compressive stress in the parallel one.

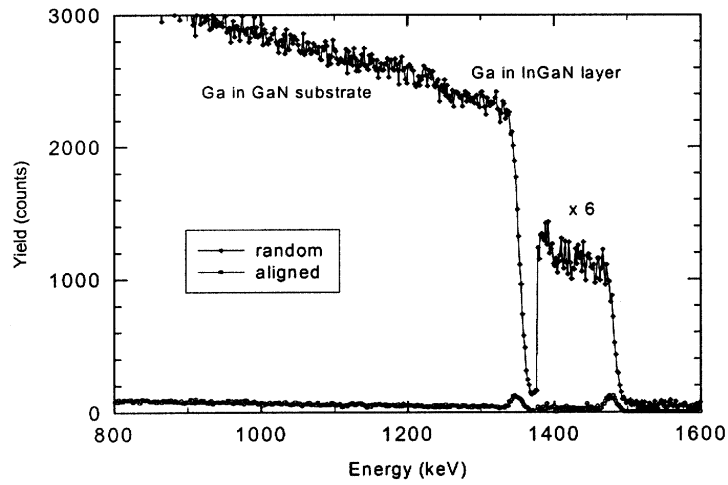


Fig. 9. Random and aligned spectra for InGaN/GaN heterostructure.

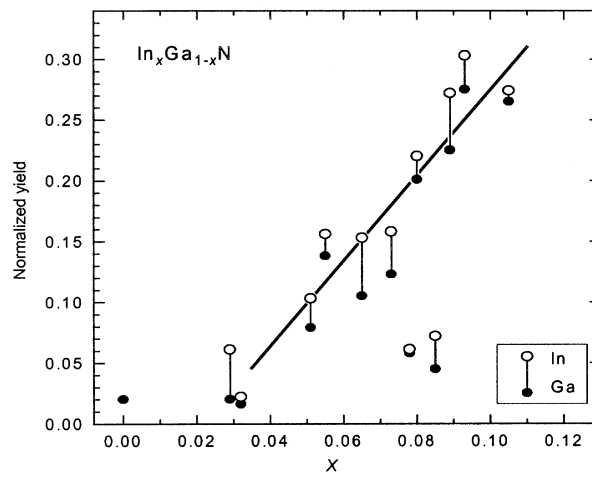


Fig. 10. Minimum channeling yields for In and Ga in the $In_xGa_{1-x}N$ epilayer as a function of x .

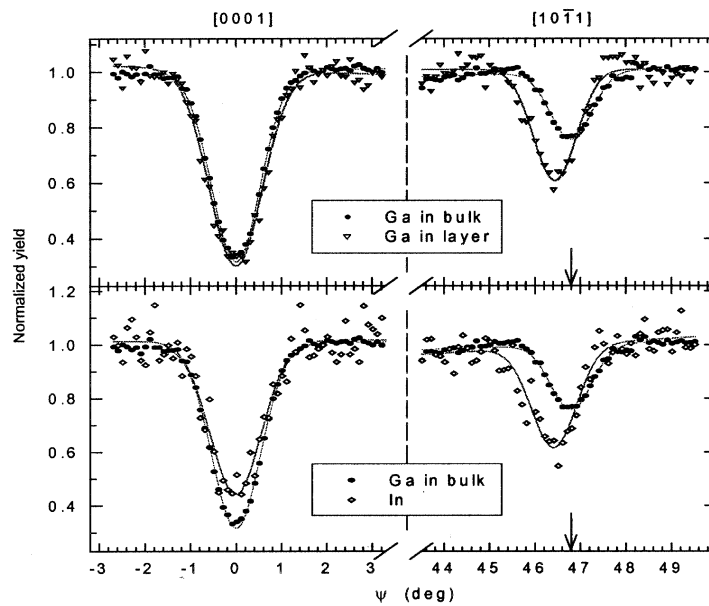


Fig. 11. Angular dips measured along the $(1\bar{2}10)$ plane for two different axes. The dips obtained for the bulk Ga were compared with dips measured for the epilayer for: In (a) and (b), and Ga (c) and (d), respectively.

4.3. Conclusions

The great advantage of RBS/channeling when applied to analysis of $\text{In}_x\text{G}_{1-x}\text{aN}$ layers with $0 < x < 0.15$ can be produced by MOCVD technique on GaN/sapphire is that it allows determination of variety of parameters. These are:

- In content in strained layers can be directly measured,
- magnitudes of tetragonal distortion and strain can be determined by measurement of angular scans across principal, i.e. normal to the surface axis and one of the other axes with low crystallographic indices,
- crystalline quality can be deduced from aligned spectra.

The last observation revealed continuous increase of χ_{\min} with x indicating In precipitation. Apparently raising stress caused by In oversaturation is a driving force for phase segregation. This hypothesis is also confirmed by the split of PL spectrum into two peaks as observed in some samples. It is generally accepted that phase segregation leads to the relaxation of strained epilayers, however, the value of 3.4 eV of PL peak energy for $x = 0$ [14] and channeling angular scans clearly indicate that the layers are still strained.

5. Monte Carlo Simulation of Channeling Spectra

Evaluation of channeling data measured at different temperatures requires consideration of several usually neglected factors. First of all, changes of thermal vibration amplitudes of crystal atoms have to be taken into account. Moreover, the III-N semiconductor compounds are rather sensitive to the He-ion bombardment, especially at low temperatures. Thus, the production of defects by the analyzing beam and their partial annealing upon warming up cannot be neglected. With this respect only the Monte Carlo simulations of channeling spectra can be successfully applied. Such simulations were performed using the computer code developed at SINS Warsaw. For calculations the crystal is divided into “slices” each of them containing one atomic plane. The particle trajectory is calculated as a binary collision with each sequential atom. Thermal vibrations of atoms are also included by randomly changing their position around the regular lattice positions. Moreover, the stopping power of channeled beam is impact parameter dependent and is calculated according to the modified Lindhard approximation [15]:

$$\varepsilon_{\text{ch}} = (1-\alpha) \varepsilon_{\text{R}} + \alpha \varepsilon_{\text{R}} n_{\text{e}}(r)/n_{\text{e}}$$

where: ε_{R} stopping cross section for random direction, $n_{\text{e}}(r)$ and n_{e} are local and average electron density. For perfectly channeled particles $\alpha=0.5$ whereas for the random direction $\alpha=0$.

The amplitudes of thermal vibrations for 300 K and 21 K were determined by fitting the aligned spectra shown in Fig.12 with our Monte Carlo simulation code. The thermal vibration amplitudes were considered equal for each component specie and amounted to $u_{21\text{K}} = 5.0$ pm and $u_{\text{RT}} = 6.7$ pm. These amplitudes were then used in simulations of implanted crystals.

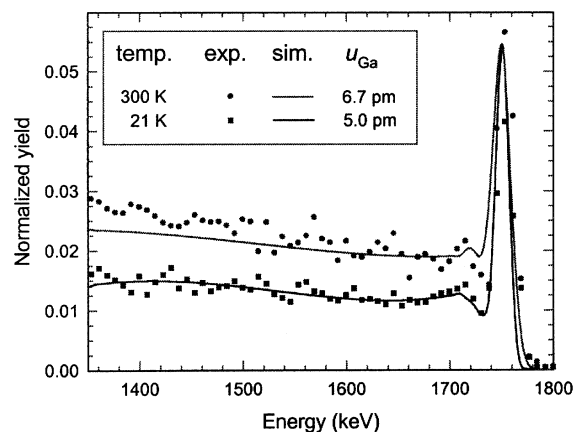


Fig. 12. Aligned spectra taken for the same GaN single crystal at two different temperatures.

Selfinterstitial atoms, vacancies and antisites are considered as simple defects in compound crystals. The contribution of the two last defects to the dechanneling yield is usually negligible. Since in this case σ_D can be calculated analytically [2] it seems that it would be the easiest task for the channeling analysis. However, the problems arise if the defect content is so high that a part of the aligned spectrum is close to the random one. The possible defect clustering and increasing influence of multiple scattering can make such an analysis unreliable.

A typical example of this kind analysis is illustrated in Fig. 13. The first MC calculations were performed using $\alpha = 0$ and somewhat surprisingly they fitted the experimental spectrum very well. Since the aligned spectrum exhibits very low damage level in the near surface region (1650–1450 keV) the use of α close to 0.5 seemed to be more appropriate. In spite of this presumption the spectrum calculated with $\alpha = 0.5$ is shifted to lower energies well behind the damage peak. The depth distribution calculated with $\alpha = 0$ fits well the defect distribution calculated with the TRIM code whereas that with $\alpha = 0.5$ is located significantly deeper. In addition, the defect distribution calculated using the two-beam approximation method (TBA) coincides well with that of TRIM. In order to check whether the TRIM estimates are correct the projected range of implanted hydrogen was measured using NRA. Accidentally the implanted H distribution almost overlaps with the MC defect profile calculated with $\alpha = 0.5$. Consequently, the real defect profile must be located at shallower depth.

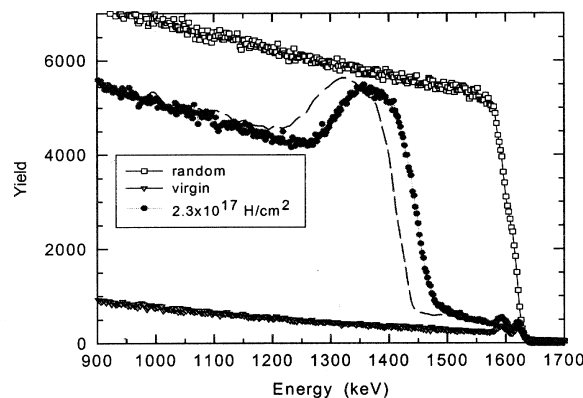


Fig. 13. Random and aligned spectra for GaAs single crystal implanted with $2.3 \times 10^{17} \text{ H/cm}^2$. The solid lines show the result of Monte Carlo simulations with $\alpha = 0$. The spectrum calculated with $\alpha = 0.5$ is shown by dotted line.

5.1. Conclusions

The Monte Carlo method for channeling spectra simulations enables not only detailed analysis of the perfection of the crystalline structure of analyzed samples but also can provide information on physical parameters difficult or even impossible to obtain using other experimental methods. This especially concerns the amplitudes of thermal vibration of lattice atoms. Monte Carlo evaluation of channeling spectra taken at different temperatures can be used for determination of such amplitudes and consequently of Debye temperature.

6. Hydrogen Implantation in GaAs

6.1. Background

The performance of semiconductor micro- and optoelectronic devices can be greatly enhanced if one can freely integrate different materials. An effective integration method has remained a challenge due to lattice constant mismatch between semiconductor systems. Heteroepitaxial growth of highly mismatched materials can result in layers containing large concentrations of defects, which degrade or inhibit device operation. Because of this limit of heteroepitaxial growth, a variety of methods of material joining techniques have been developed over the last decade [16]. One of the most elegant methods is direct wafer bonding technology. Bonding by Van der Waals forces occurs when two clean and smooth surfaces are placed in contact.

6.2. Results

Hydrogen ion implantation in (100) GaAs single crystals was performed at ITME Warsaw at temperatures ranging from 45°C to 160°C. Implantation energy was 50 keV and the doses ranged from 4×10^{16} H/cm² to 4×10^{17} H/cm². Depth distribution of hydrogen was measured using the $^{15}\text{N}(p,\alpha\gamma)^{12}\text{C}$ nuclear reaction at SUNY Albany, whereas, the 2 MeV ^4He -ion channeling was applied for defect analysis at SINS Warsaw. Surface morphology after hydrogen bombardment and thermal treatment leading to the surface layer exfoliation was studied by means of SEM (scanning electron microscopy) and optical microscopy. Surface roughness was determined by the Alphastep profilometer in terms of the roughness parameter Ra, i.e. the mean arithmetic value of the surface irregularities. Surface blistering occurs if the ion dose exceeds a given critical value, which in turn depends on the target temperature during implantation.

As shown in Fig.14, no surface defects induced by ion implantation at temperatures below 100°C were observed up to a highest used ion dose of 4×10^{17} H/cm². Blistering and flaking occur upon ion implantation at temperatures exceeding 100°C at ion doses already less than 1×10^{17} H/cm². The measured critical ion dose amounted to 9×10^{16} H/cm² at 140°C and decreased to 7×10^{16} H/cm² at 160°C. The increase of the ion dose over the critical value at a given temperature results in the increase of the amount of blisters and their dimensions. Variation of the surface roughness parameter, Ra, with the ion dose is shown in the inset in Fig.14. One notes that blisters grow more rapidly at higher temperatures.

Structural defect formation and transformation was studied by means of RBS/channeling. Fig. 15 shows spectra for H implantation at 45°C (curves 2,3,6) and at 140°C (curves 4,5). As can be seen, hydrogen implantation at 45°C produces damage peaks that increase with the increase of the ion dose. In all cases, even for the heavily damaged crystal implanted with 2.3×10^{17} H/cm² only simple defects and/or small amorphous clusters were detected [17]. This is in agreement with the observation that no detectable blisters or other forms of surface deformation were observed after low temperature hydrogen implantation up to the fluence of 4.0×10^{17} H/cm². Surprisingly, the damage peak for samples implanted at 140°C was significantly greater than that for samples implanted with the same dose at a lower temperature (cf. curves 2 and 3, and curves 4 and 5 in Fig. 15). One could expect the opposite effect because of the increased defect mobility at elevated temperatures leading to the enhanced defect recombination probability.

Results of the NRA analysis are shown in Fig.16. The concentration profile of hydrogen implanted with a dose of 6×10^{16} H/cm² was obviously not influenced by the implantation temperature (120°C) and post implantation annealing up to 300°C. Additionally, similar results were obtained for implantation carried out at 200°C or post implantation annealing at 400°C. Taking into account very good depth resolution of the NRA (approx. 10 nm) only short-range rearrangement of hydrogen atoms can occur at temperatures below 400°C.

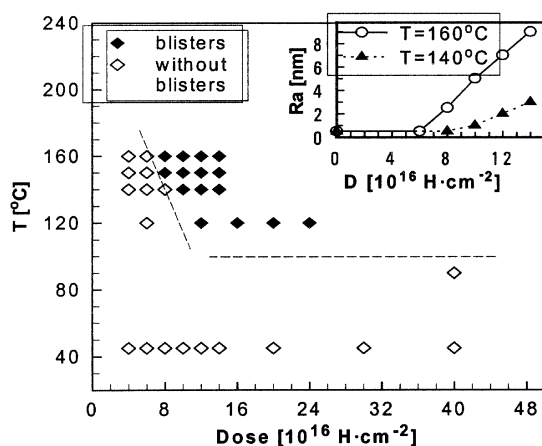


Fig. 14. Dose and temperature boundaries of blister formation in hydrogen implanted GaAs. The inset shows the roughness parameter dependence on the implanted hydrogen dose.

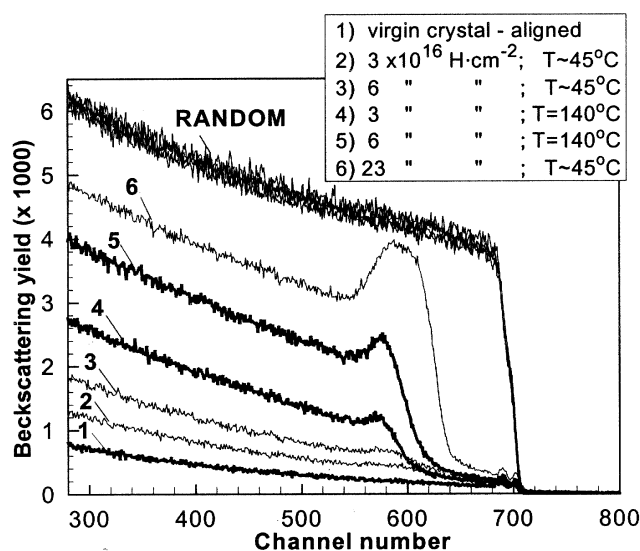


Fig. 15. Random and aligned RBS spectra for GaAs single crystals implanted with various hydrogen doses at two different temperatures.

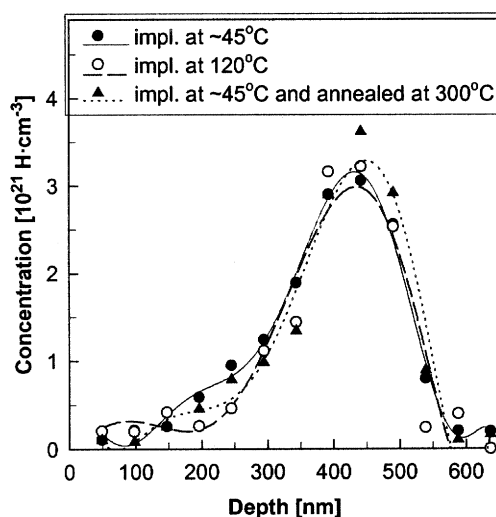


Fig. 16. Hydrogen concentration profiles for GaAs single crystals implanted with $6 \times 10^{16} \text{H/cm}^2$ at different temperatures as determined by the NRA analysis.

6.3. Conclusions

In the first part of the reported experiments, the conditions for blisters formation were investigated. Blistering is directly responsible for the formation of microcracks which in turn produce layer splitting. No blistering was observed at temperatures below 100°C even after implantation with a dose as large as $4 \times 10^{17} \text{H/cm}^2$. In order to provoke blistering in such samples an annealing at temperatures exceeding 400°C is necessary [18]. Blistering is much more easily obtained upon hot implantation. There are two distinct temperature regions: at temperatures below 90°C no blisters were found, whereas, at temperatures exceeding 120°C appreciably high blister density can be observed. In the second range the temperature at which blistering occurs depends on the implantation dose. The growth of blister dimensions with increasing implantation temperature is reflected in the rapid increase of surface roughness.

The complementary investigations of defect behavior and hydrogen depth distributions gave some insight into the mechanism of blister formation. The important conclusion from the NRA

analysis is that the hydrogen concentration profile is altered neither upon hot implantation nor upon annealing at temperatures at least not exceeding 300°C. Thus, at these conditions, the distance of hydrogen atom migration most probably does not exceed a few nanometers. According to Rauhala and Räsänen [18] the maximum damage distribution is located at the same depth as that of the hydrogen atom distribution. This was confirmed by our RBS/channeling measurements. Moreover, the detailed study of the damage structure [19] revealed that after RT implantation only displaced atoms and/or small amorphous clusters are formed. The substantial increase of the damage peak after hydrogen implantation at temperatures above 140°C as compared to that measured for the sample implanted with the same dose at 45°C is somewhat unusual. One could expect the opposite effect, i.e. a decrease of the damage peak due to greater defect mobility. It is worth pointing out that at this temperature only defects in the Ga sublattice are mobile in GaAs, whereas, defect mobility threshold for As sublattice lies above 300°C [20]. Thus, important defect transformations cannot be expected in the studied temperature range. Furthermore, the study of hydrogen diffusion in GaAs [21] clearly indicated that hydrogen mobility is largely suppressed by the presence of radiation damage. All these factors lead to the conclusion that the unusual increase of damage peaks in channeling spectra for samples implanted at 140°C is due to the formation of hydrogen-defect complexes in which matrix atoms become displaced from their lattice sites. One notes, that according to the data shown in Fig.14 at the applied doses no blisters are formed. Since gas bubbles and voids have relatively low dechanneling cross-sections such defects cannot be the dominant kind of defect. Therefore, the observed hydrogen-defect complexes of different morphology containing multiple hydrogen atoms bounded to displaced matrix atoms can be considered as precursors of the hydrogen bubble and eventually blister formation. They are effective traps for mobile hydrogen atoms and stabilize the radiation damage produced by ion implantation. The prerequisite of such complex formation is high enough hydrogen concentration. Their formation is thermally activated: small complexes can only coalesce if the implantation temperature exceeds 120°C or after annealing at temperatures above 400°C.

6.4. *Hydrogen Content Analysis in GaN*

GaN single crystals and epilayers are usually produced as a n-type. This is apparently due to the easy formation of N vacancies during the growth. The p-type GaN, which is necessary for the formation of p-n junctions, is difficult to obtain. This is most probably due to the incorporation of large quantities of hydrogen atoms already during the growth process. Hydrogen is known to passivate the p dopants leading to reduction of their electrical activity. Hydrogen content in GaN was measured by means the ERD (M.Budnar) and the NRA (W.Lanford and FZ Rossendorf) techniques. The obtained results can be summarized as follows:

- single crystals contain in the average less than 0.1 at% of H, which is below the detection limit of both methods,
- thin foils and sintered powders contained between 0.5 to 5 at% of H depending on the growth conditions, however, no direct correlation was observed,
- extensive H outdiffusion was observed at the beginning of the analysis indicating release of hydrogen atoms from the outermost layers. After this initial period the reaction yield has stabilized.

REFERENCES

- [1] DOOLITTLE, L.R., Nucl. Instr. and Meth. **B9** (1985), 344.
- [2] FELDMAN, L.C., MEYER, J.W., PICRAUX, S.T., Materials Analysis by Ion Channeling (Academic Press, New York, 1982).
- [3] ZIEGLER, J.F.,BIERSACK, J.P, LITTMARK, U. The stopping and Range of Ions in Solids, vol.1 (Pergamon Press, New York, 1985).
- [4] Kabayashi, H., Gibson, W. M., Appl. Phys. Lett. **73** (1998) 1406.
- [5] LIMMER, W., RITTER, W., SAUER, R., MENSCHING, B., LIU, C., RAUSCHENBACH B., Appl. Phys. Lett. **72** (1998) 2589.

- [6] LIU, C., MENSCHING, B., ZEITLER, M., VOLZ, K., RAUSCHENBACH, B., Phys. Rev. **B57** (1998) 2530.
- [7] MIYACHI, M., TANAKA, T., KIMURA, Y., OTA H., Appl. Phys. Lett. **72** (1998) 1101.
- [8] PONG , B.J., PAN, C.J., TENG, Y.C., CHI, G.C., LI, W.-H., LEE, K.C., J. Appl. Phys. **83** (1998) 5992.
- [9] NAKAMURA, S., SENOH, M., NAGAHAMA, S., IWASA, N., YAMADA, T., MATSUSHITA, T., KIYOKU, H., SUGIMOTO, Y., KOZAKI, T., UMEMOTO, H., SANNO, M., CHOCHO, K., Appl.Phys.Lett., **72** (1998) 211.
- [10] MATSUOKA, T., SASAKI, T., KATSUI, A., Optoelectron., **5** (1990) 53.
- [11] DOPPALAPUDI, D., BASU, S.N., LUDWIG, K.F., MOUSTAKAS, D., J.Appl.Phys., **84**(1998)1389.
- [12] POWELL, R.C., LEE, N.-E., KIM, Y.-W., GREENE, J.E., J.Appl.Phys., **73** (1993) 189.
- [13] PASZKOWICZ, W., Phil.Mag. **A 79** (1998) 1145.
- [14] MCCLUSKEY, M.D., VAN DE WALLE, C.G., MASTER, C.P., ROMANO, L.T., JOHNSON, N.M., Appl.Phys.Lett., **73** (1998) 2725.
- [15] LINDHARD, J, J.Mat.Fys.Medd.Dan.Vid.Selsk. **34** (1965) nr.14.
- [16] BRUEL, M., Electronics Lett. **31** (1995) 1201–1202.
- [17] JALGUEIER, E., ASPAR, B., POCAS, S., MICHAUD, J. F., ZUSSY, M., PAPON, A. M., BRUEL, M., Electronics Lett. **34** (1998) 408–409.
- [18] RAUHALA, E., RÄISÄNEN, J., Nucl.Instr. and Meth. **B94** (1994) 245–250.
- [19] STONERT, A., TUROS, A., NOWICKI, L., BREEGER, B., Nucl.Instr. and Meth. **B161-163** (2000) 496–500.
- [20] TUROS, A., STONERT, A., BREEGER, B., WENDLER, E., WESCH, W., FROMKNECHT, R., Nucl.Instr.and Meth. **B148** (1999) 401–405.
- [21] RÄISÄNEN, J., KEINONEN, J., KARTTUNEN, V., KOPONEN, I., J.Appl. Phys. **64** (1998) 2334–2336.

STUDY OF IMPURITY MIGRATION PROCESSES IN SEMICONDUCTORS USING THE RBS, NRA AND ERD TECHNIQUES

L.P. CHERNENKO, A.JU. DIDYK, A.P. KOBZEV, O.A. NIKONOV, V.A. SKURATOV
Joint Institute for Nuclear Research,
Dubna, Russian Federation

M. KULIK, D. MACZKA
Institute of Physics, Maria Curie-Sklodowska University,
Lublin, Poland

Abstract

This report contains the results of investigations done on different samples by the RBS, NRA and ERD techniques to solve a number of problems in different fields of materials science. The elemental depth profiles of silicon samples with a Ta covering layer irradiated with fast Kr ions are studied. The migration of Ta atoms in the Si sample was observed after posterior annealing. Possibilities to create oxygen-enriched layers on the surface of a GaAs single crystal are investigated by implantation of In ions. A ten times increase in oxygen atoms content is observed in the transparent surface layer. The contents of the basic and impurity elements are determined for 6 samples of a LiNbO₃ single crystal. Incorporation of hydrogen into a LiNbO₃ single crystal for different orientations of the crystal axis is studied. The X-cut direction appears preferable in comparison with the Z-cut direction. The interdiffusion process between the Si and Ge layers in a Si/Ge amorphous superlattice structure is studied. In addition, the existence of an oxygen impurity in the layers and a thin SiO₂ layer on the substrate surface is revealed. The limiting experimental depth resolution of the RBS method is evaluated using high-grade multilayer samples.

1. Introduction

During the last three years, various investigations were fulfilled by using the ion beams of the EG-5 accelerator of the Frank Laboratory of Neutron Physics under the auspices of the Co-ordinated Research Programme F1.20.11 "Application of MeV Ion Beams for Development and Characterisation of Semiconductors Materials". The experiments were carried out in the following fields:

1. Study of impurity migration induced by fast heavy ion irradiation. The RBS and NRA methods are applied.
2. RBS and NRA investigations of oxygen contents in the surface layer of a GaAs single crystal implanted with In ions applying RBS and NRA methods.
3. Study of hydrogen and oxygen contents in LiNbO₃ crystals at various orientations of the crystal axis.
4. RBS and NRA investigations of element depth profiles in a multilayer Si/Ge structure.
5. Determination of the depth resolution limit in experimental conditions of the RBS method using layered ⁵²Cr/⁵⁷Fe structures.

In recent years, continuous efforts have been undertaken to achieve a better understanding of damage production in various materials by fast heavy ions. Most intensely investigated are oxides [1]. Recently, a phenomenological description of latent track formation was given for dielectrics and semiconductors [2], and for magnetic insulators [3]. Metals have been considered for a long time as not showing any track formation process. Semiconductors, however, seem to have received less attention. Only a few articles presented experimental results in semiconductors irradiated by high energy heavy ions (see, for example refs. [4–6]). Another study attempted to systematically examine the migration of electrically active impurities into silicon. Different techniques, such as RBS, NRA, ERD, and SIMS, are used to study the impurity migration in silicon.

During the last decade, the development of the multilayer electronic systems' technology utilized as laser junctions has caused an increasing interest in studying the existence of layers enriched with oxygen in A_3B_5 compounds. For these materials, particularly for GaAs and InAs, experiments about the creation of stable chemical compounds on their surface are very important [7]. Most works are concerned with determination of external agents, such as ion implantation or light irradiation, which influence the oxidation process in the surface layers [8–10].

Non-destructive RBS and NRA techniques were applied to study depth profiles of dopands in GaAs implanted with In. Changes of optical parameters (refractive index and extinction coefficient) for two annealing temperatures were studied by the ellipsometric method for one wavelength.

Lithium niobate ($LiNbO_3$) based optical waveguides are considered to be an outstanding material for construction of sophisticated optoelectronics structures. One of the most promising techniques for the fabrication of such waveguides is annealed proton exchange (APE). A large increase of an extraordinary refractive index and a slight decrease of an ordinary refractive index following the APE process together with a large value of the electrooptical coefficient make the guides suitable for application in dynamical integrated optical components. Moreover, after the doping of the material with laser active elements, the waveguides can be used as planar optical amplifiers and waveguide lasers.

The APE waveguides have already been introduced into practical use. However, there are still several fundamental issues, which have not been yet entirely solved. One of them is the problem of the relation between the composition of waveguiding layers and their optical and electrooptical properties.

Synthetic compositionally modulated materials, such as Si/Ge multilayers, are not equilibrium structures. In particular, they have high interfacial gradients and for sufficient atomic mobility changes in the composition profile are expected to occur. The mechanism of their diffusion homogenization is still indefinite. First of all, the diffusion asymmetry (manifested in strong concentration dependence of interdiffusion coefficients) and strong porosity formation during diffusion mixing are the most important factors indicating the need of a better understanding of the above-mentioned process. Stability of the material, its resistance to composition changes is obviously of importance for practical applications.

Possibilities of the RBS technique to resolve thin layers are discussed in [11,12]. The need of turning back to this problem is due to development of manufacturing technologies of thin layered structures. The RBS technique is an effective tool of non-destructive testing of the content and structure of the near-surface layers. Thin-layer structures allow best realization of the advantages of the RBS technique in the depth resolution because the influence of straggling on the achieved resolution is the smallest. Most interesting, in this respect, are the experimental results obtained for high-grade thin-layer samples consisting of mid-atomic weight elements.

2. Experimental

The RBS and NRA techniques were developed at the EG-5 accelerator in the Frank Laboratory of Neutron Physics of the Joint Institute for Nuclear Research. The EG-5 accelerator produces proton and 4He ion beams in the energy range of 0.7 – 3.5 MeV with the energy spread less than 0.5 keV. The beam energy is controlled with an accuracy of 1–2 keV.

The vacuum chamber for the RBS, NRA and ERD methods was positioned on the number 3 beam line of the EG-5 accelerator. The targets were mounted on a 4-position holder in the vacuum chamber. The angle of their surface with respect to the beam direction can be varied from 0° to 90° without opening the chamber. During the experiment, the vacuum in the target chamber was maintained at a pressure of 10^{-4} Pa with a sublimation pump. The spectra of scattered ions were measured at the angles 135° and 170° . The spectra of recoiled protons were measured at the angle 30° .

A charged particle spectrometer was set to reach the best energy resolution close to the principle limit due to fundamental fluctuations in nuclear elastic scattering and the ionisation process. Thus, an energy resolution of 10 keV is obtained for 5.5 MeV α -particles. The aperture in front of the detector is 4.4 mm in diameter. The processing of the experimental spectra was performed using the computer code DVBS [13].

3. Results

3.1. Impurity migration into silicon under the influence of fast heavy ion irradiation

In the first part of this report, we present the results in the field of radiation stimulated impurity migration in silicon with deposited layers of some impurities (Pd, Ta, and Fe). The samples of silicon single crystals were covered with thin layers of Ta (Pd, Fe). The thicknesses of the silicon substrate and Ta layer were 300 μm , and 165 nm, respectively. The samples were irradiated with 210 MeV Kr ions with the fluence $F_t = 3 \cdot 10^{13}$ ions/cm² and then annealed in vacuum at the temperature of 700°C for one hour. A RBS analysis of irradiated and nonirradiated samples was performed.

Fig. 1. shows the energy spectra for 2.4 MeV $^4\text{He}^+$ ions scattered at the angle 170° for both irradiated and nonirradiated samples of silicon covered with Ta. One can see a big difference between the curves. Processing these spectra, we have obtained the depth profiles for Ta, Si, and O. It can be seen from Fig.2. that after annealing and irradiation (IA), the thickness of the layer containing Ta and O atoms is about 520 nm, and only 350 nm and 230 nm, respectively, for the annealed but nonirradiated sample (A). The increasing migration of Ta and O atoms in the sample irradiated with Kr ions can be attributed to a so called "track structure" (a destructive zone along the projected ranges of Kr ions).

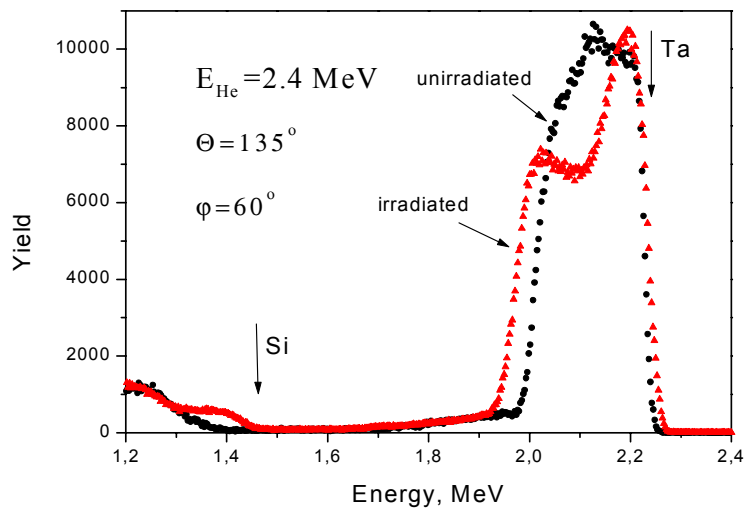


Fig. 1. The RBS spectra of Si samples covered with Bi and irradiated and not irradiated with fast Kr ions.

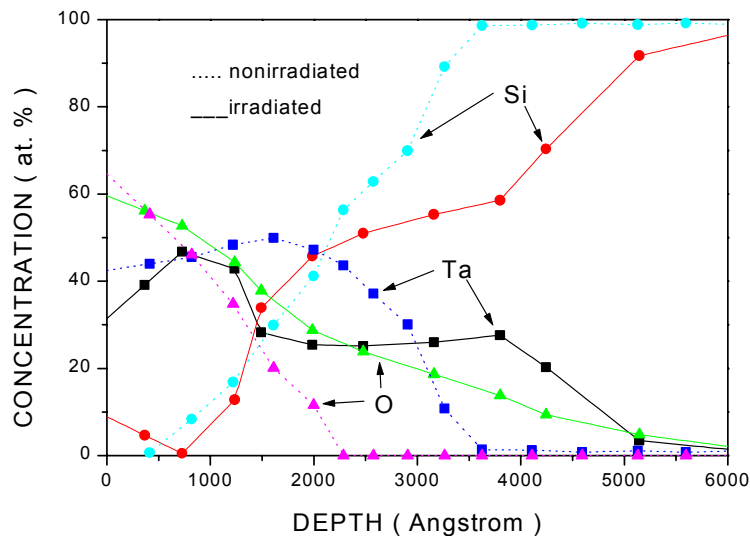


Fig. 2. The depth profiles for all elements of the irradiated and nonirradiated Si samples covered with Ta.

The integration of the Fick equation for diffusion leads to the following solution for the impurity profile after annealing:

$$C(x,t) = Q/(\pi Dt)^{1/2} \exp(-x^2/(4Dt)) \quad (1)$$

where Q is the remaining amount of atoms per area unit measured after annealing, D is the diffusion coefficient, and t is the annealing time. One can make estimations of the squares under the concentration curves for Ta atoms (A and IA) using the following expression:

$$C_{\text{tot}} = n \int C(x,t) dx \quad (2)$$

where n is the atomic density in atoms per cm³. Comparing C_{tot} with the initial quantity of Ta atoms on the silicon surface without annealing and irradiation, we can conclude that in all these cases the quantity of Ta atoms is the same. This fact proves the obtained experimental data.

A satisfactory fit of the experimental profiles of O atoms for both A and IA cases and of Ta atoms in the case A can be carried out. One can also use expression (1) for the Ta concentration curve in the IA case but with a significant error due to the depth region from 150 to 375 nm, where the Ta concentration is almost constant. The following values of the adjustable parameters for the diffusion of oxygen atoms D_{IA}^O, D_A^O, and Ta atoms, D_{IA}^{Ta}, D_A^{Ta} have been found:

$$\begin{aligned} D_{\text{IA}}^{\text{O}} &\cong 6.3 * 10^{-14} \text{ cm}^2/\text{s} \text{ and } D_{\text{A}}^{\text{O}} \cong 1.5 * 10^{-14} \text{ cm}^2/\text{s} \\ D_{\text{IA}}^{\text{Ta}} &\cong 6.8 * 10^{-14} \text{ cm}^2/\text{s} \text{ and } D_{\text{A}}^{\text{Ta}} \cong 1.5 * 10^{-14} \text{ cm}^2/\text{s}. \end{aligned}$$

There is a big difference between the diffusion coefficients in the cases A and IA. This fact allows us to conclude that the migration rate of impurities in the samples irradiated with fast heavy ions is greater than that in nonirradiated ones.

In [2], the Kr ion track diameter in silicon was calculated, R_{tr} = 5.7 Å. The calculation of the relative total square of the damaged area was performed in a simple way:

$$\Delta S/S = Ft \pi R^2 = 0.306 \quad (3)$$

If the migration of the impurities takes place through the ion tracks, the migration coefficient D_{IA} should be reduced for the appropriate area (see Eq.(3)).

The irradiation of silicon with 210 MeV Kr ions caused heavy ion track formation in the area with the diameter 2R_{tr} and a density lower than that of the undamaged material. Thus, the impurity atoms can diffuse easier along the projected range of Kr ions in the area with the reduced density.

Analogous investigations have been carried out for silicon covered with Fe and Pd. The differences between the depth profiles of these elements for the irradiated and nonirradiated samples have not been found by the RBS method. Some of the above mentioned experiments have been published in [14,15,16].

3.2. Oxygen contents in the surface layer of a GaAs single crystal implanted with In ions

The determination of the depth profiles of oxygen atoms in the investigated samples was carried out using the ¹⁶O(α,α)¹⁶O nuclear reaction that has a very narrow and a quite intensive resonance at the energy 3.045 MeV. As it can be clearly seen in Fig. 3, for this incident energy the resonance is just in the surface layer. Thus, we have quite a high yield of ⁴He ions scattered by oxygen atoms. For each sample some spectra were measured in the energy region from 3.03 MeV to 3.07 MeV with a step of 5 keV.

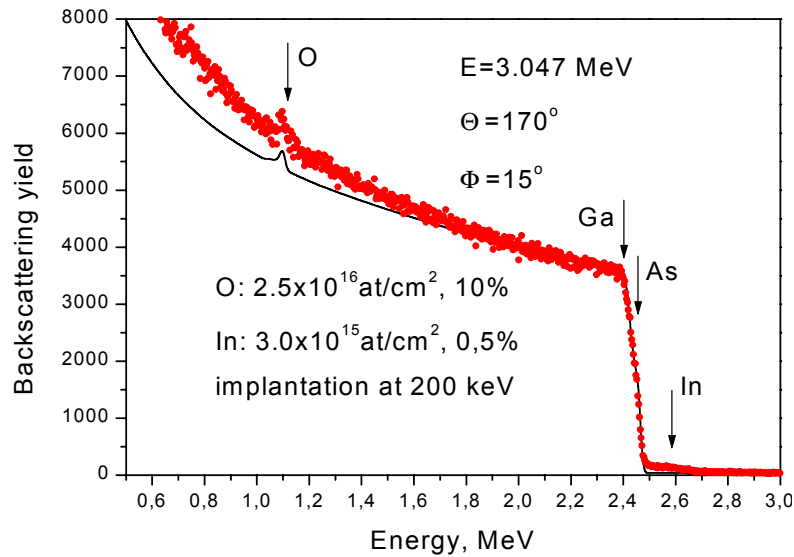


Fig. 3. The backscattering spectrum for the sample implanted and annealed at 800°C.

The concentration depth profiles of all elements for the sample implanted and annealed at the temperature 800°C have been obtained. The concentration of In atoms on the surface reaches 0.3% and decreases to zero at the depth $4.29 \times 10^{17} \text{ cm}^{-2}$. The atomic concentration of oxygen has a maximum value of 30% on the surface and it drops to zero at the same depth.

The refractive index n_s and the absorption coefficient k_s of the substrate as well as the refractive index n_{ox} of the native oxide layer increased after the implantation of the samples with In ions. However, posterior annealing almost restored the optical properties of the substrate but the refractive index of the native oxide layer did not change after annealing, though its thickness increased.

The depth profiles of all elements in the implanted but unannealed sample have been obtained also. The depth profile of In atoms is almost equal to that in the above mentioned sample, but $5 \times 10^{15} \text{ cm}^{-2}$ oxygen atoms there are in it only and they occupy the surface layer of $2.7 \times 10^{16} \text{ cm}^{-2}$ depth. An equal number of oxygen atoms, within the experimental errors, are in the surface layer of the virgin (unimplanted and unannealed) sample.

TABLE 1. THE THICKNESS OF NATIVE OXIDE LAYERS IN nm

| Exposition in air | GaAs unimplanted | | | GaAs implanted | | |
|----------------------|------------------|-----------|------|----------------|-----------|------|
| | Before RTA | After RTA | | Before RTA | After RTA | |
| | | 600° | 800° | | 600° | 800° |
| Initial | 4.5 | 5.0 | 5.1 | 4.7 | 4.8 | 4.8 |
| After year | 4.4 | 5.0 | 5.0 | 5.1 | 6.5 | 7.2 |

The RBS estimated thickness of the surface layer containing In atoms is about 90 nm immediately before and after RTA. This result agrees with the calculation performed by the computer simulation code TRIM which gives for the extrapolated range of In ions $R_p=62.0 \text{ nm}$, $dR_p= 26.9 \text{ nm}$. Also, it means that the In depth distribution does not change essentially during the diffusion of oxygen atoms.

As a result local stresses occur as confirmed by the measurement of Raman spectra [17]. It may be also a reason why the optical properties haven't been restored fully after annealing. The presence of the restored but not fully ordered structure of the doped crystal is a suitable material into which oxygen can diffuse from the air.

Therefore, we can conclude, that In ion implantation and posterior annealing at temperature higher than 600°C, result in a ten times increase in the oxygen atom content occurs and the thickness of the transporence layer covering the surface of the implanted GaAs single crystal also increases [18].

3.3. Element analysis of lithium niobat doped with hydrogen

The next topic is an element analysis of lithium niobate (LiNbO₃) modified using annealed proton exchange (APE). The virgin and doped with hydrogen samples are prepared by Dr. J. Hradilova-Spirkova in the Institute of Chemical Technology (Prague, Czech Republic).

Six samples (3 X-cut and 3 Z-cut) were investigated by the RBS, NRA and ERD techniques. Figure 4 shows the ERD spectra for a virgin (standard-X) and a hydrogen enriched sample (367 X). In these cases, in order to determine the hydrogen concentration, 2336 keV ⁴He ions were used to bombard the target and the recoiled protons were registered after passing throw Al-filter. The 367 X sample contains about 20% hydrogen atoms and there are the rather high yield of recoiled protons but hydrogen atoms are located at the surface of virgin sample (standard-X), and less than 1% hydrogen atoms there are in itself virgin sample.

Fig. 5 shows the spectrum of 1.745 MeV protons scattered by 368 X samples. The scattering of protons allows to measure oxygen concentration at the depth up to 10 mkm, because the protons have a lower energy losses then α -particles. As it is seen, the oxygen as well as niobium concentration doesn't change upon the depth. A some pike due to the carbon growth at the surface of the sample during the exposition presents at the spectrum. This layer contains 5.6×10^{16} at/cm² of carbon. It is well seen because a wide resonance there is in reaction ¹²C(p,p)¹²C at the energy of 1.726 MeV.

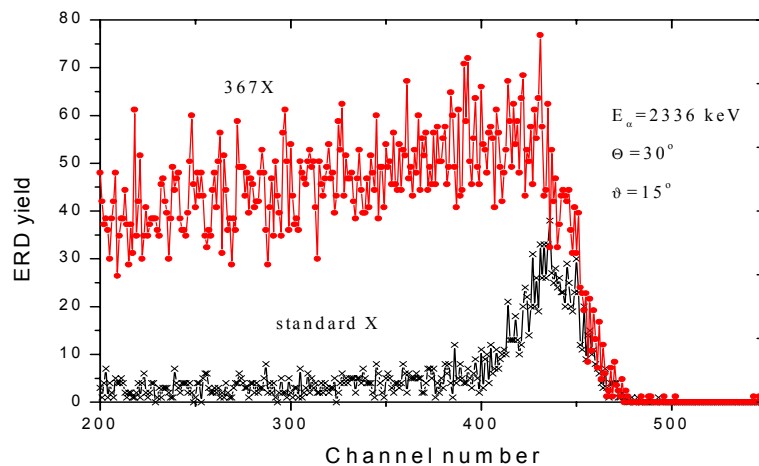


Fig.4. Spectra of recoiled protons after a bombardment by 2.336 MeV ions of 367X and standard-X samples.

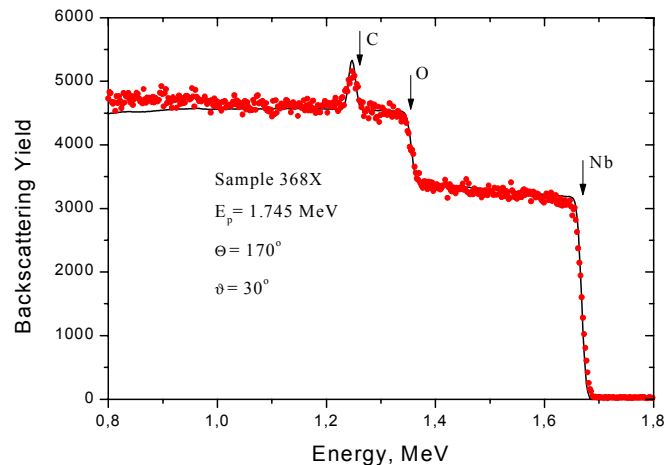


Fig.5. Experimental (points) and calculated (line) spectra of protons backscattered by a 368X sample.

TABLE 2. THE ELEMENT CONCENTRATION FOR X-CUT AND Z-CUT LITHIUM NIOBATE CRYSTALS.

| Sample | Concentration, at.% | | | |
|------------|---------------------|----|----|----|
| | Nb | O | Li | H |
| 367X | 16 | 48 | 16 | 20 |
| 368X | 19 | 54 | 19 | 8 |
| Standard X | 20 | 59 | 20 | 1 |
| 385Z | 20 | 53 | 20 | 7 |
| 382Z | 15 | 45 | 15 | 25 |
| Standard Z | 20 | 60 | 20 | 0 |

Table 2 shows the concentrations of all elements for 6 samples what have been measured. Concentration of Li atoms can't be determined neither by RBS nor ERD methods, and this values, showed in the table, were used for the calculation of effective energy losses of protons for every sample. So, the ratio C_O/C_{Nb} remains quite unchanged for all the samples and it is about 3. These results confirmed hypotheses, that the X-cuts are better attainable for incorporation of foreign particles into the lithium niobate structure. The explanation for that may be access to a cleavage plane, that is a plane of vacant octahedrons. That access is than better in the X-cut comparing with the Z-cut, which are oriented perpendicularly to the three-fold axes.

This research has been fulfilled in accordance with the decisions of the First Co-ordination Meeting.

3.4. Element depth profiling of multilayer Si/Ge structure

This part of the report is devoted to the studying of interdiffusion of amorphous Si/Ge multilayer structures. Dr. A. Kiss from the Institute of Nuclear Research Hungarian Academy of Science (Debrecen, Hungary) has prepared the samples for analysis.

The element depth profiling in the Si/Ge multilayer structure has been performed by the RBS and NRA methods. The determination of the depth profiles of oxygen atoms in the investigated samples was carried out using the $^{16}\text{O}(\alpha,\alpha)^{16}\text{O}$ nuclear reaction. Ten spectra were measured in the energy region from 3.04 MeV to 3.112 MeV with the step of 10 keV. The angles of the incident beam with respect to the surface of the samples φ were 10° and 6° .

One of the spectra is shown at Fig. 6. All silicon and germanium layer are seen at the spectrum as the peaks. But the depth resolution is worse for deeper layers due to the straggling effect. An experimental spectrum agrees with calculated one in all details with the good precision. Moreover only one model of the multilayer structure has been used in order to describe all experimental spectra obtained for difference energies.

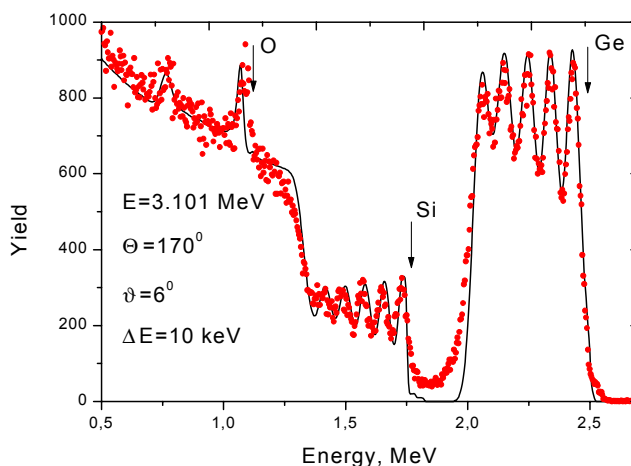


Fig.6. Experimental (points) and calculated (line) spectra of 3.045 MeV ^4He ions scattered at 170° from Si/Ge multilayer structure.

A layered structure with the degraded interfaces is observed. All layers contain some oxygen impurity (10–13%), and there is SiO₂ layer with the thickness 177 Å situated between the multilayer structure and Si wafer. Full thickness of Ge-layers is about 130 Å and full thickness of Si-layers is about 231 Å including the mixed layers with the thickness 64.7 Å. So, a complete structure of the sample has been reconstructed by undamaged technique.

3.5. Determination of the depth resolution limit of the RBS method applying the high grade ⁵²Cr/⁵⁷Fe thin layer structures

The depth resolution of the RBS technique is determined by a well known expression, i.e.

$$\delta x = \delta E / [K \frac{S_{in}}{\cos \vartheta_1} + \frac{S_{out}}{\cos \vartheta_2}] \quad (4)$$

where δE is the energy resolution of the method; K is the kinematic factor, which depends on the mass of the incident particle M_1 , mass of scattered particle M_2 and the scattering angle Θ as:

$$K = \left(\frac{\sqrt{M_2^2 - M_1^2 \sin^2 \Theta} + M_1 \cos \Theta}{M_2 - M_1} \right)^2 \quad (5)$$

S_{in} and S_{out} are the energy loss factors along the inward and outward paths of the scattered particle, respectively; ϑ_1 and ϑ_2 are the angles between the sample normal and the direction of the incident beam and of the scattered particle respectively.

The energy resolution of the RBS technique is determined by the energy resolution of the detector, energy spread of the incident beam and the scattering geometry. In general, the energy resolution of silicon planar detectors is limited by fundamental causes [19] up to 8 keV for 5.5 MeV α -particles. The energy spread of the beam does not exceed 500 eV for Van de Graaff-type accelerators. However an imperfect design of the beam collimator increases the energy spread at the edge of aperture due to beam scattering. The scattering geometry influences the resolution in various ways. First of all, the solid angle of the detector occupies some region of scattering angles and this increases the kinematic factor spread in accordance with eq.(5). Some change in the kinematic factor due to finite dimension of the beam spot takes place as well. It is evident that for glancing incidence the dimension of the beam spot increases exactly in the scattering plane as $d/\cos\vartheta_1$. By the way, in the case of normal incidence (scattering angle 170°, solid angle 0.002 sr, beam diameter 1mm) it is possible to neglect the influence of the scattering geometry in comparison with the detector resolution. However the geometry contribution appears important in the case of glancing incidence. At the same time, the decreasing of the beam diameter results in a decrease of the beam spot, but the energy spread increases due to scattering at the edge of the aperture.

On the other hand, it is clear from eq.(4) that the inward and outward pathways increase essentially for glancing incidence of the beam on the target surface. In fact, the depth resolution corresponds to the thickness of the layer for which the sum energy losses for inward and outward pathways are equal to the energy resolution of the RBS method. So, for $\vartheta_1=80^\circ$ the depth resolution increased 5 times concerning to normal incidence (We do not consider the Cornell geometry which also allows enhancement of the depth resolution). Usually, the depth resolution for the RBS technique is declared to be about 10 nm. The experimental results obtained for very thin layers of middle mass elements are considered to evaluate the limiting depth resolution attainable with the RBS technique.

The first studied sample is the trilayer structure ⁵²Cr/⁵⁷Fe/⁵²Cr on an Al₂O₃ substrate with a thickness of the layers 7.3-7.4-7.3 nm, respectively. The thickness of the layer is known exactly because the technology of growth is well worked out. It is necessary to say that each element only contains one isotope.

Several spectra were collected for the every incident angle in order to have more full information about the samples. According to eq. (4), $\vartheta_1 = 83^\circ$ is accepted as optimal and Fig. 7. shows the appropriate spectrum. Its specific feature consists of superposition of scattering spectra on the first (Cr) and second (Fe) layers. The third layer, however, gives a separate peak in spite of the energy straggling effect.

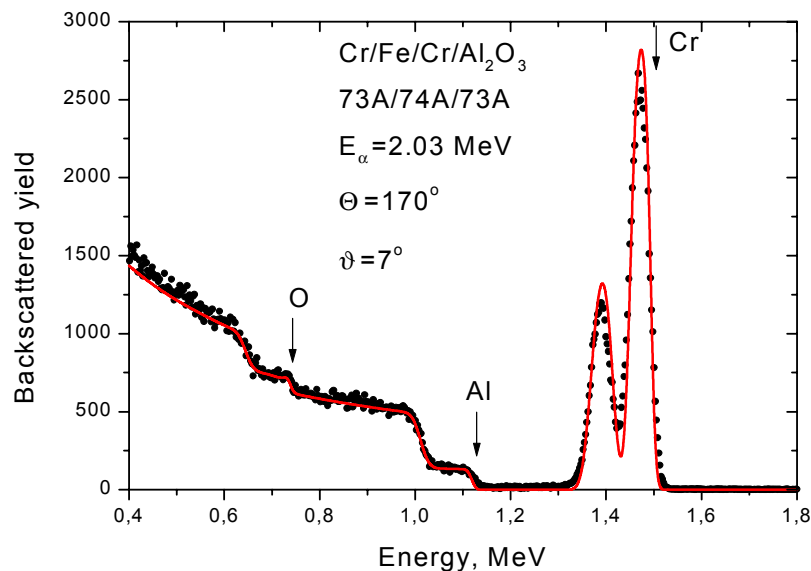


Fig. 7. Energy spectrum ^4He ions backscattered at a trilayer structure: (points) experimental data and (curve) results of a simulation for the energy resolution of 10 keV. Vertical arrows indicate the kinematic boundaries for the different elements.

The computer-simulated spectrum agrees satisfactorily with the experimental one in the description of the layers and the substrate. However, the calculation shows that the layered structure is not ideal. One can see from the spectrum that some fragments of the substrate go through all three layers to the surface (the arrows show Al and O kinematic boundaries). However, the contribution of these fragments is rather small – the trilayer structure covers the major part of the sample surface. The calculated spectrum has a sharper slope than the experimental one at the edges of the layers and the calculated yields in the peaks also appear to be somewhat higher. These discrepancies cannot be removed by changing of the model or increasing the energy straggling (the energy straggling is accepted equal to two Bohr values). Probably, these discrepancies can be explained by the presence of some structural imperfection.

The best description of the experimental spectrum for the assumed spectrometer resolution of 10 keV is obtained using a model sample consisting of three major layers, and two additional layers of mixed composition. The calculation shows that the thickness of the mixed composition layers reaches 5 nm. The summary thickness of the trilayer structure derived from the calculation is 21 ± 0.2 nm and it is larger than the rated thickness. It is obvious, that some substrate fragments contribute to the thickness for each layer and increase the total thickness of the sample.

Summarizing, one can point out that 5–7 nm layers consisting of middle mass elements are well resolved with the RBS technique using planar silicon detectors. The RBS spectrum contains information about not only the thickness but also the structure of layers to the depth about 40 nm.

An attempt to resolve layers of a smaller thickness, prepared using an advanced technology, has been made in a five-layer sample. The thickness of the layers determined using their rate of growth is 1.85–2.75–1.85–2.75–6.47 nm for Cr/Fe/Cr/Fe/Cr/Al₂O₃ structure.

Two Fe layers of 2.75 nm thickness divided by a 1.85 nm Cr layer are not resolved in the experimental spectrum. At the same time the first Cr layer looks like a separated peak in the calculated spectrum whose intensity, however, is twice less than intensity of the 6.45 nm Cr layer.

The layers of mixed composition on the boundary of one-element layers are incorporated into the model, which leads to better agreement between the experimental and calculated spectrum. So, in this way the influence of the sample roughness is partly taken into account. The thickness of the mixed composition layer amounts to about 1.5 nm. Of course, mixed composition layers cannot compensate completely the influence of the roughness and in particular, on the sample-vacuum interface their influence cannot be taken into account. The total thickness of the five-layer structure obtained by processing of the experimental spectrum is 19.7 nm, which is somewhat larger than the thickness measured during growing of the layers (15.7 nm).

So, the fulfilled experiments have shown:

1. Layered structures are similar to an ideal one in their properties (element contents and thicknesses are close to the value determined from technological conditions, the maximal roughness amounts to 5 nm and 1.5nm for two different samples).
2. The maximal resolution reached with the RBS technique in the IBM geometry applying a silicon planar detector amounts to 2 nm.
3. The RBS technique allows obtaining information about the contents, structure and roughness of the substrate and layers themselves with a period of several nanometers.

REFERENCES

- [1] TOLEMONDE, M., BOUFFARD, S., and STUDER, F. Nucl. Instr. and Meth. in Phys. Res. B91, 108 (1994).
- [2] DIDYK, A. Yu., VARICHENKO, V.S. Radiation measurements, 25, No 1–4, 119 (1995).
- [3] SZENES, G. Phys. Rev. B51, 8096 (1995).
- [4] DIDYK, A. Yu., VARICHENKO, V.S., ZAITSEV, A.M. JINR Commun. R14-95-144, Dubna, 1995.
- [5] DIDYK, A. Yu., KUZMIN, V.A., JINR Commun. R17-96–335, Dubna, 1996.
- [6] RAMOS, S.M.M., CANUT, B., AMBRI, M., CLEMENT, C., DOORYHEE, E., PITAVALL, M., THEVENARD, P., TOULEMONDE, M. Nucl. Instr. and Meth. in Phys. Res. B107, 254 (1996).
- [7] HOLLINGER, G., SKHEYTA, R., AND GENDRY, M., Phys. Rev. B49 (16) 1159–11172 (1994).
- [8] KAGADEI, V. A., PROSKUROVSKY D.I., Journal of Vacuum Science & Technology A-Vacuum Surfaces & Films. 16(4): 2556–2561, 1998 Jul-Aug.
- [9] ALAY, J. L., J. Appl. Phys. 77(7) 3010–3022 (1995).
- [10] TONE, K., IDE, Y. AND YAMADA, M., Jap. J. Appl. Phys. 32 5661–5665 (1993), part 1, N12A, December 1993.
- [11] CHU, W.-K, MAYER, J. W, NICOLET, M. A. Backscattering Spectrometry. New York: Academic Press. 1978. p. 198.
- [12] WILLIAMS, J.S. AND MÖLLER, W. Nucl. Instr. and Meth. 1978. V. 157. p. 213.
- [13] SHIROKOV, D.M., BOHAC, V. Nucl. Instr. and Meth. in Phys. Res. B84, 497–506 (1994).
- [14] KOBZEV, A.P., NIKONOV, O.A., DIDYK, A. Yu., SKURATOV, V.A. The Migration of Ta into Si under Influence Swift Heavy Ions Irradiation. Annual Report 1997. Frank Laboratory of Neutron Physics, Joint Institute for Nuclear Research. Dubna.
- [15] NEUSTROEV, E.P., SMAGULOVA, S.A., SKURATOV, V.A., DIDYK, A. Yu., ANTONOVA, I.V., OBODNIKOV, B.I., POPOV, V.P. Nucl. Instr. and Meth. in Phys. Res. B . Vol.146 N1-4 p.323–328 (1998).
- [16] DIDYK, A. Yu., KOBZEV, A.P., ORELOVICH, O, L., SEMINA, V.K., JINR Commun. E14–2000–107, Dubna, 2000.
- [17] AKIMOV, A.N., VLASUKOVA, L.A., KOMAROV, F.F., AND KULIK, M., J. Appl. Spectr. **59**, 96–100 (1993).
- [18] KULIK, M., KOBZEV, A.P., MACZKA, D., Preprint of JINR, E15-99–265, Dubna , 1999.
- [19] VERBITSKAYA, E, EREMIN, V, STROKAN, N, KEMMER, J, SCHMIDT, B, AND VON BORANY, J. Nucl. Instr. and Meth. 1994. B84. p. 51.

COMPARISON OF THE RESULTS ON THE ANALYSIS OF SEMICONDUCTOR MATERIALS BY ERDA AND RBS METHODS

M. BUDNAR, P. PELICON, A. RAZPET, B. ZORKO
Jozef Stefan Institute,
Ljubljana, Slovenia

Abstract

The final results of the project SLO10037 are presented. Experimental arrangement for the RBS/ERDA spectrometry at the J.Stefan Institute (JSI) 2 MV Tandetron was applied for the measurements of samples exchanged between the CRP collaborating groups. The analysis was done on various samples, including LiNbO_3 , GaN, CuInSe_2 , and several standards. The inter-comparative RBS/ERDA study of the samples has been performed and the results showed satisfactory agreement.

1. Scope of the project

The main aim of the JSI contribution to the CRP was to apply the already installed IBA techniques on the “real” problems faced when studying the composition and concentration profiles of the semiconductor and similar materials. The RBS and ERDA methods have been proved as a reliable experimental research tools for this purpose.

The following problems have been addressed in the study:

- to perform and clarify open questions of the RBS analysis of CuInSe_2 and $\text{CuIn}_{(1-x)}\text{Ga}_x\text{Se}_2$ samples,
- to analyze the results and the procedures of the RBS inter-comparison of TaN_x samples,
- to analyze the results and procedures of the ERDA inter-comparison measurements,
- to make the analysis of the comparative measurements on LiNbO_3 samples,
- to perform the H profiles in the GaN samples.

In this respect the two RBS arrangements installed recently at the HVEE TANDETRON MC 4117 2MV accelerator in Ljubljana served as the experimental set-ups. With the first one, RBS/ERDA station, the incidence of the projectiles onto the target was normally at 75° , take-off for RBS at 150° , and 25° for ERDA (using reflection geometry). Depth resolution achieved with RBS was 10–20 nm and for ERDA 25–50 nm. The estimations made for the RBS sensitivity gave 0.1 at. % for elements above Al and 10 at. % for the ones bellow Mg. The ERDA sensitivity for H was 0.1 at. %. Thin Al foils (3.6 μm) were used with ERDA to select the scattered He projectiles from the measured H spectrum. The second one, PIXE/RBS station, served with the incidence angle of projectiles on the target at 90° , and the take-off angle was up to 165° . The measurements were done mostly with He ions with energies of up to 2.1 MeV, and partly by Li ions having energies of up to 3 MeV.

As agreed at the RCM [1] of the CRP “*Application of MeV Ion Beams for Development and Characterization of Semiconductor Materials*” collaboration between the participants has been reestablished. The JSI team worked with the following groups on the inter-comparison analysis exercise of the semiconductor materials:

- *Structure of CuInSe_2 and $\text{CuIn}_{1-x}\text{Ga}_x\text{Se}_2$ thin films*: Atomic Energy Centre, Dhaka (M. Khaliqzaman), University of Albany (W.Lanford)
- *Inter-comparison of TaN_x (and additionally, Ge-H-Si-O/Si) with RBS*: University of Albany (W.Lanford), Atomic Energy Centre, Dhaka (M. Khaliqzaman),
- *Inter-comparison of H standards with ERDA and NRA*: University of Albany (W.Lanford),
- *Inter-comparison of H contents in LiNbO_3* : Institute of Chemical Technology, Prague (J.Hradilová-Špírková), University of Albany (W.Lanford), Joint Institute of Nuclear Research, Dubna (Kobzev),

- *H profiles in LiNbO₃* : Institute of Nuclear Physics, Řež (J.Vacík) , Institute of Chemical Technology, Prague (J.Hradilová-Špirková) , Institute of Physics, Prague (H.Turčičová),
- *H profiles in GaN single crystals and epilayers* : Institute of Nuclear Studies, Swierk-Otwock (A.Turos).

2. Results

The main emphasis of the JSI contribution has been given to the inter-comparison of analytical approaches between the collaborating laboratories. On the basis of the results achieved the improvements of the existing RBS/ERDA and PIXE/RBS arrangement have been done. The work performed can be described in some more details as follows.

2.1. Cross comparison of RBS analysis of CuInSe₂ and CuIn_{1-x}Ga_xSe₂ samples

For this task the samples were exchanged between J.Stefan Institute (JSI), and Atomic Energy Centre (AEC). The CuInSe₂ and CuIn_{1-x}Ga_xSe₂ samples prepared at AEC were sent to JSI, and several thin film standards (TiN, CuN, etc.), prepared at JSI, were mailed back to AEC. All the samples as received from AEC have been measured and analyzed at JSI. Evaluation of concentration profiles for the AEC samples was not simple from the RBS analytical point of view due to their complicated stoichiometry composition.

At the moment there is no information if the measurements and analysis of the JSI standards have been performed at AEC and what are the results.

The RBS measurements were done at the PIXE/RBS chamber with He¹⁺ ions at 2100 keV energy. The measurements were current-normalized by measuring the charge collected on the entire measuring chamber. The dose was 10 μCb per sample. The energy resolution of the detector was estimated to be 15 keV at 2 MeV. The spectral data were simulated using SIMNRA code [2].

The results for eight samples analyzed are given in Table 1. The expected composition can be reproduced relatively well though several admixtures can be detected which probably stem from handling of the samples [3].

2.2. Cross comparison of the RBS procedures for “general” thin film analysis

The TaN_x samples from University of Albany (UA) were sent to J.Stefan Institute (JSI) and Atomic Energy Center (AEC) for the RBS measurements and analysis. In this report the inter-comparison between the JSI and the UA results is presented [4–7]. At JSI the current-normalized RBS measurements with 1.8 MeV He¹⁺ beam were performed, scattering angle was 160°, incidence was at 90°, and charge was 5 μCb (with 5 nA current). It showed up that the determination of the stoichiometry composition in TaN_x films was strongly dependent on the quality of the impact current normalization. The cross-comparison of the results demonstrated the failure of the substrate normalization approach for this type of samples. By electric insulation of the entire measuring chamber a precise current normalization of the RBS spectra was achieved. The data obtained by *the current normalization method* led to excellent agreement between the JSI and the UA results (Fig.1 and Table 2). Due to wide interest in thin nitride layers (tool coatings, surface hardening, etc.) the cross-comparison study resulted in benefits which are of great importance for further IBA studies at JSI.

For further testing of the RBS arrangements two different Ge-H-Si-O/Si samples (H239, H289) were additionally prepared at UA, and sent to JSI and AEC for analysis. The JSI results are given in Table 3. For this purpose the He¹⁺ ions had energy of 2.03 (2.1) MeV, RBS scattering angle was 150° (160°), and the charge collected was 10 μCb at the JSI measurements.

TABLE 1. COMPOSITION AND CONCENTRATIONS PROFILES FOR $\text{CuIn}_{(1-x)}\text{Ga}_x\text{Se}_2$ SAMPLES AS PREPARED BY AEA.

| LAYER | Kh1A | | | Kh2A | | | Kh2Se1A | | | Kh2Se3B | | | | | | | | | | | | | | |
|--------|---|-------------|-----|------|---|-------------|---------|-----|---|-------------|-----|-----|-----|-----|-----|-----|-----|-----|-----|-----|-----|-----|-----|-----|
| | Thickness 10^{15} at/cm ² | Composition | | | Thickness 10^{15} at/cm ² | Composition | | | Thickness 10^{15} at/cm ² | Composition | | | | | | | | | | | | | | |
| | | Cu | Ga | Se | | In | O | Si | | Cu | Ga | Se | In | O | Si | | | | | | | | | |
| LAYER1 | 160 | .25 | .05 | .52 | .18 | 200 | .14 | .07 | .52 | .13 | .14 | 160 | .28 | .07 | .45 | .20 | 260 | .32 | .10 | .25 | .10 | .23 | | |
| LAYER2 | 190 | .24 | .05 | .53 | .18 | 190 | .14 | .07 | .60 | .08 | .11 | 130 | .27 | .09 | .48 | .16 | 300 | .29 | .11 | .30 | .12 | .18 | | |
| LAYER3 | 170 | .20 | .05 | .53 | .22 | 220 | .16 | .07 | .57 | .20 | | 190 | .26 | .09 | .47 | .18 | 300 | .25 | .13 | .36 | .24 | .02 | | |
| LAYER4 | 150 | .18 | .08 | .52 | .22 | 100 | .18 | .08 | .50 | .24 | | 170 | .22 | .09 | .48 | .21 | 120 | .15 | .12 | .48 | .25 | | | |
| LAYER5 | 120 | .15 | .10 | .50 | .23 | 100 | .20 | .09 | .40 | .20 | .11 | 150 | .21 | .10 | .47 | .22 | 200 | .12 | .14 | .47 | .22 | .05 | | |
| LAYER6 | 120 | .15 | .10 | .43 | .18 | 100 | .17 | .10 | .32 | .11 | .30 | 120 | .20 | .10 | .47 | .21 | 120 | .11 | .12 | .22 | .05 | .43 | .07 | |
| LAYER7 | 120 | .13 | .07 | .36 | .10 | 120 | .14 | .09 | .24 | .08 | .45 | 120 | .19 | .10 | .39 | .18 | .14 | 120 | .08 | .07 | .19 | .05 | .45 | .16 |
| LAYER8 | 180 | .10 | .05 | .18 | .06 | 180 | .10 | .09 | .16 | .04 | .61 | 220 | .17 | .07 | .32 | .10 | .24 | 120 | .08 | .07 | .10 | .02 | .53 | .20 |
| LAYER9 | - | | | | | - | | | | | | 180 | .10 | .05 | .18 | .06 | .48 | - | | | | | | |

(Table 1. cont.)

| LAYER | Kh2tB | | | Kh3C | | | Kh4A | | | KhUnA | | | | | | | | | | | | |
|--------|---|-------------|-----|------|---|-------------|------|-----|---|-------------|-----|-----|-----|-----|-----|-----|-----|-----|-----|-----|--|--|
| | Thickness 10^{15} at/cm ² | Composition | | | Thickness 10^{15} at/cm ² | Composition | | | Thickness 10^{15} at/cm ² | Composition | | | | | | | | | | | | |
| | | Cu | Ga | Se | | In | O | Si | | Cu | Ga | Se | In | O | Si | | | | | | | |
| LAYER1 | 160 | .20 | .06 | .45 | .13 | 160 | .14 | .10 | .23 | .10 | .43 | 160 | .19 | .10 | .40 | .12 | 300 | .75 | .25 | | | |
| LAYER2 | 270 | .20 | .07 | .50 | .17 | 190 | .14 | .10 | .37 | .10 | .29 | 250 | .18 | .10 | .50 | .13 | 300 | .58 | .42 | | | |
| LAYER3 | 320 | .20 | .09 | .50 | .18 | 220 | .17 | .10 | .40 | .16 | .17 | 320 | .18 | .10 | .50 | .13 | 170 | .02 | .57 | .41 | | |
| LAYER4 | 300 | .19 | .09 | .50 | .17 | 80 | .18 | .10 | .38 | .22 | .12 | 220 | .15 | .11 | .49 | .13 | 170 | .03 | .62 | .35 | | |
| LAYER5 | 300 | .19 | .09 | .49 | .16 | 80 | .15 | .10 | .36 | .16 | .23 | 220 | .12 | .12 | .45 | .11 | 320 | .12 | .65 | .23 | | |
| LAYER6 | 100 | .17 | .10 | .25 | .11 | 100 | .17 | .10 | .28 | .11 | .34 | 400 | .11 | .12 | .22 | .05 | 360 | .29 | .59 | .12 | | |
| LAYER7 | 120 | .14 | .09 | .24 | .08 | 120 | .14 | .07 | .24 | .08 | .47 | 120 | .09 | .08 | .17 | .03 | - | | | | | |
| LAYER8 | 180 | .10 | .09 | .16 | .04 | 180 | .10 | .09 | .16 | .04 | .61 | 180 | .08 | .07 | .18 | .02 | - | | | | | |
| LAYER9 | - | | | | | - | | | | | | - | | | | | - | | | | | |

BULK (500.000 at/cm²) O 0.625 Na 0.10 Si 0.25 Ca 0.025 = SiO₂ with admixtures.

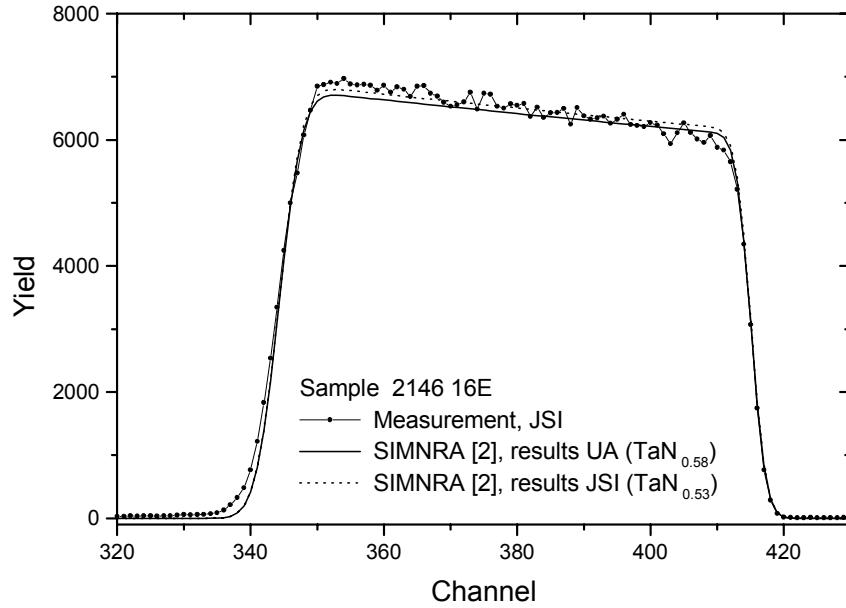


Fig. 1. Inter-comparison between the UA and the JSI results on the TaN_x sample (2146 16E) measured at JSU by current-normalization RBS approach.

TABLE 2. RESULTS OF THE INTER-COMPARATIVE MEASUREMENTS ON THE UA TaN_x SAMPLES. THE JSI RESULTS ARE PRESENTED AS OBTAINED BY CURRENT NORMALIZATION (IJS-CURRENT) AND FROM SUBSTRATE STECHIOMETRY (IJS-SUBSTRATE).

| Label | Comparison of results for the TaN_x films | | | | | |
|----------|---|-------------|---------------|--|-------------|---------------|
| | stechiometry label - x | | | Layer thickness [10^{15} at/cm ²] | | |
| | UA | JSI-current | JSI-substrate | UA | JSI-current | JSI-substrate |
| 2061 0E | 0.07 | 0.07 | 0.3 | 1170 | 1200 | 1250 |
| 2579 0C | 0.02 | 0 | 0.4 | 1470 | 1460 | 1700 |
| 2146 16E | 0.58 | 0.53 | 0.8 | 1670 | 1640 | 1700 |
| 2587 16C | 0.39 | 0.4 | 0.9 | 1930 | 1850 | 2250 |
| 2105 18E | 0.85 | 0.75 | 1.2 | 1750 | 1720 | 1900 |
| 2587 18C | 0.71 | 0.61 | 1.2 | 2100 | 2000 | 1900 |
| 1964 20E | 1.07 | 0.92 | 1.3 | 1750 | 1670 | 1820 |
| 2429 20C | 0.91 | 0.85 | 1.2 | 2100 | 2000 | 2240 |
| 814 22E | 1.50 | 1.63 | 1.9 | 800 | 760 | 1100 |
| 1198 22C | 1.50 | 1.44 | 1.9 | 1050 | 1000 | 1100 |
| 1960 BE | 0.83 | 0.85 | 1.0 | 1700 | 1640 | 1700 |
| 2304 BC | 0.86 | 0.82 | 1.1 | 2200 | 2010 | 2160 |

TABLE 3. INTER-COMPARISON ON THE UA Ge-H-Si-O/Si SAMPLES

| | H239 | | H289 | |
|---------|--|-------------------|--|-------------------|
| | Thickness [10^{15} at/cm ²] | Composition Ge Si | Thickness [10^{15} at/cm ²] | Composition Ge Si |
| LAYER 1 | 6700 | 0.24 0.76 | 9270 | 0.67 0.33 |
| LAYER 2 | 100.000 | 1.00 | 100.000 | 1.00 |

2.3. Cross comparison of the hydrogen standards with ERDA and RBS

Two H standards (ASM20, ASM35) as prepared at University of Albany (UA) were sent to J.Stefan Institute (JSI), and analyzed on H profiles by ERDA method. The He^{1+} ions with energy of 1.8 MeV were applied at 77.5° incidence, take-off angle for ERDA was 24° (Al foil 6 μm), take-off angle for RBS was at 150° , and collected charge was 20 μCb . The same samples were analyzed with NRA at UA, previously. The inter-comparison (Table 4) gives fairly satisfactory results. It is worthwhile to mention that the JSI ERDA arrangement and analytical procedures used have been checked extensively already before. In this respect several samples with known H composition, or the ones with known H profiles, were measured.

TABLE 4. HYDROGEN CONCENTRATIONS IN THE UA SAMPLES AS MEASURED BY NRA AT UA AND BY ERDA AT JSI

| Sample | UA | | JSI | |
|--------|------------|---------------------|--|---------------------|
| | H/Si ratio | Concentration (at%) | Stechiometry | Concentration (at%) |
| ASM 20 | 0.58 | 22.4 | $\text{Si}_{1.0} \text{N}_{1.4} \text{H}_{0.66}$ | 21.67 |
| ASM 35 | 0.26 | 11.5 | $\text{Si}_{1.0} \text{N}_{1.0} \text{H}_{0.26}$ | 10.6 |

2.4. Comparison of H contents in LiNbO_3

Some selected LiNbO_3 samples were studied on H profiles in collaboration between Institute of Chemical Technology (ICT), University of Albany (UA), Joint Institute of Nuclear Research (JINR), and J.Stefan Institute (JSI). The LiNbO_3 samples prepared in Prague were distributed to the other three institutions and the comparative analysis was performed. At UA the H analysis of the ICT samples was done by the ^{15}N nuclear reaction method. The JINR laboratory applied the RBS, NRA and ERDA methods, and for ERDA they used 3.1 MeV He ions. The JSI group made the analysis by ERDA method with 1.8 MeV He^{1+} ions. The results show fairly good agreement (within 20–30 %) as given in Table 5 and Fig.2.

2.5. Determination of H profiles in LiNbO_3

In this activity Institute of Chemical Technology (ICT), Institute of Physics (IP), Institute of Nuclear Physics (INR), and J.Stefan Institute (JSI) were involved.

The lithium niobate (LiNbO_3), prepared as the X- or Z-cut crystals, is known as a perspective optical guide material due to its extraordinary refractive index. The ways how to achieve a sharp refractive index change in a thin surface layer have been studied intensively, and the proton exchange (PE) fabrication by the adipic acid treatment showed some excellent results in this respect. Therefore the scientific subject attacked in the study was the H profile at the surface of LiNbO_3 , after chemical (PE) or plasma treatment of the material.

For H profiles measurements the ERDA arrangement at JSI has been chosen. The He^{1+} projectiles were applied at energy of 1.8 MeV in the reflection geometry with incident angle of 75° , take-off angle of 24° , after transverse of 6 μm thick Al foil. The profiles obtained showed good agreement with the previously measured Li profiles, as determined by the NDP method [8]. The analytical results obtained from the H profiles confirmed the hypothesis following from the Li concentration profiles determination (Fig.3.). Namely, higher concentrations of hydrogen on the surface correspond to lower Li concentration what confirm the PE expectations for the particular cuts.

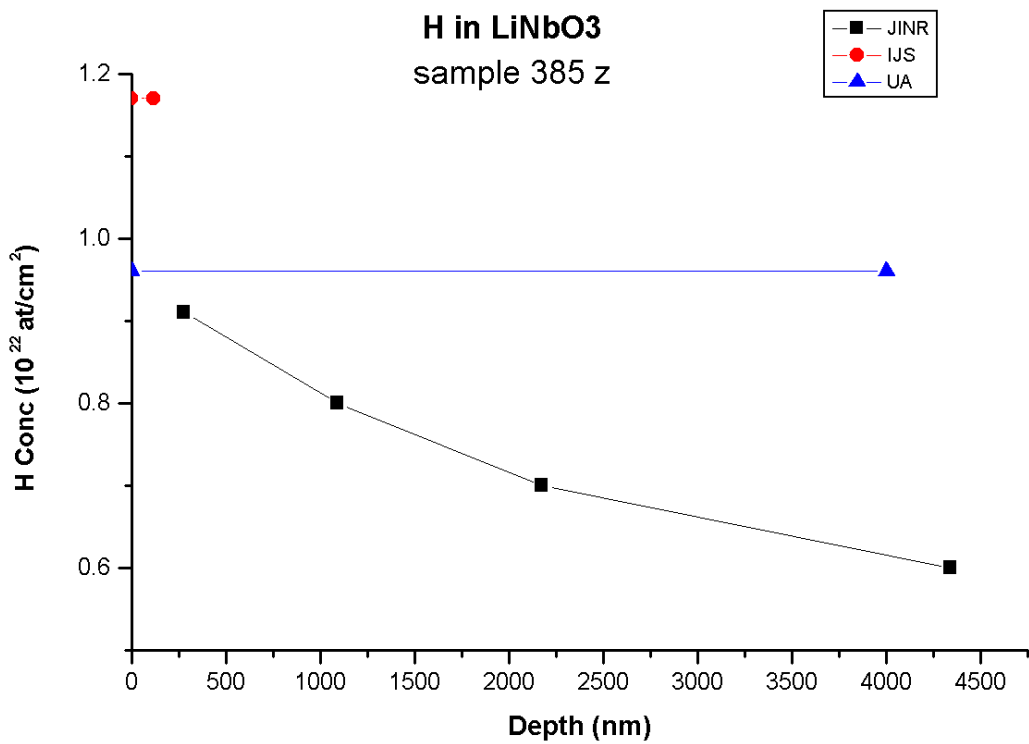
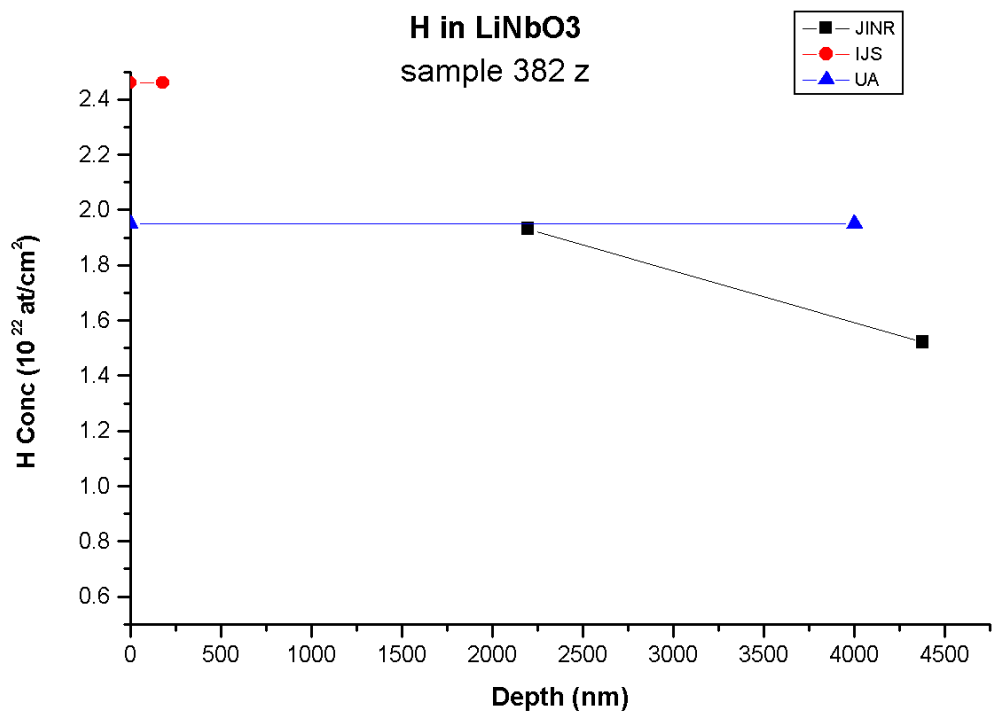


Fig. 2. Inter-comparison of H concentrations in the ICT LiNbO₃ sample as measured by NRA at UA, and ERDA at JINR and NR.

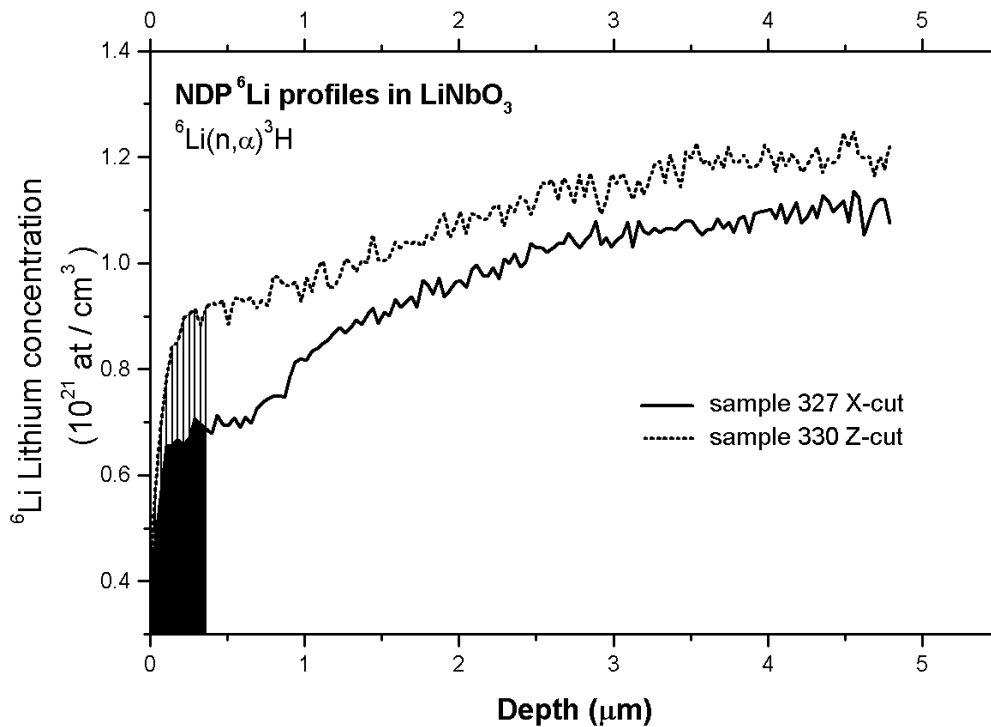
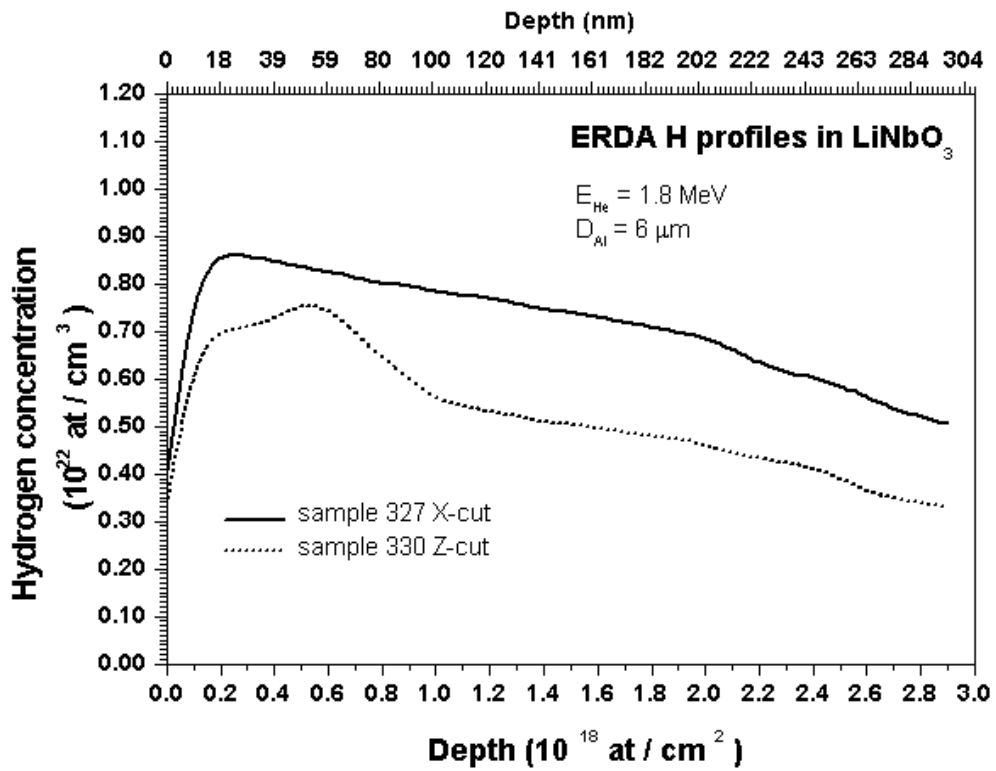


Fig. 3. H profiles on X- and Z-cut on the PE LiNbO₃ sample from ICT.

Still more, due to the excellent ERDA sensitivity for determination of H contents in thin surface layers ($< 0.5 \mu\text{m}$ for 2 MeV He) some better insight in the fabrication process has been obtained. The results of the common work were presented at several international conferences [10–13]. Also the paper related to the subject was published in the Nucl. Instr. Meth. [14]. In connection with this research some of the members from the Prague group (J.Hradilová-Špírková, H.Turčičová, P.Nekvindova, M.Slunečko) visited the JSI facility, and member of Ljubljana group (M.Budnar) visited Prague at the end of 1998 having a seminar there [9]. In year 2000 collaboration continued with the visit of P.Nekvindova when measurements on several LiNbO_3 samples were repeated and the data analyzed. The results confirmed the previous conclusions.

2.6. Determination of H content in GaN single crystals and epilayers

The GaN samples prepared at Institute of Nuclear Studies (INS) were sent to J. Stefan Institute (JSI), and analyzed on H profiles by the ERDA method. The experimental set-up was identical to the one at the LiNbO_3 measurements. As assured by the Swierk-Otwock group (INS) the preliminary results (Table 6) were satisfactory, but more profound studies on the GaN H profiles would need further work. There is a possibility to continue with these activities later on if INS would express further interest. It means that the scientific problem should be exchanged in more details and several additional samples should be measured to achieve statistically more relevant results.

TABLE 6. H PROFILES IN GaN SAMPLES PREPARED BY INS

| | GaN - foil | | GaN - sintered | |
|---------|--|--------------------------|--|--------------------------|
| | Thickness 10^{15} at/cm^2 | Composition Ga N H Pb | Thickness 10^{15} at/cm^2 | Composition Ga N H Pb |
| LAYER1 | 1000 | 1 1 0.07 - | 300 | 0.5 1.5 0.016 0.003 |
| LAYER2 | | | 300 | 0.6 1.4 0.016 0.003 |
| LAYER3 | | | 300 | 0.65 1.35 0.016 0.003 |
| LAYER4 | | | 300 | 0.7 1.3 0.016 0.003 |
| LAYER5 | | | 300 | 0.75 1.25 0.016 0.003 |
| LAYER6 | | | 300 | 0.85 1.15 0.016 0.003 |
| LAYER7 | | | 300 | 0.88 1.12 0.016 0.003 |
| LAYER8 | | | 300 | 0.92 1.08 0.016 0.003 |
| LAYER9 | | | 300 | 0.96 1.04 0.016 0.003 |
| LAYER10 | | | 50000 | 1.0 1.0 0.016 0.003 |

2.7. Conclusions

The J.Stefan Institute (JSI) group fulfilled a majority of tasks identified at the First CRP Co-ordination Meeting and signed under the 10037/R- contracts, as follows :

- to perform and clarify open questions of the RBS analysis of CuInSe_2 and $\text{CuIn}_{(1-x)}\text{Ga}_x\text{Se}_2$ samples,
- to analyze the results and the procedures of the RBS inter-comparison of TaN_x samples,
- to analyze the results and procedures of the ERDA inter-comparison measurements,
- to make the analysis of the comparative measurements on LiNbO_3 samples,
- to perform the H profiles in the GaN samples.

Standard IBA depth profiling methods, as used for the analytical work in the laboratory routinely, were applied to solve the given tasks. Main result of collaboration within the CRP was that it contributed to improvement of the analytical capabilities of the JSI laboratory. Many of the results achieved were also published in the international scientific community as seen from the references.

It seems worth to continue with the research activities started and to solve some of still open problems. In this respect the contacts already established between the participating groups should be very helpful. Still better output could be expected from the CRP if the meetings between the participants would be more often and the exchange of the results prompter.

ACKNOWLEDGEMENT

The authors would like to thank IAEA for accepting and financing this study as well for coordinating the CRP in a very successful manner.

REFERENCES

- [1] Report of the First RCM on the CRP “*Application of MeV Ion Beams for Development and Characterization of Semiconductor Materials*”, 2–5 June, Vienna, Austria.
- [2] MAYER, M., Forschungszentrum Jülich, Institut für Plasmaphysik, 1998.
- [3] PELICON, P., BUDNAR, M., ZORKO, B., RAZPET, A., *Characterization of thin films and surfaces by IBA techniques*, Nuclear Energy in Central Europe ‘99, Portorož, Sep 1999, NECE Book of abstracts, p.67.
- [4] LANFORD, W.A., PELICON, P., ZORKO, B., BUDNAR, M., *Determination of the nitrogen concentration in the TaN_x thin films by current-normalized RBS*, draft manuscript, sent to UA (W. Lanford) in Jan 2000.
- [5a] PELICON, P., BUDNAR, M., ZORKO, B., RAZPET, A., *Characterization of thin films and surfaces by IBA techniques*, Int. Conference Nuclear Energy in Central Europe ‘99, Portorož, Sep 1999, NECE Book of abstracts, p.67.
- [5] PELICON, P., BUDNAR, M., ZORKO, B., RAZPET, A., *Characterization of thin films and surfaces by Ion-Beam Analytical Techniques*, paper presented at the Int. Conference on Nuclear Energy in Central Europe, NECE Proceedings, Portorož, Sep 1999, p.595.
- [6] PELICON, P., BUDNAR, M., ZORKO, B., RAZPET, A., *Characterization of thin films and surfaces by IBA techniques*, *Materiali in tehnologije* 34 (2000) p.161.
- [7] PELICON, P., BUDNAR, M., ZORKO, B., RAZPET, A., *Merjenje lastnosti tankoplastnih struktur in površin s hitrimi ioni*, abstract submitted to the 8th Slovenian Meeting on Physics Applications, Moravske toplice 1999.
- [8] VACÍK, J., ČERVENA, J., HNATOWICZ, V., HAVRANEK, V., FINK, D., *Acta Physica Hungarica* 75 (1–4) (1994) 369.
- [9] BUDNAR, M., *The Ion Beam Analytical (IBA) Methods at the J.Stefan Institute TANDETRON*, invited seminar given at Institute of Physics, Prague, Dec 1998.
- [10] BUDNAR, M., ZORKO, B., PELICON, P., ŠPIRKOVÁ-HRADILOVÁ, J., KOLAROVA-NEKVINDOVA, P., TURČIČOVÁ, H., *ERDA study of H⁺ incorporated into lithium niobate optical layers*, poster presented at Int. Conference on Ion Beam Analysis, IBA-14, Dresden, 1999, P1–136.
- [11] NEKVINDOVA, P., ŠPIRKOVÁ, J., VACÍK, J., PERINA, V., BUDNAR, M., ZORKO, B., PELICON, P., SCHRÖFEL, J., *Properties of H:LiNbO₃ optical layers*, poster at XIVth Int.Symposium on the Reactivity of Solids, August 27–31, 2000, Budapest (Poster no.38).
- [12] NEKVINDOVA, P., ŠPIRKOVÁ, J., VACÍK, J., ČERVENA, J., BUDNAR, M., ZORKO, B., PELICON, P., SCHRÖFEL, J., *Properties of hydrogen containing optical layers in lithium niobate*, oral presentation at Solid State Chemistry 2000, September 3–8, 2000, Prague (Book of Abstracts, p.89).
- [13] RAZPET, A., ZORKO, B., BUDNAR, M., PELICON, P., NEKVINDOVA, P., ŠPIRKOVÁ, J., *Hydrogen profiles in lithium niobate optical layers*, presented at the CAARI 2000, Denton, Nov 2000.
- [14] BUDNAR, M., ZORKO, B., PELICON, P., ŠPIRKOVÁ-HRADILOVÁ, J., KOLAROVA-NEKVINDOVA, P., TURČIČOVÁ, H., *ERDA study of H incorporated into lithium niobate optical layers*, *Nucl.Instr.Meth.Phys.Res.* B161–163 (2000) 568.

STUDY OF THE COMPOSITION OF CuInSe_2 AND $\text{CuIn}_{1-x}\text{Ga}_x\text{Se}_2$ SEMICONDUCTOR THIN FILMS PREPARED BY EVAPORATION FOLLOWED BY ANNEALING USING RBS AND PIXE AND THEIR PROPERTIES

S.M. FIROZ HASAN, M. KHALIUZZAMAN, S.K. BISWAS, L. QUADIR,
M. ASAD SHARIFF, M. MASHIUR RAHMAN
Atomic Energy Centre,
Dhaka, Bangladesh

Abstract

Thin films of copper, indium and selenium have been deposited one above another onto a glass substrate by sequential and successive thermal evaporation of the individual elements in a vacuum to get a stacked layer. This stack was subsequently thermally annealed *in situ* at various temperatures and for different duration to form the compound of copper indium di-selenide, CuInSe_2 (CIS). The stoichiometric, structural and optical properties of the films have been measured by proton-induced X ray emission (PIXE) spectroscopy, X ray diffraction (XRD) and spectrophotometry in the photon wavelength range of 300 to 2500 nm, respectively. The influence of post-deposition annealing temperature and duration, and of Cu/In ratio on the optical and structural properties of the CIS films has been investigated. The films annealed at 350°C for 15 min have been found to have better qualities. The absorption coefficients of the films vary between 10^3 and 10^5 cm^{-1} in the measured wavelength range of photons, which do not vary systematically with the Cu/In ratios unlike the band gap energies that vary indirectly with the same ratios for In-rich films. The crystallites of all but the extremely In-rich films have (112) preferred orientations. The copper indium gallium di-selenide, $\text{CuIn}_{1-x}\text{Ga}_x\text{Se}_2$ (CIGS) films were also prepared by the same technique as for CIS. According to the decision of the first RCM held during 2–5 June 1998, at the IAEA HQ, Vienna; four sets of CIGS films were prepared under different experimental conditions and distributed among participant laboratories for cross comparison of RBS analysis. The results obtained have been analysed. Some discrepancies have arisen regarding the nominal (during growth) and experimentally measured (RBS and XRF) concentrations of Ga in the CIGS samples. With a view to retaining the Ga in CIGS, some new samples, having changed growth condition, were prepared and their compositions were measured by energy dispersive X ray (EDX) method. The compositional variations have been correlated with optical parameters.

1. Introduction

The ternary compound of copper indium diselenide CuInSe_2 (popularly referred to as CIS), in the form of thin film, has emerged as one of the most prospective materials to be used as an efficient absorber of solar radiation in thin-film solar cell devices [1–8] due to its high optical absorption coefficient ($\approx 10^5 \text{ cm}^{-1}$), near-optimum band gap energy ($\approx 1 \text{ eV}$), p-type conduction capability and high environmental stability.

It has been reported in the literature [9–10] that band gap energy of CIS can be increased by adding Ga in the sample i.e. if $\text{CuIn}_{1-x}\text{Ga}_x\text{Se}_2$ (CIGS) is prepared instead of CIS. Larger bandgap is likely to increase the open circuit voltage in photovoltaic devices. The properties of CIS and CIGS thin films are, mainly, dependent on their stoichiometry. Unlike binary compounds, extrinsic doping has not come out with remarkable success to modulate the properties of ternaries and quaternaries. In the case of ternary and quaternary compounds native defects play major role to control the stoichiometry. Formation of native defects is, among other parameters, dependent on the metallic atomic ratios in CIS and CIGS. Therefore, our intention has been to study the modulation of the properties of CIS and CIGS by varying Cu/In and In/Ga ratios in the compound during growth process, respectively.

In this investigation, we have employed the SEL technique [11–14] to deposit CIS and CIGS films and have used PIXE and EDX method to determine their compositions, respectively. Subsequently some stoichiometric CIS films were prepared and the post-deposition annealing condition was optimised through structural and optical characterisation. The optical properties of the films were studied by transmittance and reflectance measurements using a dual beam spectrophotometer in the photon wavelength range of 300 to 2500 nm.

2. Compositional Measurements

We previously measured the compositions of ten CIS samples utilizing PIXE method [15]. The experimental setup used for the irradiation of the samples by proton beam is shown in Fig. 1. The proton beam from the 3-MeV Van de Graaff accelerator of the Atomic Energy Centre, Dhaka, was passed through two tantalum collimators, each of 2 mm in diameter and a 4 mm clean-up aperture. The beam was then extracted into the air through 1.12 mg/cm² kapton window. The sample was bombarded with this external beam for 2 μ C of charge with beam current intensity of about 5 nA.

The characteristic X rays emitted from the samples were detected with an Ortec Si (Li) detector. The X ray pulses, after amplification, were analyzed with Canberra series 35 pulse height analyzer. A typical X ray spectrum obtained from a CIS sample is shown in Fig. 2. The peaks for copper, selenium and indium are indicated in the spectrum. Two peaks below the channel number 210 are due to the constituents of the glass substrate on which the film was deposited. Details of the method of calculation of the atomic composition by PIXE have been addressed in Ref. [15].

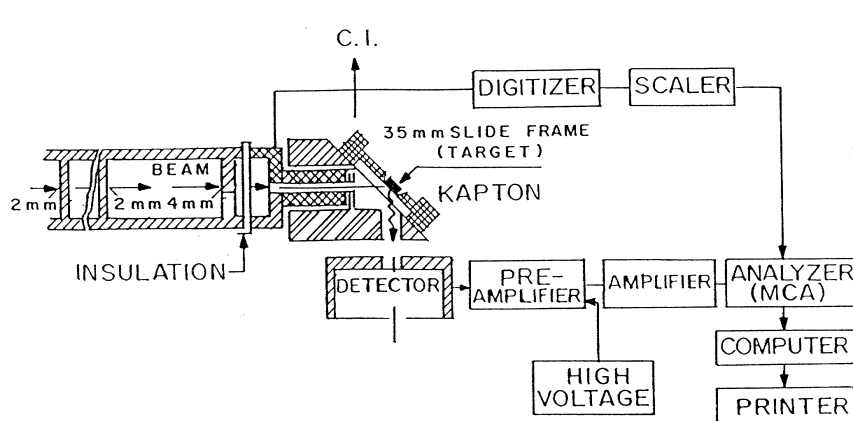


Fig. 1. Experimental setup for PIXE measurement.

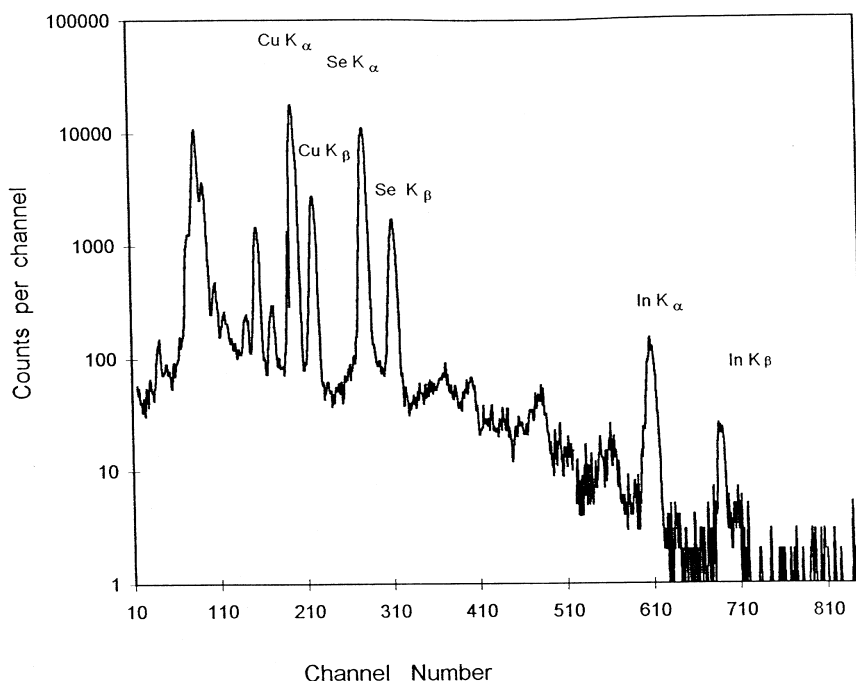


Fig. 2. Compositional analysis of CIS by PIXE.

3. Results and Discussion

Copper Indium Di-selenide

Fig. 3. shows the optical transmittance spectra of six samples that are annealed *in situ* at different temperatures and for different duration. It is clear, among the 15 minutes' annealed films, that the ternary compound of CIS does not form at the annealing temperature of 200°C (sample 25), as the corresponding spectrum does not show any well-defined absorption region. If the sample is annealed at 250°C (sample 26), it attains semi-conducting properties, which indicates that the formation of compound starts above the annealing temperature of 200°C. The samples annealed at 250°C and 400°C, however, do not show the desired largest near infrared (NIR) transmittance. The absorption regions are also essentially blunt. The transmittance spectrum attains its best shape for the sample annealed at 350°C for 15 minutes (21). From the spectra it is also noted that neither 10 minutes' nor 20 minutes' annealing at 350°C gives better characteristics than sample 21. The superior nature of the film annealed at 350°C for 15 min has also been manifested in Fig. 4. This sample (21) has sharper fundamental absorption region and lower NIR absorption. The values of the absorption coefficient, α and the energy gap, E_g of these samples, as calculated from the photon energy axes intercepts of the plot of $(\alpha h\nu)^2$ versus $(h\nu)$, where, h is Planck's constant and ν is the photon frequency, are illustrated in the inset of Fig. 4. The E_g of sample 21 is nearest to the optimum value (≈ 1 eV).

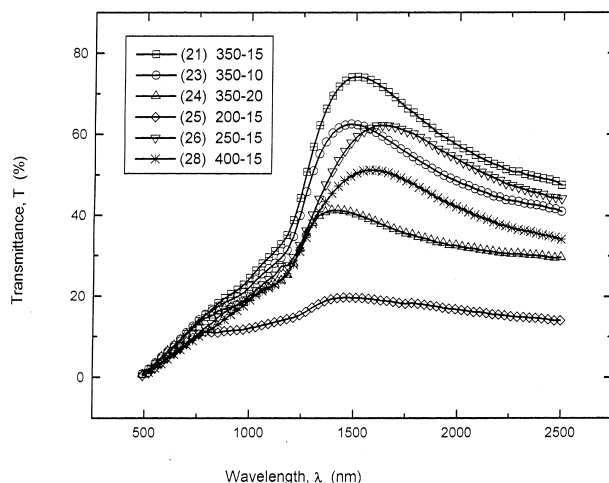


Fig. 3. Transmittance spectra of CuInSe_2 thin films having different growth conditions.

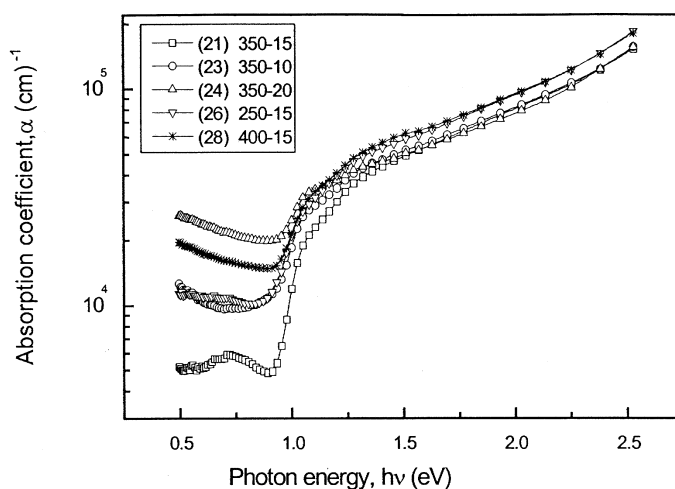


Fig. 4. Optical absorption coefficient spectra and band gap energy of the CuInSe_2 thin films having different growth conditions.

The variation of absorption coefficient with photon energy of CIS films annealed at 350°C for 15 min, having different Cu/In ratios are shown in Fig. 5. No systematic variation for the absorption coefficient with Cu/In ratio of these indium-rich films, above the fundamental absorption region, was obtained. The energy gaps of these samples have been calculated to be 0.967, 0.975 and 0.978 eV for Cu/In ratios of 0.958, 0.632 and 0.579, respectively, (inset) which show the inverse variation of E_g with Cu/In ratios. Hence, it is seen that, among the indium-rich films, more indium-rich films have higher energy gaps than less indium-rich ones.

The X ray diffraction patterns of CIS films having identical compositions and annealed *in situ* at 200°C, 250°C and 350°C for 15 minutes are shown in Fig. 6. All the films show the three intense peaks (112), (220/204) and (116/312) that indicate the crystalline phases of CIS. The intensities of the two doublets 220/204 and 116/312 peaks increase with annealing temperatures. It is further noted that the 116/312 peak does not split if the sample is annealed at 200°C for 15 minutes. The splitting of this peak begins at 250°C. At 350°C the splitting of this peak becomes sharper and well defined. The faint (103), (211) and (105/213) peaks are observed in the film annealed at 350°C for 15 minutes. These observations confirm that if the sample is annealed at 350°C for 15 minutes, it attains chalcopyrite crystalline phase. This happens because annealing causes the movement of the atoms to form the compound. The atoms favour certain temperature for interdiffusion. Before annealing, Se does not, generally, diffuse as it is in amorphous state. On annealing Se moves into the intermediate stage and CIS is formed at certain temperature [16]. Thus, both optical and structural measurements confirm the better quality of the film annealed at 350°C for 15 min.

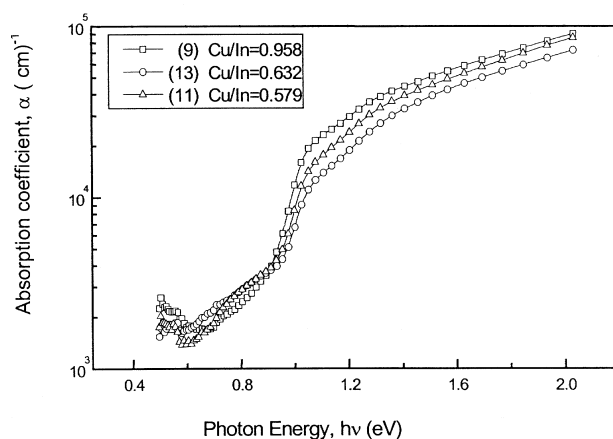


Fig. 5. Optical absorption coefficient and band gap energy spectra of the $CuInSe_2$ thin films having different compositions.

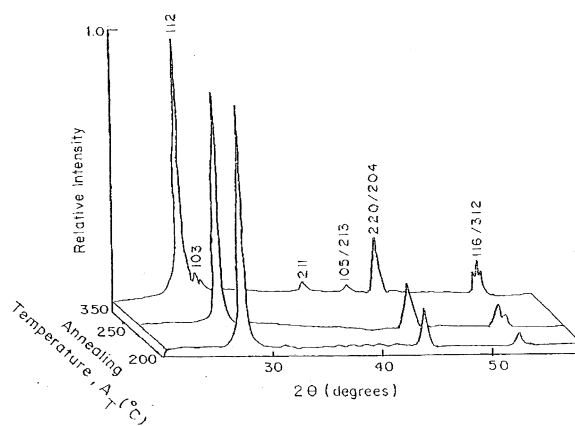


Fig. 6. The X ray diffraction pattern of CIS films having different post-deposition annealing temperatures.

It is noted in Fig. 7. that the near stoichiometric film has minor XRD peaks (211, 103), which are the strong indication that it attains chalcopyrite structure. It is further observed that the films have preferred orientation perpendicular to the (112) plane, which is independent of the annealing temperature (Fig. 6.) but depends on the Cu/In ratios (Fig. 7.). Extremely In-rich films do not have (112) preferred orientation. Tuttle et al [16] found preferred orientation perpendicular to the (220) plane instead of (112) plane for the Cu-poor films. Proper orientation is necessary to use the material, as an absorber in the solar cell for in that case there will be minimum lattice mismatch with the window material.

Copper Indium Gallium Di-selenide

The CIGS films were also prepared by the same technique as for CIS. According to the decision of the first RCM held between 2–5 June 1998, at the IAEA HQ, Vienna; four sets of $\text{CuIn}_{1-x}\text{Ga}_x\text{Se}_2$ (CIGS) thin film samples were prepared under different experimental conditions and distributed among participant laboratories for cross comparison of RBS analysis. The growth conditions of the films are summarized in Table 1. The nominal total film thickness was 388 nm. The compositional measurements have been performed by RBS method in Ion Beam Laboratories, State University of New York, USA, by a 4 MeV He beam. The X ray fluorescence (XRF) studies were done with Sn X rays bombarding the targets.

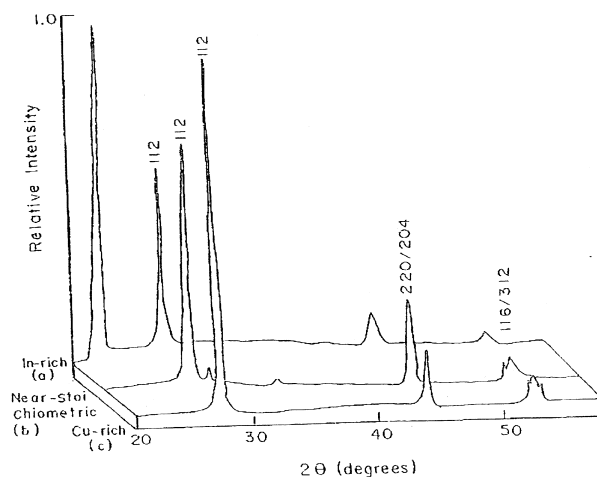


Fig. 7. The X ray diffraction pattern of CIS films having different compositions.

TABLE 1. THE GROWTH CONDITIONS OF CIGS FILMS

| Sample No. | Growth conditions | | | |
|------------|--|----------------------------|---|----------------------|
| | Annealing Temperature A_T ($^{\circ}\text{C}$) | Annealing Time A_t (Min) | $\text{CuIn}_{1-x}\text{Ga}_x\text{Se}_2$ ($x=\dots\dots\dots$) | Enhanced Selenium(%) |
| 1B | 350 | 15 | 0.20 | 30 |
| 2B | 350 | 15 | 0.25 | 30 |
| 3C | 350 | 15 | 0.30 | 30 |
| 4B | 350 | 15 | 0.35 | 30 |
| 2tD | 350 | 30 | 0.25 | 30 |
| 2Se1B | 350 | 15 | 0.25 | 25 |
| 2Se3A | 350 | 15 | 0.25 | 35 |

One representative RBS spectrum of CIGS (sample 1B) is shown in Fig. 8. There are three peaks due to Cu, In and Se and the relative intensities are close to the nominal values. The experimental data were simulated by RUMP. The data exceed the simulation for the Cu peak. They fit better to the simulation if a thin Ga layer is included as illustrated in Fig.9. In an attempt to detect Ga, X ray fluorescence (XRF) measurements were also done. An XRF spectrum is shown in Fig. 10. It is observed that the Ga peak is very weak compared to both the Cu and Se peaks. With a view to retaining the Ga, some new CIGS samples, having changed growth parameters (sequence: Glass-In-Ga-Se-Cu instead of Glass-In-Se-Ga-Cu), were prepared and their compositions were measured by EDX method.

The SEM images and EDX spectra for $\text{CuIn}_{1-x}\text{Ga}_x\text{Se}_2$ films with $x = 0, 0.20$ and 0.30 are shown in Figs. 11(a,b,c) and 12(a,b,c), respectively. The grain structure is somewhat prominent in 11b/12b in which Ga inclusion is optimal among the three samples. The sample 11b/12b is also near-stoichiometric. The optical transmittance and reflectance of the films are shown in Fig.13. The peak of transmittance shifts systematically towards higher energy with the Ga inclusion. The absorption coefficient and energy gap, E_g , of the samples are illustrated in Fig.14. It is obvious that the E_g increases with the partial replacement of In atoms by Ga atoms in CIGS. It seems, however, reasonable to guess that Ga inclusion in CIGS has some limiting values beyond which the sample properties deteriorate. To confirm this conclusion, further studies are required.

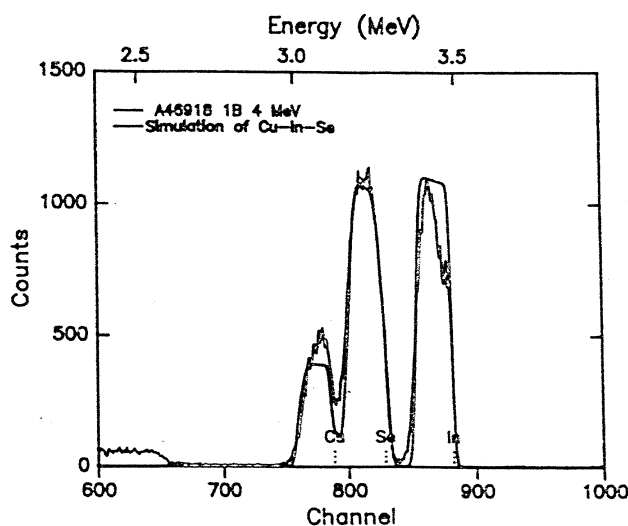


Fig. 8. The simulated RBS spectrum of CIGS film.

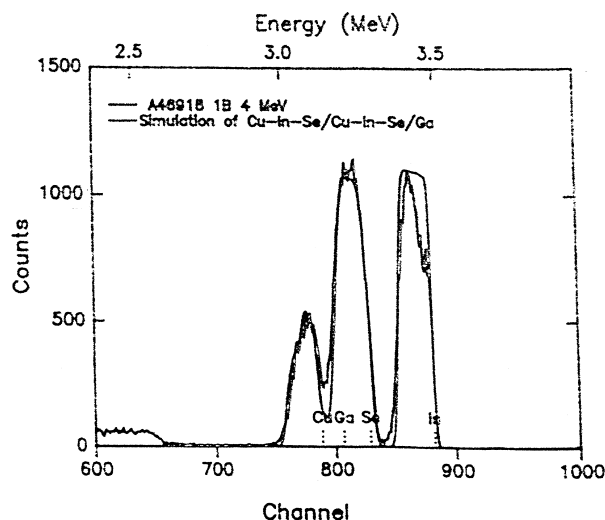


Fig. 9. The simulated RBS spectrum of CIGS film considering a Ga layer.

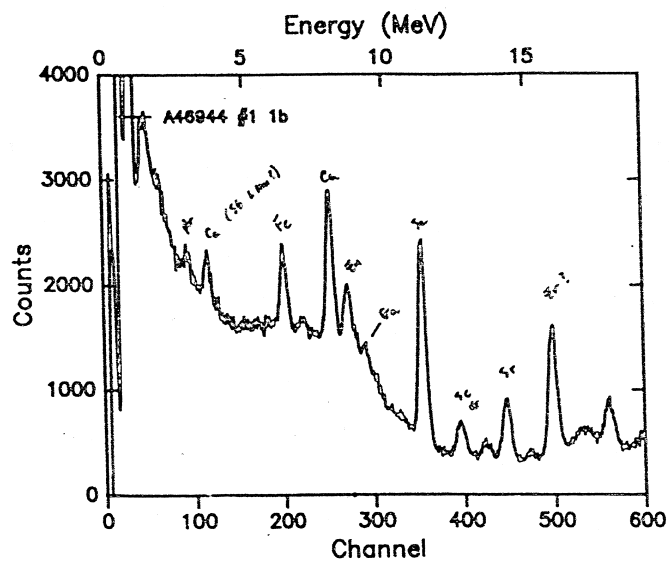


Fig. 10. The X ray fluorescence spectrum of CIGS film.



Fig. 11(a,b,c). The SEM images of CIGS films having various compositions.

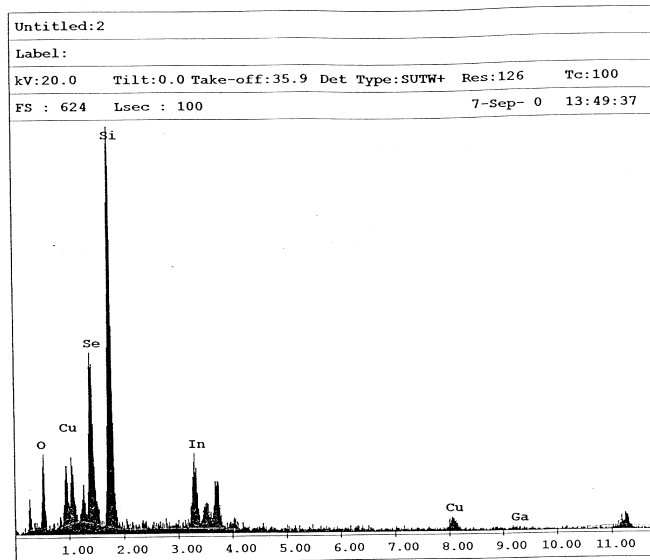


Fig. 12(a). The EDX spectra of the CIGS film ($x=0$).

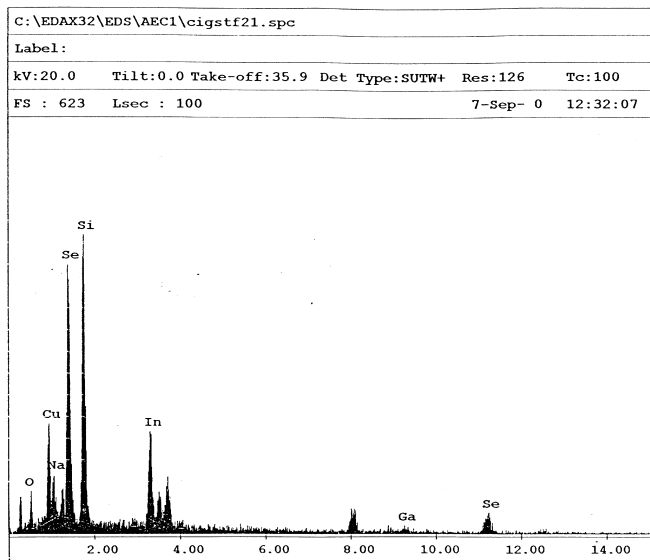


Fig. 12(b). The EDX spectra of the CIGS film ($x=0.20$).

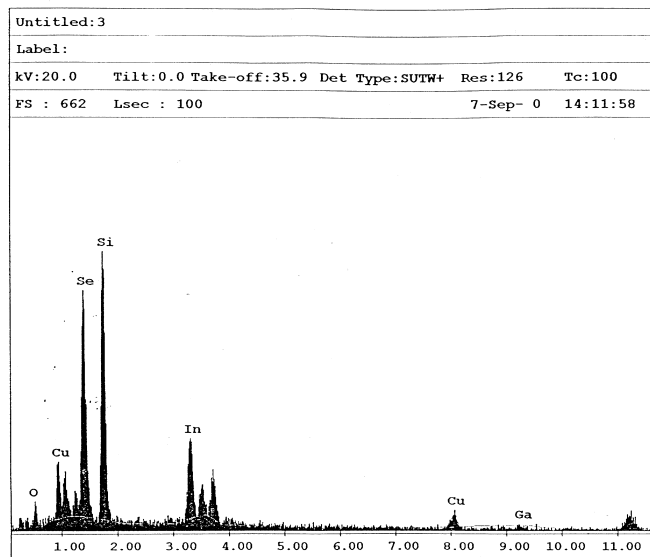


Fig. 12(c). The EDX spectra of the CIGS film ($x=0.30$).

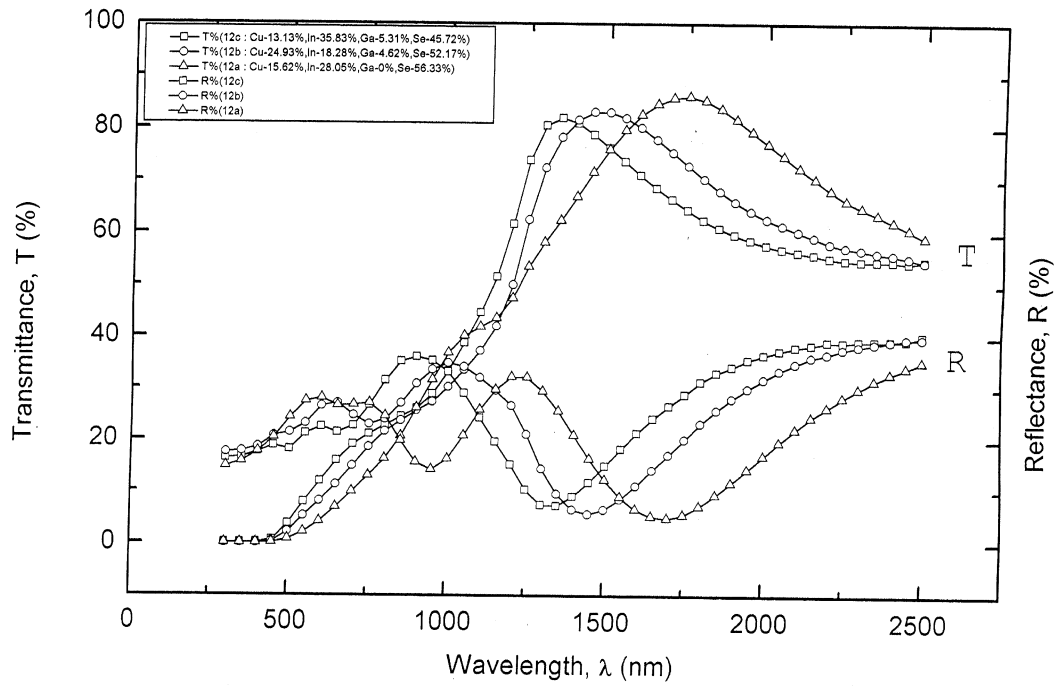


Fig. 13. The transmittance and reflectance spectra of CIGS films having various compositions.

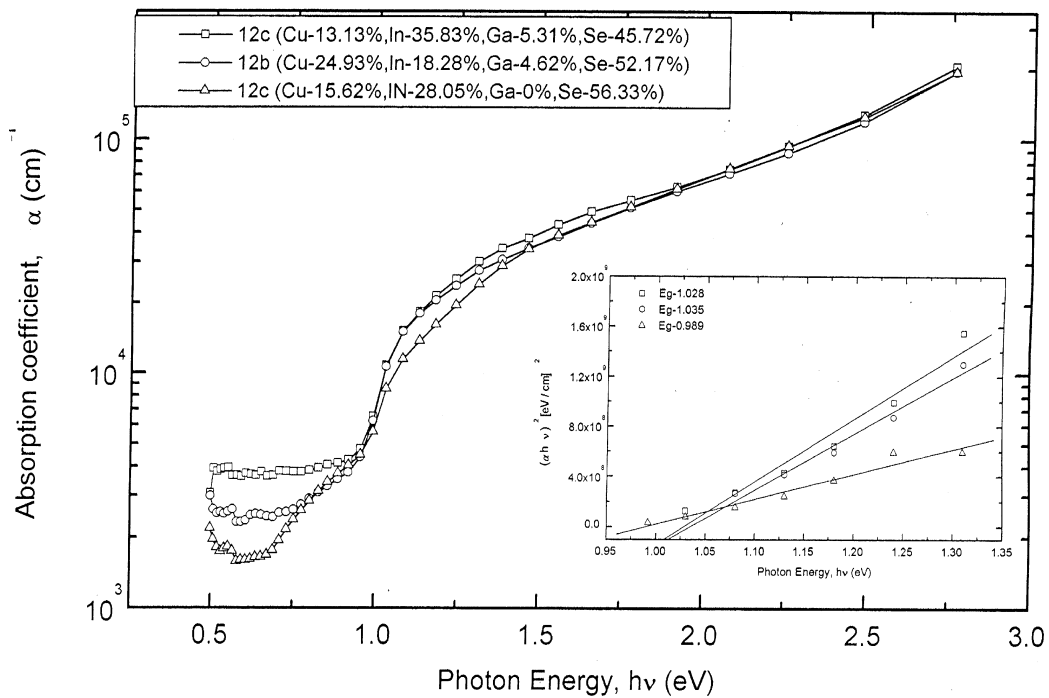


Fig. 14. The absorption coefficient spectra and energy gaps of CIGS films having various compositions.

4. Conclusions

Near-stoichiometric CIS films prepared by SEL technique followed by *in situ* thermal annealing at 350°C for 15 min appear to have reasonably acceptable optical and structural properties to be used as solar energy absorbers.

Controlled and limited replacement of In atoms by Ga atoms in CIS would result in higher energy gaps but the Ga addition also enhances the undesirable SBG absorption.

ACKNOWLEDGEMENTS

The authors wish to acknowledge their indebtedness to the concerned IAEA authority for extending an opportunity to work on such a scientifically and technologically important topic. They are grateful to Bangladesh Atomic Energy Commission (BAEC) for permitting them to work on the project. The authors owe much to the leading scientists : (i) Prof. Dr. Wm. A. Lanford, Ion Beam Laboratories, Department of Physics, University at Albany, State University of New York, New York, USA, (ii) Prof. Dr. Milos Budnar, Dept. of Low & Medium Energy Physics, Jozef Stefan Institute, Ljubjana, Slovenia and (iii) Dr. A. Z. Kiss, Institute of Nuclear Research, Hungarian Academy of Sciences, Debrecen, Hungary, because they have so generously extended their cooperation to measure the elemental composition of CIGS films for cross comparison. Thanks are also due to the respected colleagues: Prof. Dr. Ehsanul Huq, Prof. Dr. A. S. M. A. Haseeb and Dr. Quamrul Ahsan, Dept. of Materials and Metallurgical Engineering, Bangladesh University of Engineering & Technology (BUET) for their help in measuring composition of CIGS films by EDX method.

REFERENCES

- [1] WASIM, S. M., Solar Cells **16** (1986) 289
- [2] NEUMANN, H., Solar Cells **16** (1986) 317
- [3] TUTTLE, J. R., ALBIN, D., MATSON, R. J., NOUFI, R., J. Appl. Phys. **66** (1989) 4408
- [4] KAVCAR, N., CARTER, M. J., HILL, R., Sol. Energy Mater. Sol. Cells **27** (1992) 13
- [5] SCHMIDT, J., ROSCHER, H. H., LABUSCH, R., Thin Solid Films **251** (1994) 116
- [6] ADURODIJA, F. O., CARTER, M. J., HILL, R., Sol. Energy Mater. Sol. Cells **37** (1995) 203
- [7] ZWEIGART, S., SUN, S. M., BILGER, G. SCHOCK, H. W., Sol. Energy Mater. Sol. Cells **41/42** (1996) 219
- [8] GUILLEN, C., HERRERO, J., Sol. Energy Mater. Sol. Cells **43** (1996) 47
- [9] YAMAGUCHI, T., MATSUFUSA, J., YOSHIDA, A., J. Appl. Phys. **72** (1992) 5657
- [10] SCHWARTZ, R. J., GRAY, J. L., Proc. IEEE Photovoltaic Specialists Conf. Vol. 1, Kissimimee, Florida, USA, 1990, p570.
- [11] FIROZ HASAN, S. M., QUADIR, L., BEGUM, KH. S., SUBHAN, M. A., MANNAN, KH. M., Vacuum **55** (1999) 17
- [12] FIROZ HASAN, S. M., QUADIR, L., BEGUM, KH. S., SUBHAN, M. A., MANNAN, KH. M., Sol. Energy Mater. Sol. Cells **58** (4) (1999) 349
- [13] FIROZ HASAN, S. M., SUBHAN, M. A., MANNAN, KH. M., J. Phys. D: Appl. Phys. **32** (1999) 1302
- [14] FIROZ HASAN, S. M., SUBHAN, M. A., MANNAN, KH. M., Optical Materials **14** (2000) 329
- [15] KHALIQUZZAMAN, M., BISWAS, S. K., KHAN, A.H., FIROZ HASAN, S. M., SUBHAN, M. A., QUADIR, L., Nucl. Instrum. Meth. **B114** (1996) 332
- [16] TUTTLE, J. R., ALBIN, D.S., GORAL, J. P., NOUFI, R., Proc. IEEE Photovoltaic Specialists Conf. Vol. 1, Kissimimee, Florida, USA, 1990, p748.

ABBREVIATIONS

| | |
|-------------|--|
| EPD | Experimental Physics Department, University of Torino |
| SINR | Shanghai Institute of Nuclear Research, Shanghai |
| IRB | Ruder Bosković Institute, Zagreb |
| AEC | Atomic Energy Centre, Dhaka |
| UA | University of Albany SUNY, Albany |
| ATOMKI | Institute of Nuclear Research of the Hungarian Academy of Sciences, Debrecen |
| JINR | Joint Institute for Nuclear Research, Dubna |
| ICT | Institute of Chemical Technology, Prague |
| IP CAS | Institute of Physics of Czech Academy of Sciences, Prague |
| NPI CAS | Nuclear Physics Institute of Czech Academy of Sciences, Rez |
| <i>SINS</i> | <i>Soltan Institute for Nuclear Studies, Swierk</i> |
| JNP | Institute of Nuclear Physics, Almaty |

CONTRIBUTORS TO DRAFTING AND REVIEW

| | |
|--------------------|---|
| Asad Shariff, M. | Atomic Energy Centre, Bangladesh |
| Beke, D.L. | Kossuth L. University, Hungary |
| Biswas, S.K. | Atomic Energy Centre, Bangladesh |
| Budnar, M. | Jozef Stefan Institute, Slovenia |
| Červená, J. | Czech Academy of Sciences, Czech Republic |
| Chernenko, L.P. | Joint Institute for Nuclear Research, Russian Federation |
| Daróczy, L. | Kossuth L. University, Hungary |
| Didyk, A.JU. | Joint Institute for Nuclear Research, Russian Federation |
| Ditrói, F. | Institute of Nuclear Research of the Hungarian Academy of Sciences, Hungary |
| Elekes, Z. | Institute of Nuclear Research of the Hungarian Academy of Sciences, Hungary |
| Fazinic, S. | International Atomic Energy Agency |
| Firoz Hasan, S.M. | Atomic Energy Centre, Bangladesh |
| Guo, Panlin | Chinese Academy of Sciences, China |
| Hnatowicz, V. | Czech Academy Of Sciences, Czech Republic |
| Jaksic, M. | Rudjer Boskovic Institute, Croatia |
| Kazdaev, K.H.R. | Atomic Energy Agency of the Rep. of Kazakhstan, Kazakhstan |
| Kazdaev, R.KH. | Institute of Nuclear Physics of National Nuclear Center, Kazakhstan |
| Khaliquzzaman, M. | Atomic Energy Centre, Bangladesh |
| Kiss, A.Z. | Hungarian Academy of Sciences, Hungary |
| Kobzev, A.P. | Joint Institute for Nuclear Research, Russian Federation |
| Kulik, M. | Maria Curie-Sklodovska University, Poland |
| Langer, G.A. | Kossuth L. University, Hungary |
| Lanford, W.A. | University of Albany, United States of America |
| Li, Xiaolin | Chinese Academy of Sciences, China |
| Lu, Jiqing | Chinese Academy of Sciences, China |
| Manfredotti, C. | University of Turin, Italy |
| Maczka, D. | Maria Curie-Sklodovska University, Poland |
| Meermanov, G.B. | Institute of Nuclear Physics of National Nuclear Center, Kazakhstan |
| Mészáros, S. | Institute of Nuclear Research of the Hungarian Academy of Sciences, Hungary |
| Mushiur Rahman, M. | Atomic Energy Centre, Bangladesh |
| Nekvindová, P. | Institute of Chemical Technology, Czech Republic |
| Nikonov, O.A. | Joint Institute for Nuclear Research, Russian Federation |
| Nowicki, L. | The Andrzej Soltan Institute for Nuclear Studies, Poland |
| Pelicon, P. | Jozef Stefan Institute, Slovenia |
| Peřina, V. | Czech Academy of Sciences, Czech Republic |
| Quadir, L. | Atomic Energy Centre, Bangladesh |
| Razpet, A. | Jozef Stefan Institute, Slovenia |
| Simon, A. | Institute of Nuclear Research of the Hungarian Academy of Sciences, Hungary |
| Skuratov, V.A. | Joint Institute for Nuclear Research, Russian Federation |
| Stonert, A. | The Andrzej Soltan Institute for Nuclear Studies, Poland |
| Turčičová, H. | Czech Academy of Sciences, Czech Republic |
| Turos, A. | The Andrzej Soltan Institute for Nuclear Studies, Poland |
| Špírková, J. | Institute of Chemical Technology, Czech Republic |

| | |
|----------------|---|
| Vacík, J. | Czech Academy of Sciences, Czech Republic |
| Wang, Jiqing | Chinese Academy of Sciences, China |
| Yang, Rongrong | Chinese Academy of Sciences, China |
| Zhu, Jieqing | Chinese Academy of Sciences, China |
| Zorko, B. | Jozef Stefan Institute, Slovenia |

